About CO and H_2 Activation Mechanisms on Fe and Mo_2C Catalysts on the Basis of Density Functional Theory Computation and Ab Initio Atomistic Thermodynamics

Kumulative Dissertation
zur
Erlangung des akademischen Grades
doctor rerum naturalium (Dr. rer. nat.)
der Mathematisch-Naturwissenschaftlichen Fakultät
der Universität Rostock

vorgelegt von
Tao Wang
geb. am 09. 10. 1986 in P. R. China

Rostock, 30.03.2015

urn:nbn:de:gbv:28-diss2015-0140-8

Die vorliegende Arbeit entstand in der Zeit von Oktober 2012 bis März 2015 am Leibniz-Institut für Katalyse e.V. an der Universität Rostock

Gutachter der Dissertation:
1) Dr. Habil HaijunJiao
Leibniz-Institut für Katalyse e. V. an der Universität Rostock
Albert-Einstein-Str. 29a, D-18059 Rostock, Deutschland

2) Prof. Dr. Ralf Ludwig
Institut für Chemie, Universität Rostock
Dr.-Lorenz-Weg 1, 18059 Rostock, Deutschland

Tag der Einreichung: 30.03.2015
Tag der Verteidigung: 30.06.2015

Acknowledgments

At first, I would like to express my sincere gratitude and thanks to my supervisor *Dr. Habil* ***Haijun Jiao*** for giving me the great opportunity to do my Ph. D studies with him. Throughout the course of my work, his knowledgeable chemistry backgrounds, excellent talents in academic and cautious attitudes benefit me greatly. Without his wonderful suggestions, encouragements and patience, I could not have finished this dissertation. He let me know how to be a researcher and a team worker. Beside academic, he and his wife (Yihua Zhang) are also kind, amiable, and perfect persons, who have given me so many helps and cares in my daily life.

I would like to thank Prof. Matthias Beller and Dr. Yong-Wang Li. They created very nice academic atmospheres for young people's future developments. It is my great honour to be a member of their big teams.

Especially, I want to give my thanks to Dr. Shengguang Wang, Dr. Qiquan Luo, Dr. Gang Feng, Dr. Xinxin Tian, Dr. Yingyong Wang for their outstanding cooperation, helpful scientific discussions as well as valuable friendship, kind care and great help to me.

I would also like to thank all the brothers and sisters of LIKAT for the precious friendship, which had made my time in Germany a pleasant and worthwhile experience. They are Dr. Yuehui Li, Dr. Qiang Liu, Jianbin Chen, Dr. Xinjiang Cui, Dr. Chaonan Zheng, Dr. Yuting Fan, Dr. Ailing Qiao, Dr. Bin Li, Dr. Xiaofeng Wu, Dr. Lin He. Dr. Wanfang Li, Dr. Kaiwu Dong, Dr. Feng Chen, Dr. Xianjie Fang, Dr. Lipeng Wu, Dr. Shu-ping Luo, Dr. Yang Li, Haoquan Li, Chaoren Shen, Delong Han, Tian Xia, Jie Liu, Jianbo Feng, Yanyu Yang, Chen Jin.

In addition, I am thankful to my former colleagues in 908 group of SXICC and I really appreciated the times that I have spent with them. They are Dr. Chunfang Huo, Dr. Dongbo Cao, Dr. Xiaodong Wen, Dr. Xiaohu Yu, Dr. Yanni Li, Shaoli Liu, Yun Shi, Xingwu Liu, Xunhua Zhao, Shu Zhao, Rui Gao, Qiang Li, Bingyin Wang, Peng Zhao, Yurong, He.

I would also like to express my thanks to Mr Malte Willert and Matthias Linke for their technical support during this work.

Finally, I would like to thank my parents, my wife and cute son for giving me encouragements and supports during my studies.

Universität Rostock

Abstract

About CO and H_2 Activation Mechanisms on Fe and Mo_2C Catalysts on the Basis of Density Functional Theory Computation and Ab Initio Atomistic Thermodynamics

Tao Wang
Leibniz-Institut für Katalyse e.V. an der Universität Rostock

This thesis mainly focuses on theoretical investigations of CO and H_2 activation on the surfaces of iron and molybdenum carbide (Mo_2C) catalysts, which have been used in Fischer-Tropsch synthesis and alcohol synthesis. On the iron surfaces, H_2 adsorption is dissociative while CO adsorption states are coverage dependent; i.e.; molecular adsorption at high coverage and dissociative adsorption at very low coverage, as well mixed molecular and dissociative adsorption are possible at medium coverage. On the basis of atomistic thermodynamics, the computed CO and H_2 desorption states, temperatures and energies on the Fe(100), (110) and (111) surfaces are in good agreement with the available experimental results. For the Mo_2C catalysts, the stabilities and compositions of the surfaces are found to be highly dependent on the carburization conditions. Such differences in surface structures result in their distinct CO and H_2 activation activities. All these results shed new insights into the understanding of CO and H_2 activation mechanisms of heterogeneous catalysts, and form the basis for further rational investigation of hydrogenation mechanisms.

Die vorliegende Arbeit konzentriert sich hauptsächlich auf theoretischen Untersuchungen von CO- und H_2-Aktivierung auf den Oberflächen von Eisen und Molybdäncarbid (Mo_2C) Katalysatoren, die in Fischer-Tropsch-Synthese und Alkohol-Synthese verwendet wurden. Auf den Eisenoberflächen, H_2-Adsorption ist dissoziativ, während der CO-Adsorptionszustand vom Deckungsgrad abhängig ist, d.h. molekulare Adsorption beim hohen Deckungsgrad, dissoziative Adsorption bei sehr niedrigem Deckungsgrad, als auch gemischte molekulare und dissoziative Adsorption beim mittleren Deckungsgrad. Die auf der Grundlage der atomistischen Thermodynamik berechneten CO- und H_2-Desorptionszustände, Temperaturen und Energien auf den Fe(100), (110) und (111) Oberflächen stimmen sehr gut mit den experimentellen Ergebnissen überein. Für die Mo_2C Katalysatoren, die Stabilitäten und Zusammensetzungen der Oberflächen sind sehr stark von den Bedingungen der Aufkohlung anhängig; und solche Unterschiede in den Oberflächenstrukturen führen in verschiedenen CO- und H_2-Aktivierung Aktivitäten. Alle diese Ergebnisse werfen neue Einblicke in das Verständnis der CO- und H_2-Aktivierungsmechanismen von heterogenen Katalysatoren, und bilden die Grundlage für weitere rationale Untersuchungen der Hydrierungsmechanismen.

Table of Contents

1 Introduction 1

1.1 CO and H_2 activation on metallic iron catalyst 2

1.1.1 UHV surface science studies 4

1.1.1.1 Iron surface structures 5

1.1.1.2 CO adsorption on iron surfaces 6

1.1.1.3 H_2 adsorption on iron surfaces 10

1.1.2 Theoretical studies 12

1.1.2.1 CO adsorption and activation on iron surfaces 12

1.1.2.2 H_2 adsorption and activation on iron surfaces 16

1.2 CO and H_2 activation on Mo_2C catalysts 18

1.2.1 UHV studies of Mo_2C catalyst 20

1.2.1.1 Properties of Mo_2C surfaces 21

1.2.1.2 CO and O_2 adsorption on Mo_2C surfaces 21

1.2.1.3 Hydrocarbons reforming reactions 22

1.2.1.4 HDS and HDN reaction 24

1.2.2 Theoretical studies of Mo_2C catalyst 24

1.3 References 29

2 Objectives of this work 43

3 Summary and Publications 44

3.1 High Coverage CO Activation Mechanisms on Fe(100) from Computations 44

3.2 Coverage-Dependent CO Adsorption and Dissociation Mechanisms on Iron Surfaces from DFT Computations 45

3.3 Hydrogen Adsorption Structures and Energetics on Iron Surfaces at High Coverage 46

3.4 Stable Surface Terminations of orthorhombic Mo_2C Catalysts and their CO Activation Mechanisms 47

3.5 High Coverage CO Adsorption and Dissociation on the Orthorhombic $Mo_2C(100)$ Surface 48

3.6 Dissociative Hydrogen Adsorption on the Hexagonal Mo_2C Phase at High Coverage 49

3.7 Coverage Dependent Adsorption and Co-adsorption of CO and H_2 on the CdI2-antitype Metallic $Mo_2C(001)$ Surface 50

Curriculum Vitae

Selbstständigkeitserklärung

List of Abbreviations

AES	*auger electron spectroscopy*
CASTEP	*Cambridge Sequential Total Energy Package*
DPI	*dual polarization interferometry*
DFT	*density functional theory*
DOS	*density of state*
EELS	*electron energy loss spectroscopy*
FTS	*Fischer-Tropsch synthesis*
GGA	*generalized gradient approximation*
HDN	*hydrodenitrogenation*
HDS	*hydrodesulfurization*
HDH	*hydrodehalogenation*
ISS	*ion scattering spectroscopy*
LDA	*local density approximation*
LEED	*low-energy electron diffraction*
ML	*monolayer*
NEXAFS	*near edge X-ray absorption fine structure*
PW91	*correlation functional proposed by Perdew and Wang in 1991*
PBE	*correlation functional proposed by Perdew, Burke and Ernzerhof*
PAW	*projected-augmented-waves*
STM	*scanning-tunnelling microscopy*
SIMS	*secondary ion mass spectrometry*
TDS	*thermal desorption spectroscopy*
TPD	*temperature programmed desorption*
TMCs	*Transition metal carbides*
TPSR	*temperature programmed surface reaction*
USPP	*ultrasoft pseudopotentials*
VASP	*Vienna Ab initio Simulation Package*
WF	*work function*
WGS	*water gas shift*
XPS	*X-ray photoelectron spectroscopy*

1 Introduction

As very important and useful basic chemicals, carbon monoxide (CO) and hydrogen (H_2) have found wide applications in energy societies as well as value-added bulk and fine chemical productions. Most representative examples are Fischer-Tropsch synthesis (FTS),[1] alcohol synthesis and hydrogen production from water-gas shift (WGS) reaction.[2] Among these processes, FTS had attracted great attentions for providing low-sulfur diesel fuels.[3,4] This process is a key component of gas to liquids technology, which produces synthetic lubrication oils and synthetic fuels typically from coal, natural gas, or biomass (Figure 1). The conversion of CO and H_2 mixtures into aliphatic products obviously should be a multi-step reaction with different sorts of intermediates. The conversion of CO to alkanes involves C-O bond cleavage via hydrogenation and hydrogenolysis as well as the formation of C-C and C-H bonds. These reactions are assumed to proceed via the initial formation of surface-bound metal carbonyls. The CO molecules are speculated to undergo dissociation into surface carbon and oxygen atoms, which possibly oxidize and carburize the catalysts. Other potential intermediates are C1 fragments, including formyl (CHO), hydroxycarbene (HCOH), hydroxylmethyl (CH_2OH), methyl (CH_3), methylene (CH_2), methylidyne (CH) and hydroxymethylidyne (COH).

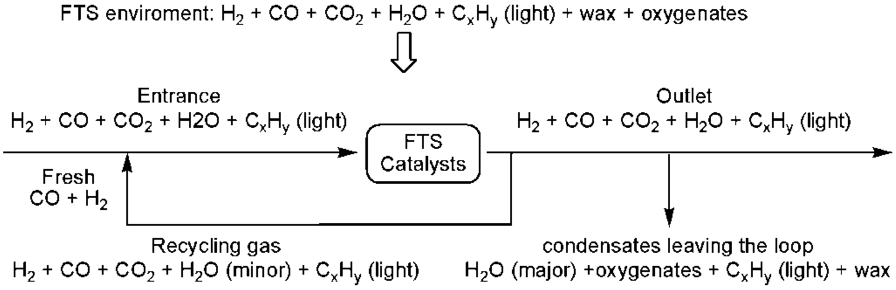
FTS enviroment: $H_2 + CO + CO_2 + H_2O + C_xH_y$ (light) + wax + oxygenates
Entrance
$H_2 + CO + CO_2 +$ H2O $+ C_xH_y$ (light)
FTS Catalysts
Outlet
$H_2 + CO + CO_2 + H_2O + C_xH_y$ (light)
Fresh CO + H_2
Recycling gas
$H_2 + CO + CO_2 + H_2O$ (minor) $+ C_xH_y$ (light)
condensates leaving the loop
H_2O (major) +oxygenates $+ C_xH_y$ (light) + wax

Figure 1: Schematic steps of complex Fischer-Tropsch synthesis

Nowadays, both experimental studies and theoretical modelling are attractive in the field of academic researches. Generally, theoretical and experimental investigations might have very intrinsic relationships in catalysis (**Figure 2**). There are mainly three steps in experimental research, i.e., using model catalysts to investigate reaction mechanisms and characterize surface properties on the basis of extensive surface science techniques under ultra-high vacuum conditions; in turn, performing fundamental laboratory work to investigate catalytic properties under practical condition (temperature and pressure); and finally performing large scale industrial applications on the basis of the obtained information. To deeply understand the intrinsic nature of experimental phenomena, it is desired to combine experiments tightly with theoretical studies. For several decades a major goal in catalysis study has been the rational development of state of the art materials. To achieve this goal, not only specific experimental characterization but also detailed DFT computation can play a complementary and decisive role.[5] Commonly DFT can describe the structures and properties of materials at atomic scales but only under ideal condition (0K and 0 atm). On the basis of DFT calculation, *ab initi*o atomistic thermodynamics can simulate surface stability and morphology of catalysts at different temperature, pressure and reaction atmosphere, and micro-kinetics can model the reaction mechanisms at given reaction conditions. Ideally, the interplay of informative experimental studies and accurate DFT computations can synergistically provide insights into surface structures of catalysts and rationalize the catalytic activities, and in turn, facilitate the rational design of novel selective catalysts.[6]

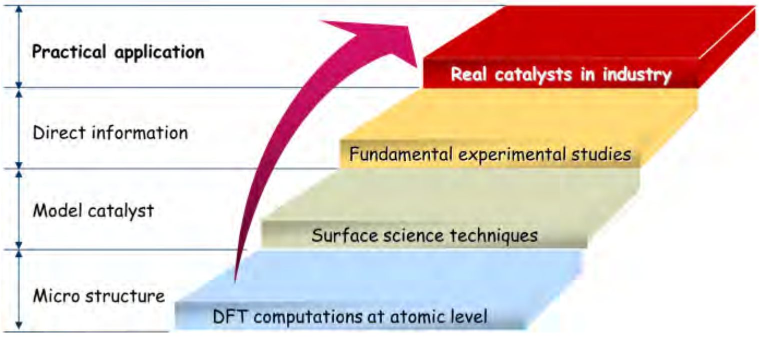
Practical application
Direct information
Model catalyst
Micro structure
Real catalysts in industry
Fundamental experimental studies
Surface science techniques
DFT computations at atomic level

Figure 2: Interplay between theory and experiment

1.1 CO and H_2 activation on metallic iron catalyst

From the wide investigations into FTS, mainly three reaction mechanisms were proposed and widely accepted. In the surface carbide mechanism (Figure 3),[7,8] the chain growth is proposed by CH_2 insertion. The first step is the dissociative adsorption of CO and H_2, followed by the formation of CH_2 entities which can combine and insert in growing chains. Chain termination can take place either by abstraction or addition of a hydrogen atom from or to the growing chain. This mechanism can well explain the formation of hydrocarbons, but fails to rationalize the formation of oxygenated products.

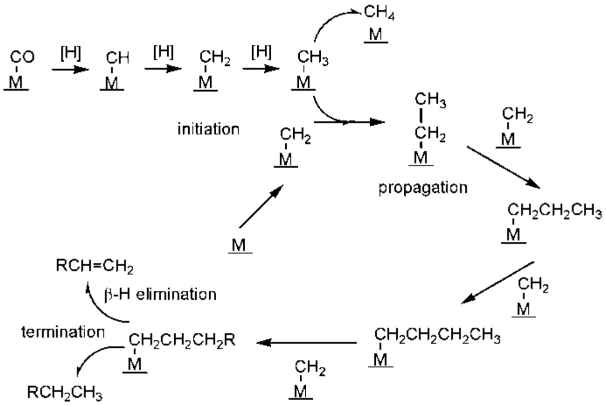
CO
M
[H]
CH
M
[H]
CH2
M
[H]
CH3
M
CH4
M
initiation
CH2
M
CH3
CH2
M
CH2
M
propagation
CH2CH2CH3
M
M
CH2
M
RCH=CH2
β-H elimination
termination
CH2CH2CH2R
M
CH2
M
CH2CH2CH2CH3
M
RCH2CH3

Figure 3: Schematic steps of surface carbide mechanism

In the surface enol mechanism (Figure 4), the chain growth is through CO non-dissociative adsorption. The surface H atoms react with the chemisorbed CO to form enolic (HCOH) entities which either combine through a surface polymerization condensation reaction with loss of water,[9] or the individual hydrogenation of the enolic entities to form water and CH_2 groups which can grow chains like the surface carbide mechanism.[10, 11] Experimentally, this mechanism is supported by infrared spectroscopy studies. For example, the formation of M=CHOH species is detected by the CO/H_2 co-adsorption on the iron based FTS catalysts. Interestingly, the chemisorbed CO and H_2 have a fixed ratio of 1:1, which is independent with the composition of syngas (CO/H_2) in the gas phase. Mass spectroscopy studies indicate that HCHO is the major intermediate but enol intermediates with long chains are hardly detected in this mechanism, which is regarded as the major drawback of the enol mechanism. However, enol mechanism can clearly verify the formation of branched products, which cannot be explained by the carbide mechanism. Till now, there is no conclusive evidence to support the enol mechanism, although M=CHOH might be the reaction intermediate from the reduction of CO into CH_4 or acyl reduction into alky.

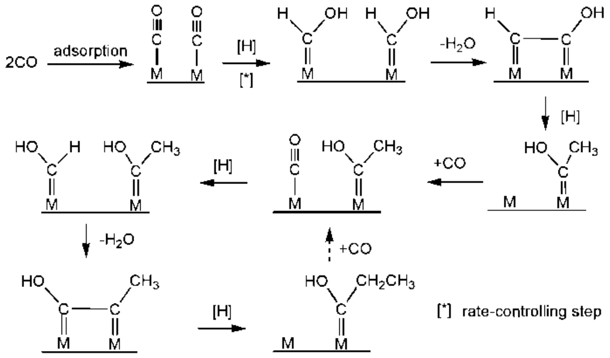

Figure 4: Schematic steps of surface enol mechanism

In the CO insertion mechanism (Figure 5), the chain growth undergoes CO insertion in the metal-carbon bonds. A CO molecule is inserted into the metal-H bond in the first step, and the formed surface formyl species is hydrogenated to CH_3 by nearby chemisorbed hydrogen atoms. Subsequently, CO can be inserted into the metal-carbon bond and the resulting enol species can be hydrogenated again. Chain growth takes place by repeating this step.[12-14] However, whether the M=$COCH_3$ species can exist under FTS reaction condition is still unknown, especially at high temperature and low CO partial pressure. On the basis of the tests of formaldehyde, glyoxal and CO/H_2 interactions with Al_2O_3 supported Rh catalyst, no formyl species was detected. Despite of great improvements in the understanding of CO insertion mechanism, more experimental supports are highly desired.

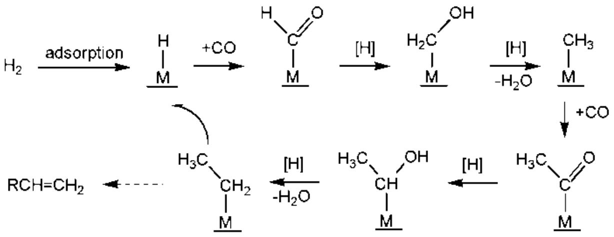

Figure 5: Schematic steps of surface CO insertion mechanism

On the basis of the quite different properties of FTS catalysts and reaction conditions as well as the diversity of FTS products distribution, many different reaction intermediates are possible on the surfaces of catalysts, and they will finally form the same products through different reaction mechanisms. As the result, there is still no available comprehensive and deep understanding of the detailed FTS mechanisms. In most cases, the above referred three mechanisms are widely regarded to work together. A recent FTS reaction mechanism investigation on the Fe_5C_2(001) surface[15] indicates the cooperation and coexistence of carbide and CO insertion mechanisms and each of them plays a complementary role to another; i.e., the chain initiation came from the CO insertion mechanism and chain growth followed the carbide mechanism.

Experimentally iron (Fe), cobalt (Co) and ruthenium (Ru) are the most widely investigated catalysts. Among these catalysts, Ru-based catalysts are most active for CO hydrogenation and are able to work at low temperatures (<150 °C) and to produce long-chain hydrocarbons even without any promoters.[16] However, the high costs and scarcity hinder their industrial-scale applications. As the result Co- and Fe-based catalysts have been widely applied industrially. Co-based catalysts are generally more active and selective to linear long chain hydrocarbons and are typically more resistant to deactivation by water.[17] Thus, Co-based catalysts have attracted much attention for the synthesis of long-chain linear hydrocarbons, such as wax and diesel fuels. However, Fe-based catalysts are much more advantageous. For example, they are much cheaper than Co-based catalysts and can be operated in a wide range of temperatures as well as CO/H_2 ratios without significant increase in CH_4 selectivity, whereas Co-based catalysts only work well under carefully selected temperatures and CO/H_2 ratios. Moreover, Fe-based catalysts cannot only be used for the production of linear alkane fuels but are also suitable for the production of alkenes or oxygenates, which are important chemical feedstock. In addition, Fe-based catalysts exhibit much higher activity in WGS reaction, which is helpful for the conversion of synthesis gas with lower H_2/CO ratios derived from coal or biomass. Therefore, Fe-based catalysts are quite attractive for coal to liquid (CTL) or biomass to liquid (BTL) technology and for the production of alkenes from synthesis gas.[18,19]

In this respect, the investigations of interaction mechanisms of CO and H_2 with Fe-based catalysts are essential and necessary for deep understanding into FTS processes and they have attracted great attentions from academic research and industrial applications. More specifically, the adsorption, desorption, dissociation and reactions of CO and H_2 on Fe-based catalysts are very essential steps in association with the catalytic activities. As one of the active phases in Fe-based catalysts, metallic iron has attracted great attentions. Diverse experimental techniques and state of the art theoretical calculations have been explored to investigate the interaction of CO and H_2 with iron single crystalline surfaces in the last two decades.

1.1.1 UHV surface science studies

In principle, surface science is the study of physical and chemical phenomena occurring at the interface of two phases, including solid-liquid interfaces, solid-gas interfaces, solid-vacuum interfaces and liquid-gas interfaces. It includes the fields of surface physics and chemistry.[20] The study of surfaces involves both physical and chemical analysis techniques. Several modern methods can probe surfaces with thickness of 1–10 nm. These include X-ray photoelectron spectroscopy (XPS), Auger electron spectroscopy (AES), low-energy electron diffraction (LEED), electron energy loss spectroscopy (EELS), thermal desorption spectroscopy (TDS), ion scattering spectroscopy (ISS), secondary ion mass spectrometry (SIMS), dual polarization interferometry (DPI), near edge X-ray absorption fine structure (NEXAFS), scanning-tunnelling microscopy (STM) and so on. Many of these techniques require vacuum as they rely on the detection of electrons or ions emitted from the surface under study. Moreover, ultra-high vacuum (UHV), in the range of 10^{-7} pascal pressure or higher, is necessary to reduce surface contamination by residual gas. Surface science is of particular importance to heterogeneous catalysis and can explore surface properties at molecular level by using small-area single crystals and a combination of electron, ion, photon, and molecular beam scattering techniques. For UHV surface science studies about the interactions of CO and H_2 with iron surfaces, the TDS (TPD), LEED, XPS and HREELS techniques were widely used.

1.1.1.1. Iron surface structures

Many early surface sciences and theoretical studies discussed the structures, relaxation and stability of iron surfaces. The surface structures and stabilities as well as possible adsorption sites of iron surfaces are well known. Spencer *et al.*[21] firstly calculated the surface energies and relaxations of three low miller index surfaces and the computed relaxation values show good agreement with the experiment; i.e.; more open surface can relax stronger, in the order of (110) < (100) < (111) and the surface energy values are in the order of (110) < (100) < (111) before and after relaxation. Błoński and Kiejna[22] also systematically calculated the structural, electronic, and magnetic properties of seven bcc iron surfaces and built the equilibrium shape of iron crystalline. On the basis of the surface energies, the stability order of these surfaces is (110) < (100) < (211) < (310) < (111) = (321) < (210). In general, the low Miller index (100), (110) and (111) surfaces build the basic structures of iron particle, while the high miller index (210), (211), (310) and (321) surfaces represent the stepped and kinked structures.

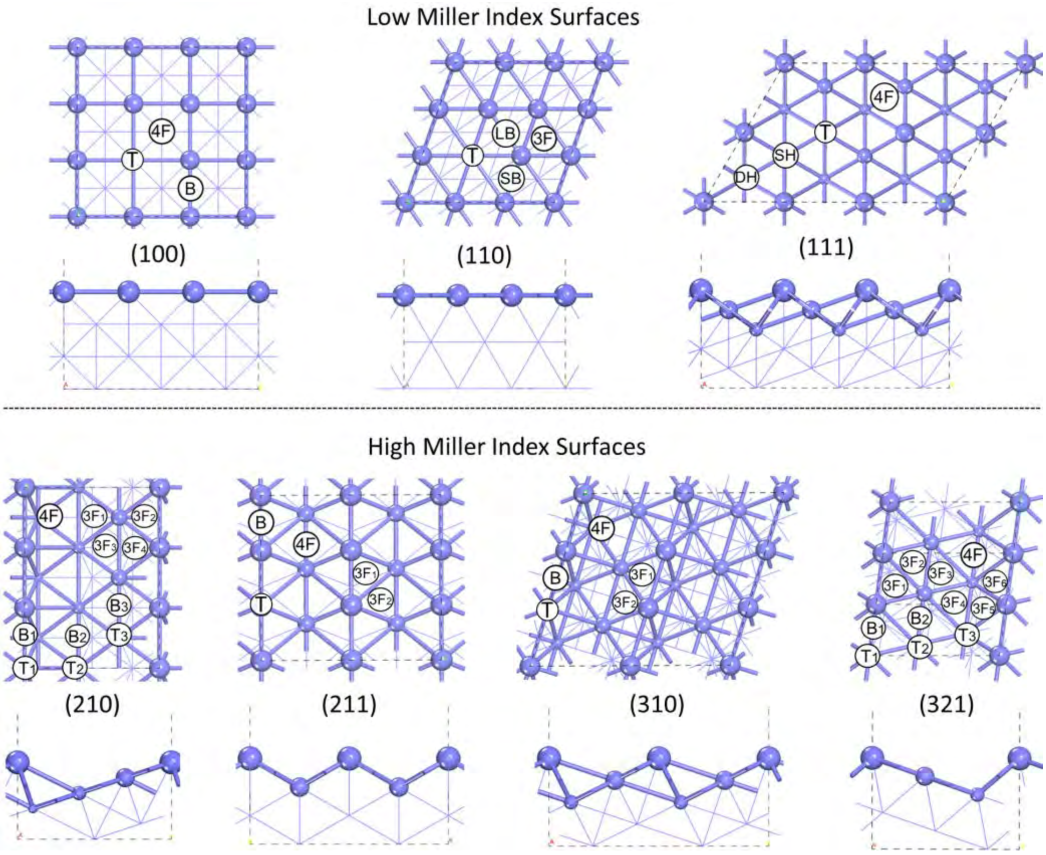

Figure 6: Schematic surface structures and possible active sites on iron surfaces

As shown in Figure 6, each iron surface has different structures and adsorption sites. For these three low Miller index surfaces, the (100) surface is flat and has top (**T**), bridge (**B**) and 4-fold hollow (**4F**) sites, the (110) surface is also flat and has top (**T**), short-bridge (**SB**), long-bridge (**LB**) and 3-fold (**3F**) sites. The (111) surface is very open and has top (**T**), shallow-hollow (**SH**), deep-hollow (**DH**) and 4-fold hollow (**4F**) sites. On the high-index surfaces, the surface structures become more complex and more adsorption sites are available. For example, the (210) surface has eleven adsorption sites, i.e.; three top (**T$_1$**, **T$_2$**, **T$_3$**), three bridge (**B$_1$**, **B$_2$**, **B$_3$**), four 3-fold (**3F$_1$**, **3F$_2$**, **3F$_3$**, **3F$_4$**) and one 4-fold (**4F**) sites; the (211) surface has five adsorption sites, i.e.; one top (**T**), one bridge (**B**), two 3-fold (**3F$_1$**, **3F$_2$**) and one 4-fold (**4F**) sites; the (310) surface also has five adsorption sites, i.e.; one top (**T**), one bridge site (**B**), two 3-fold (**3F$_1$**, **3F$_2$**) and one 4-fold (**4F**) sites; and the (321) surface has twelve adsorption sites; i.e.; three top (**T$_1$**, **T$_2$**, **T$_3$**), two bridge (**B$_1$**, **B$_2$**), six 3-fold (**3F$_1$**, **3F$_2$**, **3F$_3$**, **3F$_4$**, **3F$_5$**, **3F$_6$**) and one 4-fold (**4F**) sites.

1.1.1.2. CO adsorption on iron surfaces

Generally CO bonding to transition metals is usually described in terms of the donation and back donation mechanism[23,24] where CO bonds to a transition metal by donating electrons from the carbon 5σ orbital to the metal d orbital, forming an σ bond. In return, the metal donates electrons from occupied *d* orbital into the CO 2π* anti-bonding orbital, forming a π bond. This results in a lengthened and weakened C-O bond, as evidenced by the lower CO stretch frequency. The CO is usually observed to bond with the C-O axis perpendicular to the surface with the carbon end down. Early surface science studies focused on the adsorption and desorption states of CO on the low miller index Fe(100), Fe(110) and Fe(111) surfaces since they are responsible for the basic structures of metallic iron catalyst. The available CO adsorption properties from experiments are listed in Table 1.

Table 1: Experimental CO adsorption state, desorption temperatures (T) and energies (E_d, kcal/mol) as well as C-O vibrational frequencies ($\nu_{C\text{-}O}$) on iron surfaces (T for top, B for bridge, F for hollow, SH for shallow hollow and DH for deep hollow)

Surface	state	T	E_d	Site	$\nu_{C\text{-}O}/cm^{-1}$
(100)[a]	α_1	(220-250K)	14.3-19.1	T	(1900-2070)
	α_2	(306-340K)	20.3-25.1	B	
	α_3	(400-440K)	28.7-29.9	4F	(1180-1245)
	β	(750-820K)			
(110)[b]	α	(400-420K)	23.0	T	(1890-1985)
	β	(675-800K)			
(111)[c]	α_1	(325-340K)	21.0	T	(1945-2015)
	α_2	(400-420K)	25.0-32.0	SH	(1735-1860)
				DH	(1325-1530)
	β	(650-750K)			

(a) Ref. 38-42. (b) Ref. 25,28,29,30,32. (c) Ref. 50-52

Among these three surfaces, the close packed Fe(110) surface is firstly investigated since it is most stable. For instance, Broden *et al.*[25] studied CO adsorption on the Fe(110) surface by using UPS and LEED measurements and found a molecular CO adsorption at room temperature and a dissociative adsorption at 385K. Jensen *et al.*[26] applied angle-resolved UPS to study CO adsorption on the Fe(110) surface and a large binding energy separation (1.5 eV) between 1π and 5σ orbital was found and this indicated that the C-O bond has been stretched by 0.1 Å, which could be a dissociation precursor at room temperature. However, a later similar work by Maruyama *et al.*[27] found that the 1π and 5σ separation is only 0.5 eV. More interestingly, the CO-axis orientation on the Fe(110) surface depends on coverage; i.e.; it is inclined at low coverage, and upright with increasing coverage while becomes inclined at saturation coverage. Yoshida and Somorjai[28] found an ordered molecular CO adsorption at 270K and a dissociative adsorption at 400K on the Fe(110) surface by using LEED and TDS. Erley[29] investigated CO chemisorption on the Fe(110) surface at 120K by using LEED and HREELS measurements and found the shifts of the Fe-C stretching frequency from 456 to 500 cm^{-1} up to 0.7L (0.25 ML) and from 484 to 444 cm^{-1} at 0.7 to 1.5L (0.5 ML) as well as the C-O stretching frequency from 1890 to 1985 cm^{-1} with the increase of exposure. Gonzalez *et al.*[30] studied CO adsorption and desorption kinetics on the Fe(110) surface by using TDS and found a molecular CO desorption at 400-420K and a re-combinative desorption at 675-800K, while surface defects facilitate CO dissociation. In a Laser induced thermal desorption study of CO on the Fe(110) surface, Wedler *et al.*[31] found that the desorption maximum amplitude depends on laser pulse intensity and CO coverage. A work function (WF) study revealed a facile equilibrium between adsorption and desorption at room temperature, while dissociation at above 380K for CO on the Fe(110) surface.[32]

Apart from the CO adsorption on the clean Fe(110) surface, the effect of other additives was also widely investigated. Brodén *et al.*[33] investigated the effect of K on CO adsorption on Fe(110) surface, it was found that K enhances the adsorption strength and the saturation coverage of CO. The UPS spectra show that the 4σ peak of CO is shifted by 0.8 eV to higher binding energies with K doping on the Fe(110) surface and the 1π-5σ orbital at 21.2 eV is split into a double peak. Zhu *et al.*[34] reported a HREELS investigation of CO and K co-adsorption on the Fe(110) surface. Three distinct adsorption states of CO co-adsorbed with K are found and they belong to strong (α_1), intermediate (α_2), and weak (α_3) interaction with the co-adsorbed K, respectively. Correspondingly, the distance between the CO molecule and the nearest K neighbor is shortest for α_1, medium for α_2 and longest for α_3. Wang and Deng[35] investigated the effect of TiO_x overlayer on CO adsorption on Fe(110), and found that the deposition of TiO_x on the Fe surface greatly enhanced the dissociation of CO even at 170K. The suppress of CO adsorption in this TiO_x/Fe(110) system is attributed to not only the sites blocking by TiO_x but also the dissociated CO. These results also verified the findings that TiO_2 modified transition metal catalysts have a low uptake of CO but high activity in CO hydrogenation, especially in methanation. The above results clearly revealed that top CO adsorption configuration is favored on Fe(110) at different coverage and the CO dissociation takes place at about 400K. There are one molecular desorption peak at about 400K and a re-combinative desorption peak at 675-800K on the CO TPD spectrum.

On the less stable Fe(100) surface, Rhodin and Brucker[36] applied UPS, LEED and AES measurements to investigate CO chemisorption. On the clean surface, the UPS spectrum presents two peaks at 10.6 and 7.1 eV, which are attributed to the 4σ and 1π-5σ orbital of the chemisorbed CO, respectively, whereas the adsorption of sulfur on the surface depleted the *d* state of Fe near the E_F and reduced the ability of Fe to donate electrons back to the 2π* orbital of CO. The UPS results also indicated that molecular CO adsorption at 98-223K, while dissociation at about 300K. Similarly, Benziger *et al*.[37] also studied the adsorption and desorption of CO on the clean Fe(100) and Fe(100) surface with adlayers of carbon, oxygen, sulfur and potassium by using XPS and TPD. Three molecular CO desorption peaks at 250 (α_1), 340 (α_2) and 430K (α_3) as well as a dissociative CO desorption peak at 800K (β) were located on the clean surface and the activation barrier for CO dissociation is predicted to be 105 kJ/mole. It is also found that the C, O and S adlayers weaken CO adsorption, while K enhances CO adsorption and increases the amount of CO dissociation. Moon *et al*.[38,39] also investigated the adsorption and activation of CO on the clean and sulfur modified Fe(100) surface by using XPS and TPD, they also found three molecular CO adsorption states (220K (α_1), 306K (α_2) and 440K (α_3), and they are sequentially filled and a re-combinative desorption state (β) at 820K. Sulfur reduces CO dissociation by blocking the sites for dissociated carbon and oxygen atoms. Moreover, no evidence for long-range electronic effects was obtained. Vink *et al*.[40] reported a study of CO adsorption on the clean as well as C and O covered Fe(100) surface, it is found that the interaction of CO with the clean Fe(100) surface occurred in two stages; i.e., i) CO dissociation into C and O with a coverage of about 0.25ML at 300K, ii) reversible molecular CO adsorption. After the CO dissociation stage, the reversible CO adsorption is coverage dependent and the adsorption heat is in the range of 100±4 to 84 kJ/mole. However, on the 0.5 ML C and O covered Fe(100) surface, the heat of reversible CO adsorption is coverage independent, where the value is 77±4 and 74±10 kJ/mole, respectively. Moon *et al*.[41] reported an unusually low CO stretching frequency at 1201 cm^{-1} for a chemisorbed CO molecular state (α_3) on Fe(100) by using HREELS, which is proposed to be the precursor state of CO dissociation. Benndorf *et al*.[42] also found this unusually low C-O stretching frequency of 1180-1245 cm^{-1} with coverage lower than 1ML, while the adsorption states with vibration frequency of 1900-2055cm^{-1} became popular at high coverage which is due to that CO bound with the molecular axis perpendicular to the surface. Moon *et al*.[43] applied NEXAFS to further reveal the molecular orientation of the α_3 adsorption state. It is found that the CO molecule is tilted by 45±10° with respect to the surface, which allows direct interaction of the oxygen end of CO with the iron surface. The C-O bond is found to be elongated by 0.07±0.02 Å. On the basis of a combined polar and azimuthal X-ray photoelectron diffraction results, Saiki *et al*.[44] proposed a more accurate structural picture of the highly tilted α_3 adsorption state on the Fe(001) surface. The CO molecular is tilted at an angle of 55±2° with respect to the surface and probably occupying the fourfold hollow site.

Cameron *et al*.[45] studied CO chemisorption on the Fe(100) surface by using XPS, LEED, TPD and UPS. All their results about the adsorption states and desorption temperatures of CO are consistent with the early related studies but they focused on the discussion into molecular orbitals of different CO adsorption states. For the α_1 state, a strong 4σ line is centered at 11.7 eV and the 1π (9.4 eV) as well as 5σ (6.9 eV) are also clearly resolved. For the α_2 state, a strong 4σ line is centered at 11.2 eV, and the 1π and 5σ orbital are fused into a single peak which exhibits poorly defined maxima at 8.2 and 7.6 eV. For the α_3 state, it exhibits none of the traditional lines that associated with molecularly chemisorbed CO. There is only a broad weak feature in the position where the 4σ orbital is anticipated and a large featureless peak located in the 1π and 5σ region of the spectrum and all of these indicate that the bonds normally associated with chemisorbed CO are substantially perturbed in this adsorption state, which may result from the bonding of O with surface Fe atoms. Dwyer *et al*.[46] examined the chemical nature of the π-bonded α_3 state by using NEXAFS obtained by the fluorescence yield measurement. The results indicated that CO molecule in the α_3 state is either extensively re-hybridized or tilted with respect to the surface normal.

By using HREELS and temperature-programmed surface reaction (TPSR) techniques, Lu *et al.*[47] studied CO adsorption and dissociation on the Fe(100) surface at 423K, and found CO dissociation at coverage lower than 0.15 ML, while CO desorption at coverage higher than 0.15ML. Lu *et al*.[48] also investigated the effects of post-dosed species on the adsorption properties of CO on Fe(100) by using HREELS, TPD, AES and LEED techniques. It is found that the α_3 adsorption state is the only adsorption configuration after heating to 383K and CO is located on the 4-fold hollow sites. However, when exposed CO (α_3) covered Fe(100) surface to the O_2 and CH_3SH, the pre-adsorbed 4-fold hollow sites CO is forced to migrate to lower coordination sites and the post-dosed species served as the poison of the CO dissociation reaction on the Fe(100) surface. Gladh *et al.*[49] studied the bonding mechanism of the pre-dissociative hollow (α_3) phase and non-dissociative atop (α_1) phase of CO on the Fe(100) surface by using X-ray emission spectroscopy (XES) and density functional theory (DFT) calculations, a π-donation/π* back donation scheme is proposed for CO in the 4-fold hollow site.

On the basis of the above extensive investigations of CO interaction with the Fe(100) surface, some general properties are found; i.e.; three molecular CO adsorption states (α_1, α_2 and α_3) at about 220-250, 306-340, and 400-440K as well as one re-combinative desorption of dissociated C and O atoms at around 750-820K (β state). The α_3 adsorption state is located on the 4-fold hollow site with an unusually low CO stretching frequency of 1210 cm^{-1} and is also the most stable adsorption configuration, which represents the CO dissociation precursor state.

The Fe(111) surface is very open and has a periodic, nearly step-like character along the surface and there are three high symmetrical adsorption sites referred to as the on-top, shallow-hollow, and deep-hollow sites originating in the first, second and third atomic layers, respectively. Compared with the Fe(110) and (100) surface, the Fe(111) surface is least stable. There are also extensive investigations into the interaction of CO on the Fe(111) surface. Yoshida and Somorjai[28] reported three CO desorption states at 370, 420 and 700K on the Fe(111) surface based on their LEED and TDS measurements. In a combined HREELS, LEED, TDS and WF study of CO adsorption on the Fe(111) surface, Seip *et al*.[50] found three different non-dissociative CO adsorption states as identified by C-O stretch frequencies at 1530 cm^{-1} (a), 1800 cm^{-1} (b) and 2000 cm^{-1} (c). For the TDS results, the sharp peak at 400K (α_2 state) belongs to CO adsorption at the shallow hollow site (b state), the α_1 desorption peak at 340K belongs to CO adsorption at the top (c state) and deep hollow (a state) sites, and the β state at 800K comes from the re-combinative desorption of the adsorbed C and O atoms. Similarly, on the basis of LEED, TDS and HREELS study of CO adsorption on the Fe(111) surface, Bartosch *et al.*[51] confirmed three molecular CO adsorption states at 245K (α_1), 325K (α_2), and 400K (α_3) as well as a re-combinative adsorption state at 750K (β). They also identified the C-O vibration frequencies of each adsorption configuration; i.e., 1940 to 2015 cm^{-1} for the top site, 1735 to 1860 cm^{-1} for the shallow hollow site as well as 1325 to 1485 cm^{-1} and 1520 to 1575 cm^{-1} for the deep hollow site. In a TPD and time resolved electron energy loss spectroscopy (TREELS) study of CO adsorption on the Fe(111) surface, Whitman *et al.*[52] found that CO site occupancy depends on coverage and temperature. The kinetics studies revealed that dissociation occurs at about 300K when all CO adsorbed in the shallow hollow site. The dissociation of CO need energy of 20±5 kcal/mol and the resulting adsorbed atomic C and O re-combinatively desorbed at about 760 K with $E \approx 48$ kcal/mol. At higher coverage, in addition to dissociation, some of the CO in the shallow hollow desorbed with $E_d \approx 32$ kcal /mol. In conclusion, CO adsorption on the Fe(111) surface has mainly three molecular adsorption states at top, shallow hollow and deep hollow sites at low temperature as well as a re-combinative desorption state from dissociated C and O atoms at high temperature.

1.1.1.3. H_2 adsorption on iron surfaces

In addition to CO, H_2 is essential in both ammonia[53] and Fischer-Tropsch syntheses[54]. Hence, investigating hydrogen interaction on the surface of iron particles also provides an ideal example for understanding structure and reactivity relationships in heterogeneous catalysis. Despite significant industrial importance of hydrogen interaction with iron surfaces, few systematic studies about this system were reported. Early surface science investigations of hydrogen interaction with metallic iron catalysts mainly focused on the adsorption states and desorption and temperatures on the surfaces as well as the reconstructions of surfaces. All related information from experiments was listed in **Table 2** for easy comparison.

Experimentally, equilibration and exchange reaction between H_2 and D_2 on polycrystalline films as well as on the iron (100), (110) and (111) surfaces indicate that hydrogen adsorbs dissociative on iron catalyst and the polycrystalline films have much higher activity in this reaction than any other single crystalline surface, where the order is (poly) > (110) > (100) > (111).[55]

Table 2: Desorption states, temperatures (K) and energies (E_d, kcal/mol) as well as binding energies (E_b, kcal/mol) of hydrogen on iron surfaces from UHV surface science experiments

Surface	state	T	E_d	E_b
(110)[a]	β_1	340	24	65
	β_2	430-480	26	
(100)[b]	β_1	300	18	
(111)[c]	β_1	240	13	62
	β_2	310	18	
	β_3	375-400	21	
(211)[d]	α_{1-3}	210-270	9-12	
	β	350	19.6-24.2	

(a) Ref. 37,56. (b) Ref. 28,56. (c) Ref. 28,56 (d) 62,63

Bozso *et al.*[56] studied hydrogen chemisorption on the iron (100), (110) and (111) surfaces by applying LEED, TDS, UPS and work-function measurement under UHV conditions and provided the adsorption as well as desorption properties of hydrogen on these surfaces. On the Fe(110) surface, the TPD spectra were recorded with a heating rate of 7K/sec after H_2 exposures between 0.4 and

3500 L at 140K; and the saturation of the adsorbed layer (1 ML) was formed under the highest exposure. The spectra show two desorption states (β_1 and β_2) in superposition. The temperature maximum of the β_1 state is about 340K, whereas the β_2 state shifts towards 480-430K. Analysis into the total desorption area shows that both states exist with equal hydrogen concentration on the surface at saturation of the adsorbed layer.

On the Fe(100) surface, there are two desorption peaks and the temperature maximum of the β_1 state is about 300K, whereas the β_2 state shifts towards 430-400K. There are no ordered surface structures over the whole range of coverage from LEED. On the Fe(111) surface, three desorption states (β_1, β_2 and β_3) in the range of 200-450K were found. The temperature maximum of the β_1 and β_2 states is about 240 and 310K, respectively, whereas the β_3 state shifts towards 375-400K. Yoshida and Somorjai[28] also investigated the chemisorption of hydrogen on the iron surfaces. The TPD results revealed that there are two H_2 desorption peaks at about 340 and 400K on both Fe(110) and Fe(111) surfaces. Moreover, dissociative hydrogen adsorption was found on the clean iron (100) and (111) surfaces. Benziger *et al*.[37] investigated the adsorption properties of H_2 on the clean as well as C, O, S and K covered Fe(100) surface by using XPS and TPD, the binding energy of dissociatively adsorbed hydrogen on the clean Fe(100) surface is found to be 86 kJ/mole and the presences of C, O and S on the surface reduced the binding energy of H_2 while K enhanced the adsorption. Imbihl *et al.*[57] found the formation of ordered over-layer structures on the Fe(110) surface during the dissociative adsorption of hydrogen on the basis of their LEED studies. A $c(2\times2)$ phase was formed at hydrogen coverage (θ_H) of 0.5ML, which is transferred into a $c(3\times3)$ phase at $\theta_H = 0.67$ML. Similarly, Nichtl-Pecher *et al*.[58] reported a LEED study of hydrogen adsorption on the Fe(110) surface and found a new 2×2-2H superstructure with graphitic arrangement of adatoms. This structure can reversibly transform to the $c(2\times2)$ phase at about 80K, and both phases of hydrogen induce the same type of weak reconstruction of the substrate.

Since hydrogen adsorption on solid surfaces always causes the reconstructions,[59] many studies also investigated the effects of hydrogen on the structures of iron surfaces. Sokolov *et al*.[60] found the oscillatory multilayer relaxation of Fe(211) surface by using LEED, which is usual for clean metal surfaces. In addition to the oscillatory multilayer relaxation of clean Fe(211) surface, Hassold *et al*.[61] reported a missing row type reconstruction of the Fe(211) surface caused by hydrogen adsorption, where every second close packed atomic row is removed. Schmiedl *et al*.[62] reported a LEED and TDS study of the interaction of hydrogen with the Fe(211) surface and found a metastable commensurate phase at lower than 200K and a reconstructed phase at higher than 200K. These unreconstructed and reconstructed phases are found to correspond to those two H desorption states at 250K (α) and 350K (β) in the thermal desorption spectra, respectively. Schmiedl *et al.*[63] further studied the structural, thermodynamics and kinetic properties of hydrogen on the Fe(211) surface by using LEED, TDS and work-function measurement and found that the activation barrier for the transition from the commensurate phase to reconstructed phase is 0.34±0.04 eV and the hydrogen desorption energy is 1.05±0.02 eV. To clearly explore the adsorption structure of hydrogen on iron surfaces, Merrill *et al*.[64] reported a LEED, AES, TPSR and HREELS study of hydrogen adsorption on the Fe(100) surface. It is found that hydrogen prefers to adsorb symmetrically on the 4-fold hollow site (β_2 state) at low coverage and covert to asymmetric three-fold sites (β_1 state) within the hollow at higher coverage, and two adsorption configurations coexisted at saturation coverage with the asymmetric moiety dominating. Suo *et al*.[65] reported two peaks of hydrogen desorption at about 350 and 425K on the supported iron catalyst in their studies about the chemical and structural effects of silica in Fe-based FTS catalysts.

In addition to the individual adsorption properties of CO and H_2, their co-adsorption is also important and interesting for understanding complex reaction mechanisms, especially in the FTS reactions. However, very limited surface science investigation about this topic on the iron surfaces is available. Burke *et al*.[66] Investigated the effect of CO on the thermal desorption properties of hydrogen on the Fe(100) surface. It is found that low coverage of CO adsorption on the H pre-covered surface broadens the desorption peaks and reduces the desorption temperatures of hydrogen and the dominant effect of the co-adsorbed CO is to weaken the Fe-H bond. The saturation coverage of CO is unaffected by pre-adsorbed hydrogen but the CO desorption features below 350K are quite different from those on the clean surface while those above 350K is similar. However, the saturation coverage of hydrogen on the CO pre-covered surface is reduced and hydrogen adsorption is blocked at the CO coverage of 0.58 ML.

1.1.2. Theoretical studies

In heterogeneous catalysis, not only specific experimental characterization but also high level theoretical computation played a complementary and decisive role. Ideally, interplay of informative experimental studies and accurate theoretical computations can synergistically provide insights into surface structures of catalysts and rationalize the catalytic activities, and in turn, facilitate the rational design of novel selective catalysts. In this respect, in addition to the extensive experimental studies, CO and hydrogen interaction with iron single crystalline surfaces also has been widely studied theoretically. Table 3 summarizes the available theoretical results about CO adsorption for general discussion and comparison.

1.1.2.1. CO adsorption and activation on iron surfaces

For understanding CO interaction with iron surfaces, early studies in 1980s mainly applied semi-empirical[67,68] and Hatree-Fock[69] methods. By using infinite slab and finite cluster models with the DMOL code to study CO adsorption on the Fe(001) surface, Nayak *et al.,*[70] found that the 4-fold hollow site is energetically most preferred and the C-O bond length is 1.30 Å, which is found to correspond to the α_3 adsorption state in TPD measurement with the unusual low C-O frequency at 1200 cm^{-1}. The top and bridge sites correspond to the α_1 and α_2 adsorption states, respectively. The calculated results revealed that the α_1 state CO is bound more strongly than the α_2 state CO by 7.6 kcal/mol. In an attempt to further clarify the adsorption properties of CO, Sorescu *et al.,*[71] computed the adsorption of CO, C and O atoms as well as CO dissociation on the Fe(100) surface by using the ultrasoft pseudopotentials (USPP) to describe electron-ion interactions and the PW91 functional within the generalized gradient approximation (GGA) to calculate exchange-correlation energy as implemented in VASP code. It is found that CO on the 4-fold site (α_3 state in TPD) is most stable and has dissociation barrier in the range of 1.06-1.22 eV, while CO on the bridge site (α_2 state) is more stable than on the atop site (α_1 state) at low coverage and the atop site becomes more stable than the bridge site at high coverage.

Table 3: Adsorption energies (E_{ads}, eV), dissociation barriers (E_a, eV) and dissociation energies (E_r, eV) of the most stable one CO adsorption configuration as well as the CO stretching frequencies (υ_{CO}, cm^{-1}), the CO distances (R, Å) in the adsorbed initial states (IS) and dissociating transition states (TS) on seven iron surfaces

E_{ads}	E_a	E_r^a	υ_{CO}	$R_{C\text{-}O}$ (IS)	$R_{C\text{-}O}$ (TS)	Ref
(100)						
-1.62 (cluster)				1.30		70
-2.02 (PW91-2×2)	1.06		1246	1.32		71
-1.90 (RPBE-2×2)				1.32		71
-2.54 (PW91-2×2)	1.14		1158	1.32		72
-2.17 (PBE-2×2)	1.07		1189	1.32	1.93	84
-2.14 (PBE-3×4)	1.03	-0.93 (-1.20)	1172	1.32	1.93	89
(110)						
-1.95 (PW91-2×2)				1.16		75
-1.88 (PBE-2×2)	1.52		1928		1.74	76
-1.58 (RPBE-2×2)						76
-1.67 (PKZB-2×2)						76
-2.00 (PBE-2×2)				1.17		77
-1.88 (PBE-2×2)	1.52				1.74	84
-1.88 (PBE-3×4)	1.51	-0.46 (-0.74)	1900	1.18	1.75	89
(111)						
-2.45 (PBE-√3×√3)	1.39			1.19		78,79
-2.08 (RPBE-√3×√3)	1.53				2.00	79
-2.09 (PBE-√3×√3)	1.20				1.80	84
-2.13 (PBE-2×3)	1.17	0.06 (-0.09)	1739	1.20	1.85	89
(210)						
-2.00 (PBE-3×2)	1.11 (PBE-3×2)	-0.32 (-0.82)	1115	1.33	1.97	89
(211)						
-2.41 (PW91-2×1)	0.78			1.28	1.83	82
-1.92 (RPBE-2×1)	0.93					82
-1.72 (PBE-2×2)	1.02			1.28	1.93	84
-1.94 (PBE-4×2)	1.06	-0.20 (-0.39)	1274	1.28	1.95	89
(310)						
-1.85 (PW91-2×1)	0.94		1147	1.33	1.80	83
-2.10 (PBE-2×2)	0.91		1134	1.33		84
-2.13 (PBE-3×2)	0.98	-0.39 (-1.07)	1104	1.33	1.93	89

(a) Dissociation energy in parenthesis is related to the most stable adsorbed C and O atoms after diffusion

Bromfield *et al.*,[72] applied projected-augmented-waves (PAW) pseudopotentials and GGA-PW91 method to study CO interaction on the Fe(100) surface and found that CO adsorption and dissociation are coverage dependent. Three coverage were considered; i.e., at 0.25 ML, CO can only stably adsorb at fourfold hollow sites with the molecular axis tilted away from the surface normal; at 0.5 ML, CO can adsorb either at fourfold hollow sites with a titled geometry or at top sites with a vertical orientation; at saturation coverage (1 ML), CO can adsorb only in a vertical orientation. By using the same calculation methods, this group reported some other work about CO interaction with Fe(100) surface. Curulla-Ferré *et al.*[73] investigated the effect of sulfur on the adsorption properties of CO on the Fe(100) surface, and found that the adsorption energy of CO is only considerably affected at short distance between sulfur and CO, which supported the idea that the effect of sulfur is short ranged. For CO dissociation, sulfur only slightly affected the dissociation energy barrier but significantly affected the reaction energy, i.e.; CO dissociation is exothermic by 0.34 eV on the sulfur-free Fe(100) while endothermic by 0.32 eV on the surface with 0.25ML sulfur. Elahifard *et al*.[74] calculated CO dissociation mechanisms at different coverage on the Fe(100) surface. It is found that CO direct dissociation is the major route on the clean surface, while H-assisted CO dissociation contributed under conditions favoring the existence of very few empty sites.

On the most stable Fe(110) surface, there are also extensive studies about CO adsorption. Stibor *et al.,*[75] calculated the CO adsorption on the Fe(110) surface at different coverage by using VASP code with PAW-LDA-PW91 method. It revealed that CO adsorption on top site is most stable at low coverage, while that on long bridge site becomes most stable at high coverage. However, the theoretically predicted C-O vibration frequencies at the CO coverage of 0.5ML disagreed with experimental findings, and they attributed this disagreement to the overestimation of the stability of long bridge adsorption configuration by DFT method. By applying GGA method and different exchange and correlation functional, Jiang and Carter[76] studied CO adsorption and dissociation on the Fe(110) surface, and their results show that PW91, PBE, RPBE and PKZB methods can yield the correct site preference at 0.25ML, while only PKZB predicts the correct site preference at 0.5ML. They also reported CO dissociation barrier of 1.52 eV on top site on the Fe(110) surface at 0.25ML with PBE. Sun *et al.*[77] investigated the spin-resolved electronic states of CO on the Fe(110) surface using spin-polarized metastable-atom de-excitation spectroscopy (SPMDS) and first principles DFT, and found the existence of the adsorbate-induced $2\pi^*$ state beside CO 4σ and 5σ /1π states.

On the Fe(111) surface, Chen *et al.,*[78] carried out a systematic DFT study using the CASTEP package program with the USPP-GGA-PBE method to investigate CO adsorption at different coverage. It revealed that shallow hollow adsorption is most stable at 1/3 and 1/2 ML; shallow hollow and bridge adsorptions coexist at 1ML, while bent atop and triply capping adsorptions are most favorable at 2ML. By using the same calculation methods, Huo *et al.,*[79] studied CO dissociation on the clean and hydrogen pre-covered Fe(111) surfaces and found that the H-assisted CO dissociation is more favourable than CO direct dissociation. Similarly, Li *et al.*[80] also found that H-assisted CO dissociation on Fe(111) was more favored than direct CO dissociation by using VASP code with PAW-GGA-RPBE method. Recently, Booyen *et al.*[81] also calculated the adsorption and dissociation of CO on the clean and C covered Fe(111) surface by using VASP code with PAW-GGA-PBE/RPBE method, and found that the adsorption of CO is slightly enhanced at the CO-C distance larger than 3 Å, while weakened when the distance is small. Moreover, the dissociation of CO becomes more facile as C is deposited and the Fe(111) surface is likely to become carbided as found under the reaction conditions of the Fischer–Tropsch process.

In addition to the low miller index iron surfaces, there are also some investigations into CO interaction with high miller index surfaces. Borthwick *et al.,*[82] reported CO chemisorption on the Fe(211) surface by using the CASTEP code with the USPP-GGA-PW91 method and single-crystal adsorption calorimetric method. In their study, the adsorption state at the 3-fold site involving one top-layer and two second-layer metal atoms is most stable, they also found that CO dissociation is particularly facile and the Fe(211) surface is optimal for FTS. Lo *et al.,*[83] studied CO adsorption and dissociation on the stepped Fe(310) surface at 0.25 and 0.50 ML by using VASP code with UUSP-GGA-PW91 method. It is found that CO adsorption prefers the hollow sites of the Fe(100) terrace with adsorption energy of 42.7 kcal/mol, which is similar with that on the regular Fe(100) surface. The adsorption of CO becomes stronger with the coverage increasing from 0.25 to 0.5ML. They also proposed two CO dissociation pathways on this surface and their individual contributions to the overall CO decomposition rate depended on the coverage. It is finally predicted that the presence of 30% (310) steps may lead to 20% increment in overall CO dissociation, which substantially facilitates the formation of methane and other hydrocarbon molecules. Sorescu[84] studied CO adsorption, diffusion and activation on the kinked Fe(710) and Fe(310) surfaces and performed a systematic comparison with those on the Fe(100), Fe(110), Fe(111) and Fe(211) surfaces by using VASP code with PAW-GGA-PBE method. It is found that CO dissociation on Fe(710) and Fe(310) requires the smallest activation energies in the regime of low coverages. The analysis of the activation properties of CO on these flat, stepped and kinked surfaces indicates the existence of a direct correlation between the apparent activation energy and the re-bonding energy of the non-interacting products of the reaction.

Despite of these extensive theoretical studies about CO adsorption and activation on iron single crystalline surfaces (Table 3), it is still difficult for a systematic comparison among different surfaces because those data have been obtained by using very diverse models and methods. Furthermore, despite of its importance in experiment for practical applications, the coverage dependent CO adsorption and dissociation is hardly referred in the early theoretical investigations, although the CO pre-adsorption on the FTS catalysts surfaces have widely detected experimentally.[85-87] In this respect, studies of high coverage CO activation are essential to understand the initial steps of FTS process as well as reactions involving CO deeply and more practically. Moreover, it is also very necessary to consider the effect of conditions such as temperature and pressure on the adsorption and dissociation states of CO on iron surfaces. On the basis of the above considerations, we recently reported related studies to solve these questions.[88,89] On one hand, the active phases of catalysts in heterogeneous catalysis are polycrystalline and always very complex, the reasonable way to get a deep and reasonable understanding into the active sites and catalytic properties is to consider all possibilities. Therefore, we performed a systematic DFT study of CO adsorption, dissociation as well as desorption on iron (100), (110), (111), (210), (211) and (310) surfaces by using the same calculation method. On the other hand, the coverage effect was included throughout our calculations where the CO adsorption and dissociation from the lowest to saturation coverage were calculated. Moreover, thermodynamics was applied to consider the effects of temperature and pressure on the adsorption and dissociation properties of CO on metallic iron catalysts. Our results revealed that adsorption configurations, states and dissociation of CO are coverage dependent. For example, only molecular CO adsorption is possible at high coverage while both molecular and dissociative adsorption is possible at medium coverage, and only dissociative CO adsorption is likely at low coverage. Our thermodynamic study also correctly predicted the desorption temperatures and adsorption states of CO on each surface, where the results on the Fe(100), (110) and (111) surfaces are in good agreement with available experimental data. Moreover, the phase diagrams of CO adsorption can clearly give the stable CO adsorption state and coverage at any given temperature and CO partial pressure. Our results gave a more rational initial state of CO adsorption on the solid surfaces which provided the basis for a reasonable micro-kinetic modelling of CO related reactions.

1.1.2.2. H_2 adsorption and activation on iron surfaces

For the interaction of hydrogen with iron catalysts, there are very limited available theoretical calculations compared with the extensive experimental studies. Table 4 summarizes the available theoretical results about hydrogen adsorption for general discussion and comparison. Early Hartree-Fock calculations using cluster models by Walch[90] revealed that H prefers the 4-fold hollow site on the Fe(100) surface. Juan and Hoffmann[91] analyzed the bonding of H to Fe using qualitative band structure calculations in the framework of extended Hückel tight-bonding theory and the ASED-MO cluster method and compared the changes in iron electronic structures upon the introduction of H into bulk Fe and H adsorption on Fe(110) surface. It is found that the Fe-H interaction occurs mainly via Fe 4s and H 1s orbitals with a small contribution of both 4p and 3d Fe orbitals, where H is found to be negatively charged on the surface and in the lattice. Moreover, the formation of Fe-H bond is at the expense of Fe-Fe bond, which diminishes the strength of the local Fe-Fe bond to about 30% of its original value.

Cremaschi *et al*.[92] performed Ab initio calculations to study the chemisorption of atomic H on the Fe(110) surface with a cluster model. The LB, SB and 3F sites were found to have similar H atom adsorption strength and H diffusion into the bulk through the SB site has a much higher activation barrier than via the LB and 3F sites. Eder *et al.*[93]calculated the adsorption of H atom on the Fe(110) and Fe(100) surfaces in their investigations into the initial stages of water oxidation of iron surfaces by using USPP-GGA-PBE method. It is found that the 3F hollow site is most favorable H adsorption site on the Fe(110) surface while the bridge and 4F hollow sites have similar adsorption energy on the Fe(100) surface. Moreover, H is stronger bound on Fe(110) than on Fe(100).

Jiang *et al*.,[94] studied the interaction of hydrogen with the Fe(110) surface as a function of coverage by using VASP code with PAW-GGA-PW91 method. It is found that the quasi three-fold site is the only stable minimum while the short and long bridge sites are the transition states for H diffusion. Charge density analysis suggests that the H-Fe interaction is quite covalent, with only 0.1 electron transferred from Fe atoms to H in the three-fold site. Jiang *et al*.,[95] also reported a periodic spin-polarized DFT calculation of hydrogen adsorption, absorption and dissolution as well as diffusion on and in bcc iron by using similar calculation methods. It is found that H prefers to stay on the Fe surface instead of sub-surfaces or in bulk, and H dissolution in bulk Fe is endothermic, which is consistent with the known low solubility of H in pure Fe. Hydrogen diffusion into bulk Fe on the (100) surface is found to be much easier than on the (110) surface. The mobility of H in bcc Fe is very high due to the low diffusion barrier.

Table 4: Adsorption energies (eV) of hydrogen atom with respect to H_2 molecule on iron surfaces

(100)					
Adsorption sites	top	Bridge	4F		Ref
USPP-GGA-PBE-(2×2)	+0.17 (1/4 ML)	-0.36 (1/4 ML)	-0.35 (1/4 ML)		93
PAW-GGA-PBE	+0.20 (1/9 ML)	-0.34 (1/9 ML)	-0.38 (1/9 ML)		95
(1×1), (2×2) and (3×3)	+0.23 (1/4 ML)	-0.32 (1/4 ML)	-0.38 (1/4 ML)		
	+0.45 (1.00 ML)	-0.24 (1.00 ML)	-0.40 (1.00 ML)		
USPP-GGA-PW91-(2×2)	+0.20 (1/4 ML)	-0.32 (1/4 ML)	-0.31 (1/4 ML)		96
	+0.33 (1/2 ML)	-0.28 (1/2 ML)	-0.34 (1/2 ML)		
	+0.44 (1.00 ML)	-0.22 (1.00 ML)	-0.38 (1.00 ML)		
PAW-GGA-PW91-(2×2)	+0.20 (1/4 ML)	-0.36 (1/4 ML)	-0.40 (1/4 ML)		
		-0.29 (1/2 ML)	-0.40 (1/2 ML)		
	+0.44 (1.00 ML)	-0.25 (1.00 ML)	-0.41 (1.00 ML)		
PAW-GGA-rPBE-(2×2)	+0.32 (1/4 ML)	-0.21 (1/4 ML)	-0.23 (1/4 ML)		
		-0.13 (1/2 ML)	-0.23 (1/2 ML)		
	+0.57 (1.00 ML)	-0.07 (1.00 ML)	-0.23 (1.00 ML)		
USPP-GGA-PBE-(2×2)	+0.26 (1/4 ML)	-0.28 (1/4 ML)	-0.36 (1/4 ML)		99
PAW-GGA-PBE-(3×4)	+0.05 (1/12 ML)	-0.46 (1/12 ML)	-0.36 (1/12 ML)		101
(110)					
	top	SB	LB	3F	
cluster	-0.07 (< 1/10ML)	-0.47 (< 1/10ML)	-0.50 (< 1/10ML)	-0.45 (< 1/10ML)	92
USPP-GGA-PBE-(2×2)	+0.06 (1/4 ML)	-0.51 (1/4 ML)	-0.63 (1/4 ML)	-0.69 (1/4 ML)	93
PAW-GGA-PW91-(2×2)	-0.02 (1/4 ML)	-0.55 (1/4 ML)	-0.69 (1/4 ML)	-0.74 (1/4 ML)	94
	+0.31 (1.00 ML)	-0.39 (1.00 ML)	-0.51 (1.00 ML)	-0.65 (1.00 ML)	
PAW-GGA-PW91-(1×1)	+0.18 (1.00 ML)	-0.37 (1.00 ML)	-0.40 (1.00 ML)	-0.57 (1.00 ML)	100
PAW-GGA-PBE-(4×4)	-0.01 (1/16 ML)	-0.53 (1/16 ML)	-0.64 (1/16 ML)	-0.69 (1/16 ML)	101
(111)					
	top	B	SH	DH	
PAW-GGA-PBE-(3×3)	+0.16 (1/9 ML)	-0.51 (1/9 ML)	-0.44 (1/9 ML)	-0.09 (1/9 ML)	101
	T-SH	SH-SH	SH-4F	4F-4F	
USPP-GGA-PBE-$\sqrt{3}\times\sqrt{3}$	-0.41 (2/3 ML)	-1.39 (2/3 ML)	-1.38 (2/3 ML)	-1.33 (2/3 ML)	97
(dissociative H_2 adsorption)	-0.41 (1.00 ML)	-1.40 (1.00 ML)	-1.25 (2.00 ML)	-1.35 (1.00 ML)	
	-0.44 (2.00 ML)			-1.17 (2.00 ML)	
USPP-GGA-rPBE-$\sqrt{3}\times\sqrt{3}$	-0.12 (2/3 ML)	-1.12 (2/3 ML)	-1.08 (2/3 ML)	-0.99 (2/3 ML)	
(dissociative H_2 adsorption)	-0.13 (1.00 ML)	-1.11 (1.00 ML)		-1.00 (1.00 ML)	
	-0.17 (2.00 ML)		-0.91 (2.00 ML)	-0.81 (2.00 ML)	
(310)					
	B	3F1	3F2	4F	
USPP-GGA-PBE-(2×1)	-0.14 (1/2 ML)	-0.54 (1/2 ML)	-0.33 (1/2 ML)	-0.38 (1/2 ML)	99

Similarly, Sorescu[96] also systematically studied the adsorption and diffusion of hydrogen on the Fe(100) surface by using VASP code with both USPP-GGA-PBE and PAW-GGA-PBE methods. It is found that the site preference depends on hydrogen coverage and H diffusion from surface to subsurface is more difficult than migration on the surface. Huo *et al.*,[97] also calculated the adsorption and diffusion of hydrogen on the Fe(111) surface by using CASTEP program with USPP-GGA-PBE method. It is found the top-shallow bridge site to be most favored, followed by the quasi 4-fold site (qff), while the top site (t) is not competitive. Furthermore, the adsorbed atomic hydrogen (H) has a high mobility because of the small diffusion barrier. The local density of state (LDOS) analysis reveals that the Fe-H bond involves mainly the Fe 4s and 4p and H 1s orbitals with less contribution of the Fe 3d orbital for the tsb and qff sites, while the Fe 4s, 4p, and 3d orbitals all participate in the Fe-H (top) bond. van Steen and van Helden[98] calculated the dissociation of H_2 on the clean as well as CO and C pre-covered Fe(100) surface by using CASTEP code with USPP-GGA-RPBE method. It is found that the presence of CO and C blocks several sites for hydrogen adsorption and increases the H_2 dissociation barrier, which will result in a significant decrease in the rate constant of the dissociative H_2 adsorption process.

Fabiani[99] studied the adsorption properties of hydrogen on the Fe(310) surface by using DFT calculations and compared those on the Fe(100) surface. It revealed that the site preference of hydrogen is different on these two surfaces despite of their similar structures. The most favorable adsorption configuration of H on Fe(310) surface is located on the 3 fold hollow site, while that on the Fe(100) surface is the 4-fold hollow site. Faglioni *et al.*[100] reported a systematic DFT study about the coverage dependent hydrogen adsorption on the closest packed surface of all nine group VIII transition metals, where the interaction of H on the Fe(110) and Fe(111) surfaces was included and the site preference of H adsorption on these two surfaces was found to be consistent with early DFT calculations. They also reported a simple statistical treatment of hydrogen interaction with metal surfaces to model the thermal desorption properties and found good agreement with available TPD spectra.

Recently, we reported a systematic DFT investigation into the interaction of hydrogen with Fe(100), (110), (111), (210), (211), (310) and (321) surfaces.[101] Dissociative H_2 adsorption is found to be very favorable on all these surfaces. Our calculated results combined with atomistic thermodynamics methods provide some interesting insights into the understanding of hydrogen interaction with solid surfaces. For example, the computed hydrogen desorption temperatures and energies on the (100), (110), (111), and (211) surfaces as well as the Fe−H binding energies on the (110) and (111) surfaces agree well with the available experimental surface science data. Moreover, at typical hydrogen reduction temperature (675 K), the mainly exposed (110) and (310) facets were predicted to represent the active surfaces from our theoretical modeling, as supported by the transmission electron microscopy study. Our results provided an example for the investigation and understanding into the surface structures and active facets of heterogeneous catalysts under experimental conditions.

1.2 CO and H_2 activation on Mo_2C catalysts

In addition, transition metal carbides (TMCs) are also a serious of promising hydro-treating catalysts in heterogeneous catalysis. These materials are always generated by incorporating carbon atoms into the lattices of transition metals.[102, 103] Structurally, TMCs belong to interstitial carbides which are derived primarily from relatively large transition metals acting as host lattices for small carbon atoms, which occupy the interstices of close-packed metal atoms.[104] Interstitial carbides are characterized by extreme hardness but at the same time extreme brittleness. They have very high melting points (typically about 3000-4000 °C) and retain many of the properties associated with metals, i.e.; high conductivity of heat and electricity as well as metallic lustre. These physical properties have facilitated TMCs as cutting tools and hard-coating materials.[105] At elevated temperatures, some interstitial carbides retain the mechanical properties of metals, such as malleability. Most transition metals form interstitial carbides of several stoichiometries,[106] and the bonding in TMCs can be described as a mixture of metallic, covalent and ionic components.[107] Throughout the periodic table, all transition metals can form carbides except the second and third rows of Group 9-10 metals (Rh, Ir, Pd, and Pt).

Carbides of Group 4-6 transition metals are thermodynamically more stable and possess catalytic properties greatly improved over those of parent transition metals. Therefore, the chemical properties of TMCs have attracted great interests from both academic researches and industrial applications. In the past few decades, great attentions were focused on the promising catalytic properties of TMCs in heterogeneous catalysis since the pioneer work of Levy and Boudart[108] about the Pt-like catalytic property of tungsten carbide. These carbides always have similar or even better catalytic activity and selectivity to their parent metals as well as high tolerance to poisoning. Moreover, their refractory characters facilitate the resistance to sintering under experimental condition. TMCs also found wide applications as supporting materials in electro-catalysis since they are chemically stable in acidic environment, have excellent mechanical durability and possess high electric conductivity.[109] Bimetallic and mixed carbides have also been considered as important materials due to their enhanced catalytic properties originated from the complementary effects of single metal carbides.

Among these TMCs, molybdenum carbide (Mo_2C) has attracted great attentions in heterogeneous catalysis for its excellent hydro-treating properties. The crystal structure of Mo_2C was firstly determined experimentally by Westgren and Phragmen[110] in 1926. The lattice parameters of Mo_2C were reported to be a = 3.002 Å and c = 4.724 Å by Kuo and Hägg in 1952,[111] and a = 3.00292 Å and c = 4.72895 Å by Fries and Kempter in 1960.[112] The Mo atoms in these reported Mo_2C structures are arranged in a hexagonal close packing while the carbon atoms are arranged statistically in the octahedral holes (the number of holes is twice the number of C atoms). This structure is widely known as the hexagonal phase. However, this phase can be further divided into two types on the basis of the arrangement of carbon atoms,[113] i.e.; one is the C6-type with a space group of P3m1; where the carbon atoms only arrange in one layer and it is also called CdI_2-antitype since it is similar with the CdI_2 structure. Another one is the L'3-type with the space group of $P6_3/mmc$, where the carbon atoms are arranged randomly about all possible sites but in both layers systematically. Since the carbon atoms in the hexagonal L'3-type occupy half of the octahedral holes randomly, Haines *et al*.,[114] considered different possible carbon atoms arrangements on the basis of experiment as well as *ab initio* calculations, and found that the eclipsed configuration is most stable and also the most likely candidate for the disordered hexagonal structure. Shi *et al*.,[115] also computed the stability of different possible structures of the hexagonal L'3-type and found that the eclipsed configuration is thermodynamically most stable.

Apart from the hexagonal structure, an orthorhombic structure with the space group of Pbcn was also reported. The lattice parameters were reported to be a = 4.724, b = 6.004 and c = 5.199 Å by Parthe *et al*.,[113] in 1963, as well as a = 4.732, b = 6.037 and c = 5.204 Å by Christensen in 1977.[116] In this structure, the Mo atoms are hexagonal close packed, but deformed to an orthorhombic symmetry, and the carbon atoms orderly occupy half of the octahedral holes.

On the basis of these structures, Dubois *et al*.,[117] and Epicier *et al*.,[118] systematically studied their transformation at high temperatures. It revealed that the orthorhombic Mo_2C (space group Pbcn) is most stable below 1350°C and changes to the hexagonal CdI_2-antitype (space group P3m1) at 1350-1960°C, while the hexagonal L'3-type structure is most stable with temperature higher than 1960°C.

Generally, all three Mo_2C structures have been widely accepted and analyzed. Despite of extensive studies of Mo_2C, it is confusion in the definition of the orthorhombic and hexagonal Mo_2C. Some authors referred to the orthorhombic Mo_2C as α-Mo_2C while hexagonal as β-Mo_2C, although the Joint Committee on Power Diffraction Standards (JCPDS) data files defined the hexagonal Mo_2C and orthorhombic Mo_2C as α and β, respectively.[119] For clarity, in our discussion, we have used the following nomenclature (**Figure 7**); CdI_2-antitype Mo_2C (hexagonal C6 structure type with the space group of P3m1), eclipsed Mo_2C (hexagonal L'3-type structure with the space group of P63mmc) and the orthorhombic Mo_2C (space group Pbcn).

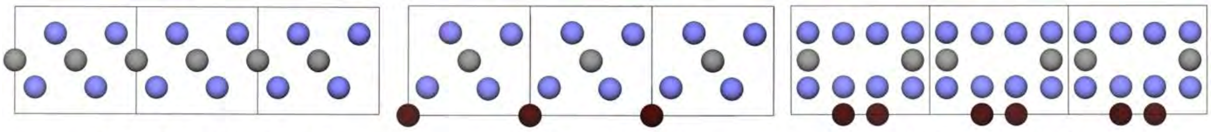

(a) CdI_2-antitype-Mo_2C (b) Eclipsed-Mo_2C (c) Orthorhombic-Mo_2C

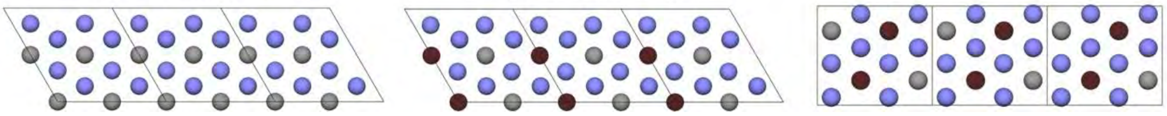

Figure 7: Schematic side and top views of three Mo_2C cells (Blue balls for Mo atoms, gray balls for the first layer C atoms and black balls for the second layer C atoms).

On the basis of the three Mo_2C phases, extensive studies have revealed that Mo_2C had promising activities in many reactions originally catalyzed by noble metals (**Figure 8**), such as CO hydrogenation for alcohol synthesis,[120-123] WGS reaction for hydrogen production,[124,125] Hydrogenolysis,[126] HDS,[127,128] HDN,[129,130] and HDH[131-133] in petroleum refining, isomerization and reforming,[134-138] aromatization.[139-142] On the basis of these catalytic properties of Mo_2C, extensive UHV surface science investigations and theoretical modelling works were reported to explore the detailed interaction and reaction mechanisms of related reactions.

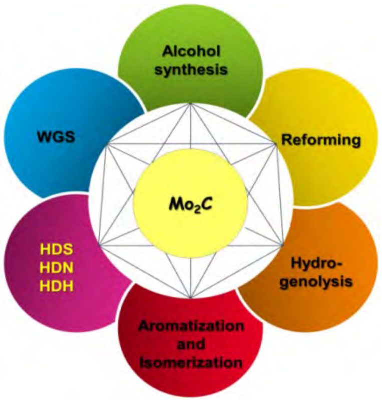

Figure 8: Mo_2C catalysed heterogeneous reactions

1.2.1. UHV studies of Mo_2C catalyst

To provide fundamental information about the surface properties of Mo_2C, many systematic surface science investigations were reported. Early UHV surface science studies mainly focused on the adsorption and activation of CO, H_2 and CO_2 on the pure Mo as well as modified Mo surfaces by using

LEED, XPS, EELS and TDS.[143-149] The formation of thin carbide layers in the interfacial region between a transition metal substrate and a thin carbon over-layer was found to ultimately either enhance or degrade the functionality of a multi-layer structure.[150,151] As the result, the modification of Mo surface reactivity upon carbide film formation attracted great attentions. For example, it is proved that the formation of surface carbide on the Mo(110) surface is an electronic effect rather than pure site-blocking by carbon atoms, and results in important changes in the catalytic activity.[152] The bulk properties, preparation, characterization and catalytic activities of carbide and nitride over-layers on early transition metal surfaces have been systematically reviewed by the pioneering works of Chen.[153,154]

1.2.1.1. Properties of Mo_2C surfaces

To study the structural and electronic properties of Mo_2C surfaces, many previous surface science investigations focused on the preparation and characterization of pure Mo_2C surfaces. A series of studies revealed that the structure of Mo_2C surface is dependent on the annealing temperature and time. For example, Lo *et al.*[155] observed a $(\sqrt{3}\times\sqrt{3})R30°$ C-terminated structure on the $Mo_2C(0001)$ surface by STM with annealing temperatures below 960 K and the C atoms were found to occupy the threefold hollow sites of the Mo layer. Clair *et al.*,[156] characterized the prepared (0001) surface of orthorhombic Mo_2C by Ar ion bombardment and annealing as well as XPS and LEED, and all the results supported the idea that the surface changes from Mo-terminated to C-terminated with annealing temperatures above 1300 K. Sugihara *et al.*,[157] also applied LEED, XPS and angle resolved photoelectron spectroscopy to study the structure of orthorhombic $Mo_2C(0001)$ surface, a C-rich MoC-like surface is formed when it is annealed at 1600K and the valance band of the surface consists of the Mo-4d, Mo 4d-C 2p hybrid and C-2s bands. They further investigated the detailed electronic structure of $Mo_2C(0001)$ by using resonant photoemission spectroscopy and it is found that the valence band is mostly composed of Mo 4d-C 2p hybrid states and the band near the Fermi level (0-1 eV) is mostly composed of Mo 4d orbitals.[158] Kato *et al.*,[159] studied the surface electronic structure of orthorhombic $Mo_2C(0001)$ by using angle-resolved photoemission spectroscopy and found an electronic state localized to the surface including substantial contribution of Mo-4d orbitals in the second layer.

1.2.1.2. CO and O_2 adsorption on Mo_2C surfaces

In heterogeneous catalysis, CO and O_2 are the most popular applied probe molecules in characterizing surface properties of catalysts. For the Mo_2C catalyst, oxygen is found to be able to modify the catalytic properties of Mo_2C surfaces because of the formation of oxycarbide layer.[160,161] Moreover, CO and O_2 are two important species in CO hydrogenation reactions. As the result, extensive surface science techniques were applied to explore the interactions of CO and O with the Mo_2C surfaces as well as surface oxidation. Wang *et al.*,[162] studied CO chemisorption on the hexagonal Mo_2C catalyst and the RAIRS results at 100K show a single CO vibrational stretching frequency at 2057-2072 cm^{-1}, which belongs typically to on-top adsorption. For the TDS results, one molecular desorption peak at 325K for the top adsorption and a re-combinative desorption peak at 1200K for the dissociated C and O were found. St. Clair *et al.*,[163] investigated the adsorption of CO and O_2 on the Mo- and C terminated orthorhombic $Mo_2C(0001)$ surfaces by using TPD, and found both molecular CO adsorption and O_2 dissociative adsorption. It is also found that the saturation coverage of CO and O_2 is not significantly altered between Mo- and C-terminations. Bugyi and Solymosi[164] investigated the interaction of CO with clean and K-covered $Mo_2C/Mo(100)$ surfaces by using HREELS, AES and TPD techniques. They found CO molecular adsorption at 140K and dissociative adsorption at 300-350 K. They also found that K incorporation can decrease the amount of CO molecular adsorption but promote CO dissociative adsorption. Edamoto *et al*.,[165] studied the oxidation process of $Mo_2C(0001)$ using photoelectron spectroscopy and found that the adsorbed oxygen atoms interact with both Mo and C atoms and form an oxycarbide layer on the surface. As the oxygen-adsorbed surface is heated at ≥ 800 K, the C–O bonds are broken and the adsorbed O atoms are bound only to Mo atoms.[166] Óvári *et al*.,[167] investigated the interaction of oxygen with the surface and subsurface of carburized Mo(100) surface at different temperatures, and found O_2 dissociative adsorption on the carbide layer at room temperature and CO formation at 500-600K. Moreover, higher O_2 doses at 800 K results in the inward diffusion of O and the partial oxidation of the Mo atoms. With further increase of temperature to 900K, the depletion of bulk C atoms start and the concentration of surface carbon decrease gradually. At 1265K,[168] the carbide phase can be transformed into an oxide layer in the presence of O_2 and this process starts firstly in the outermost layer but at higher oxygen concentration subsurface oxidation can occur. However, the formed oxide layer can also be transformed back to carbide layer by heating in the ethylene atmosphere and a pure Mo layer could be achieved as an intermediate state during the transformation. Kato *et al*.,[169] studied the adsorption of oxygen on the C-terminated hexagonal $Mo_2C(0001)$ surface and found that the oxygen atoms adsorb on the Mo atoms in the second layer, and the adsorbed oxygen induces a peculiar state around the Fermi level. Edamoto *et al*.,[170] applied angle-resolved photoemission spectroscopy to investigate the electronic structure and reactivity of the oxygen modified $Mo_2C(0001)$ surface, and found that the adsorption of oxygen increases the intensity of the emissions around the Fermi level because of the formation of the O 2p-induced states at 4.1 and 5.3 eV at the Γ point and the reactivity of the surface toward H_2O adsorption is enhanced by pre-adsorption of oxygen.

1.2.1.3. Hydrocarbons reforming reactions

Supported Mo_2C catalysts were found to present excellent activity in the reforming of CH_4 and other hydrocarbons into synthesis gas and aromatics, depending on the types of supports. On the basis of these backgrounds, Solymosi group reported extensive surface science studies into the reactivity of hydrocarbons on Mo_2C surfaces by using iodo-compound as the source of C_xH_y species. For example, the formation and reaction of CH_3 on the $Mo_2C/Mo(111)$ surface were studied by using TPD, XPS and HREELS measurements. The CH_3 species generated by CH_3I dissociation above 140K was mainly transferred into hydrogen, methane and ethylene.[171] For the reactions of CH_2 and C_2H_5 species on the $Mo_2C/Mo(111)$ surface,[172] CH_2 undergoes self-hydrogenation to CH_4 at 300 K and dimerization into C_2H_4 at 222-280K, while C_2H_5 species undergoes hydrogenation and dehydrogenation to give ethane and ethylene. Apart from CH_3I, they also investigated the reactions of CH_3Cl on the ZSM-5, Mo_2C/ZSM-5 and Mo_2C/SiO_2 catalysts by using TPD and FTIR.[173] It is found that the formation of methoxy and alkene carbocation on ZSM-5 occurs at above 473K and the decomposition of CH_3Cl yields propylene, ethylene, butane, methane and benzene in decreasing selectivity. However, the addition of Mo_2C only slightly influences the above processes on ZSM-5 catalyst but promotes the cleavage of C-Cl bond in CH_3Cl on SiO_2. By using TPD, XPS and HREELS techniques, they investigated the adsorption and reactions of C_3H_5, C_3H_7, C_6H_5 and C_4H_9 on the Mo_2C/Mo(100) surface by using C_3H_5I, C_3H_7I, C_6H_5I, and C_4H_9I as the sources of C_xH_y species, These formed C_xH_y species react in different ways on the surface, i.e.; the adsorbed C_3H_5 undergoes hydrogenation to propene and propane,[174] while C_3H_7 undergoes dehydrogenation into propene and hydrogenation into propane.[175] The reaction of C_6H_5 leads to the formation of biphenyl, benzene and benzyne.[176] The adsorbed C_4H_9 mainly undergoes surface disproportionation reaction to produce butene and butane.[177] Apart from the catalytic activities in the aromatization of alkanes, Mo_2C on ZSM-5 support was also found to be able to markedly enhance ethanol aromatization. As the result, Farkas and Solymosi[178] studied the adsorption and reactions of ethanol on the Mo_2C/Mo(100) surface by using work function, TPD and HREELS measurements. It revealed that the condensed ethanol layer desorbs at 162 K, while the chemisorbed ethanol desorb at 346 K. The other irreversibly bonded species can form different compounds including hydrogen, acetaldehyde, methane, ethylene and CO. Similarly, they also studied the adsorption, desorption and dissociation of dimethyl ether and diethyl ether on the Mo_2C surface.[179] It is found that the major part of the adsorbed molecules desorbs intact, and a smaller fraction decomposes to H_2, CO and CH_4 for dimethyl ether, while H_2, CO, C_2H_4 and CH_4 for diethyl ether.

On the basis of the above systematic investigations into the reactions of $C_xH_yO_z$ species on the pure Mo_2C surface, the Solymosi group studied the effect of potassium on those reactions since potassium is always regarded as an electron donation promoter. They studied CO_2 adsorption on the clean and K-covered Mo_2C/Mo(100) surfaces, since CO_2 is the oxidant for oxidative dehydrogenation of ethane on Mo_2C catalyst,[180,181] the change of the linear structure of CO_2 into more reactive bent form is an important step. On the K-free surface,[182] CO_2 is very weakly adsorbed and desorbs at 190 K. However, the adsorbed K atoms greatly increase the CO_2 binding energy and reduce CO_2 to CO_2^- anion radical. The highly activated CO_2 dissociates to adsorbed CO and O at low K coverage and disproportionates into adsorbed CO and CO_3 at and above monolayer K.[183] The effect of K promotion on the adsorption and reactions of C_3H_7I,[184] CH_2I_2,[185] as well as CH_3I and C_2H_5I[186] was also systematically studied by using TPD, XPS, HREELS and work function, where potassium was found to be an effective promoter for the rupture of C–I bond and this effect was explained by the extended electron donation to adsorbed alkyl iodide in one hand, and by the direct interaction between potassium and I on the other hand. Moreover, the incorporation of K enhances the adsorption of surface species and facilitates the coupling reaction of C_xH_y species. Similar conclusions were reached for the effects of potassium on the adsorption and dissociation pathways of methanol and ethanol on the Mo_2C/Mo(100) surface,[187] i.e.; K stabilizes the adsorbed alcohols and CH_3OH decomposition yields H_2, CO and CH_4, while C_2H_5OH decomposition produces H_2, CO, acetaldehyde and ethylene.

1.2.1.4. HDS and HDN reaction

In addition to the above refereed hydro-treating reactions, Mo_2C catalysts also present high activity in the HDS of S-containing molecules. Rodriguez *et al.*,[188] reported a synchrotron-based high resolution photoemission study of thiophene adsorption and decomposition on the clean Mo(110) as well as C- or S-modified molybdenum (MoC_x and MoS_x) surfaces. It is found that thiophene can easily decompose into surface C and H_2S on these surfaces with increasing temperature. However, MoS_x is much less active in thiophene dissociation even after introducing a large number of sulfur vacancies in the sulfide or after promoting it with nickel. They further investigated the chemistry of SO_2, H_2S, and CH_3SH on C-modified Mo(110) and Mo_2C powders by using XANES, and Mo_2C was found to be able to break the S-O, S-H, and S-C bonds very easily at temperatures below 300 K.[189] St Clair *et al.*,[190] reported the first UHV study of thiophene adsorption on the hexagonal-$Mo_2C(0001)$ single crystal surface by using XPS, UPS, LEED and TPD techniques. It is found that irreversible thiophene adsorption results in surface C and S as well as gaseous H_2, while reversible thiophene adsorption results in molecular desorption at 198 K and 345 K.

1.2.2. Theoretical studies of Mo_2C catalyst

Computations mainly play the complementary roles of experimental studies of the properties of Mo_2C systems. For example, Haines *et al.*,[191] carried out a combined experimental and theoretical study about the structures as well as the compressibility of different Mo_2C at high pressure, and found that Mo_2C is highly incompressible with a bulk modulus of 307 GPa and the orthorhombic Mo_2C was found to be very slightly lower in energy than the disordered hexagonal phase, and the eclipsed configuration is most stable among those possible disordered hexagonal phases

On the basis of only DFT studies, Liu and Rodriguez reported extensive pioneering work about the properties of molybdenum carbide. They firstly investigated the relative stability and chemical activities of molybdenum carbides, nitrides as well as phosphides where molybdenum phosphides were found to display the highest reactivity toward CO and sulfur adsorption.[192] They investigated the effects of carbon concentration on the stability and chemical performance of molybdenum carbide and predicated the metallocarbohedrene Mo_8C_{12} to be the most attractive catalyst compared with bulk $Mo_2C(001)$ and MoC(001) surfaces because of its high stability and moderate chemical activity in CO and S adsorption.[193] On the basis of the stable structures of Mo_8C_{12}, orthorhombic-$Mo_2C(001)$ and face centered cubic MoC(001) surfaces, Liu *et al.*,[194] calculated the desulfurization of SO_2 as well as thiophene and found that the orthorhombic $Mo_2C(001)$ surface and Mo_8C_{12} are very reactive toward SO_2 and able to break S-O bond, and the behavior of Mo_8C_{12} illustrates the interplay of ligand and steric effects in nanoparticles of metal compounds. For comparison, Liu *et al.*,[195] further reported XPS and DFT studies of HDS reactions on the $Ni_2P(001)$ and orthorhombic $Mo_2C(001)$ surfaces, where the orthorhombic $Mo_2C(001)$ surface has higher activity. However, Ni_2P is predicted to be a better catalyst for HDS since Mo_2C has too strong adsorption of S. Since the formation of MoS_xC_y compounds has been observed on/in the surface of MoS_2 catalysts during the HDS process, Liu *et al.*,[196] studied sulfur adsorption and sulfidation of transition metal carbides by applying periodic slab models, $Mo_{14}C_{13}$

nanocrystals and Mo_8C_{12} cluster where the Mo_8C_{12} was found to display better catalytic activity in HDS. To further explore the catalytic properties of Mo_2C, Liu *et al.*,[197] calculated the detailed mechanism of WGS reaction on the Mo- and C-terminations of orthorhombic $Mo_2C(001)$ surface as well as the Cu(111) surface, where the formed Mo oxycarbide was found to have higher activity than Cu catalyst. To explain the availability of carbon removal from TMCs and formation of metal oxocarbide compounds by oxidation, they performed a systematic DFT study about the adsorption of atomic oxygen on the (001) surface of early TMCs and provide useful information about the site preference of O atom on different TMCs.[198] Recently, dos Santos Politi *et al.*,[199] computed the atomic and electronic structures of the bulk and low Miller-index surfaces of the hexagonal and orthorhombic Mo_2C as well as face centered cubic MoC, and found the orthorhombic Mo_2C phase to have stronger metallic character. Although they did not systematically study the catalytic properties, it is worth highlighting the quite complete studies about the geometric and electronic structure of those Mo_2C phases. Recently, this group reported a DFT study of CO_2 activation and hydrogenation on two molybdenum carbides,[200] it is found that the Mo-termination of orthorhombic $Mo_2C(001)$ surface can break the C-O bond easily while the C-termination as well as face centred cubic MoC(001) surface have limited ability in C-O bond cleavage. The ratio of carbon in carbide is proved to be essential when designing catalysts for the activation and conversion of CO_2.

To explore the hydro-treating properties of molybdenum carbide, Tominaga and Nagai group also reported extensive theoretical investigations. Firstly, Nagai *et al.*,[201] present a combination of experimental and Monte Carlo simulation studies to understand the adsorption properties of CO on the molybdenum carbide with different Mo/C ratio. It is found that the Mo_2C_{2x} with x = 0.4 has the highest ability in CO adsorption since it is rich in carbon-deficient sites. However, molecular dynamics can only predict the approach of CO to the Mo_2C surface but cannot predict the chemisorption of CO on the molybdenum or carbon atoms of molybdenum carbides. They applied cluster models to study the relative stability and reactivity of surface species of Mo_2C and Mo metal in CO_2 hydrogenation,[202] where Mo_2C was found to present higher activity than Mo metal. Furthermore, the WGS reaction mechanism was systematically calculated and the formation of CO_2 from the combination of CO and surface O is the rate determining step.[203] Apart from CO_2 hydrogenation and WGS reaction, Tominaga and Nagai also studied the mechanisms of methane reforming[204] as well as thiophene HDS[205] on the hexagonal Mo_2C surface. On the basis of DFT calculations and mass spectroscopic measurements, Tominaga *et al.*,[206] recently studied CO hydrogenation on both clean and cobalt doped hexagonal CdI_2-like $Mo_2C(100)$ surface and they ruled out the possible formation of CH_3OH on both catalysts. All of these calculations provided useful information for the deep understanding into the mechanisms catalyzed by Mo_2C.

On the basis of early surface science experiments under UHV condition, the group of Juan investigated the adsorption and decompositions of methanol,[207, 208] methyl iodide[209] as well as CO[210,211] on the clean and potassium doped Mo_2C surfaces. For methanol adsorption on the clean orthorhombic $Mo_2C(001)$ surface, the abstraction of H from OH group is found to be energetically favorable. With the doping of potassium on the surface, the C–O bond distance increases while the O–

H bond distance decreases, which makes it possible for a C–O bond breakage on K covered surface. Similarly, the incorporation of K also promotes the dissociation ability of the C–I bond in methyl iodide. Moreover, K promoter was found to strengthen CO adsorption but increases CO dissociation barrier. Although the detailed mechanisms of methanol and methyl iodide decomposition as well as CO hydrogenation were not systematically calculated by this group, all their DFT results were supported by early surface science investigations which facilitated the combination of DFT calculations and experiment studies in solving chemical problems.

Another potential application of Mo_2C catalyst is the hydrogenolysis reaction in petrol refining. It is known that the commercial catalysts for hydrodesulfurization (HDS) and hydrodenitrogenation (HDN) processes are cobalt and nickel doped Mo_2S catalysts. However, Mo_2C was thought to exhibit promising activity in deep HDS and HDN because of its similar properties with noble metals. Kotarba *et al.*,[212] applied species-resolved thermal alkali desorption techniques, work-function measurements and DFT calculations to reveal the effect of potassium doping on electronic surface properties of molybdenum carbide. It is found that the changes in the catalyst work function with K addition show a remarkable correlation with the catalytic rate of indole HDN over Mo_2C. However, DFT calculation only plays a complementary role in this study. For the HDN of N-containing compounds, two parallel routes are possible, i.e.; direct C-N bond breaking (DDN, direct denitrogenation) or indirect (HYD, hydrogenation) nitrogen removal depending on the hydrogen attack on the heterocyclic or carbocyclic ring, respectively. On the basis of DFT calculations, Piskorz *et al.*,[213] found that indole HDN over Mo_2C catalyst favours the HYD route. In addition to the above calculated HDN mechanism of indole, this group also reported a kinetic study of the deep HDS of dibenzothiophene[214] over Mo_2C supported on a carbon black composite and two types of active sites on the catalyst were proposed to account for the zero order DDS route and first order HYD route, respectively.

In recent years, Sholl group also reported many interesting DFT works about the properties of Mo_2C catalyst. On the basis of the calculated surface energies of seven low-index orthorhombic Mo_2C surfaces, the equilibrium crystal shape of Mo_2C was predicated by Wulff construction and the (011) is found to be most stable. Then, the adsorption of K and Rh as well as their effects on the adsorption of H and CO were also investigated, where the incorporation of K was found to weaken the adsorption strength of H and CO.[215] They also reported a combination of infrared spectroscopy and DFT study into the effect of rubidium on the selectivity of CO hydrogenation on alumina-supported Mo_2C,[216] it revealed that the addition of Rb decreases the hydrocarbon production rate while increases the alcohol selectivity. Recently, Sholl applied two DFT-based charge assignment methods; namely, the Bader and density derived electrostatic and chemical (DDEC) methods to calculate the partial charges in a series of Mo containing dense materials and compared with experimental measured X-ray absorption near-edge spectroscopy (XANES) energies.[217] It is found that the linear relation between DDEC charges and XANES energies can be used in characterizing the degree of reduction in supported catalyst samples.

Apart from the above systematic investigations from different groups, there are also some individual interesting works about the properties of Mo_2C catalyst. Rocha *et al.*[218] reported a theoretical and experimental study into the adsorption of benzene on the Mo_2C surface and proposed a detailed benzene hydrogenation mechanism, i.e.; benzene molecule would interact with the hydrogen pre-covered on the Mo_2C surface via Eley-Riedeal mechanism to produce cyclohexane and vacant sites; and the catalyst is then deactivated by the subsequent strong adsorption of other benzene molecules to these vacant sites. However, Zhou *et al*.[219] proposed that the weakly adsorbed benzene would follow the Langmuir–Hinshelwood hydrogenation mechanism on the orthorhombic Mo_2C (0001) surface based on DFT calculations. Liu *et al*.[220] studied the adsorption of both C_6H_6 as well as cyclohexadiene, cyclohexene and cyclohexane (C_6H_8, C_6H_{10}, and C_6H_{12}) on the Mo termination of the orthorhombic Mo_2C(0001) surface and further confirmed the proposed Langmuir–Hinshelwood hydrogenation mechanism of benzene. Rocha *et al*.,[221] also investigate the occlusion of hydrogen by molybdenum carbide on the basis of the experimental TPD and DFT calculation. It is found that hydrogen occlusion during the synthesis of molybdenum carbide is the reason for the deactivation of Mo_2C catalyst during the hydrogenation of benzene when the reaction is performed at atmospheric pressure. For the hydro-treating reactions, many systematic DFT works discussed the detailed reaction mechanisms. Qi *et al.,*[222] investigated the mechanism of CO hydrogenation on two Mo_2C surfaces where the orthorhombic Mo_2C(100) surface was proved to have higher activity in CH_4 formation than hexagonal Mo_2C(101) surface. For the adsorption and hydrogenolysis of ethane on orthorhombic Mo_2C (100) and hexagonal Mo_2C (101),[223] the same reaction mechanism was found on these two surfaces and the rate limiting step is the decomposition of C_2H_5 into CH_2+CH_3. Xing *et al*.[224] calculated the detailed reaction mechanism of ethanol decomposition on the orthorhombic Mo_2C(100) surface, the energetic information about the formation of different products and byproducts were clearly provided and the barrier of C-C bond cleavage was found to decrease as the losing of H atoms in intermediate, which indicated that the C-C bond cleavage may become possible at the late dehydrogenation steps in the whole reaction processes. For the detailed mechanism study, the (101) surface of the hexagonal eclipsed Mo_2C is found to be promising for CO-free hydrogen production from formic acid decomposition.[225] A DFT study of promoter effect of on the catalytic property of hexagonal eclipsed Mo_2C(001) surface by Zhao *et al*.[226] found that the incorporation of Ni reduces the barrier of carbon oxidation on the surface which is beneficial for preventing carbon deposition and increasing CO selectivity. Recently, molybdenum carbide found wide applications in biomass chemistry for the sessions of C-O, C-C and C-H bonds.

Ren *et al*.,[227] applied oxygen and carbon monoxide as probe molecules to characterize the catalytically active sites of both Mo and C terminations of orthorhombic Mo_2C(0001) surface, where metallic character is found on both the clean and oxygen doped surfaces. To understand the initial steps of CH_4 dry reforming and hydrodenitrogenation of nitrogen-containing molecules, Ren *et al*., further calculated the adsorption energetics of CO_2, H, CH_x ($x = 0$–3) and C_2H_4[228] as well as NO, NO_2, pyridine and pyrrole[229] on the orthorhombic Mo_2C(0001) surface, and all these results provide useful information for mechanism studies. Shi *et al*.,[115] systematically calculated all the possible structures of hexagonal Mo_2C cells and found the Mo_2C with an eclipse structure is most stable. On the basis of this eclipse Mo_2C cell, the stabilities of those low index miller surfaces where the (011) and (101) were found to be most stable. Shi *et al.*,[230] applied a $Mo_{31}C_{12}$ cluster to model the catalytic properties of the hexagonal eclipsed $Mo_2C(001)$ surface and the Mo termination was found to have higher activity in CO and NO adsorption as well as dissociation than the C termination.

In summary, extensive UHV surface science and theoretical investigations of the catalytic properties of Mo_2C catalyst have revealed the promising and wide usages of this catalyst. Among these reactions that catalysed by Mo_2C, the CO and H_2 played important roles either as reactant or product. Therefore, a deep understanding of CO and H_2 interaction mechanisms with Mo_2C is essential for the related reactions such as alcohol synthesis, WGS, HDS and HDN. Early surface science studies of this system mainly focused on the surface structure and CO desorption states on the model catalyst such as orthorhombic $Mo_2C(0001)$ surface, while theoretical modelling mainly concerned the CO and H_2 interaction with simple Mo_2C surfaces at very ideal conditions such as 0 K and 0 atm. There is no doubt that such extensive investigations can provide primary but very useful information for understanding this system at atomic scale. However, many key factors, such as reactant coverage, reaction temperature and pressure, should be considered to provide more useful information for practical applications. Moreover, Co-adsorption properties of reactants on the surfaces also should be considered since most of reactions contained more than one reactant.

To address the above concerns, some related theoretical works about the effects of reaction conditions on the catalytic properties of Mo_2C catalyst are available. For example, on the basis of atomistic thermodynamic method under the consideration of temperature, pressure and gas composition, Wang *et al.*, calculated the surface stabilities and morphologies of Mo_2C catalyst under different carburization conditions. It showed that the (101) surface of the hexagonal eclipsed Mo_2C phase is most stable,[231] which is in agreement with the results from X-ray diffraction[232] and high resolution transmission electron microscopy.[233] Medford *et al.*[234] also studied the thermodynamics of elementary steps of synthesis gas reactions on the orthorhombic $Mo_2C(001)$ surface by considering the effects of temperature, pressure and reactants mixtures. It is found that the Mo-termination exhibits similar activity in carbon related reactions as transition metals such as Ru and Ir.

In this respect, this part of the dissertation mainly focused on the on the effects of experimental conditions such as temperature, pressure as well as gas compositions on the properties of Mo_2C catalysts as well as reaction mechanisms by using atomistic thermodynamics method and micro-kinetics method. We first computed the properties of twenty-two terminations of low index orthorhombic Mo_2C surfaces[235] and found that structures and compositions as well as catalytic activities of surfaces have intrinsic relationships with carburization conditions. On the basis of the computed Gibbs free energies, we studied the relationship among temperature, equilibrium coverage and partial pressure of CO, O_2 and H_2 on the hexagonal eclipsed Mo_2C surfaces,[236-238] and found good agreement between the predicated and the experimentally detected spectra of temperature programmed CO and H_2 desorption at low temperature. In addition, we investigated the coverage dependent CO adsorption, desorption and dissociation on the Mo- and C terminations of the orthorhombic $Mo_2C(100)$ surface and showed coverage dependent CO activation mechanisms.[239]

1.3 References

(1) Anderson, R. B. *The Fischer-Troposch Synthesis*, Academic Press, Orlando, FL, **1984**, p. 3.

(2) Kelly, R. D.; Goodman, D. W.; In: King, D. A.; Woodruff, D. P. (Eads), *The Chemical Physics of Solid Surfaces and Heterogeneous Catalysis*, Vol. 4, Elsevier, Amsterdam, **1982**, p. 427.

(3) Fischer, F.; Tropsch, H. Über die Herstellung synthetischer Ölgemische (Synthol) durch Aufbau aus Kohlenoxid und Wasserstoff. *Brennstoff Chem*. **1923**, *4*, 276-285.

(4) Fischer, F.; Tropsch, H. Die Erdölsynthese bei gewöhnlichem Druck aus den Vergasungsprodukten der Kohlen. *Brennstoff Chem*. **1926**, *7*, 97-116.

(5) van Santen, R. A.; Neurock, M. *Molecular Heterogeneous Catalysis: A Conceptual and Computational Approach*, Wiley-VCH, Weinheim, **2006**.

(6) Honkala, K.; Hellman, A.; Remediakis, I. N.; Logadottir, A.; Carlsson, A.; Dahl, S.; Christensen, C. H.; Nørskov, J. K. Ammonia Synthesis from First-Principles Calculations. *Science* **2005**, *307*, 555-558.

(7) Biloen, P.; Helle, J. N.; Sachtler, W. M. H. Incorporation of Surface Carbon into Hydrocarbons during Fischer-Tropsch Synthesis: Mechanistic Implications. *J. Catal*. **1979**, *58*, 95-107.

(8) Dictor, R. A.; Bell, A. T. Fischer-Tropsch Synthesis over Reduced and Unreduced Iron Oxide Catalysts. *J. Catal*. **1986**, *97*, 121-136.

(9) Kummer, J. F.; Emmett, P. H. Fischer-Tropsch Synthesis Mechanism Studies. The Addition of Radioactive Alcohols to the Synthesis Gas. *J. Am. Chem. Soc*. **1953**, *75*, 5177-5183.

(10) Vannice, M. A. The Catalytic Synthesis of Hydrocarbons from Carbon Monoxide and Hydrogen. *Catal. Rev. Sci. Eng*. **1976**, *14*, 153-191.

(11) Huff Jr, G. A.; Satterfield, C. N. Intrinsic Kinetics of the Fischer-Tropsch Synthesis on a Reduced Fused-Magnetite Catalyst. *Ind. Eng. Chem. Proc. Des. Dev*. **1984**, *23*, 696-705.

(12) Pichler, H.; Schulz, H. Neuere Erkenntnisse auf dem Gebiet der Synthese von Kohlenwasserstoffen aus CO und H_2. *Chem. Ing. Tech*. **1970**, *42*, 1162-1174.

(13) Henrici-Olive, G.; Olive, S. The Fischer-Tropsch Synthesis: Molecular Weight Distribution of Primary Products and Reaction Mechanism. *Angew. Chem. Int. Ed*. **1976**, *15*, 136-141.

(14) Masters, C. The Fischer-Tropsch Reaction. *Adv. Organomet. Chem*. **1979**, *17*, 61-103.

(15) Cao, D.-B.; Li, Y.-W.; Wang, J.; Jiao, H. Chain Growth Mechanism of Fischer-Tropsch Synthesis on Fe_5C_2(001). *J. Mol. Catal. A* **2011**, *346*, 55-69.

(16) Schulz, H. Short History and Present Trends of Fischer–Tropsch Synthesis. *Appl. Catal. A*: *Gen*. **1999**, *186*, 3-12.

(17) Iglesia, E. Design, Synthesis, and Use of Cobalt-Based Fischer-Tropsch Synthesis Catalysts. *Appl. Catal. A: Gen.* **1997**, *161*, 59-78.

(18) Davis, B. H. Fischer−Tropsch Synthesis: Comparison of Performances of Iron and Cobalt Catalysts. *Ind. Eng. Chem. Res*. **2007**, *46*, 8938-8945.

(19) de Smit, E.; Weckhuysen, B. M. The Renaissance of Iron-Based Fischer-Tropsch Synthesis: on the Multifaceted Catalyst Deactivation Behaviour. *Chem. Soc. Rev*. **2008**, *37*, 2758-2781.

(20) Prutton, M. *Introduction to Surface Physics*. Oxford University Press: Oxford. **1994**.

(21) Spencer, M. J. S.; Hung, A.; Snook, I. K.; Yarovsky, I. Density Functional Theory Study of the Relaxation and Energy of Iron Surfaces. *Surf. Sci*. **2002**, *513*, 389-398.

(22) Błoński, P.; Kiejna, A. Structural, Electronic, and Magnetic Properties of bcc Iron Surfaces. *Surf. Sci*. **2007**, *601*, 123-133.

(23) Dewar, M. J. S. *Bull. Soc. Chim. Fr*. **1951**, *18*, C79.

(24) Chatt, J.; Duncanson, L. A. *J. Chem. Soc.* **1953**, 2939-2947.

(25) Brodén, G.; Gafner, g.; Bonzel, H. P. A UPS and LEED/Auger Study of Adsorbates on Fe(110). *Appl. Phys*. **1977**, *13*, 333-342.

(26) Jensen, E. S.; Rhodin, T. N. CO Chemisorption on Fe(110) Studied by Angle-Resolved Photoemission. *Phys. Rev. B* **1983**, *27*, 3338-3350.

(27) Maruyama, T.; Sakisaka, Y.; Kato, H.; Aiura, Y.; Yanashima, H. CO on Fe(110): an Angle-Resolved Photoemission Study. *Surf. Sci*. **1994**, *304*, 281-290.

(28) Yoshida, K.; Somorjai, G. A. The Chemisorption of CO, CO_2, C_2H_2, C_2H_4, H_2 and NH_3 on the Clean Fe(100) and (111) Crystal Surfaces. *Surf. Sci.* **1978**, *75*, 46-60.

(29) Erley, W. Vibrational Spectra of CO Chemisorbed on Fe (110). *J. Vac. Sci. Technol*. **1981**, *18*, 472-475.

(30) Gonzalez, L.; Miranda, R.; Ferrer, S. A Thermal Desorption Study of the Adsorption of CO on Fe(110); Enhancement of Dissociation by Surface Defects. *Surf. Sci*. **1982**, *119*, 61-70.

(31) Wedler, G.; Ruhmann, H. Laser Induced Thermal Desorption of Carbon Monoxide from Fe(110) Surfaces. *Surf. Sci*. **1982**, *121*, 464-486.

(32) Wedler, G.; Ruhmann, H. Study of the Adsorption and Decomposition of CO on Fe(110) with an Improved Vibrating Capacitor. *Appl. Surf. Sci*. **1983**, *14*, 137-148.

(33) Brodén, G.; Gafner, G.; Bonzel, H. P. CO Adsorption on Potassium Promoted Fe(110). *Surf. Sci*. **1979**, *87*, 295-314.

(34) Zhu, L.; Bao, S.; Xu, C. Y.; Xu, Y. B. HREELS Investigation of CO and K Coadsorption on Fe(110). *Surf. Sci*. **1992**, *260*, 267-270.

(35) Wang, H. L.; Deng, J. Z. Effect of TiO_x Overlayer on the Adsorption of CO on Fe(110). *Surf. Sci*. **1993**, *291*, 370-380.

(36) Rhodin, T. N.; Brucker, C. F. Effect of Surface Deactivation on Molecular Chemisorption: Co on α-Fe(100) Surfaces. *Solid State Commun*. **1977**, *23*, 275-279.

(37) Benziger, J.; Madix, R. J. The Effects of Carbon, Oxygen, Sulfur and Potassium Adlayers on CO and H_2 Adsorption on Fe(100). *Surf. Sci.* **1980**, *94*, 119-153.

(38) Moon, D. W.; Dwyer, D. J.; Bernasek, S. L. Adsorption of CO on the Clean and Sulfur Modified Fe(100) Surface. *Surf. Sci.* **1985**, *163*, 215-229.

(39) Moon, D. W.; Bernasek, S. L.; Lu, J. P.; Gland, J. L; Dwyer, D. J. Activation of Carbon Monoxide on Clean and Sulfur Modified Fe(100). *Surf. Sci*. **1987**, *184*, 90-108.

(40) Vink, T. J.; Gijzeman, O. L. J.; Geus, J. W. CO Interaction with Fe(100): Effects of Carbon and Oxygen Adlayers on CO Adsorption Isotherms. *Surf. Sci.* **1985**, *150*, 14-23.

---

(41) Moon, D. W.; Bernasek, S. L.; Dwyer, D. J.; Gland, J. L. Observation of an Unusually Low Carbon Monoxide Stretching Frequency on Iron(100). *J. Am. Chem. Soc*. **1985**, *107*, 4363-4364.

(42) Benndorf, C.; Krüger, B.; Thieme, F. Unusually Low Stretching Frequency for CO Adsorbed on Fe(100). *Surf. Sci. Lett*. **1985**, *163*, L675-L680.

(43) Moon, D. W.; Cameron, S.; Zaera, F.; Eberhardt, W.; Carr, R.; Bernasek, S. L.; Gland, J. L.; Dwyer, D. J. A Tilted Precursor for CO Dissociation on the Fe(100) Surface. *Surf. Sci. Lett.* **1987**, *180*, L123-L128.

(44) Saiki, R. S.; Herman, G. S.; Yamada, M.; Osterwalder, J.; Fadley, C. S. Structure of an Unusual Tilted State of CO on Fe(001) from x-ray Photoelectron Diffraction. *Phys. Rev. Lett*. **1989**, *63*, 283-286.

(45) Cameron, S.; Dwyer, D. J. A Study of π-Bonded Carbon Monoxide on Iron(100). *Langmuir* **1988**, *4*, 282-288.

(46) Dwyer, D. J.; Rausenberger, B.; Cameron, S. D.; Lu, J. P.; Bernasek, S. L.; Fischer, D. A.; Parker, D. H.; Gland, J. L. Fluorescence Yield Near Edge Spectroscopy of π-Bonded CO on Fe(100). *Surf. Sci*. **1989**, *224*, 375-385.

(47) Lu, J. P.; Albert, M.R.; Bernasek, S. L. Adsorption and Dissociation of CO on Fe(100) at Low Coverage. *Surf. Sci.* **1989**, *217*, 55-64.

(48) Lu, J. P.; Albert, M.R.; Bernasek, S. L. Effects of Postdosed Species on Preadsorbed Carbon Monoxide on Iron (100): Adsorption Site Conversion Caused by Site Competition. *J. Phys. Chem*. **1990**, *94*, 6028-6033.

(49) Gladh, J.; Öberg, H.; Li, J. B.; Ljungberg, M. P., Matsuda, A.; Ogasawara, H.; Nilsson, A.; Pettersson, L. G. M.; Öström, H. X-ray Emission Spectroscopy and Density Functional Study of CO/Fe(100). *J. Chem. Phys*. **2012**, *136*, 034702 .

(50) Seip, U.; Tsai, M. C.; Christmann, K.; Kuppers, J.; Ertl, G. A TDS and HREELS Study of CO Adsorbed on a Potassium Promoted Fe(111) Surface. *Surf. Sci*. **1984**, *139*, 29-42.

(51) Bartosch, C. E.; Whitman, L, J.; Ho, W. The Adsorption, Interconversion, and Dissociation of CO on Fe(111). *J. Chem. Phys*. **1986**, *85*, 1052-1060.

(52) Whitman, L. J.; Richter, L. J.; Gurney, B. A.; Villarrubia, J. S.; Ho, W. CO Adsorption Site Occupations on Fe(111) vs Coverage and Temperature: The Kinetics of Adsorption and Reaction. *J. Chem. Phys*. **1989**, *90*, 2050-2062.

(53) Ertl, G. Reactions At Surfaces: From Atoms To Complexity. *Angew. Chem. Int. Ed*. **2008**, *47*, 3524-3535.

(54) Thüne, P. C.; Weststrate, C. J.; Moodley, P.; Saib, A. M.; van de Loosdrecht, J.; Miller, J. T.; Niemantsverdriet, J. W. Studying Fischer-Tropsch Catalysts Using Transmission Electron Microscopy And Model Systems Of Nanoparticles On Planar Supports. *Catal. Sci. Technol*. **2011**, *1*, 689-697.

(55) Cavalier, J. C.; Chornet, E. Hydrogen-Deuterium Exchange on Iron: Kinetic Anisotropies. *Surf. Sci*. **1976**, *60*, 125-146.

---

(56) Bozso, F.; Ertl, G.; Grunze, M.; Weiss, M. Chemisorption of Hydrogen on Iron Surfaces. *Appl. Surf. Sci*. **1977**, *1*, 103-119.

(57) Imbihl, R.; Behm, R. J.; Christmann, K.; Ertl, G.; Matsushima, T. Phase Transitions of A Two-Dimensional Chemisorbed System: H on Fe(110). *Surf. Sci*. **1982**, *117*, 257-266.

(58) Nichtl-Pecher, W.; Gossman, J.; Hammer, L.; Heinz, K.; Müller, K. Adsorption of Hydrogen on Fe(110) at Cryogenic Temperatures Investigated by Low Energy Electron Diffraction. *J. Vac. Sci. Technol. A* **1992**, *10*, 501-507.

(59) Christmann, K. Interaction of Hydrogen with Solid Surfaces. *Surf. Sci. Rep*. **1988**, *9*, 1-163.

(60) Sokolov, J.; Shih, H. D.; Bardi, U.; Jona, F.; Marcus, P. M. Multilayer Relaxation of Body-Centred-Cubic Fe(211). *J. Phys. C: Solid State Phys*. **1984**, *17*, 371-383.

(61) Hassold, E.; Löffler, U.; Schmiedl, R.; Grund, M.; Hammer, L.; Heinz, K.; Müller, K. Hydrogen Induced Missing Row Reconstruction of Fe(211). *Surf. Sci*. **1995**, *326*, 93-100.

(62) Schmiedl, R.; Nichtl-Pecher, W.; Heinz, K.; Müller, K. Hydrogen on Fe(211): Commensurate and Reconstructed Phases. *Surf. Sci*. **1990**, *235*, 186-196.

(63) Schmiedl, R.; Nichtl-Pecher, W.; Hammer, L.; Heinz, K.; Müller, K. Hydrogen Adsorption on Fe(211): Structural, Thermodynamic and Kinetic Properties. *Surf. Sci*. **1995**, *324*, 289-304.

(64) Merrill, P. B.; Madix, R. J. Hydrogen Bonding on Iron: Correlation of Adsorption and Desorption States on Fe(100) and Perturbation of the Fe-H Bond with Coadsorbed CO. *Surf. Sci*. **1996**, *347*, 249-264.

(65) Suo, H. Y.; Wang, S. G.; Zhang, C. H.; Xu, J.; Wu, B. S.; Yang, Y.; Xiang, H. W.; Li, Y.-W. Chemical and Structural Effects of Silica in Iron-Based Fischer-Tropsch Synthesis Catalysts. *J. Catal.* **2012**, *286*, 111-123.

(66) Burke, M. L.; Madix, R. J. Effect of CO on Hydrogen Thermal Desorption from Fe(100). *Surf. Sci*. **1990**, *237*, 20-34.

(67) Mehandru, S. P.; Anderson, A. B. Binding and Orientations of CO on Fe(110), (100), and (111): A Surface Structure Effect from Molecular Orbital Theory. *Surf. Sci*. **1988**, *201*, 345-360.

(68) Blyholder, G.; Lawless, M. A Theoretical Study of the Site of CO Dissociation on Fe(100). *Surf. Sci*. **1993**, *290*, 155-162.

(69) Meehan, T. E.; Head, J. D. A Theoretical Comparison of CO Bonding on the Fe(100) Surface. *Surf. Sci*. **1991**, *243*, L55-L62.

(70) Nayak, S. K.; Nooijen, M.; Bernasek, S. L.; Blaha, P. Electronic Structure Study of CO Adsorption on the Fe(001) Surface. *J. Phys. Chem. B* **2001**, *105*, 164-172.

(71) Sorescu, D. C.; Thompson, D. L.; Hurley, M. M.; Chabalowski, C. F. First-Principles Calculations of the Adsorption, Diffusion, and Dissociation of a CO Molecule on the Fe(100) Surface. *Phys. Rev. B* **2002**, *66*, 035416.

(72) Bromfield, T. C.; Ferre, D. C.; Niemantsverdriet, J. W. A DFT Study of the Adsorption and Dissociation of CO on Fe(100): Influence of Surface Coverage on the Nature of Accessible Adsorption States. *Chem. Phys. Chem.* **2005**, *6*, 254-260.

---

(73) Curulla-Ferré, D.; Govender, A.; Bromfield, T. C.; Niemantsverdriet, J. W. A DFT Study of the Adsorption and Dissociation of CO on Sulfur-Precovered Fe(100). *J. Phys. Chem. B* **2006**, *110*, 13897-13904.

(74) Elahifard, M. R.; Jigato, M. P.; Niemantsverdriet, J. W. Direct Versus Hydrogen-Assisted CO Dissociation on the Fe (100) Surface: a DFT Study. *Chem. Phys. Chem*. **2012**, *13*, 89-91.

(75) Stibor, A.; Kresse, G.; Eichler, A.; Hafner, J. Density Functional Study of the Adsorption of CO on Fe(110). *Surf. Sci*. **2002**, *507-510*, 99-102.

(76) Jiang, D. E.; Carter, E. A. Adsorption and Dissociation of CO on Fe(110) from First Principles. *Surf. Sci.* **2004**, *570*, 167-177.

(77) Sun, X.; Forster, S.; Li, Q. X.; Kurahashi, M.; Suzuki, T.; Zhang, J. W.; Yamauchi, Y.; Baum, G.; Steidl, H. Spin-Polarization Study of CO Molecules Adsorbed on Fe(110) Using Metastable-Atom Deexcitation Spectroscopy and First-Principles Calculations. *Phys. Rev. B* **2007**, *75*, 035419.

(78) Chen, Y. H.; Cao, D. B.; Jun, Y.; Li; Y.-W.; Wang, J.; Jiao, H. J. Density Functional Theory Study of CO Adsorption on the Fe(111) Surface. *Chem. Phys. Lett.* **2004**, *400*, 35-41.

(79) Huo, C. F.; Ren, J.; Li, Y.-W.; Wang, J.; Jiao, H. J. CO Dissociation on Clean and Hydrogen Precovered Fe(111) Surfaces. *J. Catal.* **2007**, *249*, 174-184.

(80) Li, H. J.; Chang, C. C.; Ho, J. J. Density Functional Calculations to Study the Mechanism of the Fischer–Tropsch Reaction on Fe(111) and W(111) Surfaces. *J. Phys. Chem. C* **2011**, *115*, 11045-11055.

(81) Booyens, S.; Bowker, M.; Willock, D. J. The Adsorption and Dissociation of CO on Fe(111). *Surf. Sci*. **2014**, *625*, 69-83.

(82) Borthwick, D.; Fiorin, V.; Jenkins, S. J.; King, D. A. Facile Dissociation of CO on Fe{211}: Evidence from Microcalorimetry and First-Principles Theory. *Surf. Sci.* **2008**, *602*, 2325-2332.

(83) Lo, J. M.; Ziegler, T. Adsorption and Decomposition of CO on Stepped Fe(310) Surfaces. *J. Phys. Chem. C* **2008**, *112*, 3692-3700.

(84) Sorescu, D. C. Plane-Wave DFT Investigations of the Adsorption, Diffusion, and Activation of CO on Kinked Fe(710) and Fe(310) Surfaces. *J. Phys. Chem. C* **2008**, *112*, 10472-10489.

(85) Mims, C. A.; McCandlish, L. E. Evidence for Rapid Chain Growth in the Fischer-Tropsch Synthesis over Iron and Cobalt Catalysts. *J. Phys. Chem*. **1987**, *91*, 929-937.

(86) Ojedaa, M.; Nabarb,R.; Nilekarb, A. U.; Ishikawaa, A.; Mavrikakisb, M.; Iglesia, E. CO Activation Pathways and the Mechanism of Fischer–Tropsch Synthesis. *J. Catal*. **2010**, *272*, 287-297.

(87) Loveless, B. T.; Buda, C.; Neurock, M.; Iglesia, E. CO Chemisorption and Dissociation at High Coverages during CO Hydrogenation on Ru Catalysts. *J. Am. Chem. Soc*. **2013**, *135*, 6107-6121.

(88) Wang, T.; Tian, X.; Li, Y.-W.; Wang, J.; Beller, M.; Jiao, H. High Coverage CO Activation Mechanisms on Fe(100) from Computations. *J. Phys. Chem. C* **2014**, *118*, 1095-1101.

(89) Wang, T.; Tian, X.; Li, Y.-W.; Wang, J.; Beller, M.; Jiao, H. Coverage-Dependent CO Adsorption and Dissociation Mechanisms on Iron Surfaces from DFT Computations. *ACS Catal.* **2014**, *4*, 1991-2005.

---

(90) Walch, S. P. Model Studies of the Interaction of H Atoms with bcc Iron. *Surf. Sci*. **1984**, *143*, 188-203.

(91) Juan, A.; Hoffmann, R. Hydrogen on the Fe(110) Surface and Near Bulk Bcc Fe Vacancies: A Comparative Bonding Study. *Surf. Sci*. **1999**, *421*, 1-16.

(92) Cremaschi, P.; Yang, H.; Whitten, J. L. Ab initio chemisorption studies of H on Fe(110). *Surf. Sci*. **1995**, *330*, 255-264.

(93) Eder, M.; Terakura, K.; Hafner, J. Initial Stages of Oxidation of (100) and (110) Surfaces of Iron Caused by Water. *Phys. Rev. B* **2001**, *64*, 115426.

(94) Jiang, D. E.; Carter, E. A. Adsorption and Diffusion Energetics of Hydrogen Atoms on Fe(110) from First Principles. *Surf. Sci*. **2003**, *547*, 85-98.

(95) Jiang, D. E.; Carter, E. A. Diffusion of Interstitial Hydrogen Into and through bcc Fe from First Principles. *Phys. Rev. B* **2004**, *70*, 064102.

(96) Sorescu, D. C. First Principles Calculations of The Adsorption and Diffusion of Hydrogen on Fe(100) Surface and in the Bulk. *Catal. Today* **2005**, *105*, 44-65.

(97) Huo, C. F.; Li, Y.-W.; Wang, J.; Jiao, H. Surface Structure and Energetics of Hydrogen Adsorption on the Fe(111) Surface. *J. Phys. Chem. B* **2005**, *109*, 14160-14167.

(98) van Steen, E.; van Helden, P. A DFT Study of Hydrogen Dissociation on CO- and C-Precovered Fe(100) Surfaces. *J. Phys. Chem. C* **2010**, *114*, 5932-5940.

(99) Fabiani, F. C.; Fratesi, G.; Brivio, G. P. Adsorption of H_2S, HS, S, and H on A Stepped Fe(310) Surface. *Eur. Phys. J. B* **2010**, *78*, 455-460.

100 Faglioni, F.; Goddard III, W. A. Energetics of Hydrogen Coverage on Group VIII Transition Metal Surfaces and a Kinetic Model for Adsorption/Desorption. *J. Chem. Phys*. **2005**, *122*, 014704.

(101) Wang, T.; Wang, S. G.; Luo, Q. Q.; Li, Y.-W.; Wang, J.; Beller, M.; Jiao, H. Hydrogen Adsorption Structures and Energetics on Iron Surfaces at High Coverage. *J. Phys. Chem. C* **2014**, *118*, 4181-4188.

(102) Storms, E. K. *The Refractory Carbides*, Academic Press: New York, **1967**.

(103) Toth, L. E. *Transition Metal Carbides and Nitrides*; Academic Press: New York, **1971**.

(104) Greenwood, N. N.; Earnshaw, A Chemistry of the Elements. Oxford: Pergamon Press. **1984**, p. 318-322.

(105) Gubanov, V. A.; Ivanovsky, A. L.; Zhukov, V. P. *Electronic Structure of Refractory Carbides and Nitrides*; Cambridge University Press: Cambridge, **1994**.

(106) Ettmayer, P.; Lengauer, W. Carbides: *Transition Metal Solid–State Chemistry.* in Encyclopedia of Inorganic Chemistry 1st ed.; King, B. R. John Wiley & Sons. **1994**.

(107) Lee, J.S.; Hyun, T.H. Metal carbides. In Encyclopedia of Catalysis, 1st ed.; Horvath, I. T. Ed.; John Wiley & Sons: New York, NY, USA, **2003**.

(108) Levy, R. B.; Boudart, M. Platinum-Like Behavior of Tungsten Carbide in Surface Catalysis. *Science* **1973**, *181*, 547-549.

(109) Liu, Y.; Kelly, T. G.; Chen, J. G.; Mustain, W. E. Metal Carbides as Alternative Electrocatalyst Supports. *ACS Catal*. **2013**, *3*, 1184-1194

(110) Westgren, A.; Phragmen, G. Z. Röntgenanalyse der Systeme Wolfram-Kohlenstoff und Molybdgn-Kohlenstoff. *Anorg. Chem*. **1926**, *156*, 27-36.

(111) Kuo, K.; Hagg, G. A New Molybdenum Carbide. *Nature* **1952**, *170*, 245-246.

(112) Fries, R.J.; Kempter, C. P. Dimolybdenum Carbide. *Anal. Chem.* **1960**, *32*, 1898-1898

(113) Parthe, E.; Sadagopan, V. The Structure of Dimolybdenum Carbide by Neutron Diffraction Technique. *Acta Crystallogr*. **1963**, *16*, 202-205.

(114) Haines, J.; Leger, J. M.; Chateau, C.; Lowther, J. E. Experimental and Theoretical Investigation of Mo_2C at High Pressure *J. Phys.: Condens. Matter* **2001**, *13*, 2447-2454.

(115) Shi, X. R.; Wang, S. G.; Wang, H.; Deng, C. M.; Qin, Z. F.; Wang, J. Structure and Stability of β-Mo_2C Bulk and Surfaces: A Density Functional Theory Study. *Surf. Sci.* **2009**, *603*, 852-859.

(116) Christensen, A. N. A Neutron Diffraction Investigation on a Crystal of Alpha-Mo_2C. *Acta. Chem. Scand. A* **1977**, *31*, 509-511.

(117) Dubois, J.; Epicier, T.; Esnouf, C.; Fantozzi, G.; Convert, P. Neutron Powder Diffraction Studies of Transition Metal Hemicarbides M_2C_{1-x} - I. Motivation for a Study on W_2C and Mo_2C and Experimental Background for an in situ Investigation at Elevated Temperature. *Acta. Metall*. **1988**, *8*, 1891-1901.

(118) Epicier, T.; Dubois, J.; Esnouf, C.; Fantozzi, G.; Convert, P. Neutron Powder Diffraction Studies of Transition Metal Hemicarbide M_2C_{1-x} - II. In situ High Temperature Study on W_2C and Mo_2C_{1-x}. *Acta. Metall*. **1988**, *8,* 1903-1921.

(119) Powder Diffraction File; JCPDS International Center for Diffraction Data: Pennsylvania, **2004**.

(120) Saito, M.; Anderson, R. B. The Activity of Several Molybdenum Compounds for the Methanation of CO. *J. Catal.* 1**980**, *63*, 438-446.

(121) Oades, R. D.; Morris, S. R. Moyes, R. B. Carbon Supported Molybdenum and Molybdenum-Potassium Catalysts for the Hydrogenation of Carbon Monoxide. *Catal. Today* **1990**, *7*, 199-208.

(122) Oyama, S. T. *The Chemistry of Transition Metal Carbides and Nitrides*; Blackie Academic and Professional: Glasgow, **1996**.

(123) Zaman, S.; Smith, K. J. A Review of Molybdenum Catalysts for Synthesis Gas Conversion to Alcohols: Catalysts, Mechanisms and Kinetics. *Catal. Rev*. **2012**, *54*, 41-132.

(124) Patt, J.; Moon, D. J.; Phillips, C.; Thompson, L. Molybdenum Carbide Catalysts for Water-Gas Shift. *Catal. Lett*. **2000**, *65*, 193-195.

(125) Moon, D. J.; Ryu, J. W. Molybdenum Carbide Water-Gas Shift Catalyst for Fuel Cell-Powered Vehicles Applications. *Catal. Lett*. **2004**, *92*,17-24

(126) Lee, J. S.; Locatelli, S.; Oyama, S. T.; Boudart, M. Molybdenum Carbide Catalysts 3. Turnover Rates for the Hydrogenolysis of n-butane. *J. Catal.* **1990**, *125*, 157-170.

(127) Lee, J. S.; Boudart, M. Hydrodesulfurization of Thiophene over Unsupported Molybdenum Carbide. *J. Phys. Chem*. **1985**, *19*, 207-210.

---

(128) McCrea, K. R.; Logan, J. W.; Tarbuck, T. L.; Heiser, J. L.; Bussell, M. E. Thiophene Hydrodesulfurization over Alumina-Supported Molybdenum Carbide and Nitride Catalysts: Effect of Mo Loading and Phase. *J. Catal*. **1997**, *171*, 255-267.

(129) Nelson, N.; Levy, R.B. The Organic Chemistry of Hydrodenitrogenation. *J. Catal*. **1979**, *58*, 485–488.

(130) Al–Megren, H. A.; Gonzalez–Cortes, S. L.; Xiao, T. C.; Green, M. L. H. A Comparative Study of the Catalytic Performance of Co–Mo and Co(Ni)-W Carbide Catalysts in the Hydrodenitrogenation (HDN) Reaction of Pyridine. *Appl. Catal. A: Gen.* **2007**, *329*, 36-45.

(131) Dhandapani, B.; Oyama, S. T. Novel Catalysts for Selective Dehalogenation of CCl_2F_2 (CFC 12). *Catal. Lett*. **1995**, *35*, 353-360.

(132) Delannoy, L.; Giraudon, J. M.; Granger, P.; Leclercq, L.; Leclercq, G. Group VI Transition Metal Carbides as Alternatives in the Hydrodechlorination of Chlorofluorocarbons. *Catal. Today* **2000**, *59*, 231-240.

(133) Delannoy, L.; Giraudon, J. M.; Granger, P.; Leclercq, L.; Leclercq, G. Hydrodechlorination of CCl_4 over Group VI Transition Metal Carbides. *Appl. Catal. B Environ*. **2002**, *37*, 161-173.

(134) Naito, S.; Tsuji, M.; Miyao, T. Mechanistic Difference of the CO_2 Reforming of CH_4 over Unsupported and Zirconia Supported Molybdenum Carbide Catalysts. *Catal. Today* **2002**, *77*, 161-165.

(135) Darujati, A. R. S.; LaMont, D. C.; Thomson, W. J. Oxidation Stability of Mo_2C Catalysts under Fuel Reforming Conditions. *Appl. Catal. A: Gen*. **2003**, *253*, 397-407.

(136) Darujati, A. R. S.; Thomson, W. J. Kinetic Study of a Ceria–Promoted Mo_2C/Gamma-Al_2O_3 Catalyst in Dry-Methane Reforming. *Chem. Eng. Sci*. **2006**, *61*, 4309-4315.

(137) LaMont, D. C.; Thomson, W. J. Dry Reforming Kinetics over a Bulk Molybdenum Carbide Catalyst. *Chem. Eng. Sci*. **2005**, *60*, 3553-3559.

(138) Flores, O. G. M.; Ha, S. Study of the Performance of Mo_2C for Iso-Octane Steam Reforming. *Catal. Today* **2008**, *136*, 235-242.

(139) Wang, D. J.; Lunsford, J. H.; Rosynek, M. P. Catalytic Conversion of Methane to Benzene over Mo/ZSM-5. *Top. Catal*. **1996**, *3*, 289-297.

(140) Solymosi, F.; Cserényi, J.; Szöke, A.; Bánsági, T.; Oszkó, A. Aromatization of Methane over Supported and Unsupported Mo-Based Catalysts. *J. Catal*. **1997**, *165*, 150-161.

(141) Solymosi, F.; Szöke, A. Conversion of Ethane into Benzene on Mo_2C/ZSM-5 Catalyst. *Appl. Catal. A: Gen*. **1998**, *166*, 225-235.

(142) Barthos, R.; Bánsági, T.; Zakar, T., S.; Z. Solymosi, F. Aromatization of Methanol and Methylation of Benzene over Mo_2C/ZSM-5 Catalysts. *J. Catal*. **2007**, *247*, 368-378.

(143) Jackson, A. G.; Hooker, M. P. A LEED Study of CO and CO_2 Adsorption on Mo (110). *Surf. Sci*. **1967**, *6*, 297-308.

(144) Zaera, F.; Kollin, E.; Gland, J. L. Observation of an Unusually Low C–O Stretching Frequency: CO Chemisorption on a Mo(100) Surface. *Chem. Phys. Lett*. **1985**, *121*, 464-468.

(145) Ko, E. I.; Madix, R. J. Effects of Adsorbed Carbon and Oxygen on the Chemisorption of H_2 and Co on Mo(100). *Surf. Sci*. **1981**, *109*, 221-238.

(146) Erickson, J. W.; Estrup, P. J. The Dissociation of CO on Modified Mo(110) Surfaces. *Surf. Sci*. **1986**, *167*, 519-533.

(147) Chen, J. G.; Colaianni, M. L.; Weinberg, W. H.; Yates Jr, J. T. Direct Vibrational Detection of Surface Reaction Channels Leading to CO Dissociation and to its Inhibition on Mo(110). *Chem. Phys. Lett*. **1991**, *177*, 113-117.

(148) Colaianni, M. L.; Chen, J. G.; Weinberg, W. H.; Yates, J. T. The Adsorption and Dissociation of Carbon Monoxide on Clean and Oxygen-Modified Molybdenum(110) Surfaces. *J. Am. Soc. Chem*. **1992**, *114*, 3735-3743.

(149) He, J. W.; Kuhn, W. K.; Goodman, D. W. CO Adsorption on Clean and C-, O- and H-covered Mo(110) Surfaces: an IRAS Study. *Surf. Sci*. **1992**, *262*, 351-358.

(150) Schelz, S.; Reinke, P.; Oelhafen, P. A Monolayer Interface of Plasma–Polymerized Polystyrene on Niobium: an in Situ Electron Spectroscopy Study. *Surf. Sci*. **1993**, *293*, 275-282.

(151) Reinke, P.; Oelhafen, P. The Molybdenum-Carbon Interface: Formation and Electronic Structure of the Carbide Layer. *Surf. Sci*. **2000**, *468*, 203-215.

(152) Frühberger, B.; Chen, J. G. Modification of the Surface Reactivity of Mo(110) upon Carbide Formation. *Surf. Sci*.**1995**, *342*, 38-46.

(153) Chen, J. G. NEXAFS Investigations of Transition Metal Oxides, Nitrides, Carbides, Sulfides and Other Interstitial Compounds. *Surf. Sci*. *Rep*. **1997**, *30*, 1-152.

(154) Wu, H. H. H.; Chen, J. G. Surface Chemistry of Transition Metal Carbides. *Chem. Rev.* **2005**, *105*, 185-212.

(155) Lo, R. L.; Fukui, K. I.; Otani, S.; Iwasawa, Y. High Resolution Images of $Mo_2C(0001)$-($\sqrt{3}\times\sqrt{3}$)R30° Structure by Scanning Tunneling Microscopy. *Surf. Sci.* **1999**, *440*, L857-L861.

(156) St. Clair, T. P.; Oyama, S. T.; Cox, D. F.; Otani, S.; Ishizawa, Y.; Lo, R. L.; Fukui, K.; Iwasawa, Y. Surface Characterization of α-Mo_2C (0001) *Surf. Sci*. **1999**, *426*, 187-198.

(157) Sugihara, A.; Ozawa, K.; Edamoto, K.; Otani, S. Photoelectron Spectroscopy Study of $Mo_2C(0001)$. *Solid State Commun*. **2002**, *121*, 1-5.

(158) Sugihara, A.; Ozawa, K.; Edamoto, K.; Otani, S. Electronic Structure of $Mo_2C(0001)$ Studied by Resonant Photoemission Spectroscopy. *Solid State Commun*. **2004**, *131*, 245-249.

(159) Kato, M.; Sato, T.; Ozawa, K.; Edamoto, K.; Otani, S. Surface Electronic Structure of α-$Mo_2C(0001)$. *Surf. Sci*. **2006**, *600*, 448-452.

(160) Pham-Huu, C.; Ledoux, M.J.; Guille, J. Reactions of 2- and 3-Methylpentane, Methylcyclopentane, Cyclopentane, and Cyclohexane on Activated Mo_2C. *J. Catal*. **1993**, *143*, 249-261.

(161) Liu, N.; Rykov, S. A.; Chen, J. G. A Comparative Surface Science Study of Carbide and Oxycarbide: the Effect of Oxygen Modification on the Surface Reactivity of C/W(111). *Surf. Sci*. **2001**, *487*, 107-117.

---

(162) Wang, J.; Castonguay, M.; Deng, J.; McBreen, P. H. RAIRS and TPD Study of CO and NO on β-Mo_2C. *Surf. Sci*. **1997**, *374*, 197-207.

(163) St Clair, T. P.; Oyama, S. T.; Cox, D. F. CO and O_2 Adsorption on α-Mo_2C(0001). *Surf. Sci*. **2000**, *468*, 62-76.

(164) Bugyi, L.; Solymosi, F. Effects of Potassium on the Chemisorption of CO on the Mo_2C/Mo(100) Surface. *J. Phys. Chem. B* **2001**, *105*, 4337-4342.

(165) Edamoto, K.; Sugihara, M.; Ozawa, K.; Otani, S. Oxidation Process of Mo_2C(0001) Studied by Photoelectron Spectroscopy. *Appl. Surf. Sci*. **2004**, *237*, 498-502.

(166) Edamoto, K.; Sugihara, M.; Ozawa, K.; Otani, S. Photoelectron Spectroscopy Study of Oxygen Adsorption on Mo_2C(0001). *Surf. Sci*. **2004**, *561*, 101-109.

(167) Óvári, L.; Kiss, J.; Farkas, A. P.; Solymosi, F. Surface and Subsurface Oxidation of Mo_2C/Mo(100): Low-Energy Ion-Scattering, Auger Electron, Angle-Resolved X-ray Photoelectron, and Mass Spectroscopy Studies. *J. Phys. Chem. B* **2005**, *109*, 4638-4645.

(168) Óvári, L.; Kiss, J.; Farkas, A. P.; Solymosi, F. Reactivity of Mo_2C/Mo(100) Toward Oxygen: LEIS, AES, and XPS Study. *Surf. Sci*. **2004**, *566*, 1082-1086.

(169) Kato, M.; Sato, T.; Ozawa, K.; Edamoto, K.; Nakadai, Y.; Otani, S. Oxygen Adsorption on a Mo_2C(0001) Surface: Angle–Resolved Photoemission Study. *Surf. Sci*. **2007**, *601*, 201-208.

(170) Edamoto, K.; Nakadai, Y.; Abe, Y.; Ozawa, K. The Electronic Structure and Reactivity of the Oxygen-Modified MoC(0001) Surface. *Appl. Surf. Sci*. **2008**, *254*, 7622-7625.

(171) Solymosi, F.; Bugyi, L.; Oszko, A. Formation and Reactions of CH_3 Species over Mo_2C/Mo(111) Surface. *Catal. Lett*. **1999**, *57*, 103-107.

(172) Solymosi, F.; Bugyi, L.; Oszko, A.; Horvath, I. Generation and Reactions of CH_2 and C_2H_5 Species on Mo_2C/Mo(111) Surface. *J. Catal*. **1999**, *185*, 160-169.

(173) Cserenyi, J.; Ovari, L.; Bansagi, T.; Solymosi, F. Adsorption and Reactions of CH_3Cl on Mo_2C Based Catalyst. *J. Mol. Catal. A: Chem*. **2000**, *162*, 335-352.

(174) Bugyi, L.; Oszko, A.; Solymosi, F. The Adsorption and Surface Reactions of Allyl Iodide on the Mo_2C/Mo(100) Surface. *Surf. Sci*. **2002**, *519*, 139-149.

(175) Bugyi, L.; Oszko, A.; Solymosi, F. The Adsorption and Reactions of Propyl Iodide on Clean and Adsorbate-Modified Mo_2C/Mo(100) Surfaces. *Surf. Sci*. **2002**, *516*, 74-84.

(176) Bugyi, L.; Oszko, A.; Solymosi, F. Adsorption and Decomposition of C_6H_5I on the Mo_2C/Mo(100) Surface. *Surf. Sci*. **2003**, *539*, 1-13.

(177) Bugyi, L.; Oszko, A.; Solymosi, F. The Interaction of 1-Butyl Iodide with the Mo_2C/Mo(100) Surface. *Surf. Sci*. **2004**, *561*, 57-68.

(178) Farkas, A. P.; Solymosi, F. Adsorption and Reactions of Ethanol on Mo_2C/Mo(100). *Surf. Sci*. **2007**, *601*, 193-200.

(179) Farkas, A. P.; Solymosi, F. Adsorption and Reactions of Dimethyl and Diethyl Ethers on Mo_2C/Mo(100). *Surf. Sci*. **2008**, *602*, 1497-1506.

---

(180) Solymosi, F.; Németh, R. The Oxidative Dehydrogenation of Ethane with CO_2 over Mo_2C/SiO_2 Catalyst. *Catal. Lett*. **1999**, *62*, 197-200.

(181) Solymosi, F.; Oszko, A.; Bansagi, T.; Tolmacsov, P. Adsorption and Reaction of CO_2 on Mo_2C Catalyst. *J. Phys. Chem. B* **2002**, *106*, 9613-9618.

(182) Solymosi, F.; Bugyi, L. Effects of Potassium on the Chemisorption of CO_2 and CO on the Mo_2C/Mo(100) Surface. *Catal. Lett*. **2000**, *66*, 227-230.

(183) Bugyi, L.; Oszko, A.; Solymosi, F. Spectroscopic Study on the Formation of CO_2- on K-promoted Mo_2C/Mo(100) Surface. *Surf. Sci*. **2000**, *461*, 177-190.

(184) Farkas, A. P.; Koos, A.; Bugyi, L.; Solymosi, F. Effects of Potassium on the Reaction Pathway of C_3H_7 Species over Mo_2C/Mo (100). *Surf. Sci*. **2006**, *600*, 2355-2363.

(185) Farkas, A. P.; Bugyi, L.; Koos, A.; Solymosi, F. Effects of Potassium on the Reaction Pathways of CH_2 Fragment over Mo_2C / Mo(100). *Surf. Sci*. **2007**, *601*, 3736-3739.

(186) Farkas, A. P.; Koos, A.; Bugyi, L.; Solymosi, F. Adsorption and Reaction of Methyl and Ethyl Iodide on Potassium-Promoted Mo_2C/Mo(100) Surface. *J. Phys. Chem. C* **2008**, *112*, 18502–18509.

(187) Farkas, A. P.; Solymosi, F. Effects of Potassium on the Adsorption and Dissociation Pathways of Methanol and Ethanol on Mo_2C/Mo(100). *Surf. Sci*. **2008**, *602*, 1475-1485.

(188) Rodriguez, J. A.; Dvorak, J.; Jirsak, T. Chemistry of Thiophene on Mo(110), MoC_x and MoS_x Surfaces: Photoemission Studies. *Surf. Sci*. **2000**, *457*, L413-L420.

(189) Rodriguez, J. A.; Dvorak, J.; Jirsak, T. Chemistry of SO_2, H_2S, and CH_3SH on Carbide-Modified Mo(110) and Mo_2C Powders: Photoemission and XANES Studies. *J. Phys. Chem. B* **2000**, *104*, 11515-11521.

(190) St Clair, T. P.; Oyama, S. T.; Cox, D. F. Adsorption and Reaction of Thiophene on Alpha-Mo_2C(0001). *Surf. Sci*. **2002**, *511*, 294-302.

(191) Haines, J.; Léger, J. M.; Chateau, C.; Lowther, J. E. Experimental and Theoretical Investigation of Mo_2C at High Pressure. *J. Phys.: Condens. Matter* **2001**, *13*, 2447-2454.

(192) Liu, P.; Rodriguez, J. A. Catalytic Properties of Molybdenum Carbide, Nitride and Phosphide: a Theoretical Study. *Catal. Lett*. **2003**, *91*, 247-252.

(193) Liu, P.; Rodriguez, J. A. Effects of Carbon on the Stability and Chemical Performance of Transition Metal Carbides: A Density Functional Study. *J. Chem. Phys*. **2004**, *120*, 5414-5423.

(194) Liu, P.; Rodriguez, J. A.; Muckerman, J. T. Desulfurization of SO_2 and Thiophene on Surfaces and Nanoparticles of Molybdenum Carbide: Unexpected Ligand and Steric Effects. *J. Phys. Chem. B* **2004**, *108*, 15662-15670.

(195) Liu, P.; Rodriguez, J. A.; Asakura, T.; Gomes, J.; Nakamura, K. Desulfurization Reactions on Ni_2P(001) and α-Mo_2C(001) Surfaces: Complex Role of P and C Sites. *J. Phys. Chem. B* **2005**, *109*, 4575-4583.

(196) Liu, P.; Rodriguez, J. A.; Muckerman, J. T. Sulfur Adsorption and Sulfidation of Transition Metal Carbides as Hydrotreating Catalysts. *J. Mol. Catal. A: Chem.* **2005**, *239*, 116-124.

---

(197) Liu, P.; Rodriguez, J. A. Water-Gas-Shift Reaction on Molybdenum Carbide Surfaces: Essential Role of the Oxycarbide. *J. Phys. Chem. B* **2006**, *110*, 19418-19425.

(198) Viñes, F.; Sousa, C.; Illas, F.; Liu, P.; Rodriguez, J. A. Density Functional Study of the Adsorption of Atomic Oxygen on the (001) Surface of Early Transition-Metal Carbides. *J. Phys. Chem. C* **2007**, *111*, 1307-1314.

(199) dos Santos Politi, J. R.; Vines, F.; Rodriguez, J. A.; Illas, F. Atomic and Electronic Structure of Molybdenum Carbide Phases: Bulk and Low Miller-Index Surfaces. *Phys. Chem. Chem. Phys*. **2013**, *15*, 12617-12625.

(200) Posada-Perez, S.; Vines, F.; Ramirez, P. J.; Vidal, A. B.; Rodriguez, J. A.; Illas, F. The Bending Machine: CO_2 Activation and Hydrogenation on δ-MoC(001) and β-Mo_2C(001) Surfaces. *Phys. Chem. Chem. Phys*. **2014**, *16*, 14912-14921.

(201) Nagai, M.; Tominaga, H.; Omi, S. CO Adsorption on Molybdenum Carbides and Molecular Simulation. *Langmuir* **2000**, *16*, 10215-10220.

(202) Tominaga, H.; Nagai, M. Density Functional Study of Carbon Dioxide Hydrogenation on Molybdenum Carbide and Metal. *Appl. Catal. A* **2005**, *282*, 5-13.

(203) Tominaga, H.; Nagai, M. Density Functional Theory of Water-Gas Shift Reaction on Molybdenum Carbide. *J. Phys. Chem. B* **2005**, *109*, 20415-20423.

(204) Tominaga, H.; Nagai, M. Theoretical Study of Methane Reforming on Molybdenum Carbide. *Appl. Catal. A* **2007**, *328*, 35-42.

(205) Tominaga, H.; Nagai, M. Mechanism of Thiophene Hydrodesulfurization on Clean/sulfided β-Mo_2C(001) Based on Density Functional Theory-cis- and Trans-2-Butene Formation at the Initial Stage. *Appl. Catal. A* **2008**, *343*, 95-103.

(206) Tominaga, H.; Aoki, Y.; Nagai, M. Hydrogenation of CO on Molybdenum and Cobalt Molybdenum Carbides. *Appl. Catal. A* **2012**, *423*, 192-204.

(207) Pistonesi, C.; Juan, A.; Farkas, A. P.; Solymosi, F. DFT Study of Methanol Adsorption and Dissociation on β-Mo_2C(001). *Surf. Sci*. **2008**, *602*, 2206-2211.

(208) Pistonesi, C.; Juan, A.; Farkas, A. P.; Solymosi, F. Effects of Potassium on the Adsorption of Methanol on β-Mo_2C(001) Surface. *Surf. Sci*. **2010**, *604*, 914-919.

(209) Pronsato, M. E.; Pistonesi, C.; Juan, A.; Farkas, A. P.; Bugyi, L.; Solymosi, F. Density Functional Theory Study of Methyl Iodide Adsorption and Dissociation on Clean and K-Promoted β-Mo_2C Surfaces. *J. Phys. Chem. C* **2011**, *115*, 2798-2804.

(210) Pistonesi, C.; Pronsato, M. E.; Bugyi, L.; Juan, A. The Adsorption of CO on Potassium Doped Molybdenum Carbide Surface: An ab-initio Study. *Catal. Today* **2012**, *181*, 102-107.

(211) Pistonesi, C.; Pronsato, M. E.; Bugyi, L.; Juan, A. Theoretical Model for CO Adsorption and Dissociation on Clean and K-Doped β-Mo_2C Surfaces. *J. Phys. Chem. C* **2012**, *116*, 24573-24581.

(212) Kotarba, A.; Adamski, G.; Piskorz, W.; Sojka, Z.; Sayag, C.; Djéga-Mariadassou, G. Modification of Electronic Properties of Mo_2C Catalyst by Potassium Doping: Impact on the Reactivity in Hydrodenitrogenation Reaction of Indole. *J. Phys. Chem. B* **2004**, *108*, 2885-2892.

---

(213) Piskorz, W.; Adamski, G.; Kotarba, A.; Sojka, Z.; Sayag, C.; Djéga-Mariadassou, G. Hydrodenitrogenation of Indole over Mo_2C Catalyst: Insights into Mechanistic Events Through DFT Modeling. *Catal. Today* **2007**, *119*, 39-43.

(214) Hynaux, A.; Sayag, C.; Suppan, S.; Trawczynski, T.; Lewandowski, M.; Szymanska-Kolasa, A.; Djéga-Mariadassou, G. Kinetic Study of the Deep Hydrodesulfurization of Dibenzothiophene over Molybdenum Carbide Supported on a Carbon Black Composite: Existence of Two Types of Active Sites. *Catal. Today* **2007**, *119*, 3-6.

(215) Han, J. W.; Li, L.; Sholl, D. S. Density Functional Theory Study of H and CO Adsorption on Alkali-Promoted Mo_2C Surfaces. *J. Phys. Chem. C* **2011**, *115*, 6870-6876.

(216) Shou, H.; Li, L. W.; Ferrari, D.; Sholl, D. S.; Davis, R. J. Use of Infrared Spectroscopy and Density Functional Theory to Study the Influence of Rubidium on Alumina-Supported Molybdenum Carbide Catalyst for Higher Alcohol Synthesis from Syngas. *J. Catal*. **2013**, *299*, 150-161.

(217) Li, L. W.; Morrill, M. R.; Shou, H; Barton, D. G.; Ferrari, D.; Davis, R. J.; Agrawal, P. K.; Jones, C. W.; Sholl, D. S. On the Relationship between Mo K‑Edge Energies and DFT Computed Partial Charges. *J. Phys. Chem. C* **2013**, *117*, 2769-2773.

(218) Rocha, A. S.; Rocha, A. B.; Teixeira da Silva, V. Benzene Adsorption on Mo_2C: A Theoretical and Experimental Study. *Appl. Catal. A* **2010**, *379*, 54-60.

(219) Zhou, B. J.; Liu, X. C.; Cuervo, J.; Salahub, D. R. Density Functional Study of Benzene Adsorption on the α-Mo_2C(0001) surface. *Struct. Chem*. **2012**, *23*, 1459-1466.

(220) Liu, X. C.; Tkalych, A.; Zhou, B. J.; Köster, A. M.; Salahub, D. R. Adsorption of Hexacyclic C_6H_6, C_6H_8, C_6H_{10}, and C_6H_{12} on a Mo-Terminated α-Mo_2C (0001) Surface. *J. Phys. Chem. C* **2013**, *117*, 7069-7080.

(221) Oliveira Jr., R. R.; Rocha, A. S.; da Silva, V. T.; Rocha, A. B. Investigation of Hydrogen Occlusion by Molybdenum Carbide. *Appl. Catal. A* **2014**, *469*, 139-145.

(222) Qi, K. Z.; Wang, G. C.; Zheng, W. J. A First-Principles Study of CO Hydrogenation into Methane on Molybdenum Carbides Catalysts. *Surf. Sci*. **2013**, *614*, 53-63.

(223) Qi, K. Z.; Wang, G. C.; Zheng, W. J. Structure-sensitivity of Ethane Hydrogenolysis over Molybdenum Carbides: A Density Functional Theory Study. *Appl. Surf. Sci*. **2013**, *276*, 369-376.

(224) Xing, S. K.; Wang, G. C. Reaction Mechanism of Ethanol Decomposition on Mo_2C(100) Investigated by the First Principles Study. *J. Mol. Catal. A: Chem*. **2013**, *377*, 180-189.

(225) Luo, Q. Q.; Wang, T.; Walther, G.; Beller, M.; Jiao, H. Molybdenum Carbide Catalysed Hydrogen Production from Formic Acid - A Density Functional Theory Study. *J. Power Sources* **2014**, *246*, 548-555.

(226) Zhao, Y. H.; Li, S. G.; Sun, Y. H. Ni-Doping Effects on Carbon Diffusion and Oxidation over Mo_2C Surfaces. *J. Phys. Chem. C* **2013**, *117*, 18936-18946.

(227) Ren, J.; Huo, C. F.; Wang, J.; Li, Y.-W.; Jiao, H. Surface Structure and Energetics of Oxygen and CO Adsorption on α-Mo_2C(0001). *Surf. Sci.* **2005**, *596*, 212-221.

---

(228) Ren, J.; Huo, C. F.; Wang, J.; Cao, Z.; Li, Y.-W.; Jiao, H. Density Functional Theory Study into the Adsorption of CO_2, H and CH_x (x = 0-3) as well as C_2H_4 on α-Mo_2C(0001). *Surf. Sci.* **2006**, *600*, 2329-2337.

(229) Ren, J.; Wang, J.; Huo, C. F.; Wen, X. D.; Cao, Z.; Yuan, S. P.; Li, Y.-W.; Jiao, H. Adsorption of NO, NO_2, Pyridine and Pyrrole on α-Mo_2C(0001): A DFT Study. *Surf. Sci.* **2007**, *601*, 1599-1607.

(230) Shi, X. R.; Wang, J.; Hermann, K. CO and NO Adsorption and Dissociation at the β-Mo_2C(0001) Surface: A Density Functional Theory Study. *J. Phys. Chem. C* **2010**, *114*, 13630-13641.

(231) Wang, T.; Liu, X. W.; Wang, S. G.; Huo, C. F.; Li, Y.-W.; Wang, J.; Jiao, H. Stability of β-Mo_2C Facets from ab Initio Atomistic Thermodynamics. *J. Phys. Chem. C* **2011**, *115*, 22360-22368.

(232) Miyao, T.; Shishikura, I.; Matsuoka, M.; Nagai, M.; Oyama, S. T. Preparation and Characterization of Alumina-supported Molybdenum Carbide. *Appl. Catal. A* **1997**, *165*, 419-428.

(233) Nagai, M.; Zahidul, A. M.; Matsuda, K. Nano Structured Nickel-Molybdenum Carbide Catalyst for Low-Temperature Water-Gas Shift Reaction. *Appl. Catal. A* **2006**, *313*, 137-145.

(234) Medford, A. J.; Vojvodic, A.; Studt, F.; Abild-Pedersen, F.; Nørskov, J. K. Elementary Steps of Syngas Reactions on Mo_2C(001): Adsorption Thermochemistry and Bond Dissociation. *J. Catal*. **2012**, *290*, 108-117.

(235) Wang, T.; Luo, Q. Q.; Li, Y.-W.; Wang, J.; Beller, M.; Jiao, H. Stable Surface Terminations of Orthorhombic Mo_2C Catalysts and Their CO Activation Mechanisms. *Appl. Catal. A* **2014**, *478*, 146-156.

(236) Wang, T.; Wang, S. G.; Li, Y.-W.; Wang, J.; Jiao, H. Adsorption Equilibria of CO Coverage on β-Mo_2C Surfaces. *J. Phys. Chem. C* **2012**, *116*, 6340-6348.

(237) Shi, X. R.; Wang, S. G.; Hu, J.; Qin, Z. F.; Wang, J. Theoretical Studies on Chemisorption of Oxygen on β-Mo_2C Catalyst and Its Surface Oxidation. *Surf. Sci.* **2012**, *606*, 1187-1194.

(238) Wang, T.; Li, Y.-W.; Wang, J.; Beller, M.; Jiao, H. Dissociative Hydrogen Adsorption on the Hexagonal Mo_2C Phase at High Coverage. *J. Phys. Chem. C* **2014**, *118*, 8079-8089.

(239) Wang, T.; Li, Y.-W.; Wang, J.; Beller, M.; Jiao, H. High Coverage CO Adsorption and Dissociation on the Orthorhombic Mo_2C(100) Surface. *J. Phys. Chem. C* **2014**, *118*, 3162-3171.

2. Objectives of this work

The activation of CO and H_2 is a primary but very essential step in many industrial applications, especially in Fischer-Tropsch synthesis, alcohol synthesis and water-gas shift reaction as well as fuel cell technology. Despite of the wide ultrahigh vacuum surface science studies and theoretical investigations in exploring the interactions of CO and H_2 with the surfaces of heterogeneous catalysts, the detailed mechanisms are not well known; and further efforts to understand these processes in academic research and industrial application are highly desired.

In early theoretical investigations, many key factors were not well addressed. For example, most previous theoretical studies were mainly carried out on the basis of the adsorption and activation of single CO and H_2 molecule, and the role of reactant coverage did not attract enough attentions. In addition, the effect of reaction conditions such as temperature and pressure were hardly considered previously. This is indeed essential in setting an interplay and complementary relationship between theory and experiment for understanding the reaction mechanisms of many industrial application processes.

The major aim of this dissertation was the discussion of coverage dependent CO and H_2 adsorption and activations on iron and Mo_2C surfaces. Both catalysts are widely used in Fischer-Tropsch synthesis, alcohol synthesis and water-gas shift reaction. On the iron surfaces, H_2 adsorption is coverage independent and dissociative, in contrast, CO adsorption is coverage dependent; i.e.; molecular adsorption at high coverage and dissociative adsorption at very low coverage, as well mixed molecular and dissociative adsorption are possible at medium coverage. On the basis of atomistic thermodynamics, the computed CO and H_2 desorption states, temperatures and energies on the Fe(100), Fe(110) and Fe(111) surfaces are in well agreement with available experimental results. For the Mo_2C catalysts, the stability and composition of the surfaces are found to be highly dependent on the carburization conditions. Such differences in surface structures are reflected in their distinct CO and H_2 activation activities as well as the co-adsorption properties of CO and H_2 under different conditions.

All these results shed new insights into the understanding of CO and H_2 activation mechanisms of heterogeneous catalysts and provide the basis for further rational investigation of hydrotreating mechanisms.

3. Summary and publications

3.1 High Coverage CO Activation Mechanisms on Fe(100) from Computations

Tao Wang, Xinxin Tian, Yong-Wang Li, Jianguo Wang, Matthias Beller, Haijun Jiao*

Journal of Physical Chemistry C **2014**, *118*, 1095-1101.

Summary: CO activation on Fe(100) at different coverage was systematically computed on the basis of spin-polarized density functional theory. At the saturated coverage (11CO) on a p(3×4) surface size (24 exposed Fe atoms), top (1CO), bridge (3CO) and 4-fold hollow (7CO) adsorption configurations co-exist. The stepwise adsorption energies and dissociation barriers at different coverage reveal equilibriums between desorption and dissociation of adsorbed CO molecules. It is found that only molecular adsorption is likely for nCO = 8-11, and mixed molecular and dissociative adsorption becomes possible for nCO = 5-7, while only dissociative adsorption is favorable for nCO = 1-4. The computed CO adsorption configurations and stretching frequencies as well as desorption temperatures from ab initio thermodynamic analysis agree well with the available experimental data.

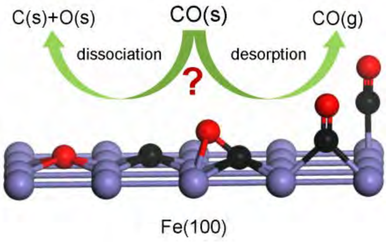

Contributions

In this paper, I planned, performed and analyzed most calculations for this manuscript. I have done the major part of writing of the manuscript. My contribution as co-author of this paper is approximately 85%.

THE JOURNAL OF
PHYSICAL CHEMISTRY C

Article

pubs.acs.org/JPCC

High Coverage CO Activation Mechanisms on Fe(100) from Computations

Tao Wang,[†] Xinxin Tian,[‡] Yong-Wang Li,[‡] Jianguo Wang,[‡] Matthias Beller,[†] and Haijun Jiao*,[†,‡]

[†]Leibniz-Institut für Katalyse e.V. an der Universität Rostock, Albert-Einstein Strasse 29a, 18059 Rostock, Germany

[‡]State Key Laboratory of Coal Conversion, Institute of Coal Chemistry, Chinese Academy of Sciences, Taiyuan, Shanxi 030001, PR China

S *Supporting Information*

ABSTRACT: CO activation on Fe(100) at different coverage was systematically computed on the basis of spin-polarized density functional theory. At the saturated coverage (11CO) on a $p(3 \times 4)$ surface size (24 exposed Fe atoms), top (1CO), bridge (3CO) and 4-fold hollow (7CO) adsorption configurations coexist. The stepwise adsorption energies and dissociation barriers at different coverage reveal equilibriums between desorption and dissociation of adsorbed CO molecules. It is found that only molecular adsorption is likely for n_{CO} = 8−11, and mixed molecular and dissociative adsorption becomes possible for n_{CO} = 5−7, while only dissociative adsorption is favorable for n_{CO} = 1−4. The computed CO adsorption configurations and stretching frequencies as well as desorption temperatures from ab initio thermodynamic analysis agree well with the available experimental data.

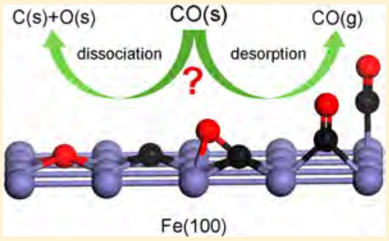

1. INTRODUCTION

In our modern daily life, CO is a very important basic chemical which has been widely applied in energy societies as well as value-added bulk and fine chemical productions. Representative examples are liquid fuels and chemicals from Fischer−Tropsch synthesis (FTS), methanol and synthetic natural gas as well as hydrogen.[1,2] Since all these chemical processes are conducted on the basis of heterogeneous catalysis; studying CO activation mechanisms on surfaces of solid catalysts can provide the essential and intrinsic information for understanding such key processes.

The interaction of CO on iron surfaces is of particular importance for understanding the initial steps in iron-based FTS, since CO dissociation is believed to be essential for CH_x formation.[3,4] Diverse experimental techniques were applied to study CO adsorption on iron single crystalline surfaces. On Fe(100), X-ray photoelectron spectroscopy (XPS) and temperature programmed desorption (TPD) studies[5−7] showed that there are three molecular adsorption states (α_1, α_2 and α_3) and CO dissociation occurs at about 440 K, while recombinative desorption of the dissociated C and O takes place at around 750−800K (β state). Further study by applying extensive surface science techniques, such as XPS, TPD, X-ray photoelectron diffraction (XPD),[8] near-edge X-ray absorption fine structure spectroscopy (NEXAFS),[9−11] and high resolution electron energy loss spectroscopy (HREELS)[12,13] revealed that the 4-fold hollow site with an unusually low CO stretching frequency of 1210 cm^{-1} is the most stable adsorption configuration, which corresponds to the α_3 state and represents the precursor state of CO dissociation. By using HREELS and temperature programmed surface reaction (TPSR) techniques, Lu et al.[14] studied CO adsorption and dissociation on the Fe(100) surface at 423 K, and found CO dissociation at coverage lower than 0.15 monolayer (ML), and CO desorption at coverage higher than 0.15 ML. The bonding mechanism of the predissociative hollow (α_3) phase and the nondissociative atop (α_1) phase of CO on the Fe(100) surface was studied by Gladh et al.[15] by using both X-ray emission spectroscopy (XES) and density functional theory (DFT) calculations, and a π donation/π* back-donation scheme is proposed for CO in the 4-fold hollow site.

In addition to the extensive experimental studies, CO interaction on iron single crystalline surfaces has been also widely studied theoretically. Early theoretical studies mainly applied semiempirical[16,17] and Hatree-Fock[18] methods in 1980s. By using both periodic slab and finite cluster models to study CO adsorption on the Fe(001) surface, Nayak et al.[19] found that the 4-fold hollow site is the energetically most preferred adsorption site, followed by the atop and bridge sites. By applying DFT calculations, Sorescu et al.[20] studied the adsorption of CO, C, and O atoms, as well as CO dissociation on the Fe(100) surface, respectively, and found that CO on the 4-fold site (α_3 state in TPD) is most stable and has dissociation barrier in the range of 24.5−28.2 kcal/mol, while CO on the bridge site (α_2 state) is more stable than on the atop site (α_1 state) at low coverage, and the atop site becomes more stable than the bridge site at high coverage. Bromfield et al.[21] studied CO interaction on the Fe(100) surface and found that CO adsorption and dissociation are coverage dependent. On the Fe(100) surface, Elahifard et al.[22] proposed CO direct

Received: October 18, 2013
Revised: December 15, 2013
Published: December 19, 2013

© 2013 American Chemical Society

dissociation at low coverage, and H-assisted CO dissociation at high coverage.

Despite these extensive DFT studies about CO adsorption on the Fe(100) surface, combined DFT and experimental studies of the adsorption, desorption, and dissociation mechanisms are still scare. In this work we have carried out comprehensive DFT computations on the adsorption, dissociation, and desorption at different CO coverage. Our ultimate goal is to understand the coverage dependence of adsorption, dissociation, and desorption processes upon the change of temperature. A direct comparison between our computed results and the available experimental data provides insights into the interaction mechanisms of CO on iron surfaces.

2. COMPUTATIONAL METHODS AND MODELS

2.1. Methods. Calculations were done by using the plane-wave based density functional theory (DFT) method implemented in the Vienna Ab Initio Simulation Package (VASP)[23,24] and periodic slab models. The electron ion interaction was described with the projector augmented wave (PAW) method.[25,26] The electron exchange and correlation energy was treated within the generalized gradient approximation in the Perdew−Burke−Ernzerhof formalism (GGA-PBE).[27] Spin-polarization calculation was included for iron systems to correctly account for its magnetic properties, and this was found essential for an accurate description of adsorption energy.[28] An energy cutoff of 400 eV and a second-order Methfessel−Paxton[29] electron smearing with σ = 0.2 eV were used to ensure accurate energies with errors less than 1 meV per atom. The vacuum layer between periodically repeated slabs was set as 10 Å to avoid interactions among slabs. To locate the CO dissociation transition states on iron surfaces, the nudged elastic band (NEB)[30] method was applied, and stretching frequencies were analyzed to characterize a transition state with only one imaginary frequency.

The adsorption energy (E_{ads}) of one CO molecule is defined as $E_{ads} = E_{CO/slab} - [E_{slab} + E_{CO}]$, where $E_{CO/slab}$ is the total energy of the slab with one CO adsorption, E_{slab} is the total energy of the bare slab and E_{CO} is the total energy of a free CO molecule in gas phase; and a more negative E_{ads} indicates a stronger adsorption.

To discuss molecular CO adsorption on Fe(100) surface at different coverage, it is necessary to find the most stable coadsorption configurations at individual coverage; i.e., one additional CO molecule was added to the previous most stable one for getting the next most stable one after considering all adsorption sites. In order to get the saturated coverage, we used the stepwise adsorption energy, $\Delta E_{ads} = E_{(CO)n+1/slab} - [E_{(CO)n/slab} + E_{CO}]$, where a positive ΔE_{ads} for $n + 1$ adsorbed CO molecules indicates the saturated adsorption with n CO molecules.

The CO dissociation barrier (E_a) is defined as $E_a = E_{TS} - E_{IS}$, the reaction energy (E_r) is defined as $E_r = E_{FS} - E_{IS}$, where E_{IS}, E_{FS}, and E_{TS} represent the total energy of the initial adsorbed CO molecule, final dissociated CO molecule (C+O atoms), and the CO dissociating transition states.

2.2. Models. Calculation of the α-Fe bulk crystal structure with a k-point mesh of 9 × 9 × 9 gives a lattice constant of 2.84 Å and a local spin magnetic moment of 2.214 μ_B, in good agreement with other DFT calculations[31,32] and experiment.[33] In order to choose a reasonable slab model for CO adsorption and dissociation at high coverage, we have tested the effects of slab thickness, surface size, and vacuum layer on CO adsorption energy extensively, and all these benchmark results are listed in the Supporting Information. On the basis of these tests, we applied the surface p(3 × 4) model for our study with four atomic layers, in which the top two layers were allowed to relax and the bottom two layers were fixed in their bulk positions. The structure and possible adsorption sites of Fe(100) surface are shown in Figure 1

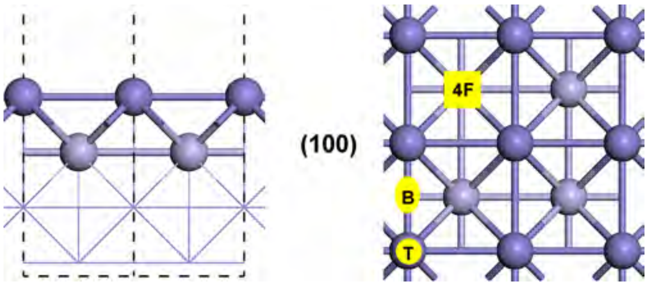

Figure 1. Schematic side and top views of Fe(100) and possible adsorption sites.

2.3. Thermodynamics. As a convenient tool to solve problems referring to real reaction conditions, *ab initio* atomistic thermodynamics method, proposed by Scheffler and Reuter,[34,35] has been widely and successfully applied in many other systems.[36−42] The detailed description of the method can be found in the Supporting Information.

3. RESULTS AND DISCUSSIONS

3.1. Molecular CO Adsorption at Saturated Coverage. There are three adsorption sites on the Fe(100) surface (Figure 1), i.e., top (**T**), bridge (**B**) and 4-fold hollow (**4F**) sites. The structures and energies (ΔE_{ads}) of the most stable adsorption sites for stepwise CO adsorption are given Figure 2. It is found that the most stable adsorption configurations for one CO molecule on this surface is located on the **4F** site with the C atom coordinating with four surface Fe atoms and the O atom interacting with two surface Fe atoms. The C−O bond length is elongated to 1.32 Å with respect to gaseous CO (1.14 Å), and the computed C−O stretching frequency is 1172 cm^{-1}. Experimentally, this adsorption configuration is assigned to the α_3 adsorption state from TDS. Our calculated adsorption energy (−2.14 eV) is similar with that (−2.17 eV) by Sorescu et al.,[43] since the same functional was used. However, results obtained with RPBE (−1.90 eV),[20] PW91 (−2.02 eV,[20] and −2.54 eV[21]) and cluster model (−1.62 eV)[19] show obvious differences due to their quite different methods and models.

From the most stable adsorption configuration of one CO, we further increased the number of adsorbed CO molecules on the surface. In order to find the most stable coadsorption configuration at high coverage, we checked different adsorption possibilities under consideration that 4-fold hollow adsorption is more stable than bridge adsorption, and bridge adsorption is more stable than top adsorption. At low coverage and at the same adsorption sites, the energy differences are rather small. At high coverage and due to their lateral repulsive interaction, however, the energy differences among these coadsorption states raise due to the change of the adsorption configuration from 4-fold site to the bridge site as well as to the top sites. Nevertheless, these changes do not affect our conclusion. All

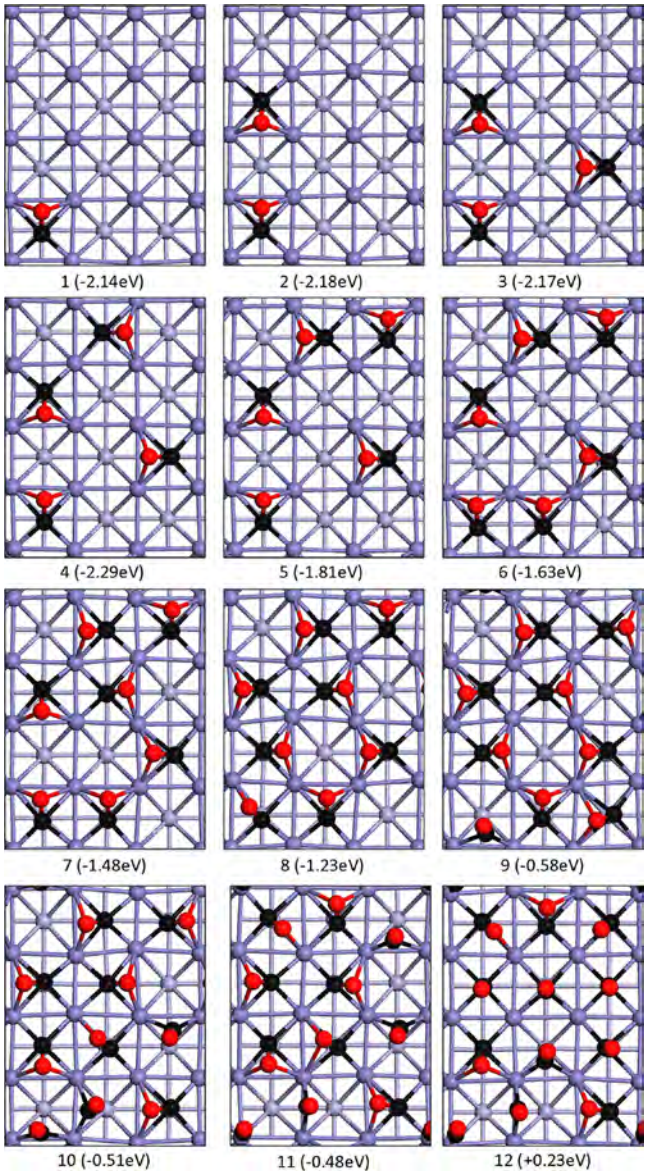

1 (-2.14eV) 2 (-2.18eV) 3 (-2.17eV)

4 (-2.29eV) 5 (-1.81eV) 6 (-1.63eV)

7 (-1.48eV) 8 (-1.23eV) 9 (-0.58eV)

10 (-0.51eV) 11 (-0.48eV) 12 (+0.23eV)

Figure 2. Structures and energies (ΔE_{ads}) of the most stable adsorption sites for stepwise CO adsorption (Blacks ball for C, red ball for O, and the other balls for Fe in different layers).

these preliminary data are summarized in the Supporting Information (Figure S1).

Figure 2 reveals that the first four adsorbed CO molecules (n_{CO} = 1−4) have the 4F adsorption configuration and very similar adsorption energies, indicating their negligible lateral repulsive interaction and their independence. With n_{CO} = 5−8, lateral repulsive interaction of the adsorbed CO molecules becomes significant and starts to affect the value of ΔE_{ads}, but all the adsorbed CO molecules still have the 4F adsorption configuration. With n_{CO} = 9, the bridge (B) adsorption configuration appears, and one B and eight 4F adsorption configurations coexist. With n_{CO} = 10, there are three B and seven 4F adsorption configurations. At the saturated coverage (n_{CO} = 11), there are one T, three B, and seven 4F adsorption configurations.

On the basis of the most stable adsorption configurations at a given coverage, it is interesting to compare the theoretically calculated and experimentally detected CO stretching frequencies. Early TPD studies[6] proved that there are three CO molecular desorption states (α_1, α_2 and α_3) at low temperature, and this supports our calculated result at the saturated coverage, where three adsorption configurations (one T, three B and seven 4F) coexist. Also HREELS[12,13] studies found three low temperature molecular adsorption states with quite different CO stretching frequencies, i.e., 1180−1245 cm^{-1} for the α_3 state and 1900−2070 cm^{-1} for the α_1 and α_2 states. Actually, our detailed analysis into CO stretching frequency at the saturated coverage also shows three ranges: 1179−1280 cm^{-1} for the 4F adsorption configuration, 1800−1850 cm^{-1} for the B adsorption configuration, and 2012 cm^{-1} for the **T** adsorption configuration. It clearly revealed that our calculated results are in good agreement with these available experimental data, indicating that our computed saturated coverage should be the same as found under experimental conditions.

3.2. Equilibrium between desorption and dissociation. In addition to the adsorption configurations at saturated coverage and their respective CO stretching frequencies, we are also interested in the desorption mechanisms of these adsorbed CO molecules at different coverage, in particular, the equilibrium between desorption and dissociation of the adsorbed CO molecules on the surface, for understanding the CO activation process.

To date, all theoretical studies are the subjects of CO adsorption and dissociation on iron surfaces at low coverage, and there are no investigations into the equilibrium between desorption and dissociation at different coverage. For the first time, we systematically computed CO dissociation at different coverage on the Fe(100) surface to find the equilibrium between desorption and dissociation. The calculated dissociation barriers of all adsorbed CO molecules on the basis of the most stable adsorption configurations in Figure 2 as the initial states at individual coverage are listed in Table 1, and the corresponding structures of initial states (IS), transition states (TS), and final states (FS) are given in the Supporting Information (Figure S2). For a direct and convenient comparison, we converted the calculated stepwise adsorption energies approximately to the reversed stepwise desorption energies. The potential energy surfaces at coverage of n_{CO} = 1−8 are shown in the Supporting Information (Figure S3).

Unlike the dissociation of one CO molecule, there are many possibilities for CO dissociation at high coverage. In order to find the energetically most favored one, we calculated the dissociation for all adsorbed CO molecules. For $n_{CO} \geq 2$, we calculated all CO dissociation barriers. After the dissociation of the first CO, the surface has $(n-1)$ adsorbed CO molecules as well as one C atom and one O atom. The next step is to calculate the dissociation barriers of those $(n-1)$ adsorbed CO molecules and to find the next most favorable one with $(n-2)$ adsorbed CO molecules as well as two C atoms and two O atoms. The procedure was repeated till the CO desorption becomes more favorable than dissociation, and the final adsorption state could be identified.

To estimate the final adsorption state, it is necessary to consider the migration of surface C and O atoms, which is very important for understanding the complex oxidation and carburization of iron surface. Since there are free adsorption sites available at low coverage, and it is possible for C or O to migrate, and indeed, the barrier for one O migration is rather low (about 0.4 eV). At high coverage with adsorbed CO as well as C and O atoms, however, the surface has very limited free sites and considerable lateral repulsive interaction among the

Table 1. CO Step Desorption Energies (ΔE_{des}, eV), and Dissociation Barriers (E_a, eV) As Well As Dissociation Energies (ΔE_{dis}, eV) at Different Coverage

*n*CO (ΔE_{des})	pathways	E_a	ΔE_{des}	ΔE_{dis}
1CO (2.14)	1CO → 1C + 1O	1.03	2.14	−1.20
2CO (2.18)	2CO → 1CO + 1C + 1O	1.04	2.18	−1.07
	1CO + 1C + 1O → 2C + 2O	1.12	2.06	−1.23
3CO (2.17)	3CO → 2CO+1C+1O	1.14	2.17	−1.18
	2CO+1C + 1O → 1CO + 2C + 2O	1.14	2.18	−0.88
	1CO + 2C + 2O → 3C + 3O	1.22	2.12	0.09
4CO (2.29)	4CO → 3CO + 1C+1O	1.17	2.29	−0.97
	3CO+1C+1O → 2CO + 2C + 2O	1.17	2.28	−0.83
	2CO+2C+2O → 1CO + 3C + 3O	1.25	2.28	−0.67
	1CO + 3C + 3O → 4C + 4O	1.31	2.40	0.25
5CO (1.81)	5CO → 4CO + 1C + 1O	1.13	1.81	−0.62
	4CO + 1C + 1O → 3CO + 2C + 2O	1.22	1.99	−0.03
	3CO + 2C + 2O → 2CO + 3C + 3O	1.22	1.48	−0.55
	2CO + 3C + 3O → 1CO + 4C + 4O	1.24	1.62	0.19
	1CO + 4C + 4O → 5C + 5O	2.48	1.30	0.17
6CO (1.63)	6CO → 5CO + 1C + 1O	1.20	1.63	−0.08
	5CO + 1C + 1O → 4CO + 2C + 2O	1.28	1.55	−0.40
	4CO + 2C + 2O → 3CO + 3C + 3O	1.25	1.56	0.06
	3CO + 3C + 3O → 2CO + 4C + 4O	1.46	1.12	0.25
	2CO + 4C + 4O → 1CO + 5C + 5O	2.44	0.49	−0.61
7CO (1.48)	7CO → 6CO + 1C + 1O	1.14	1.48	−0.28
	6CO + 1C + 1O → 5CO + 2C + 2O	1.31	1.52	−0.17
	5CO + 2C + 2O → 4CO + 3C + 3O	1.46	1.19	0.47
	4CO + 3C + 3O → 3CO + 4C + 4O	1.44	1.19	0.44
	3CO + 4C + 4O → 2CO + 5C + 5O	1.57	0.48	0,17
	2CO + 5C + 5O → 1CO + 6C + 6O	2.21	0.57	0.20
8CO (1.23)	8CO → 7CO + 1C + 1O	1.44	1.23	−0.02
	7CO + 1C + 1O → 6CO + 2C + 2O	1.44	1.14	0.07
	6CO + 2C + 2O → 5CO + 3C + 3O	1.71	0.91	0.32
	5CO + 3C + 3O → 4CO + 4C + 4O	2.53	1.05	0.41

adsorbed species, thus the migration of surface C or O should be very difficult.

For n_{CO} = 1, the computed CO dissociation barrier is much lower than own desorption energy (1.03 vs 2.14 eV), and CO dissociation is exothermic by 1.20 eV, indicating that CO dissociation is favorable both kinetically and thermodynamically. Our results agree well with the available results from literatures.[20,21,43]

For n_{CO} = 2, the dissociation barriers of these two CO molecules (1.04 and 1.12 eV) are lower than their corresponding desorption energies (2.18 and 2.06 eV), and the stepwise dissociation is exothermic by 1.07 and 1.23 eV, respectively. This shows that CO dissociation at this coverage is also favorable both kinetically and thermodynamically.

For n_{CO} = 3, the dissociation barriers of these three CO molecules (1.14, 1.14, and 1.22 eV) are lower than their corresponding desorption energies (2.17, 2.18, and 2.12 eV), and the dissociation of the first two CO molecules is exothermic by 1.18 and 0.88 eV, respectively, while that of the third CO molecule becomes slightly endothermic by 0.09 eV.

For n_{CO} = 4, the dissociation barriers of these four CO molecules (1.17, 1.17, 1.25, and 1.31 eV) are lower than their corresponding desorption energies (2.29, 2.28, 2.28, and 2.40 eV), and the dissociation of the first three CO molecules is exothermic by 0.97, 0.83, and 0.67 eV, respectively, while that of the fourth CO molecule is endothermic by 0.25 eV.

In contrast with the results for n_{CO} = 1−4, different results have been found for n_{CO} = 5−7. For n_{CO} = 5, the dissociation barriers of the first four CO molecules (1.13−1.24 eV) are lower than their corresponding desorption energies (1.48−1.99 eV). However, the dissociation barrier of the fifth CO molecule (2.48 eV) is much higher not only than own desorption energy (1.30) but also than the dissociation barriers of the first four CO molecules. This indicates that the fifth CO molecule prefers desorption from the surface instead of dissociation on the surface. Consequently, the final adsorption state has one adsorbed CO molecule as well as four C and four O atoms (CO + 4C + 4O) on the surface.

Very similar results are also found for n_{CO} = 6; i.e., the dissociation barriers of the first three CO molecules (1.20−1.28 eV) are much lower than their corresponding desorption energies. At this coverage, three adsorbed CO molecules desorb from the surface, and three adsorbed CO molecules dissociate on the surface. The final adsorption state has three adsorbed CO molecules as well as three C and three O atoms (3CO+3C +3O) on the surface.

For n_{CO} = 7, the dissociation barriers of the first two CO molecules are lower than their corresponding desorption energies while the further dissociation of other adsorbed CO become less favorable than desorption. The final adsorption state has five adsorbed CO molecules as well as two C and two O atoms (5CO + 2C + 2O) on the surface. The most favored potential energy surface of CO adsorption and dissociation at this coverage is given in Figure 3. It clearly reveals that a possible equilibrium between CO desorption from the surface and dissociation on the surface at the coverage of n_{CO} = 5−7.

For n_{CO} = 8, although the dissociation of the first three CO molecules (1.44−1.71 eV) are much lower than that of the fourth CO molecule (2.53 eV), they are higher than their corresponding desorption energies. Therefore, at this coverage, the first step should be CO desorption instead of dissociation. The final adsorption state has eight adsorbed CO molecules. It is to expect that at high coverage $n_{CO} \geq 8$, only desorption is possible because of the much low desorption energies. The final adsorption states have only adsorbed CO molecules.

These results reveal clearly that at coverage higher than $n_{CO} \geq 8$, the first step of the reaction is desorption of some adsorbed CO molecules from the surface. At coverage of n_{CO} = 7, both CO desorption from the surface and dissociation on the surface are possible, and they might form equilibrium. At coverage of n_{CO} = 5, 6, four of the adsorbed CO molecules can dissociate on the surface, and the rest of the adsorbed CO molecules desorb from the surface. At coverage of n_{CO} = 1−4, all adsorbed CO molecules can dissociate on the surface. A general trend shows that the adsorbed CO molecules prefer dissociation on the surface at low coverage, desorption from the surface at high coverage, and both CO desorption and dissociation can form equilibrium at coverage in between.

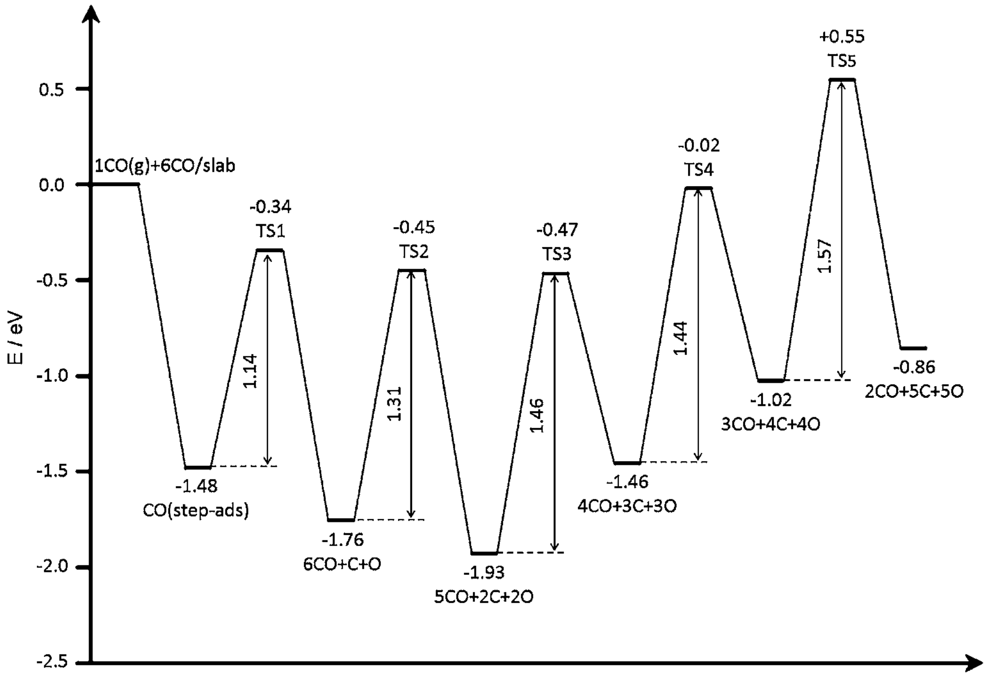

Figure 3. Potential energy surfaces of CO dissociation at the coverage of 7CO.

3.3. CO Desorption States and Temperatures on Fe(100).

On the basis of our above results, we have computed the molecular desorption states (α_1-α_3) and the recombinative desorption state (β) under the consideration of CO dissociation at low coverage and high temperature from ab initio thermodynamics. Table 2 shows the good agreement between theory and experiment in CO desorption temperature at different coverage on Fe(100) surface under ultrahigh vacuum condition (10^{-10}Torr). For the first two molecular desorption states, α_1 state shows the loss of one T adsorbed CO molecule at 275–300K, and α_2 state indicates the loss of two B adsorbed CO molecules at 325–375 K. At 400–450 K with the coverage of eight 4F adsorbed CO molecules (8CO), desorption and dissociation take place simultaneously, and four CO molecules desorb, and the other four CO molecules dissociate. Finally the recombinative desorption (β state) of the dissociative adsorbed 4C and 4O atoms takes place at 700–750 K.

Table 2. CO Desorption Mechanisms at Different Coverage and Temperature

state	coverage	T^a	T^b
α_1	$11CO_{(s)} \rightarrow 10CO_{(s)} + 1CO_{(g)}$	275–300 K	220–250 K
α_2	$10CO_{(s)} \rightarrow 8CO_{(s)} + 2CO_{(g)}$	325–375 K	306–340 K
α_3	$8CO_{(s)} \rightarrow 4C_{(s)} + 4O_{(s)} + 4CO_{(g)}$	400–450 K	400–440 K
β	$4C_{(s)} + 4O_{(s)} \rightarrow 4CO_{(g)}$	700–750 K	750–820 K

[a]Theory. [b]Experiment.

On the basis of the identified most stable molecular and dissociative CO adsorption states at different coverage, we plotted the phase diagram to show the influence of temperatures and CO partial pressures (Figure 4). The phase diagram has four regions: from the only molecular adsorption to the mixed molecular and dissociative CO adsorption, as well as to the full dissociative adsorption and full desorption.

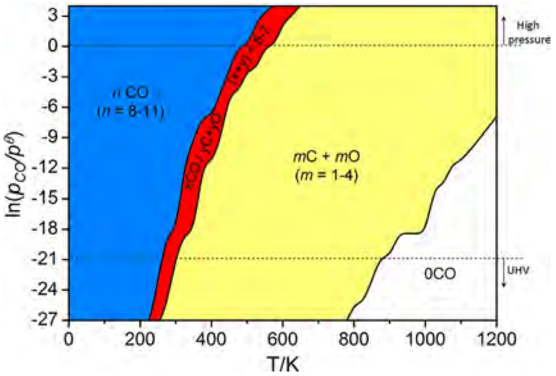

Figure 4. Equilibrium phase diagram of stable CO adsorption or dissociation states.

Apart from the agreement between theory and experiment in the three molecular adsorption states at low temperature,[6] the calculated CO dissociative adsorption also agrees with the experiments. For example, our results show full CO dissociation at the coverage with $n_{CO} = 1$–4. Considering the 24 exposed Fe atoms on the p(3 × 4) surface, the corresponding coverage for CO dissociation is 0.042, 0.083, 0.125, and 0.167 ML for n_{CO} = 1–4, respectively. On the Fe(100) surface at 423 K, Lu et al.[14] found CO dissociation at coverage lower than 0.15 ML, and CO desorption at coverage higher than 0.15 ML from HREELS and temperature programmed surface reaction (TPSR) studies. In addition, we also found the mixed molecular and dissociative CO adsorption at higher coverage from 0.208 to 0.292 ML.

Most interestingly, the phase diagram also provides the information about CO adsorption and dissociation at high temperature and high partial pressure on the Fe(100) surface. Indeed, such information is directly associated with the initial stage of the iron-based FTS catalysts, where the surfaces are proved to be precovered with CO.[44−46] On the basis of the precovered Fe(100) surface with CO as well as C and O atoms, it will be interesting to study the effects of hydrogen in CO activation, either direct dissociation or hydrogen-assisted dissociation under real experimental condition.

4. CONCLUSION

Spin-polarized density functional theory computations have been carried out to study the adsorption, dissociation, and desorption of CO on the Fe(100) surface at different coverage. Within the framework of a $p(3 \times 4)$ surface size (24 exposed surface Fe atoms), the most stable adsorption configuration changes from the 4-fold hollow site at low coverage (n_{CO} = 1−8) to the coexisted bridge and 4-fold hollow sites at the coverage of 9CO to 10CO molecules. At the saturated coverage (11CO), the most stable adsorption configuration has the coexistence of top (1CO), bridge (3CO), and 4-fold hollow (7CO) adsorption sites. The diverse molecular CO adsorption configurations at different coverage and the respective stretching frequencies are in good agreement with the available experimental data from high resolution electron energy loss spectroscopy studies.

On the basis of the computed stepwise CO adsorption energies and dissociation barriers, equilibriums between molecular and dissociative adsorption have been found. At high coverage (n_{CO} = 8−11), only molecular CO adsorption is found. For n_{CO} = 5−7, mixed molecular and dissociative CO adsorption becomes possible. At low coverage (n_{CO} = 1−4), only dissociative CO adsorption is favorable. Ab initio thermodynamic analysis reveals three desorption states from molecular adsorptions (α_1 at 275−300 K; α_2 at 325−375 K and α_3 at 400−450 K) and one recombinative desorption state from dissociative adsorptions (β at 700−750 K). The computed desorption temperatures also agree well with the available experimental data from temperature programmed surface reaction studies.

These detailed studies into the CO activation mechanisms show the insights into the initial process of iron-based Fischer−Tropsch synthesis, where CO adsorption and dissociation as well as surface carburization play the essential roles in structures, stability and activity of the catalysts. The computed CO desorption energies and dissociation barriers at different coverage and temperature provide the basis for microkinetic modeling, which is of practical importance.

■ ASSOCIATED CONTENT

Ⓢ Supporting Information

Detailed description of atomistic thermodynamics method, structures, and energies of those less stable adsorption configurations at a given coverage (Figure S1), structures of IS, TS, FS (Figure S2), as well as potential energy surfaces (Figure S3) of CO dissociation at different coverage are included. This material is available free of charge via the Internet at http://pubs.acs.org.

■ AUTHOR INFORMATION

Corresponding Author

*E-mail: haijun.jiao@catalysis.de.

Notes

The authors declare no competing financial interest.

■ ACKNOWLEDGMENTS

This work was supported by National Natural Science Foundation of China (No. 21273262), National Basic Research Program of China (No. 2011CB201406), Chinese Academy of Sciences and Synfuels CHINA. Co., Ltd. We also acknowledge general finical support from the BMBF and the state of Mecklenburg-Western Pommerania.

■ REFERENCES

(1) Anderson, R. B. *The Fischer-Troposch Synthesis*, Academic Press, Orlando, FL, 1984, p 3.

(2) Kelly, R. D.; Goodman, D. W.; In: King, D. A.; Woodruff, D. P., Eds. *The Chemical Physics of Solid Surfaces and Heterogeneous Catalysis*; Elsevier: Amsterdam, 1982; Vol. 4, p 427.

(3) Fischer, F.; Tropsch, H. Die Erdölsynthese bei Gewöhnlichen Druck aus den Vergasungsprodkten der Kohlen. *Brennstoff Chem.* **1926**, *7*, 97−116.

(4) Brady, R. C., III; Pettit, R. Reactions of Diazomethane on Transition-Metal Surfaces and Their Relationship to The Mechanism of the Fischer−Tropsch Reaction. *J. Am. Chem. Soc.* **1980**, *102*, 6181−6184.

(5) Benziger, J.; Madix, R. J. The Effects of Carbon, Oxygen, Sulfur and Potassium Adlayers on CO and H2 Adsorption on Fe(100). *Surf. Sci.* **1980**, *94*, 119−153.

(6) Moon, D. W.; Dwyer, D. J.; Bernasek, S. L. Adsorption of CO on the Clean and Sulfur Modified Fe(100) Surface. *Surf. Sci.* **1985**, *163*, 215−229.

(7) Cameron, S.; Dwyer, D. J. A Study of π-Bonded CO on Fe(100). *Langmuir* **1988**, *4*, 282−288.

(8) Saiki, R. S.; Herman, G. S.; Yamada, M.; Osterwalder, J.; Fadley, C. S. Structure of an Unusual Tilted State of CO on Fe(001) from X-ray Photoelectron Diffraction. *Phys. Rev. Lett.* **1989**, *63*, 283−286.

(9) Moon, D. W.; Cameron, S.; Zaera, F.; Eberhardt, W.; Carr, R.; Bernasek, S. L.; Gland, J. L; Dwyer, D. J. A Tilted Precursor for CO Dissociation on the Fe(100) Surface. *Surf. Sci. Lett.* **1987**, *180*, L123−L128.

(10) Moon, D. W.; Bernasek, S. L.; Lu, J. P.; Gland, J. L; Dwyer, D. J. Activation of Carbon Monoxide on Clean and Sulfur Modified Fe(100). *Surf. Sci.* **1987**, *184*, 90−108.

(11) Dwyer, D. J.; Rausenberger, B.; Cameron, S. D.; Lu, J. P.; Bernasek, S. L.; Fischer, D. A.; Parker, D. H.; Gland, J. L. Fluorescence Yield Near Edge Spectroscopy of π-Bonded on Fe (100). *Surf. Sci.* **1989**, *224*, 375−385.

(12) Moon, D. W.; Bernasek, S. L.; Dwyer, D. J.; Gland, J. L. Observation of an Unusually Low CO Stretching Frequency on Fe(100). *J. Am. Chem. Soc.* **1985**, *107*, 4363−4364.

(13) Benndorf, C.; Krüger, B.; Thieme, F. Unusually Low Stretching Frequency for CO Adsorption on Fe(100). *Surf. Sci. Lett.* **1985**, *163*, L675−L680.

(14) Lu, J. P.; Albert, M. R.; Bernasek, S. L. Adsorption and Dissociation of CO on Fe(100) at Low Coverage. *Surf. Sci.* **1989**, *217*, 55−64.

(15) Gladh, J.; Öberg, H.; Li, J. B.; Ljungberg, M. P.; Matsuda, A.; Ogasawara, H.; Nilsson, A.; Pettersson, L. G. M.; Öström, H. X-ray Emission Spectroscopy and Density Functional Study of CO/Fe(100). *J. Chem. Phys.* **2012**, *136*, 034702−9.

(16) Mehandru, S. P.; Anderson, A. B. Binding and Orientations of CO on Fe(110), (100) and (111): A Surface Structure Effect From Molecular Orbital Theory. *Surf. Sci.* **1988**, *201*, 345−360.

(17) Blyholder, G.; Lawless, M. A Theoretical Study of the Site of CO dissociation on Fe(100). *Surf. Sci.* **1993**, *290*, 155−162.

(18) Meehan, T. E.; Head, J. D. A Theoretical Comparison of CO Bonding on the Fe(100) Surface. *Surf. Sci.* **1991**, *243*, L55−L62.

(19) Nayak, S. K.; Nooijen, M.; Bernasek, S. L. Electronic Structure Study of CO Adsorption on the Fe(001) Surface. *J. Phys. Chem. B* **2001**, *105*, 164−172.

(20) Sorescu, D. C.; Thompson, D. L.; Hurley, M. M.; Chabalowski, C. F. First-Principles Calculations of the Adsorption, Diffusion, and Dissociation of a CO Molecule on the Fe(100) Surface. *Phys. Rev. B* **2002**, *66*, 035416.

(21) Bromfield, T. C.; Ferre, D. C.; Niemantsverdriet, J. W. A DFT Study of the Adsorption and Dissociation of CO on Fe(100):

Influence of Surface Coverage on the Nature of Accessible Adsorption States. *Chem. Phys. Chem.* **2005**, *6*, 254−260.

(22) Elahifard, M. R.; Jigato, M. P.; Niemantsverdriet, J. W. Direct versus Hydrogen-Assisted CO Dissociation on the Fe(100) Surface: A DFT Study. *Chem. Phys. Chem.* **2012**, *13*, 89−91.

(23) Kresse, G.; Furthmüller, J. Efficiency of Ab-initio Total Energy Calculations for Metals and Semiconductors Using a Plane-Wave Basis Set. *Comput. Mater. Sci.* **1996**, *6*, 15−50.

(24) Kresse, G.; Furthmüller, J. Efficient Iterative Schemes for Ab initio Total-Energy Calculations Using a Plane-Wave Basis Set. *Phys. Rev. B* **1996**, *54*, 11169−11186.

(25) Blochl, P. E. Projector Augmented-Wave Method. *Phys. Rev. B* **1994**, *50*, 17953−17979.

(26) Kresse, G. From Ultrasoft Pseudopotentials to the Projector Augmented-Wave Method. *Phys. Rev. B* **1999**, *59*, 1758−1775.

(27) Perdew, J. P.; Burke, K.; Ernzerhof, M. Generalized Gradient Approximation Made Simple. *Phys. Rev. Lett.* **1996**, *77*, 3865−3868.

(28) Kresse, G.; Hafner, J. First-Principles Study of the Adsorption of Atomic H on Ni (111), (100) and (110). *Surf. Sci.* **2000**, *459*, 287−302.

(29) Methfessel, M.; Paxton, A. T. High-Precision Sampling for Brillouin-zone Integration in Metals. *Phys. Rev. B* **1989**, *40*, 3616−3621.

(30) Henkelman, G.; Jónsson, H. Improved Tangent Estimate in the Nudged Elastic Band Method for Finding Minimum Energy Paths and Saddle Points. *J. Chem. Phys.* **2000**, *113*, 9978−9985.

(31) Jiang, E.; Carter, E. A. Carbon Dissolution and Diffusion in Ferrite and Austenite from First Principles. *Phys. Rev. B* **2003**, *67*, 214103−214113.

(32) Sorescu, D. C. First-Principles Calculations of the Adsorption and Hydrogenation Reactions of CHx (x = 0,4) Species on a Fe(100) Surface. *Phys. Rev. B* **2006**, *73*, 155420−155436.

(33) Kittel, C. *Introduction to Solid State Physics*; Wiley: New York, 1996.

(34) Reuter, K.; Scheffler, M. Composition, Structure, and Stability of RuO2(110) as a Function of Oxygen Pressure. *Phys. Rev. B* **2001**, *65*, 035406.

(35) Reuter, K.; Scheffler, M. Composition and Structure of the RuO2(110) Surface in an O2 and CO Environment: Implications for the Catalytic Formation of CO2. *Phys. Rev. B* **2003**, *68*, 045407.

(36) Li, W. X.; Stampfl, C.; Scheffler, M. Insights into the Function of Silver as an Oxidation Catalyst by Ab Initio Atomistic Thermodynamics. *Phys. Rev. B* **2003**, *68*, 165412.

(37) Rogal, J.; Reuter, K.; Scheffler, M. Thermodynamic Stability of PdO Surfaces. *Phys. Rev. B* **2004**, *69*, 075421.

(38) Grillo, M. E.; Ranke, W.; Finnis, M. W. Surface Structure and Water adsorption on Fe3O4(111): Spin-Density Functional Theory and On-Site Coulomb Interactions. *Phys. Rev. B* **2008**, *77*, 075407.

(39) Aray, Y.; Vidal, A. B.; Rodriguez, J.; Grillo, M. E.; Vega, D.; Coll, D. S. First Principles Study of Low Miller Index RuS_2 Surfaces in Hydrotreating Conditions. *J. Phys. Chem. C* **2009**, *113*, 19545−19557.

(40) Zasada, F.; Piskorz, W.; Cristol, S.; Paul, J. F.; Kotarba, A.; Sojka, Z. Periodic Density Functional Theory and Atomistic Thermodynamic Studies of Cobalt Spinel Nanocrystals in Wet Environment: Molecular Interpretation of Water Adsorption Equilibria. *J. Phys. Chem. C* **2010**, *114*, 22245−22253.

(41) Wang, T.; Liu, X. W.; Wang, S. G.; Huo, C. F.; Li, Y. W.; Wang, J. G.; Jiao, H. Stability of β-Mo2C Facets from Ab Initio Atomistic Thermodynamics. *J. Phys. Chem. C* **2011**, *115*, 22360−22368.

(42) Wang, T.; Wang, S. G.; Li, Y. W.; Wang, J. G.; Jiao, H. J. Adsorption Equilibria of CO Coverage on β-Mo2C Surfaces. *J. Phys. Chem. C* **2012**, *116*, 6340−6348.

(43) Sorescu, D. C. Plane-Wave DFT Investigations of the Adsorption, Diffusion, and Activation of CO on Kinked Fe(710) and Fe(310) Surfaces. *J. Phys. Chem. C* **2008**, *112*, 10472−10489.

(44) Mims, C. A.; McCandlish, L. E. Evidence for Rapid Chain Growth in the Fischer−Tropsch Synthesis over Iron and Cobalt Catalysts. *J. Phys. Chem.* **1987**, *91*, 929−937.

(45) Ojedaa, M.; Nabarb, R.; Nilekarb, A. U.; Ishikawaa, A.; Mavrikakisb, M.; Iglesia, E. CO Activation Pathways and the Mechanism of Fischer−Tropsch Synthesis. *J. Catal.* **2010**, *272*, 287−297.

(46) Loveless, B. T.; Buda, C.; Neurock, M.; Iglesia, E. CO Chemisorption and Dissociation at High Coverages during CO Hydrogenation on Ru Catalysts. *J. Am. Chem. Soc.* **2013**, *135*, 6107−6121.

3.2 Coverage-Dependent CO Adsorption and Dissociation Mechanisms on Iron Surfaces from DFT Computations

Tao Wang, Xinxin Tian, Yong-Wang Li, Jianguo Wang, Matthias Beller, Haijun Jiao*

ACS Catalysis **2014**, *4*, 1991-2005.

Summary: CO adsorption structures and energetics on the iron (100), (110), (111), (210), (211) and (310) surfaces from the lowest coverage up to saturation have been computed using spin-polarized density functional theory and ab initio thermodynamics. It is found that different adsorption configurations on each of these surfaces at high coverage can co-exist. The stepwise adsorption energies and dissociation barriers at different coverage reveal equilibriums between desorption and dissociation of adsorbed CO molecules. Only molecular CO adsorption is possible at very high coverage and only dissociative CO adsorption at very low coverage, while mixed molecular and dissociative CO adsorption becomes possible at medium coverage. The computed stable adsorption configurations and the respective C-O and Fe-C stretching frequencies as well as desorption temperatures on the (100), (110) and (111) surfaces agree very well with the available experimental data. Such agreements between theory and experiment validate our computational methods, and allow to reasonably predict the experimentally unknown CO activation mechanisms on the (210), (211) and (310) surfaces. Our results might provide some references for the studies of CO related reaction mechanisms.

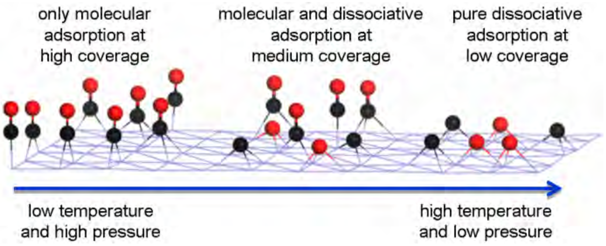
only molecular adsorption at high coverage
molecular and dissociative adsorption at medium coverage
pure dissociative adsorption at low coverage
low temperature and high pressure
high temperature and low pressure

Contributions

In this paper, I planned, performed and analyzed most calculations for this manuscript. I have done the major part of writing of the manuscript. My contribution as co-author of this paper is approximately 85%.

ACS Catalysis
Research Article
pubs.acs.org/acscatalysis

Coverage-Dependent CO Adsorption and Dissociation Mechanisms on Iron Surfaces from DFT Computations

Tao Wang,[†] Xin-Xin Tian,[‡] Yong-Wang Li,[‡] Jianguo Wang,[‡] Matthias Beller,[†] and Haijun Jiao*[,†,‡]

[†]Leibniz-Institut für Katalyse e.V. an der Universität Rostock, Albert-Einstein Strasse 29a, 18059 Rostock, Germany
[‡]State Key Laboratory of Coal Conversion, Institute of Coal Chemistry, Chinese Academy of Sciences, Taiyuan, Shanxi 030001, People's Republic of China

S *Supporting Information*

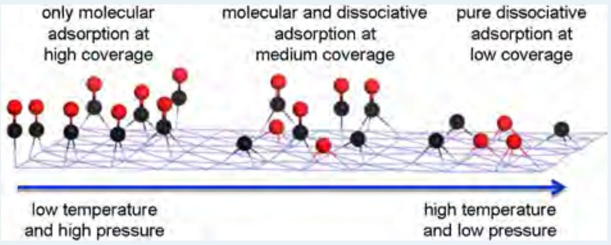
only molecular adsorption at high coverage
molecular and dissociative adsorption at medium coverage
pure dissociative adsorption at low coverage
low temperature and high pressure
high temperature and low pressure

ABSTRACT: CO adsorption structures and energetics on the iron (100), (110), (111), (210), (211), and (310) surfaces from the lowest coverage up to saturation have been computed using spin-polarized density functional theory and ab initio thermodynamics. It is found that different adsorption configurations on each of these surfaces at high coverage can coexist. The stepwise adsorption energies and dissociation barriers at different coverage reveal equilibriums between desorption and dissociation of adsorbed CO molecules. Only molecular CO adsorption is possible at very high coverage and only dissociative CO adsorption at very low coverage, whereas mixed molecular and dissociative CO adsorption becomes possible at medium coverage. The computed stable adsorption configurations and the respective C−O and Fe−C stretching frequencies as well as desorption temperatures on the (100), (110), and (111) surfaces agree very well with the available experimental data. Such agreements between theory and experiment validate our computational methods and allow us to reasonably predict the experimentally unknown CO activation mechanisms on the (210), (211), and (310) surfaces. Our results might provide some references for the study of CO related reaction mechanisms.

KEYWORDS: *DFT, CO, adsorption, dissociation, iron surfaces, high coverage*

1. INTRODUCTION

As a very important and useful basic chemical, carbon monoxide (CO) has found wide applications in energy societies as well as value-added bulk and fine chemical productions. The most representative examples are Fischer−Tropsch synthesis (FTS),[1] alcohol synthesis, and hydrogen production from the water−gas shift (WGS) reaction.[2] To understand these key processes deeply, it is very necessary and essential to study CO adsorption and dissociation mechanisms on the surfaces of heterogeneous catalysts. Because of the significant relevance of CH_x formation in the FTS process,[3,4] CO adsorption and dissociation mechanisms on iron surfaces have attracted great attention from academic researchers and for industrial applications. More specifically, the adsorption, desorption, and dissociation of CO on iron surfaces are very essential steps in association with the catalytic activities. In the last two decades, diverse experimental techniques and state of the art theoretical calculations have been explored to investigate the interaction of CO with iron single crystalline surfaces.

On the Fe(110) surface, Yoshida and Somorjai[5] found an ordered molecular CO adsorption at 270 K and a dissociative adsorption at 400 K by using low-energy electron diffraction (LEED) and thermal desorption spectroscopy (TDS). Broden et al.[6] also found a molecular CO adsorption on the Fe(110) surface at room temperature and a dissociative adsorption at 385 K in an ultraviolet photoemission spectroscopy and LEED study. Erley[7] investigated CO chemisorption on the Fe(110) surface at 120 K by using LEED and high resolution electron energy loss spectroscopy (HREELS) and found the shifts of the Fe−C stretching frequency from 456 to 500 cm^{-1} up to 0.7 L (0.25 ML) and from 484 to 444 cm^{-1} at 0.7−1.5 L (0.5 ML) as well as the C−O stretching frequency from 1890 to 1985 cm^{-1} with an increase in exposure. Gonzalez et al.[8] studied CO adsorption and desorption kinetics on the Fe(110) surface by using TDS and found a molecular CO desorption at 400−420 K and a recombinative desorption at 675−800 K, and that surface defects facilitate CO dissociation. In a laser-induced thermal desorption study of CO on the Fe(110) surface, Wedler et al.[9] found that the desorption maximum amplitude depends on laser pulse intensity and CO coverage. A work function study (WF)[10] revealed a facile equilibrium between adsorption and desorption at room temperature and dissociation above 380 K for CO on the Fe(110) surface.

On the Fe(100) surface, three molecular CO adsorption states (α_1, α_2, and α_3) at about 220−250, 306−340, and 400−440 K as well as one recombinative desorption of dissociated C and O atoms at around 750−820 K (β state) were detected by applying surface science techniques such as X-ray photoelectron spectroscopy (XPS) and temperature-programmed desorption (TPD),[11−13] and CO dissociation was observed at about 440 K.

Received: March 4, 2014
Revised: April 29, 2014

© XXXX American Chemical Society

Further study by applying XPS, TPD, X-ray photoelectron diffraction,[14] near-edge X-ray absorption fine structure spectroscopy,[15−17] and HREELS[18,19] identified the 4-fold hollow site with an unusually low CO stretching frequency of 1210 cm^{-1} as the most stable adsorption configuration (α_3), representing the CO dissociation precursor state. By using HREELS and temperature-programmed surface reaction techniques, Lu et al.[20] studied CO adsorption and dissociation on the Fe(100) surface at 423 K and found CO dissociation at coverage lower than 0.15 monolayer (ML) and CO desorption at coverage higher than 0.15 ML. The bonding mechanism of the predissociative hollow (α_3) phase and the nondissociative atop (α_1) phase of CO on the Fe(100) surface was studied by Gladh et al.[21] by using X-ray emission spectroscopy and density functional theory (DFT) calculations, and a π-donation/π* back-donation scheme is proposed for CO in the 4-fold hollow site. Wilcox et al.[22] systematically studied the adsorption mechanism and electronic structure of CO on the FeCo(100) alloys and compared it with those on the pure Fe(001) and Co(0001) surfaces.

In a combined HREELS, LEED, TDS and WF study of CO on the Fe(111) surface, Seip et al.[23] found the sharp peak at 400 K (α_2 state) in TDS belonging to CO adsorption at the shallow hollow site, the α_1 state at high exposure belonging to CO adsorption at the atop and deep-hollow sites, and the β state coming from the recombinative desorption of the adsorbed C and O atoms. A similar study of CO adsorption on the Fe(111) surface by applying low-temperature exposure and high-resolution data by Bartosch et al.[24] confirmed three CO adsorption states and found a previously unobserved CO stretching vibration at 1325 cm^{-1}. In a TPD and time-resolved electron energy loss spectroscopy study of CO adsorption on the Fe(111) surface, Whitman et al.[25] found that CO site occupancy depends on coverage and temperature.

In addition to the extensive experimental studies, CO adsorption on iron single crystalline surfaces also has been widely studied theoretically. Early studies in the 1980s applied mainly semiempirical[26,27] and Hatree−Fock[28] methods. By using infinite slab and finite cluster models to study CO adsorption on the Fe(001) surface, Nayak et al.[29] found that the 4-fold hollow site is the energetically most preferred adsorption site, followed by the atop and bridge sites. Sorescu et al.[30] computed the adsorption of CO, C, and O atoms as well as CO dissociation on the Fe(100) surface and found that CO on the 4-fold site (α_3 state in TPD) is the most stable and has a dissociation barrier in the range of 1.06−1.22 eV, whereas CO on the bridge site (α_2 state) is more stable than on the atop site (α_1 state) at low coverage, and the atop site becomes more stable than the bridge site at high coverage. Bromfield et al.[31] studied CO interaction on the Fe(100) surface and found that CO adsorption and dissociation are coverage dependent. On the Fe(100) surface, Elahifard et al.[32] proposed CO direct dissociation at low coverage and H-assisted CO dissociation at high coverage.

The DFT study of CO adsorption on the Fe(110) surface at different coverage by Stibor et al.[33] revealed that CO adsorption on the top site is the most stable at low coverage but on the long bridge site becomes the most stable at high coverage. Because of the disagreement with the favored top adsorption configurations at high coverage on the basis of the detected CO vibrational frequencies, they attributed this disagreement to the overestimation of the stability of the long bridge adsorption configuration by the DFT method. By applying a different exchange and correlation functional, Jiang and Carter[34] studied CO adsorption and dissociation on the Fe(110) surface, and their results show that the PW91, PBE, RPBE, and PKZB methods can yield the correct site preference at 0.25 ML, but only PKZB predicts the correct site preference at 0.5 ML. They also reported a CO dissociation barrier of 1.52 eV on the top site on the Fe(110) surface at 0.25 ML with PBE. Sun et al.[35] investigated the spin-resolved electronic states of CO on the Fe(110) surface using spin-polarized metastable-atom de-excitation spectroscopy (SPMDS) and first-principles DFT and found the existence of the adsorbate-induced 2π* state in addition to CO 4σ and 5σ /1π states.

On the Fe(111) surface, Chen et al.[36] carried out a systematic DFT study of CO adsorption at different coverage and revealed that shallow hollow adsorption is most stable at 1/3 and 1/2 ML; shallow hollow and bridge adsorptions coexist at 1 ML, and bent atop and triply capping adsorptions are most favorable at 2 ML. Huo et al.[37] studied CO dissociation on the clean and hydrogen-precovered Fe(111) surfaces by DFT calculations and revealed H-assisted CO dissociation to be more favorable than CO direct dissociation. A similar result about H-assisted CO dissociation on Fe(111) was also reported by Li et al.[38]

CO chemisorption on the Fe(211) surface was reported by Borthwick et al.[39] using first-principles DFT and a single-crystal adsorption calorimetric method. In their study, the adsorption state at the 3-fold site involving one top-layer and two second-layer metal atoms is most stable. They also found that CO dissociation is particularly facile, and the Fe(211) surface is optimal for FTS. Lo et al.[40] studied CO adsorption and dissociation on the stepped Fe(310) surface by using the DFT method at 0.25 and 0.50 ML and found significant contributions of coverage to the overall CO decomposition rate at 0.5 ML. Sorescu[41] studied CO adsorption, diffusion, and activation on the kinked Fe(710) and Fe(310) surfaces and found the smallest activation barriers for CO dissociation in the regime of low coverage compared with the Fe(100), Fe(110), Fe(111), and Fe(211) surfaces.

Despite these extensive DFT studies about CO adsorption on iron single crystalline surfaces, it is still difficult for a systematic comparison among different surfaces because those data have been obtained by using very diverse models and methods. Furthermore, the coverage-dependent CO adsorption and dissociation, apart from our recent work,[42] has not been considered previously. Because the surfaces of FTS catalysts have been proved to be CO-precovered experimentally,[43−45] studies of high-coverage CO activation are essential to understand the initial steps of the FTS process as well as reactions involving CO deeply. Because the active phases of catalysts in heterogeneous catalysis are polycrystalline and always very complex, the reasonable way to get a deep and reasonable understanding into the active sites and catalytic properties is to consider all possibilities. We therefore performed a systematic study of CO adsorption, dissociation, and desorption on iron (110), (111), (210), (211), and (310) surfaces at different coverages using the same DFT methodology. For a general comparison, we included our results of CO adsorption and dissociation on the (100) surface. Our goal is to reveal the coverage-dependent adsorption, dissociation, and desorption processes and, finally, to present the initial state of CO activation on iron surfaces, which will provide some references for the studies of CO related reaction mechanisms.

2. COMPUTATIONAL METHODS AND MODELS

2.1. Methods. All calculations were performed by applying the plane-wave-based DFT method implemented in the Vienna ab initio simulation package (VASP).[46,47] Periodic slab models were used to model the catalyst surfaces. The electron ion interaction was described with the projector augmented wave (PAW) method.[48,49] The electron exchange and correlation energy was treated within the generalized gradient approximation in the Perdew−Burke−Ernzerhof formalism (GGA-PBE).[50] Spin-polarization was included for iron systems to correctly account for the magnetic properties, and this was found essential for an accurate description of adsorption energies.[51] To acquire accurate energies with errors of <1 meV per atom, an energy cutoff of 400 eV and a second-order Methfessel−Paxton[52] electron smearing with $\sigma = 0.2$ eV were used. A vacuum layer of 10 Å was set between the periodically repeated slabs to avoid strong interactions.

The adsorption energy (E_{ads}) of one CO molecule is defined as $E_{ads} = E_{CO/slab} - [E_{slab} + E_{CO}]$, where $E_{CO/slab}$ is the total energy of the slab with one CO adsorption, E_{slab} is the total energy of the bare slab, and E_{CO} is the total energy of a free CO molecule in the gas phase; and a more negative E_{ads} indicates a stronger adsorption. To consider the coverage-dependent CO adsorption and dissociation, CO was added to the surfaces one-by-one on the basis of the most stable adsorption structure of one CO, that is, one additional CO molecule was added to the previous most stable one for getting the next most stable one after considering different adsorption sites. For getting the saturation coverage, stepwise adsorption energy (ΔE_{ads}) was applied, that is, $\Delta E_{ads} = E_{(CO)n+1/slab} - [E_{(CO)n/slab} + E_{CO}]$, where a positive ΔE_{ads} for $n + 1$ adsorbed CO molecules indicates the saturated adsorption with nCO molecules. Our stepwise adsorption energy defines the change in the adsorption energy by adding one more species to the surface, whereas the differential energy of adsorption defines the change in the average adsorption energy per coverage as a function of the coverage.[53]

To locate the CO dissociation transition states on iron surfaces, the nudged elastic band method[54] was applied, and the CO stretching frequencies were analyzed to characterize a transition state with only one imaginary frequency. The CO dissociation barrier (E_a) is defined as $E_a = E_{TS} - E_{IS}$, and the reaction energy (E_r) is defined as $E_r = E_{FS} - E_{IS}$, where E_{IS}, E_{FS}, and E_{TS} represent the total energy of the initial adsorbed CO molecule, final dissociated CO molecule (C + O atoms), and the CO dissociating transition state, respectively. We tested the corrections of zero-point energies (ZPE) to the adsorption energies of a gaseous CO molecule, the dissociation barriers, and dissociation energies of an adsorbed CO molecule on all six iron surfaces (Supporting Information Table S1). For CO adsorption energy, the maximal correction is 0.06 eV and the average absolute correction is 0.04 eV. For CO dissociation barrier, the maximal correction is 0.04 eV and the average absolute correction is 0.02 eV. For CO dissociation energy, the maximal correction is 0.07 eV and the average absolute correction is 0.05 eV. All these rather small corrections do not alter the results and conclusion without corrections; therefore, we used all energetics without ZPE corrections for our analysis and discussion.

2.2. Models. Calculation of the α-Fe bulk crystal structure with a k-point mesh of 9 × 9 × 9 gives a lattice constant of 2.84 Å and a local spin magnetic moment of 2.214 μ_B, in good agreement with other DFT calculations[55,56] and experiment.[57] For studying CO adsorption on an α-Fe catalyst, apart from the (100) surface in our previous work,[42] other five body-centered cubic (bcc) surfaces are considered: two low-index (110) and (111) surfaces for the basic structures and three high-index (210), (211), and (310) surfaces for the step and kinked structures. Theoretical studies on the surface structures and stability from the literature[58−62] are compiled in Supporting Information Table S2. All these studies show that the (110) and (100) surfaces are most stable, followed by the (211) and (310) surfaces. Depending on the models and methods, the (210) and (111) surfaces have very close surface energies and are less stable.

Different from the models reported in literature, we used much larger surface sizes in our calculations. For (110), a $p(3 \times 4)$ model with three atomic layers was used, and the first layer was allowed to relax. For (111), a $p(2 \times 3)$ model with seven atomic layers was used, and the top three layers were allowed to relax. For (210), a $p(3 \times 2)$ model with six atomic layers was used, and the top four layers were allowed to relax. For (211), a $p(4 \times 2)$ model with four atomic layers was used, and the top two layers were allowed to relax. For (310), a $p(3 \times 2)$ model with six atomic layers was used, and the top three layers were allowed to relax. The k-point mesh of 3 × 3 × 1 was used for all these surfaces. These models have been proved to be reasonable to clearly describe the properties of the corresponding Fe surfaces based on the previous work.[62,63]

2.3. Thermodynamics. As a convenient tool to solve problems referring to real reaction conditions, ab initio atomistic thermodynamics proposed by Scheffler and Reuter[64,65] has been widely and successfully applied in many other systems.[66−73] The detailed description of the method can be found in the Supporting Information.

3. RESULTS AND DISCUSSIONS

3.1. Adsorption Sites. Figure 1 shows the schematic side and top views of the six Fe surfaces along with their possible adsorption sites. The (100) surface has top (T), bridge (B), and 4-fold hollow (4F) sites; (110) has top (T), short-bridge (SB), long-bridge (LB), and 3-fold (3F) sites; (111) has top (T), shallow-hollow (SH), deep-hollow (DH), and 4-fold hollow (4F) sites. On the high-index surfaces, more adsorption sites are available. For example, (210) has 11 adsorption sites: three top (T_1, T_2, T_3), three bridge (B_1, B_2, B_3), four 3-fold ($3F_1$, $3F_2$, $3F_3$, $3F_4$), and one 4-fold (4F) sites. Surface (211) has five adsorption sites: one top (T), one bridge (B), two 3-fold ($3F_1$, $3F_2$), and one 4-fold (4F) sites. Surface (310) also has five adsorption sites: one top (T), one bridge site (B), two 3-fold ($3F_1$, $3F_2$), and one 4-fold (4F) sites.

3.2. Lowest-Coverage CO Adsorption. It is found that not all available adsorption sites can stably adsorb CO at the lowest coverage. The most stable adsorption configurations for one CO molecule on these surfaces are given in Figure 2, and the other less stable configurations are given in the Supporting Information (Figure S1). Table 1 lists the systematically computed CO adsorption energies and dissociation barriers as well as dissociation energies on these surfaces along with all available literature data. It shows clearly that all these computed data are not only different on surfaces but also method- and model-dependent in some cases.

On the Fe(100) surface, the most stable adsorption configurations of one CO molecule is located on the 4-fold site with the C atom coordinating with four surface Fe atoms

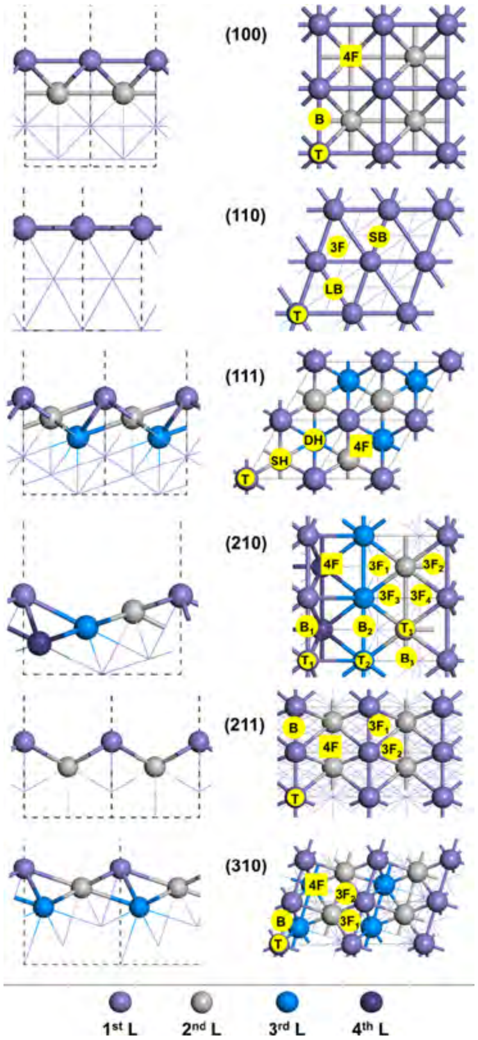

Figure 1. Schematic side and top views of Fe(100), (110), (111), (210), (211), and (310) surfaces and possible adsorption sites.

and the O atom interacting with two surface Fe atoms. The C−O bond length is elongated to 1.32 Å with respect to gaseous CO (1.14 Å), and the computed C−O stretching frequency is 1172 cm^{-1}. The calculated adsorption energy is −2.14 eV.[42] Experimentally, this adsorption configuration is assigned to the α_3 adsorption state from TDS. In addition, we also found stable adsorption configurations at the top (−1.72 eV) and bridge (−1.51 eV) sites. Our computed adsorption energy of the most stable configuration (−2.14 eV) is similar to that (−2.17 eV) by Sorescu et al.[41] because the same software and functional were used. However, the results obtained with RPBE (−1.90 eV[30]), PW91 (−2.02,[30] −2.54 eV[31]), and cluster model (−1.62 eV[29]) are obviously different on the basis of quite different methods and models.

On the Fe(110) surface, the top site forms the most stable CO adsorption configuration with a C−O distance of 1.18 Å and C−O stretching frequency of 1900 cm^{-1}. This most stable adsorption site is the same as that found at low coverage in other studies. Our computed adsorption energy (−1.88 eV) is close to the available data with PW91 (−1.95 eV)[33] and PBE (−1.88,[34] −2.00,[35] −1.88 eV[41]), but higher than those obtained with RPBE (−1.58 eV) and PKZB (−1.67 eV).[34] In addition, we also found stable adsorption configurations at the short bridge (−1.66 eV), the long bridge (−1.81 eV), and the 3-fold capping (−1.81 eV) sites, and they are close to that of the most stable adsorption configuration.

On the Fe(111) surface, the shallow-hollow site with the C atom coordinating with one Fe atom forms the most stable CO adsorption configuration, with a C−O distance of 1.20 Å and C−O stretching frequency of 1739 cm^{-1}. Our computed adsorption energy (−2.13 eV) is similar to that (−2.09 eV) with PBE in a $\sqrt{3} \times \sqrt{3}$ model.[41] A relatively larger difference is found with the results from PBE (−2.45 eV)[36] and RPBE (−2.08 eV).[37] Such differences presumably come from the use of ultrasoft pseudopotential (USPP). In addition, the top (−1.46 eV), the deep-hollow (−1.48 eV), and the 3-fold (−1.98 eV) adsorption configurations are much less stable than the most stable adsorption configuration at the shallow-hollow site.

On the (211) surface, the most stable CO adsorption configuration is the 4-fold site with the C atom coordinating to four Fe atoms and the O atom interacting with one Fe atom, the C−O distance is 1.28 Å, and the C−O stretching frequency is 1274 cm^{-1}. Our adsorption energy (−1.94 eV) is higher than that (−1.72 eV) with PBE[41] using a small super cell. The RPBE[39] value (−1.92 eV) using a small super cell is similar to our result from PBE, but they are not comparable because they used USPP to include the electron−ion interaction. The PW91 value (−2.41 eV) with a small super cell[39] is much higher than those from both PBE and RPBE. In addition, we also found two top (−1.77 and −1.67 eV) and one bridge (−1.78 eV) adsorption configurations, and they are less stable than the most stable adsorption configuration at the 4-fold site.

On the (310) surface, the most stable CO adsorption configuration is the 4-fold site with the C atom coordinating

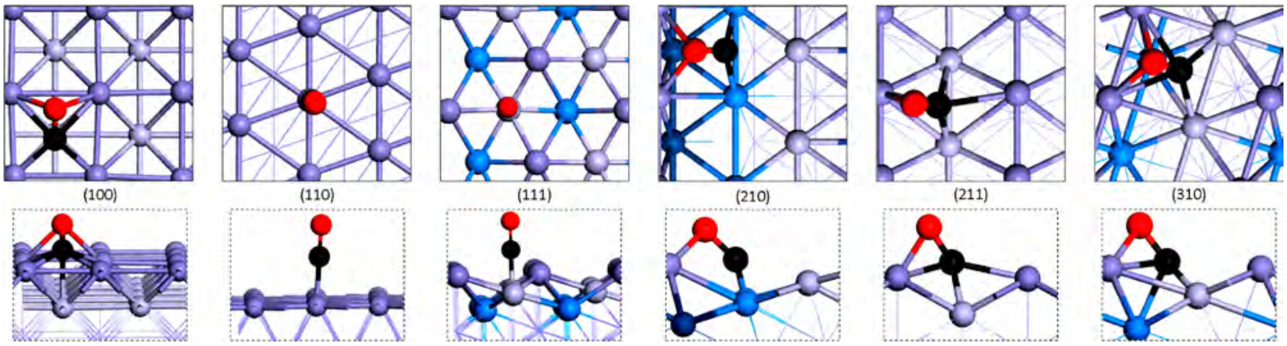

Figure 2. Structures of the most stable CO adsorption configurations on six iron surfaces (black ball, C; red ball, O; the other balls for Fe in different layers).

Table 1. Adsorption Energies (E_{ads}), Dissociation Barriers (E_a), and Dissociation Energies (E_r) of the Most Stable CO Adsorption Configuration As Well As the C−O Stretching Frequencies (υ_{CO}), the C−O Distances (R) in the Adsorbed Initial States (IS), and Dissociating Transition States (TS) on Six Iron Surfaces

E_{ads}, eV	E_a, eV	$E_r{}^a$, eV	υ_{CO}, cm^{-1}	R_{C-O} (IS), Å	R_{C-O} (TS), Å	ref
			(100)			
−1.62 (cluster)				1.30		29
−2.02 (PW91, 2 × 2)	1.06		1246	1.32		30
−1.90 (RPBE, 2 × 2)				1.32		30
−2.54 (PW91, 2 × 2)	1.14		1158	1.32		31
−2.17 (PBE, 2 × 2)	1.07		1189	1.32	1.93	41
−2.14 (PBE, 3 × 4)	1.03	−0.93 (−1.20)	1172	1.32	1.93	42
			(110)			
−1.88 (PBE, 3 × 4)	1.51	−0.46 (−0.74)	1900	1.18	1.75	this work
−1.95 (PW91, 2 × 2)				1.16		33
−1.88 (PBE, 2 × 2)	1.52		1928		1.74	34
−1.58 (RPBE, 2 × 2)						34
−1.67 (PKZB, 2 × 2)						34
−2.00 (PBE, 2 × 2)				1.17		35
−1.88 (PBE, 2 × 2)	1.52				1.74	41
			(111)			
−2.13 (PBE, 2 × 3)	1.17	0.06 (−0.09)	1739	1.20	1.85	this work
−2.45 (PBE, $\surd 3 \times \surd 3$)	1.39			1.19		36, 37
−2.08 (RPBE, $\surd 3 \times \surd 3$)	1.53				2.00	37
−2.09 (PBE, $\surd 3 \times \surd 3$)	1.20				1.80	41
			(210)			
−2.00 (PBE, 3 × 2)	1.11	−0.32 (−0.82)	1115	1.33	1.97	this work
			(211)			
−1.94 (PBE, 4 × 2)	1.06	−0.20 (−0.39)	1274	1.28	1.95	this work
−2.41 (PW91, 2 × 1)	0.78			1.28	1.83	39
−1.92 (RPBE, 2 × 1)	0.93					39
−1.72 (PBE, 2 × 2)	1.02			1.28	1.93	41
			(310)			
−2.13 (PBE, 3 × 2)	0.98	−0.39 (−1.07)	1104	1.33	1.93	this work
−1.85 (PW91, 2 × 1)	0.94		1147	1.33	1.80	40
−2.10 (PBE, 2 × 2)	0.91		1134	1.33		41

[a] Dissociation energy in parentheses is related to the most stable adsorbed C and O atoms after diffusion.

with four Fe atoms and the O atom interacting with two surface Fe atoms. The C−O distance is 1.33 Å, and the C−O stretching frequency is 1104 cm^{-1}. Our computed adsorption energy (−2.13 eV) is close to the reported PBE-$p(2 \times 2)$[41] value (−2.10 eV) because the same software and functional were used. A relative smaller value (−1.85 eV[40]) was reported by using USPP and PW91 as well as a small supercell $p(2 \times 1)$, which may overestimate the lateral repulsive interaction. In addition, we also found two tilted top (−1.60 and −1.79 eV) and one 4-fold (−1.72 eV) adsorption configurations, and they are much less stable than the most stable adsorption configuration at the 4-fold site.

On the (210) surface, the most stable adsorption configuration is the 4-fold site with the C atom coordinating with two deep-layer Fe atoms and the O atom interacting with two surface Fe atoms with a C−O distance of 1.33 Å and CO stretching frequency of 1115 cm^{-1}. We also found two top (−1.69 and −1.74 eV) and three 3-fold (−1.70, −1.72, and −1.63 eV) adsorption configurations, and they are much less stable than the most stable adsorption configuration at the 4-fold site (−2.00 eV). Because no theoretical studies about CO adsorption on this surface are available, no comparison with our data can be made.

Although CO interaction on iron single crystalline surfaces has been intensively studied in recent decades, a general and critical comparison among the results obtained with different models and methods is neither easy nor straightforward.[74] At first, the lowest coverage for different surface sizes indeed represents different coverage, and reducing the surface size to create high coverage is not a reasonable choice. Generally, models with larger surface sizes show stronger adsorption than models with smaller surface sizes, and this is probably due to the difference in lateral repulsive interaction. As summarized in Table 1, PBE gives higher adsorption energies than the RPBE, and this is due to the intrinsic properties of these methods. In addition, different methods for solving electron−ion and electron−electron interactions as well as basis sets also give different results. It is noted that different computational parameters can also result in quite different results. However, it is reported that different methods and functional on the basis of the same surface model can give very close structural as well as kinetic and thermodynamic parameters. For example, PAW−PBE and USPP−PW91 with VASP, and USP−PBE and USPP−PW91 with CASTEP to calculate the hydrogenation and the respective C−C coupling reactions of carbon species on the $Fe_5C_2(001)$ surface.[75]

In contrast, our results enable a direct and systematic comparison in CO adsorption at low coverage. On the (100), (111), and (310) surfaces, the most stable adsorption configurations have almost identical adsorption energies, but the adsorbed CO is more strongly activated on the (100) and (310) surfaces than on the (111) surface on the basis of the computed C−O distances (1.32 and 1.33 vs 1.18 Å, respectively) or the CO-stretching frequencies (1172 and 1104 vs 1793 cm^{-1}, respectively), although CO has moderate adsorption energies (−2.00 and −1.94 eV, respectively) on the (210) and (211) surfaces, but it is highly activated on the basis of the computed C−O distances (1.33 and 1.28 Å, respectively) or C−O stretching frequencies (1144 and 1273 cm^{-1}, respectively). On the most stable (110) surface, CO has not only the lowest adsorption energy (−1.88 eV), but also the weakest activation with a C−O distance and stretching frequency of 1.18 Å and 1900 cm^{-1}.

3.3. High Coverage CO Adsorption. To discuss the coverage effects of CO adsorption and activation on iron surfaces, it is necessary to find the stable adsorption configurations and energies at different coverages on each surface. As referred to in the Methods section, the computed stepwise adsorption energies (ΔE_{ads}) are applied to get the saturated coverage. The structures and energies (ΔE_{ads}) of the most stable adsorption sites for stepwise CO adsorption are given in the Supporting Information (Figures S2−S6).

On the (100) surface,[42] the first four adsorbed CO molecules (n_{CO} = 1−4) have the 4-fold adsorption configuration and very similar adsorption energies, indicating their negligible lateral repulsive interaction and their independence. At n_{CO} = 5−8, lateral repulsive interaction of the adsorbed CO molecules becomes significant and affects the value of ΔE_{ads}, but all the adsorbed CO molecules still have the 4-fold adsorption configuration. At n_{CO} = 9, the bridge adsorption configuration appears, and one bridge and eight 4-fold adsorption configurations coexist. At n_{CO} = 10, there are three bridge and seven 4-fold adsorption configurations. At the saturated coverage (n_{CO} = 11), there are one top, three bridge, and seven 4-fold adsorption configurations.

On the (110) surface (Supporting Information Figure S2), the top adsorption configuration is the most stable at low coverage, and the first three CO molecules (n_{CO} = 1−3) have the same adsorption configuration and similar stepwise adsorption energies. At n_{CO} = 4, the most stable adsorption configuration changes from the top sites to the long bridge sites, and all four CO molecules have the same adsorption configuration. At n_{CO} > 4, the 3-fold hollow and short bridge configurations appear. At the saturated coverage (n_{CO} = 8), three adsorption configurations (short bridge, long bridge, and 3-fold hollow) coexist on the surface, and the top adsorption configuration disappeared.

On the (111) surface (Supporting Information Figure S3), the shallow hollow adsorption configuration is most stable at low coverage, and the first six CO molecules (n_{CO} = 1−6) have the same adsorption mode and also very similar stepwise adsorption energies. At n_{CO} = 7, the qusi-4-fold adsorption configuration appears, and the stepwise adsorption energy decreases. At the saturated coverage (n_{CO} = 9), three adsorption configurations (top, shallow hollow and qusi-4-fold) coexist on the surface.

On the (210) surface (Supporting Information Figure S4), the most stable adsorption configuration is located at the 4-fold hollow site with n_{CO} < 6, and the top adsorption configuration appears at n_{CO} = 7. At the saturated coverage (n_{CO} = 12), two adsorption configurations coexist (top and 4-fold hollow sites). On the (211) surface (Supporting Information Figure S5), the most stable adsorption configuration is located in the 4-fold hollow site at low coverage, and the top and bridge adsorption configurations appear with coverage increase. At the saturated coverage (n_{CO} = 10), the coexistence of top, bridge, and 4-fold adsorption configurations become possible. On the (310) surface (Supporting Information Figure S6), the most stable adsorption configuration is located in the 4-fold hollow site at low coverage, and the 3-fold hollow adsorption configuration appears at n_{CO} > 7. The saturated coverage with nine CO molecules (n_{CO} = 9) has bridge and 4-fold hollow adsorption configurations.

3.4. CO Dissociation. On the basis of the most stable CO molecular adsorption configurations, we also computed CO dissociation at different coverage. The structures of the corresponding initial states (IS), transition states (TS), and final states (FS) at the lowest coverage are shown in Figure 3. Table 1 lists the computed CO dissociation barriers and the critical C−O distances along with the available literature data for comparison.

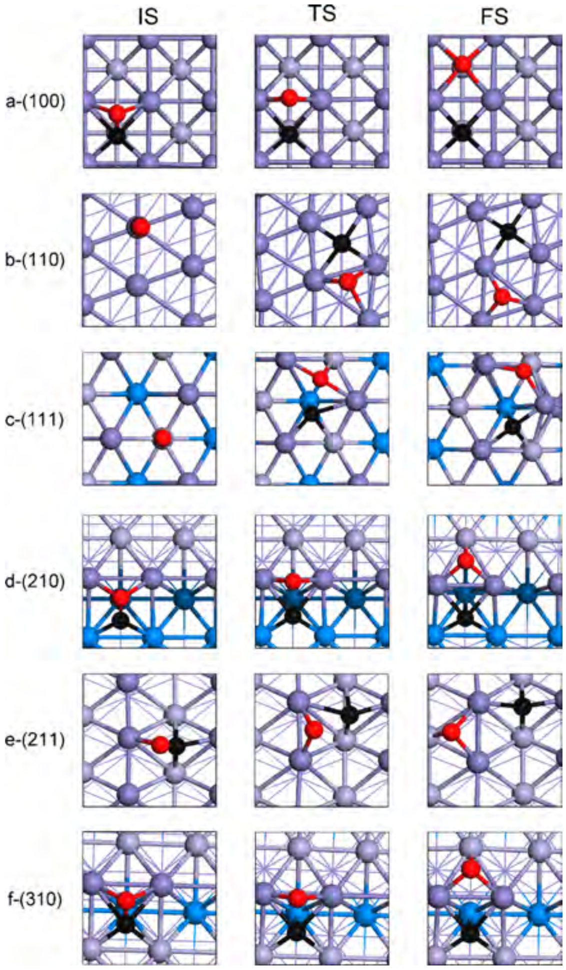

Figure 3. Initial state (IS), transition state (TS), and final state (FS) of CO dissociation from most stable adsorption sites on six iron surfaces (black ball, C; red ball, O; the other balls for Fe in different layers).

3.4.1. Lowest-Coverage CO Dissociation. As shown in Table 1, the CO dissociation barriers on the (310), (100), (211), and (210) surfaces (0.98, 1.03, 1.06, and 1.11 eV, respectively) are lower than those on the (111) and (110) surfaces (1.17 and 1.51 eV, respectively). This indicates that the CO dissociation barrier does not correlate with the surface stability (Supporting Information Table S2) because of their different initial and most stable adsorption configurations. Despite the differences in methods (PBE and PW91) and models, the computed C−O dissociation barriers on the (100) surface are very close, and the same trend is also found on the (110) surface. On the (111) surface, however, PBE gives different CO dissociation barriers because of different transition state structures, and RPBE gives a higher CO dissociation barrier than PBE by using the same transition state structure. On the (211) surface, PBE gives a higher CO dissociation barrier than PW91 because of different transition state structures, and RPBE gives a higher CO dissociation barrier than PW91 by using the same transition state structures. On the (310) surface, different methods give different transition state structures and different dissociation barriers; however, no reported data for CO dissociation on the (210) surface are available for comparison.

On the basis of the computed dissociation barriers for the most stable adsorption configurations and the computed dissociation energies for the most stable coadsorbed C and O atoms (diffusion after dissociation), we checked their Brønsted−Evans−Polanyi (BEP) relation (Figure 4). In contrast to the perfect linear BEP relation for N_2 dissociation on the same surface having the same adsorption site and the similar transition state distances over a range of pure metals with face-centered cubic crystal structures (i.e., M(211), M = Mn, Fe, Co, Ni, Cu, Mo, Ru, Rh, Pd, Ag, Ir, Pt, Au, W, and Re)[76] as well as for CO dissociation on a set of transition metals with the same or similar surface structures (i.e., Ru(0001), Rh(111), and Pd(111) as well as Os(0001), Ir(111), and Pt(111) surface),[77−79] there is no such correlation for CO dissociation on these different iron surfaces, and the correlation coefficient is miserably low ($R = 0.25$). This is due to their large geometric differences in the IS, TS, and FS, that is, the structures of the initial state (IS) and final state (FS) represent the thermodynamically most stable molecular and dissociative adsorption configurations on each surface, respectively, and their adsorption configurations differ from surface to surface as a result of their intrinsic surface structures. For example, the most stable CO adsorption configurations are located on 4-fold hollow sites on the (100), (210), (211), and (310) surfaces with the C atom in CO coordinating with many surface Fe atoms, whereas those on the (110) and (111) surfaces are located on the top sites with the C atom in CO coordinating with only one surface Fe atom. All of these differences in surface structures and CO adsorption configurations on each surface result in quite different structures of the transition and final states.

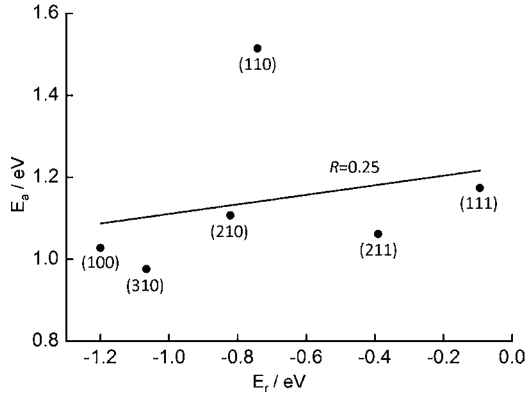

Figure 4. Correlation between CO dissociation barriers and dissociation energies.

3.4.2. High Coverage CO Dissociation. Apart from our recent study of high-coverage CO activation on the Fe(100) surface,[42] most theoretical studies of CO adsorption and dissociation on iron surfaces (Table 1) have been carried out at the lowest coverage and ideal condition. Because the available experimental adsorption or desorption energies are the average of a set of molecules in different adsorption configurations instead of a single molecule (especially at low temperature and high coverage), a direct comparison between theory and experiment is very difficult. A reasonable way to make such a direct comparison between theory and experiment in adsorption or desorption as well as dissociation properties is to include the boundary conditions, such as temperature, pressure, and coverage, in model calculation. Following the same pattern as in our previous work, we further studied CO dissociation at different coverages on another five iron surfaces and included the results on Fe(100) for comparison.

(a) Fe(100). In our previous work, we reported the CO adsorption and desorption as well as dissociation on Fe(100).[42] Our results show that only dissociative adsorption is possible for n_{CO} = 1 and 2. For n_{CO} = 3−7, the surface adsorption states have possible equilibrium between molecular and dissociative CO adsorptions. For n_{CO} = 8−11, only molecular CO adsorption can be found.

(b) Fe(110). For n_{CO} = 1 (Table 2), the computed CO dissociation barrier is lower than its desorption energy (1.51 vs 1.88 eV), and CO dissociation is exothermic by 0.46 eV, indicating that CO dissociation is favorable both kinetically and thermodynamically. The final adsorption state has only dissociative CO adsorption at this coverage.

Table 2. CO Stepwise Dissociation Barriers (E_a), Desorption Energies (ΔE_{des}), and Dissociation Energies (ΔE_{dis}) at Different Coverages on the Fe(110) Surface

nCO	pathways	E_a, eV	ΔE_{des}, eV	ΔE_{dis}, eV
1CO	1CO → 1C + 1O	1.51	1.88	−0.46
2CO	2CO → 1CO + 1C + 1O	1.48	1.86	−0.44
	1CO + 1C + 1O → 2C + 2O	1.71	1.81	+0.07
3CO	3CO → 2CO + 1C + 1O	1.57	1.82	−0.17
	2CO + 1C + 1O → 1CO + 2C + 2O	1.59	1.52	+0.24
	1CO + 2C + 2O → 3C + 3O	1.75	1.60	+1.13
4CO	4CO → 3CO + 1C + 1O	1.53	1.67	−0.24
	3CO + 1C + 1O → 2CO + 2C + 2O	2.62	1.46	+0.24
5CO	5CO → 4CO + 1C + 1O	1.70	1.56	−0.44

For n_{CO} = 2, the dissociation barrier of the first CO molecule is lower than its desorption energy (1.48 vs 1.86 eV), and CO dissociation is exothermic by 0.44 eV, indicating that first CO dissociation is favorable both kinetically and thermodynamically. For the second CO molecule, the dissociation barrier is only slightly lower than own desorption energy (1.71 vs 1.81 eV), and the dissociation becomes slightly endothermic (0.07 eV). Considering the recombinative reaction barrier of 1.64 eV, the second adsorbed CO might have equilibrium between molecular and dissociative adsorptions; therefore, the final adsorption state might have CO + C + O and 2C + 2O in equilibrium on the surface at this coverage.

For n_{CO} = 3, the dissociation barrier of the first CO molecule is lower than its desorption energy (1.57 vs 1.82 eV), and CO dissociation is exothermic by 0.17 eV; however, the dissociation barriers of the second and third CO molecules (1.59 and 1.75 eV) are higher than their corresponding desorption energies (1.52 and 1.60 eV), and the dissociation is endothermic by 0.24 and 1.13 eV, respectively. This indicates that the second and third CO molecules prefer desorption from the surface instead of dissociation on the surface. The final adsorption state has two adsorbed CO molecules as well as one C and one O atom (2CO + C + O) on the surface.

For n_{CO} = 4, the dissociation barrier of the first CO molecule is lower than its desorption energy (1.53 vs 1.67 eV), and the dissociation is exothermic by 0.24 eV. The dissociation barrier of the second CO molecule is much higher than its own desorption energy (2.62 vs 1.46 eV), and the dissociation is endothermic by 0.24 eV. This indicates that only one CO can dissociate at this coverage, and the final adsorption state has three adsorbed CO molecules as well as one C and one O atom (3CO + C + O) on the surface.

For n_{CO} = 5, the dissociation barrier of the first CO molecule is higher than its desorption energy (1.71 vs 1.56 eV). Therefore, at this coverage, the first step should be CO desorption instead of dissociation, despite the exothermic dissociation (−0.44 eV). The final adsorption state has five adsorbed CO molecules. It can be expected that at high coverage (n_{CO} = 5−8), only desorption is possible because of the very low desorption energies. The final adsorption states have only molecular CO adsorption.

(c) Fe(111). For n_{CO} = 1 (Table 3), the CO dissociation barrier is much lower than its desorption energy (1.17 vs 2.13 eV), and the dissociation process is slightly exothermic by 0.09 eV, indicating that CO dissociation is favorable kinetically but thermodynamically neutral. Considering the recombinative reaction barrier of 1.26 eV, the adsorbed CO molecule might have equilibrium between molecular and dissociative adsorptions. The final adsorption state might have equilibrium between molecular (CO) and dissociative (C + O) adsorptions.

Table 3. CO Stepwise Dissociation Barriers (E_a), Desorption Energies (ΔE_{des}), and Dissociation Energies (ΔE_{dis}) at Different Coverages on the Fe(111) Surface

*n*CO	pathways	E_a, eV	ΔE_{des}, eV	ΔE_{dis}, eV
1CO	1CO → 1C + 1O	1.17	2.13	−0.09
2CO	2CO → 1CO + 1C + 1O	1.13	2.12	−0.14
	1CO + 1C + 1O → 2C + 2O	1.14	2.16	+0.14
3CO	3CO → 2CO+1C+1O	1.27	2.12	+0.14
	2CO+1C + 1O → 1CO + 2C + 2O	1.20	2.16	+0.10
	1CO + 2C + 2O → 3C + 3O	1.02	2.06	−0.02
4CO	4CO → 3CO + 1C + 1O	1.27	2.11	+0.11
	3CO + 1C + 1O → 2CO + 2C + 2O	0.97	2.12	−0.18
	2CO + 2C + 2O → 1CO + 3C + 3O	1.97	2.13	+1.46
	1CO + 3C + 3O → 4C + 4O	2.07	1.74	+1.02
5CO	5CO → 4CO + 1C + 1O	1.23	2.12	+0.16
	4CO + 1C + 1O → 3CO + 2C + 2O	1.97	2.06	+1.18
6CO	6CO → 5CO + 1C + 1O	2.70	2.10	+1.19

For n_{CO} = 2, the dissociation barriers of both CO molecules (1.13 and 1.14 eV) are much lower than their corresponding desorption energies (2.12 and 2.16 eV), and the dissociation of the first CO molecule is exothermic by 0.14 eV, whereas that of the second CO molecule becomes endothermic by 0.14 eV. Considering their recombinative reaction barriers of 1.27 and 1.00 eV, the adsorbed CO molecules might have equilibrium between molecular and dissociative adsorption. The final adsorption state might have possible equilibrium between molecular (2CO) and dissociative (2C + 2O) adsorptions.

For n_{CO} = 3, the dissociation barriers (1.27, 1.20, and 1.02 eV) of all three CO molecules are much lower than their corresponding desorption energies (2.12, 2.16, and 2.06 eV), and the dissociation of the first two CO molecules is slightly endothermic by 0.14 and 0.10 eV, respectively, whereas that of the third CO becomes thermoneutral. Considering their recombinative reaction barriers of 1.13, 1.30, and 1.04 eV, the adsorbed CO molecules might have equilibrium between molecular (3CO) and dissociative (3C + 3O) adsorption. The final adsorption state might have possible equilibrium between molecular (3CO) and dissociative (3C + 3O) adsorptions.

For n_{CO} = 4, the dissociation barriers of the first two CO molecules (1.27 and 0.97 eV) are lower than their desorption energies (2.11 and 2.12 eV), and the dissociation of the first CO is endothermic by 0.11 eV, whereas that of the second one is exothermic by 0.18 eV. For the dissociation of the third CO molecule, this process is very endothermic (1.46 eV), although the barrier is lower than the desorption energy (1.97 vs 2.13 eV). Considering the very low recombinative reaction barriers of 0.51 eV, the third CO molecule prefers molecular instead of dissociative adsorption. The dissociation barrier of the fourth CO molecule (2.07 eV) is higher than its desorption energy (2.07 vs 1.74 eV), and the dissociation is endothermic by 1.02 eV. The fourth CO molecule prefers desorption instead of dissociation. The final adsorption state might predominately have 2CO + 2C + 2O on the surface at this coverage.

For n_{CO} = 5, the dissociation barrier of the first CO molecule is much lower than its desorption energy (1.23 vs 2.12 eV), and the dissociation process is endothermic by 0.16 eV. Considering the low recombinative reaction barriers of 1.07 eV, the first CO molecule might have an equilibrium between molecular and dissociative adsorption, although the dissociation barrier of the second CO is similar to its desorption energy (1.97 vs 2.06 eV), but this process is highly endothermic (1.18 eV), and the recombinative reaction is more favorable. Consequently, the final adsorption state might have 5CO and 4CO + C + O in equilibrium.

For n_{CO} = 6, the dissociation barrier of the first CO is 2.70 eV, which is higher than its desorption energy (2.10 eV), and this process is highly endothermic by 1.19 eV. Therefore, CO prefers desorption instead of dissociation. It is to be expected that at coverage of n_{CO} = 6−9, the final adsorption states have only molecular CO adsorption.

(d) Fe(210). For n_{CO} = 1−5 (Table 4), the computed CO dissociation barriers are much lower than their desorption energies, and the dissociation is exothermic for all adsorbed CO molecules, indicating that CO dissociation is favorable both kinetically and thermodynamically at each coverage. The final adsorption state is only dissociative (*n*C + *n*O) on the surface.

For n_{CO} = 6, the dissociation barrier of the first CO molecule is close to its desorption energy (1.58 vs 1.69 eV), and the dissociation is slightly exothermic (−0.08 eV). This indicates a possible equilibrium among molecular adsorption and desorption as well as dissociative adsorption. However, it should be noted that for the other five adsorbed CO molecules, the dissociation barriers are lower than their desorption

Table 4. CO Stepwise Dissociation Barriers (E_a), Desorption Energies (ΔE_{des}), and Dissociation Energies (ΔE_{dis}) at Different Coverages on the Fe(210) Surface

*n*CO	pathways	E_a, eV	ΔE_{des}, eV	ΔE_{dis}, eV
1CO	1CO → 1C + 1O	1.11	2.00	−0.32
2CO	2CO → 1CO + 1C + 1O	1.11	2.00	−0.21
	1CO + 1C + 1O → 2C + 2O	1.07	1.89	−0.27
3CO	3CO → 2CO + 1C + 1O	1.12	1.92	−0.22
	2CO + 1C + 1O → 1CO + 2C + 2O	1.26	1.93	−0.21
	1CO + 2C + 2O → 3C + 3O	1.11	1.87	−0.40
4CO	4CO → 3CO + 1C + 1O	1.29	1.97	−0.15
	3CO + 1C + 1O → 2CO + 2C + 2O	1.17	1.88	−0.34
	2CO + 2C + 2O → 1CO + 3C + 3O	1.28	1.88	−0.19
	1CO + 3C + 3O → 4C + 4O	1.05	1.83	−0.47
5CO	5CO → 4CO + 1C + 1O	1.26	1.69	−0.14
	4CO + 1C + 1O → 3CO + 2C + 2O	1.12	1.87	−0.36
	3CO + 2C + 2O → 2CO + 3C + 3O	1.58	1.70	−0.14
	2CO + 3C + 3O → 1CO + 4C + 4O	1.22	1.65	−0.40
	1CO + 4C + 4O → 5C + 5O	1.24	1.59	−0.10
6CO	6CO → 5CO + 1C + 1O	1.58	1.69	−0.08
	5CO + 1C + 1O → 4CO + 2C + 2O	1.28	1.63	−0.29
	4CO + 2C + 2O → 3CO + 3C + 3O	1.23	1.56	−0.15
	3CO + 3C + 3O → 2CO + 4C + 4O	1.56	1.59	−0.15
	2CO + 4C + 4O → 1CO + 5C + 5O	1.18	1.57	−0.39
	1CO + 5C + 5O → 6C + 6O	1.08	1.60	−0.20
7CO	7CO → 6CO + 1C + 1O	1.56	1.57	−0.11
	6CO + 1C + 1O → 5CO + 2C + 2O	1.25	1.59	−0.30
	5CO + 2C + 2O → 4CO + 3C + 3O	1.12	1.60	−0.07
	4CO + 3C + 3O → 3CO + 4C + 4O	1.52	1.52	−0.15
	3CO + 4C + 4O → 2CO + 5C + 5O	1.27	1.52	−0.26
	2CO + 5C + 5O → 1CO + 6C + 6O	1.39	1.39	+0.68
8CO	8CO → 7CO + 1C + 1O	1.53	1.57	−0.04
	7CO + 1C + 1O → 6CO + 2C + 2O	1.57	1.61	−0.13
	6CO + 2C + 2O → 5CO + 3C + 3O	1.30	1.59	−0.08
	5CO + 3C + 3O → 4CO + 4C + 4O	1.26	1.54	−0.16
9CO	9CO → 8CO + 1C + 1O	1.58	1.45	−0.04

energies, and the dissociation processes are exothermic. These steps are very similar to those for $n_{CO} = 5$. The final adsorption state is only dissociative (6C + 6O) on the surface.

For $n_{CO} = 7$, the dissociation barrier of the first CO molecule is close to its desorption energy (1.56 vs 1.67 eV), and the dissociation is slightly exothermic (−0.11 eV). This indicates a possible equilibrium among molecular adsorption, desorption, and dissociative adsorption. After dissociation of the first CO molecule, the second and third adsorbed CO molecules favor dissociation instead of desorption, and the dissociation is slightly exothermic. After dissociation of the first three adsorbed CO molecules, the fourth adsorbed CO molecule has a possible equilibrium among molecular adsorption, desorption, and dissociative adsorption. On the basis of the first four dissociative CO adsorptions, the fifth adsorbed CO molecule favors exothermic dissociation. For the sixth adsorbed CO molecule, the dissociation barrier is equal to its desorption energy, and the dissociation becomes highly endothermic. It is to be expected that the seventh adsorbed CO molecule will desorb instead of dissociate. The final adsorption state might have 2CO + 5C + 5O on the surface at this coverage.

For $n_{CO} = 8$, the same situation has been found as for $n_{CO} = 6$ and 7. The first CO molecule might have possible equilibrium among molecular adsorption, desorption, and dissociative adsorption on the basis of the computed dissociation barrier (1.53 eV), desorption energy (1.57 eV), and dissociation energy (−0.04 eV). After the dissociation of the first CO molecule, the subsequent three adsorbed CO molecules might have equilibrium between molecular and dissociative adsorption on the surface at this coverage. It is to be expected that the fifth adsorbed CO molecule will desorb instead of dissociate. The final adsorption state might have 4CO + 4C + 4O on the surface at this coverage.

For $n_{CO} = 9$, the dissociation barrier of the first adsorbed CO molecule is larger than its desorption energy (1.58 vs 1.45 eV), indicating the preference of desorption over dissociation. At $n_{CO} = 9–12$, only molecular adsorption is possible.

(e) Fe(211). For $n_{CO} = 1–2$ (Table 5), the computed CO dissociation barriers are much lower than their desorption energies, and the dissociation is exothermic for all adsorbed CO molecules, indicating that CO dissociation is favorable both kinetically and thermodynamically. The final adsorption state is only dissociative on the surface.

Table 5. CO Stepwise Dissociation Barriers (E_a), Desorption Energies (ΔE_{des}), and Dissociation Energies (ΔE_{dis}) at Different Coverages on the Fe(211) Surface

*n*CO	pathways	E_a, eV	ΔE_{des}, eV	ΔE_{dis}, eV
1CO	1CO → 1C + 1O	1.06	1.94	−0.20
2CO	2CO → 1CO + 1C + 1O	1.05	1.92	−0.22
	1CO + 1C + 1O → 2C + 2O	1.03	1.93	−0.14
3CO	3CO → 2CO + 1C + 1O	1.02	1.92	−0.29
	2CO + 1C + 1O → 1CO + 2C + 2O	1.30	1.94	+0.22
	1CO + 2C + 2O → 3C + 3O	1.94	1.92	+1.01
4CO	4CO → 3CO + 1C + 1O	1.29	1.92	+0.09
	3CO + 1C + 1O → 2CO + 2C + 2O	1.30	1.91	+0.73
	2CO + 2C + 2O → 1CO + 3C + 3O	1.92	1.75	+1.02
5CO	5CO → 4CO + 1C + 1O	1.44	1.62	+0.40
	4CO + 1C + 1O → 3CO + 2C + 2O	1.72	1.67	+0.61
	3CO + 2C + 2O → 2CO + 3C + 3O	1.79	1.43	+0.90
6CO	6CO → 5CO + 1C + 1O	1.10	1.37	+0.22
	5CO + 1C + 1O → 4CO + 2C + 2O	1.75	1.54	+0.92
7CO	7CO → 6CO + 1C + 1O	1.43	1.06	+0.59
8CO	8CO → 7CO + 1C + 1O	1.92	1.57	+0.65

For $n_{CO} = 3$, the dissociation barrier of the first CO molecule is lower than its own desorption energy (1.02 vs 1.92 eV), and the dissociation is exothermic (−0.29 eV). The first CO dissociation is favorable both kinetically and thermodynamically. Although the dissociation barrier of the second CO molecule is lower than its desorption energy (1.30 vs 1.94 eV), the dissociation is endothermic (0.22 eV), and the recombinative reaction becomes more favorable. For the third CO molecule, the dissociation barrier comes very close to its desorption energy (1.94 vs 1.92 eV), and the dissociation is highly endothermic (1.01 eV). Therefore, the final adsorption state might predominantly have 2CO + C + O on the surface at this coverage.

For $n_{CO} = 4$, the dissociation barrier of the first CO molecule is lower than its desorption energy (1.29 vs 1.92 eV), and the dissociation is slightly endothermic (0.09 eV). Considering the low recombinative reaction barrier of 1.20 eV, the first CO molecule might have equilibrium between molecular and dissociative adsorption. Although the dissociation barrier of the second CO molecule is lower than its desorption energy

(1.30 vs 1.91 eV), the dissociation process is strongly endothermic (0.73 eV), and the recombinative reaction becomes more favorable. For the third CO molecule, the dissociation barrier becomes higher than its desorption energy (1.92 vs 1.75 eV), and the dissociation is highly endothermic (1.02 eV). Consequently, the final adsorption state might have 4CO and 3CO + C + O in equilibrium on the surface at this coverage.

For n_{CO} = 5 and 6, although the dissociation barriers of the first CO molecules are lower than their own desorption energies, the dissociation processes are strongly endothermic, indicating that a molecular instead of dissociative adsorption is more favorable. For the second and third CO molecules, the dissociation barriers become higher than their desorption energy, and the dissociation is strongly endothermic. Therefore, the final adsorption state most likely has 5CO on the surface at this coverage. For n_{CO} = 7 and 8, the dissociation barriers of the first adsorbed CO molecule are larger than their desorption energy (1.58 vs 1.45 eV), indicating a preference for desorption over dissociation. At n_{CO} = 5−10, therefore, only molecular adsorption is possible.

(f) Fe(310). For n_{CO} = 1 (Table 6), the lower CO dissociation barrier than its own desorption energy (0.98 vs 2.13 eV) and the exothermic dissociation reaction (−0.38 eV) indicate that CO dissociation is favorable both kinetically and thermodynamically. The final adsorption state is only dissociative on the surface.

Table 6. CO Stepwise Dissociation Barriers (E_a), Desorption Energies (ΔE_{des}), and Dissociation Energies (ΔE_{dis}) at Different Coverages on the Fe(310) Surface

*n*CO	pathways	E_a, eV	ΔE_{des}, eV	ΔE_{dis}, eV
1CO	1CO → 1C + 1O	0.98	2.13	−0.38
2CO	2CO → 1CO + 1C + 1O	1.06	2.19	−0.05
	1CO + 1C + 1O → 2C + 2O	1.05	1.86	+0.05
3CO	3CO → 2CO + 1C + 1O	1.13	2.05	+0.01
	2CO + 1C + 1O → 1CO + 2C + 2O	1.22	1.73	+0.10
	1CO + 2C + 2O → 3C + 3O	0.96	1.93	−0.30
4CO	4CO → 3CO + 1C+1O	1.31	2.09	+0.08
	3CO + 1C + 1O → 2CO + 2C + 2O	1.12	2.03	−0.01
	2CO + 2C + 2O → 1CO + 3C + 3O	1.16	1.57	+0.04
	1CO + 3C + 3O → 4C + 4O	1.00	1.79	−0.08
5CO	5CO → 4CO + 1C + 1O	1.44	1.82	+0.42
	4CO + 1C + 1O → 3CO + 2C + 2O	1.22	1.76	+0.16
	3CO + 2C + 2O → 2CO + 3C + 3O	1.35	1.42	−0.02
	2CO + 3C + 3O → 1CO + 4C + 4O	1.22	1.38	+0.03
	1CO + 4C + 4O → 5C + 5O	1.03	1.28	−0.22
6CO	6CO → 5CO + 1C + 1O	1.72	1.86	+0.55
	5CO + 1C + 1O → 4CO + 2C + 2O	1.39	1.81	+0.29
	4CO + 2C + 2O → 3CO + 3C + 3O	1.23	1.35	+0.06
	3CO + 3C + 3O → 2CO + 4C + 4O	1.40	1.42	+0.14
	2CO + 4C + 4O → 1CO + 5C + 5O	1.17	1.22	−0.14
	1CO + 5C + 5O → 6C + 6O	0.91	1.32	−0.36
7CO	7CO → 6CO + 1C + 1O	1.53	0.56	−0.16

For n_{CO} = 2, the dissociation barriers of both CO molecules are lower than their desorption energies, and the dissociation processes are almost thermoneutral. Considering their low recombinative reaction barriers of 1.10 and 1.00 eV, both CO molecules might have equilibrium between molecular and dissociative CO adsorptions.

For n_{CO} = 3, the behavior of the first two CO molecules mimics those for n_{CO} = 2, and they might have equilibrium between molecular and dissociative CO adsorption; however, it should be noted that for the third adsorbed CO molecule, the dissociation barrier is lower than its own desorption energies (1.58 vs 1.69 eV), and the dissociation process becomes exothermic (−0.30 eV). The final adsorption state should be only dissociative on the surface at this coverage.

For n_{CO} = 4, the barriers for all stepwise dissociations are lower than their desorption energies, and the dissociation processes are nearly thermoneutral. Considering their recombinative barriers, the final adsorption state might have equilibrium between molecular and dissociative CO adsorptions.

For n_{CO} = 5, the barriers for all stepwise dissociation are lower than their desorption energies, and the dissociation processes are endothermic for the first two CO molecules and nearly thermoneutral for the last three CO molecules. This indicates the preferable molecular adsorption for the first two CO molecules and equilibrium between molecular and dissociative adsorption for the last three CO molecules. The final adsorption state might have equilibrium between molecular and dissociative CO adsorptions. Similar results have been found for n_{CO} = 6. However, for n_{CO} = 7, desorption is more favorable than dissociation for the first CO molecule. Therefore, for n_{CO} = 7−9, only molecular CO adsorption is possible.

3.5. CO Stable Coverage and Adsorption States with Temperature and Pressure.

On the basis of our identified molecular and dissociative CO adsorption states at different coverage, the effects of temperature and pressure on CO adsorption and activations can be estimated by applying ab initio thermodynamics. These thermodynamic data provide useful information and references for not only UHV experimental studies but also practical applications at high temperature and pressure.

On the basis of the changes in Gibbs free energies of CO adsorption at very low pressure, the changes in CO coverage on iron surfaces at different temperatures can be obtained. This is, indeed, related to the thermal CO desorption, which can be detected with TPD spectroscopy under UHV conditions. As reported in our previous work,[42] the computed molecular desorption states (α_1-α_3) and the recombinative desorption state (β) on the Fe(100) surface under the consideration of CO dissociation at low coverage agree very well with the available experimental results. Now we compare our calculated CO desorption states at the range of $p_{CO} = 10^{-9}$−10^{-14} atmosphere on the other surfaces with the available experimental data in Table 7.

On the (110) surface, there are mainly two desorption states: one molecular CO adsorption (α) at 375−450 K and one recombinative desorption state (β) of the dissociated C and O atoms at 550−675 K. Actually, Gonzalez et al.[8] observed one low-temperature molecular desorption peak at ~400−420 K and one recombinative desorption peak at about 675−800 K in the thermal desorption study of CO on the Fe(110) surface. Both theory and experiment agree very reasonably.

On the (111) surface, there are mainly two molecular desorption states at about 350−400 K (α_1) and 425−475 K (α_2) as well as one recombinative desorption state (β) at 525−575 K. Experimentally, Seip et al.[23] detected two low-temperature molecular CO desorption peaks at ~340 K (α_1) and 420 K (α_2) with the exposure temperature at 220 K on the Fe(111) surface. Bartosch et al.[24] and Whitman et al.[25] also

Table 7. CO Desorption States and Temperatures on Six Iron Surfaces

surface	state	theory	experiment
(100)	α_1	275–300 K	220–250 K[12]
	α_2	325–375 K	306–340 K[12]
	α_3	400–450 K	400–440 K[12]
	β	700–750 K	750–820 K[12]
(110)	α	375–450 K	400–420 K[8]
	β	550–675 K	675–800 K[8]
(111)	α_1	350–400 K	325–340 K[24]
	α_2	425–475 K	400–420 K[24]
	β	525–575 K	650–750 K[24]
(210)	α	325–450 K	
	β	500–600 K	
(211)	α	300–400 K	
	β	450–575 K	
(310)	α	325–475 K	
	β	525–650 K	

found two molecular CO desorption peaks at about 325 K (α_1) and 400 K (α_2) with the exposure temperatures at 83 and 100 K. In addition, they also found a recombinative desorption state (β) of the dissociated C and O atoms at about 650–750 K. All these experimental results support our theoretically computed desorption states and temperatures.

However, it should be noted that our computed temperatures of the recombinative desorption states are generally lower than the reported experimental results, and this may result from the energy barrier of the recombination of surface C and O atoms to CO, which was not included in our thermodynamics method.

On the other high miller index surfaces, we also computed both the molecular (α) and dissociative desorption states (β) as well as the temperatures. On the Fe(210) surface, there are one molecular desorption state at about 325–450 K and one recombinative desorption state at about 500–600 K. On the Fe(211) surface, one molecular desorption state at about 300–400 K and one recombinative desorption state at about 450–575 K have been computed. On the Fe(310) surface, one

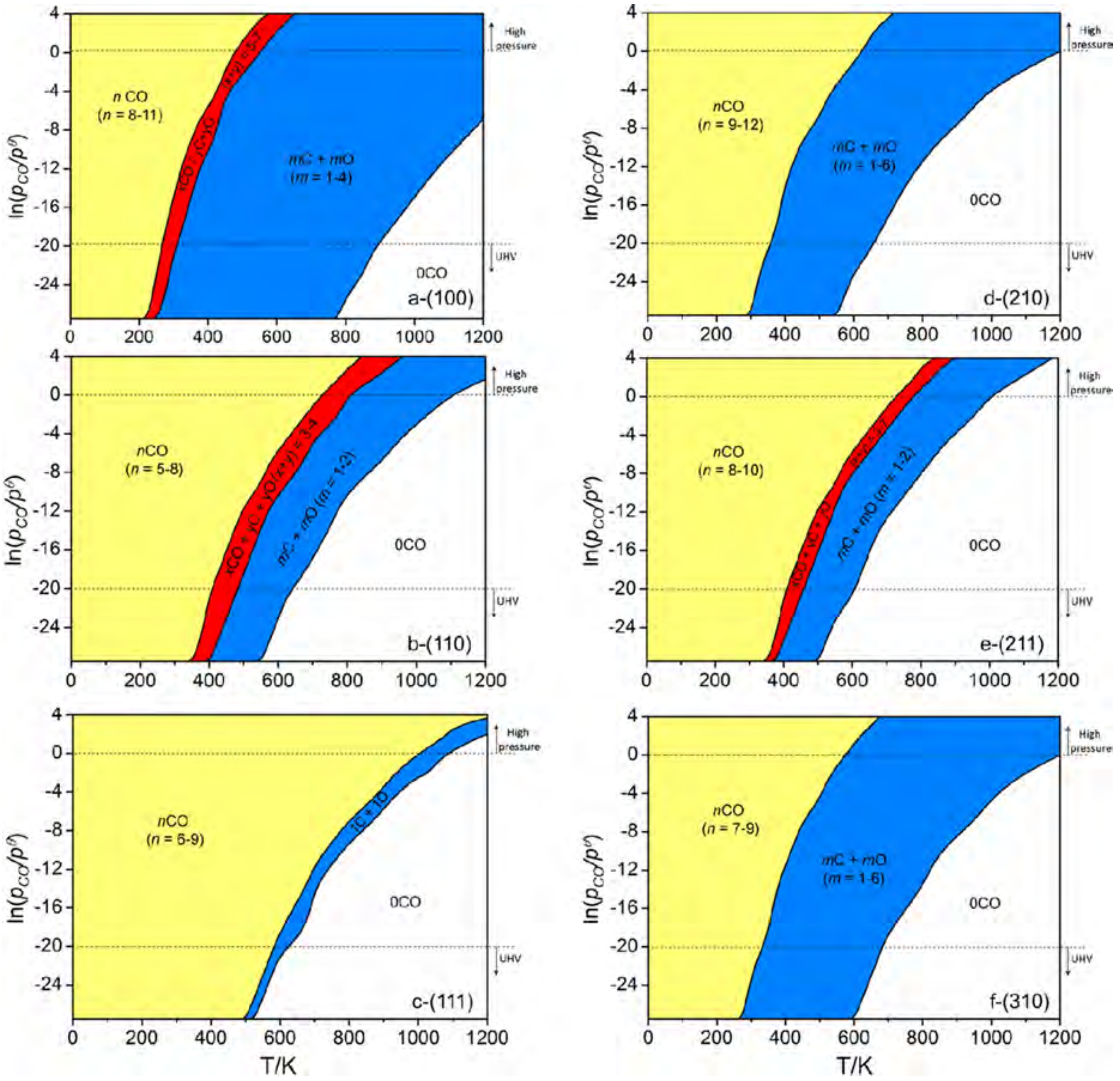

Figure 5. Phase diagram of stable CO adsorption states on six iron surfaces.

molecular desorption state at about 325–475 K and one recombinative desorption state at about 525–650 K from the adsorbed C and O atoms are found; however, there are no available UHV experimental studies of CO desorption on these surfaces. Therefore, our computed CO desorption states and temperatures on these high miller index surfaces might provide some references for further investigations using modern surface science techniques and analytical methods.

To consider the effects of temperature and pressure at the same time, we further plotted the phase diagrams (Figure 5) of stable CO adsorption states and coverage on the (100), (110), (111), (210), (211), and (310) surfaces. These phase diagrams provide useful thermodynamic information on CO adsorption states at high temperature and pressure, which is of great importance for industrial applications. Systematic comparisons show that each surface has characteristic regions at a given temperature and pressure, and this reveals their differences in CO adsorption states and coverage. On the basis of these phase diagrams, the six surfaces can be divided into two groups. The first group includes the (100), (110), and (211) surfaces that have a molecular adsorption region and a mixed molecular and dissociative adsorption region, as well as a fully dissociative region and clean surface region. The second group includes the (111), (210), and (310) surfaces, which have a molecular adsorption region, a fully dissociative region, and a clean surface region.

Actually, these thermodynamic phase diagrams provide new insights into the CO activation mechanism on iron surfaces that are quite different from previous studies at very low coverage, especially those high-temperature and -pressure regions. Taking $T = 625$ K and $p_{CO} = 40$ atm ($\ln(p_{CO}/p^{\theta}) = 3.69$) as reference, the adsorption states of CO on each surface present quite different thermodynamic characteristics; that is, only molecular CO adsorption is favorable on the (110), (111), and (211) surfaces; mixed molecular and dissociative CO adsorption are favorable on the Fe(100) surface; and only dissociative CO adsorption is favorable on the (210) and (310) surfaces.

3.6. Stretching Frequencies of Adsorbed CO Molecules.

To provide some references for additional experimental studies, we have computed all CO stretching frequencies from the lowest to the saturated coverage on all surfaces. All the individual C–O vibrational data are listed in Supporting Information (Table S3–S8); and the range for each adsorption configuration at different coverage is listed in Table 8 for comparison.

On the Fe(100) surface, HREELS studies[18] found three molecular adsorption states having very different CO stretching frequencies: 1180–1245 cm^{-1} for the α_3 state and 1900–2070 cm^{-1} for the α_1 and α_2 states. At the lowest coverage, the computed CO stretching frequency is 1172 cm^{-1} at the 4-fold hollow, 1700 cm^{-1} at the bridge, and 1900 cm^{-1} at the top sites.[42] At the saturated coverage, the calculated CO stretching frequencies show mainly three ranges; 1179–1280 cm^{-1} for the 4-fold, 1800–1850 cm^{-1} for the bridge, and 2012 cm^{-1} for the top adsorption configurations.

On the Fe(110) surface, Erley[7] reported the shift of the C–O and Fe–C stretching frequencies from 1890 to 1950 cm^{-1} and from 456 to 500 cm^{-1} with exposure up to 0.7L ($\theta_{CO} = 1/4$ ML), respectively, and from 1950 to 1985 cm^{-1} and 484 to 444 cm^{-1} with exposure in the range of 0.7–1.5 L ($\theta_{CO} = 1/2$ ML). They attributed this to the presence of the designated and displaced off-center CO adsorptions on the top site with increasing coverage. Computationally, the C–O and Fe–C stretching frequencies are 1900 and 436 cm^{-1} at $\theta_{CO} = 1/12$ ML ($n_{CO} = 1$), as well as 1888 and 1919 cm^{-1} and 436–440 cm^{-1} at $\theta_{CO} = 1/6$ ML ($n_{CO} = 2$). At $\theta_{CO} = 1/4$ ML ($n_{CO} = 3$, the same coverage as in experiment), the C–O and Fe–C stretching frequencies are 1889, 1894, and 1933 cm^{-1} and 438–447 cm^{-1}. These show reasonable agreement between theory and experiment in CO and Fe–C stretching frequencies with the exposure up to 0.7L ($\theta_{CO} = 1/4$ ML).

Table 8. C–O Vibrational Frequencies (cm^{-1}) on Six Iron Surfaces

surface	state	theory	experiment
(100)	top	2012	1900–2070[18]
	bridge	1800–1850	
	4F	1179–1280	1180–1245[18]
(110)	top	1850–1956	1890–1985[7]
(111)	top	1907–1980	1945–2015[24]
	sh	1739–1856	1735–1860[24]
	dh	1482–1569	1325–1530[24]
(210)	top	1841–1918	
	4F	1115–1313	
(211)	top	1905–2011	
	bridge	1602–1881	
	4F	1192–1526	
(310)	top	1845–1920	
	4F	1104–1330	

At coverages higher than 1/4 ML, however, the computed stretching frequencies of the adsorbed CO molecules disagree with the experimental results. For $n_{CO} = 4$ (1/3 ML), for example, the most stable adsorption configurations are located on the long bridge sites with stretching frequencies in the range of 1688–1733 cm^{-1}. For $n_{CO} = 5$ and 6, the adsorbed CO molecules on the long bridge and 3-fold have stretching frequencies in the range of 1696–1789 cm^{-1}. For $n_{CO} = 7$ and 8, short bridge, long bridge, and 3-fold adsorption configurations are possible, and the CO stretching frequencies are 1723–1800 cm^{-1} for the long bridge and 3-fold adsorption configurations and 1820–1931 cm^{-1} for the short bridge adsorption configurations. It shows clearly that all of our computed CO stretching frequencies have much lower wave numbers than the reported range of 1950–1985 cm^{-1}.

Because CO stretching frequencies are directly associated with the C–O distances at the adsorbed equilibrium states, the shift of the CO frequencies to higher wave numbers upon an increase in the coverage should come from the weakening of the Fe–CO interaction and, therefore, the shortening of the CO distance. For one CO adsorption on Fe(110), for example, the computed CO stretching frequency is 1900 cm^{-1} at the top, 1733 cm^{-1} at the short bridge, 1659 cm^{-1} at the long bridge, and 1659 cm^{-1} at the 3-fold sites.

To understand this discrepancy at coverage higher than 1/4 ML, we computed the thermodynamically less stable adsorption configurations at the top site (Supporting Information, Figure S2). For $n_{CO} = 4$–6, the top adsorption configurations are less stable than their most stable adsorption configurations by 0.22, 0.25, and 0.30 eV, respectively. The computed CO stretching frequencies of these less stable top states are 1877–1947 cm^{-1} for $n_{CO} = 4$, 1875–1956 cm^{-1} for $n_{CO} = 5$, and 1847–1954 cm^{-1} for $n_{CO} = 6$. This agrees with the experimentally observed shift of the CO frequencies to higher wave numbers upon coverage increase. In particular, the CO frequencies for $n_{CO} = 5$ are in the range of the experimentally detected 1890–1985 cm^{-1}.[7] In addition, the shift in the Fe–C frequencies from 442 to 401 cm^{-1} shows the same trend as also observed experimentally. It is also noted that for n_{CO} = 7–8, it is not possible to find such less-stable top adsorption configurations, as found for n_{CO} = 4–6. Similar discrepancies were also found by Stibor et al.[33] and Jiang et al.[34] They attributed the site preferences at different coverages to the choice of DFT methods.

On the basis of the computed CO stretching frequencies and energy differences, it is reasonable to conclude that the observed shift of the CO stretching frequencies might come from the shift of the equilibrium from the most stable adsorption configurations to the less stable top adsorption states at elevated temperature.

Early TPD studies of CO adsorption on the Fe(111) surface found three low-temperature molecular desorption states (α_0, α_1, and α_2). As discussed, we also found three CO molecular adsorption configurations coexisting on the Fe(111) surface, and they may correspond to the experimentally detected low-temperature desorption states. At the lowest coverage, the computed CO stretching frequency is 1906 cm^{-1} at the top, 1793 cm^{-1} at the shallow hollow, 1547 cm^{-1} at the deep hollow, and 1453 cm^{-1} at the 4-fold sites. At saturated coverage, the computed CO stretching frequencies are in the range of 1907–1980 cm^{-1} for the top; 1739–1856 cm^{-1} for shallow hollow; and 1482–1569 cm^{-1} for the 4-fold hollow adsorption configurations. Experimentally,[23−25] the three nondissociative CO adsorption configurations have C–O stretching frequencies of 1945–2015 (top), 1735–1860 (shallow hollow), and 1325–1530 cm^{-1} (deep hollow), respectively. However, we could not find the reported 1325 cm^{-1} frequency from the lowest to the saturated coverage.

On the Fe(210) surface (Supporting Information Figure S4) at the lowest coverage, the computed CO stretching frequencies are 1793 and 1865 cm^{-1} at the two top sites; 1739, 1644, and 1641 cm^{-1} at the three 3-fold sites; and 1115 cm^{-1} at the 4-fold hollow site. At the saturated coverage (n_{CO} = 12), top and 4-fold hollow adsorption configurations coexist, and the computed C–O stretching frequencies are in the range of 1841–1918 cm^{-1} for the top and 1115–1313 cm^{-1} for the 4-fold hollow adsorption configurations.

On the Fe(211) surface (Supporting Information Figure S5) at the lowest coverage, the computed CO stretching frequencies are 1701 and 1870 cm^{-1} at the two top sites, 1807 cm^{-1} at the bridge site, and 1274 cm^{-1} at the 4-fold hollow site. At saturated coverage (n_{CO} = 10), the coexistence of top, bridge, and 4-fold adsorption configurations becomes possible, and the C–O computed stretching frequencies are in the ranges of 1905–2011 cm^{-1} for the top, 1602–1881 cm^{-1} for the bridge, and 1192–1526 cm^{-1} for the 4-fold adsorption configurations.

On the Fe(310) surface (Supporting Information Figure S6) at lowest coverage, the computed CO stretching frequencies are 1772 and 1834 cm^{-1} at the two top sites, 1625 cm^{-1} at the 3-fold hollow site, and 1104 cm^{-1} at the 4-fold hollow site. At saturated coverage (n_{CO} = 9), both bridge and 4-fold hollow adsorption configurations are possible, and the C–O stretching frequencies are in the ranges of 1845–1920 cm^{-1} for the top and 1104–1330 cm^{-1} for the 4-fold adsorption configurations. However, there are no available experimental CO stretching frequencies on these three high-index surfaces for direct comparison with our calculated data.

■ CONCLUSION

Spin-polarized density functional theory computations have been carried out to study the adsorption, dissociation, and desorption of CO on the iron (100), (110), (111), (210), (211), and (310) surfaces at different coverages. The most stable adsorption configurations and the stepwise dissociation of the adsorbed CO molecules at different coverage have been computed. These detailed studies into the CO activation mechanisms provide some references about the initial stages of iron-based Fischer–Tropsch synthesis, in which CO adsorption and dissociation as well as surface carburization play the essential roles in the structures, stability, and activity of the catalysts. The computed CO desorption energies and dissociation barriers at different coverages and temperatures can be used for kinetic modeling, which is of practical importance.

At the lowest coverage (one CO adsorption), there are no direct correlations of the surface stabilities (surface energies) to the adsorption strengths (adsorption energies and CO stretching frequencies) as well as to the dissociation barriers and dissociation energies. This is because of their different adsorption sites and configurations. The most stable adsorption configurations and sites are coverage-dependent, and the coexistence of diverse adsorption configurations at different sites is possible at high coverage.

On the basis of the computed stepwise CO adsorption energies and dissociation barriers, equilibriums between molecular and dissociative adsorptions at high coverage have been found. On the Fe(100) surface, only dissociative adsorption is possible for n_{CO} = 1 and 2, whereas possible equilibrium between molecular and dissociative CO adsorptions are found for n_{CO} = 3–7. For n_{CO} = 8–11, only molecular CO adsorption can be found. On the Fe(110) surface, only dissociative CO adsorption is found for n_{CO} = 1, whereas equilibrium between CO + C + O and 2C + 2O is possible for n_{CO} = 2. For n_{CO} = 3 and 4, the surface adsorption states have mixed molecular and dissociative CO adsorptions coexisting; however, only molecular CO adsorption is found for n_{CO} = 5–8. On the Fe(111) surface, only dissociative CO adsorption is found for n_{CO} = 1; possible equilibrium between molecular (nCO) and dissociative (nC + nO) adsorptions is found for n_{CO} = 2, 3, and 5. For n_{CO} = 4, mixed molecular and dissociative CO coadsorption is possible. In contrast, only molecular CO adsorption is found for n_{CO} = 6–9.

On the Fe(210), only dissociative CO adsorption is favorable for n_{CO} = 1–6, whereas only molecular CO adsorption is possible for n_{CO} = 9–12. For n_{CO} = 7 and 8, the molecularly and dissociatively adsorbed CO molecules can coexist, and they might form equilibrium. On the Fe(211) surface, only dissociative CO adsorption is favorable for n_{CO} = 1–2, and only molecular CO adsorption is possible for n_{CO} = 5–10. In addition, the molecularly and dissociatively adsorbed CO molecules can coexist (n_{CO} = 3), and they might form an equilibrium (n_{CO} = 4) on the surface. On the Fe(310) surface, only dissociative adsorption is possible for n_{CO} = 1 and 3, whereas molecular and dissociative CO adsorptions are possible for n_{CO} = 2, 4, 5, and 6. For n_{CO} = 7–9, only molecular CO adsorption is preferred.

Along with the computed most stable molecular CO adsorption configurations at different coverages on the (100), (110), and (111) surfaces, the respective C–O and Fe–C stretching frequencies are in excellent agreement with the available experimental data from high-resolution electron energy loss spectroscopy studies. Particularly, our computations clearly reveal that the experimentally observed shifts of the C−O and Fe−C stretching frequencies on the (110) surface up to the change of coverage come from the change in the equilibrium from the most stable adsorption configurations to the less stable top adsorption states at elevated temperature. The computed desorption states and temperatures on the (100), (110), and (111) surfaces are in perfect agreement with the available experimental data from temperature-programmed surface reaction studies. The computed CO adsorption and dissociation as well as desorption properties on the (210), (211), and (310) surfaces at different coverages invite modern experimental investigations. Our studies will provide useful references for the studies of CO related reaction mechanisms.

The interplay in CO activation mechanisms between theory and experiment on these iron surfaces reveals the intrinsic relationship of surface structures and catalyst activities in general and might contribute to a more rational catalyst development in the future.

■ ASSOCIATED CONTENT

Ⓢ Supporting Information

Details of the ab initio thermodynamics method; effects of zero-point energies (Table S1); available reported surface energies of iron surfaces (Table S2); vibrational frequencies of adsorbed CO at different coverages on six surfaces (Tables S3−S8); structures of those less stable one-CO adsorption configurations on five iron surfaces (Figure S1); structures and stepwise adsorption energies of CO on the five iron surfaces at different coverages (Figures S2−S6); structures for the dissociation of *n*CO on the five iron surfaces (Figures S7−S11); the most favored potential energy surface for CO dissociation at all coverage on five iron surfaces (Figures S12−16). This material is available free of charge via the Internet at http://pubs.acs.org.

■ AUTHOR INFORMATION

Corresponding Author

*E-mail: haijun.jiao@catalysis.de.

Notes

The authors declare no competing financial interest.

■ ACKNOWLEDGMENTS

This work was supported by the National Basic Research Program of China (No. 2011CB201406), the National Natural Science Foundation of China (No. 21073218), the Chinese Academy of Sciences, and Synfuels CHINA Co., Ltd. We also acknowledge general financial support from the BMBF and the state of Mecklenburg-Vorpommern.

■ REFERENCES

(1) Anderson, R. B. *The Fischer-Troposch Synthesis*; Academic Press: Orlando, FL, 1984; p 3.

(2) Kelly, R. D.; Goodman, D. W. In *The Chemical Physics of Solid Surfaces and Heterogeneous Catalysis*; King, D. A., Woodruff, D. P., Eds.; Vol. 4, Elsevier: Amsterdam, 1982; p 427.

(3) Fischer, F.; Tropsch, H. *Brennstoff Chem.* **1926**, *7*, 97−116.

(4) Brady, R. C., III; Pettit, R. *J. Am. Chem. Soc.* **1980**, *102*, 6181−6184.

(5) Yoshida, K.; Somorjai, G. A. *Surf. Sci.* **1978**, *75*, 46−60.

(6) Broden, G.; Gafner, G.; Bonzel, H. P. *Appl. Phys.* **1977**, *13*, 333−342.

(7) Erley, W. *J. Vac. Sci. Technol.* **1981**, *18*, 472−475.

(8) Gonzalez, L.; Miranda, R.; Ferrer, S. *Surf. Sci.* **1982**, *119*, 61−70.

(9) Wedler, G.; Ruhmann, H. *Surf. Sci.* **1982**, *121*, 464−486.

(10) Wedler, G.; Ruhmann, H. *Appl. Surf. Sci.* **1983**, *14*, 137−148.

(11) Benziger, J.; Madix, R. J. *Surf. Sci.* **1980**, *94*, 119−153.

(12) Moon, D. W.; Dwyer, D. J.; Bernasek, S. L. *Surf. Sci.* **1985**, *163*, 215−229.

(13) Cameron, S.; Dwyer, D. J. *Langmuir* **1988**, *4*, 282−288.

(14) Saiki, R. S.; Herman, G. S.; Yamada, M.; Osterwalder, J.; Fadley, C. S. *Phys. Rev. Lett.* **1989**, *63*, 283−286.

(15) Moon, D. W.; Cameron, S.; Zaera, F.; Eberhardt, W.; Carr, R.; Bernasek, S. L.; Gland, J. L.; Dwyer, D. J. *Surf. Sci. Lett.* **1987**, *180*, L123−L128.

(16) Moon, D. W.; Bernasek, S. L.; Lu, J. P.; Gland, J. L.; Dwyer, D. J. *Surf. Sci.* **1987**, *184*, 90−108.

(17) Dwyer, D. J.; Rausenberger, B.; Cameron, S. D.; Lu, J. P.; Bernasek, S. L.; Fischer, D. A.; Parker, D. H.; Gland, J. L. *Surf. Sci.* **1989**, *224*, 375−385.

(18) Moon, D. W.; Bernasek, S. L.; Dwyer, D. J.; Gland, J. L. *J. Am. Chem. Soc.* **1985**, *107*, 4363−4364.

(19) Benndorf, C.; Krüger, B.; Thieme, F. *Surf. Sci. Lett.* **1985**, *163*, L675−L680.

(20) Lu, J. P.; Albert, M. R.; Bernasek, S. L. *Surf. Sci.* **1989**, *217*, 55−64.

(21) Gladh, J.; Öberg, H.; Li, J. B.; Ljungberg, M. P.; Matsuda, A.; Ogasawara, H.; Nilsson, A.; Pettersson, L. G. M.; Öström, H. *J. Chem. Phys.* **2012**, *136*, 034702−9.

(22) Rochana, P.; Wilcox, J. *Surf. Sci.* **2011**, *605*, 681−688.

(23) Seip, U.; Tsai, M. C.; Christmann, K.; Kuppers, J.; Ertl, G. *Surf. Sci.* **1984**, *139*, 29−42.

(24) Bartosch, C. E.; Whitman, L. J.; Ho, W. *J. Chem. Phys.* **1986**, *85*, 1052−1060.

(25) Whitman, L. J.; Richter, L. J.; Gurney, B. A.; Villarrubia, J. S.; Ho, W. *J. Chem. Phys.* **1989**, *90*, 2050−2062.

(26) Mehandru, S. P.; Anderson, A. B. *Surf. Sci.* **1988**, *201*, 345−360.

(27) Blyholder, G.; Lawless, M. *Surf. Sci.* **1993**, *290*, 155−162.

(28) Meehan, T. E.; Head, J. D. *Surf. Sci.* **1991**, *243*, L55−L62.

(29) Nayak, S. K.; Nooijen, M.; Bernasek, S. L.; Blaha, P. *J. Phys. Chem. B* **2001**, *105*, 164−172.

(30) Sorescu, D. C.; Thompson, D. L.; Hurley, M. M.; Chabalowski, C. F. *Phys. Rev. B* **2002**, *66*, 035416.

(31) Bromfield, T. C.; Ferre, D. C.; Niemantsverdriet, J. W. *ChemPhysChem* **2005**, *6*, 254−260.

(32) Elahifard, M. R.; Jigato, M. P.; Niemantsverdriet, J. W. *ChemPhysChem* **2012**, *13*, 89−91.

(33) Stibor, A.; Kresse, G.; Eichler, A.; Hafner, J. *Surf. Sci.* **2002**, *507−510*, 99−102.

(34) Jiang, D. E.; Carter, E. A. *Surf. Sci.* **2004**, *570*, 167−177.

(35) Sun, X.; Forster, S.; Li, Q. X.; Kurahashi, M.; Suzuki, T.; Zhang, J. W.; Yamauchi, Y.; Baum, G.; Steidl, H. *Phys. Rev. B* **2007**, *75*, 035419.

(36) Chen, Y. H.; Cao, D. B.; Jun, Y.; Li, Y. W.; Wang, J.; Jiao, H. J. *Chem. Phys. Lett.* **2004**, *400*, 35−41.

(37) Huo, C. F.; Ren, J.; Li, Y. W.; Wang, J.; Jiao, H. J. *J. Catal.* **2007**, *249*, 174−184.

(38) Li, H. J.; Chang, C. C.; Ho, J. J. *J. Phys. Chem. C* **2011**, *115*, 11045−11055.

(39) Borthwick, D.; Fiorin, V.; Jenkins, S. J.; King, D. A. *Surf. Sci.* **2008**, *602*, 2325−2332.

(40) Lo, J. M.; Ziegler, T. *J. Phys. Chem. C* **2008**, *12*, 3692−3700.

(41) Sorescu, D. C. *J. Phys. Chem. C* **2008**, *112*, 10472−10489.

(42) Wang, T.; Tian, X.; Li, Y. W.; Wang, J.; Beller, M.; Jiao, H. *J. Phys. Chem. C* **2014**, *118*, 1095−1101.

(43) Mims, C. A.; McCandlish, L. E. *J. Phys. Chem.* **1987**, *91*, 929−937.

(44) Ojedaa, M.; Nabarb, R.; Nilekarb, A. U.; Ishikawaa, A.; Mavrikakisb, M.; Iglesia, E. *J. Catal.* **2010**, *272*, 287−297.

(45) Loveless, B. T.; Buda, C.; Neurock, M.; Iglesia, E. *J. Am. Chem. Soc.* **2013**, *135*, 6107−6121.

(46) Kresse, G.; Furthmüller, J. *Comput. Mater. Sci.* **1996**, *6*, 15−50.
(47) Kresse, G.; Furthmüller, J. *Phys. Rev. B* **1996**, *54*, 11169−11186.
(48) Blochl, P. E. *Phys. Rev. B* **1994**, *50*, 17953−17979.
(49) Kresse, G. *Phys. Rev. B* **1999**, *59*, 1758−1775.
(50) Perdew, J. P.; Burke, K.; Ernzerhof, M. *Phys. Rev. Lett.* **1996**, *77*, 3865−3868.
(51) Kresse, G.; Hafner, J. *Surf. Sci.* **2000**, *459*, 287−302.
(52) Methfessel, M.; Paxton, A. T. *Phys. Rev. B* **1989**, *40*, 3616−3621.
(53) Digne, M.; Sautet, P.; Raybaud, P.; Euzen, P.; Toulhoat, H. *J. Catal.* **2004**, *226*, 54−68.
(54) Henkelman, G.; Jónsson, H. *J. Chem. Phys.* **2000**, *113*, 9978−9985.
(55) Jiang, D. E.; Carter, E. A. *Phys. Rev. B* **2003**, *67*, 214103−214113.
(56) Sorescu, D. C. *Phys. Rev. B* **2006**, *73*, 155420−155436.
(57) Kittel, C. *Introduction to Solid State Physics*; Wiley: New York, 1996.
(58) Vitos, L.; Ruban, A. V.; Skriver, H. L.; Kollar, J. *Surf. Sci.* **1998**, *411*, 186−202.
(59) Spencer, M. J. S.; Hung, A.; Snook, I. K.; Yarovsky, I. *Surf. Sci.* **2002**, *513*, 389−398.
(60) Blonski, P.; Kiejna, A. *Vacuum* **2004**, *74*, 179−183.
(61) Blonski, P.; Kiejna, A. *Surf. Sci.* **2007**, *601*, 123−133.
(62) Huo, C. F.; Wu, B. S.; Gao, P.; Yang, Y.; Li, Y. W.; Jiao, H. *Angew. Chem. Int. Ed.* **2011**, *50*, 7403−7406.
(63) Wang, T.; Wang, S. G.; Luo, Q. Q.; Li, Y. W.; Wang, J.; Beller, M.; Jiao, H. *J. Phys. Chem. C* **2014**, *118*, 4181−4188.
(64) Reuter, K.; Scheffler, M. *Phys. Rev. B* **2001**, *65*, 035406.
(65) Reuter, K.; Scheffler, M. *Phys. Rev. B* **2003**, *68*, 045407.
(66) Li, W.-X.; Stampfl, C.; Scheffler, M. *Phys. Rev. .B* **2003**, *68*, 165412.
(67) Rogal, J.; Reuter, K.; Scheffler, M. *Phys. Rev. .B* **2004**, *69*, 075421.
(68) Grillo, M. E.; Ranke, W.; Finnis, M. W. *Phys. Rev. .B* **2008**, *77*, 075407.
(69) Aray, Y.; Vidal, A. B.; Rodriguez, J.; Grillo, M. E.; Vega, D.; Coll, D. S. *J. Phys. Chem. C* **2009**, *113*, 19545−19557.
(70) Zasada, F.; Piskorz, W.; Cristol, S.; Paul, J. F.; Kotarba, A.; Sojka, Z. *J. Phys. Chem. C* **2010**, *114*, 22245−22253.
(71) Wang, T.; Liu, X. W.; Wang, S. G.; Huo, C. F.; Li, Y. W.; Wang, J.; Jiao, H. *J. Phys. Chem. C* **2011**, *115*, 22360−22368.
(72) Wang, T.; Wang, S. G.; Li, Y. W.; Wang, J.; Jiao, H. J. *J. Phys. Chem. C* **2012**, *116*, 6340−6348.
(73) Wang, T.; Li, Y. W.; Wang, J.; Beller, M.; Jiao, H. *J. Phys. Chem. C* **2014**, *118*, 3162−3171.
(74) Luo, Q.; Beller, M.; Jiao, H. *J. Theor. Comput. Chem.* **2013**, *12*, 1330001−28.
(75) Cao, D.-B.; Li, Y.-W.; Wang, J.; Jiao, H. *J. Phys. Chem. C* **2008**, *112*, 14884−14890.
(76) Munter, T. R.; Bligaard, T.; Christensen, C. H.; Nørskov, J. K. *Phys. Chem. Chem. Phys.* **2008**, *10*, 5202−5206.
(77) Liu, Z. P.; Hu, P. *J. Chem. Phys.* **2001**, *123*, 8244−8247.
(78) Liu, Z. P.; Hu, P. *J. Am. Chem. Soc.* **2001**, *123*, 12596−12604.
(79) Michaelides, A.; Liu, Z. P.; Zhang, C. J.; Alavi, A.; King, D. A.; Hu, P. *J. Am. Chem. Soc.* **2003**, *125*, 3704−3705.

3.3 Hydrogen Adsorption Structures and Energetics on Iron Surfaces at High Coverage

Tao Wang, Shengguang Wang, Qiquan Luo, Yong-Wang Li, Jianguo Wang, Matthias Beller, Haijun Jiao*

Journal of Physical Chemistry C **2014**, *118*, 4181-4188.

Summary: Hydrogen adsorption structures and energetics on the (100), (110), (111), (210), (211), (310) and (321) iron surfaces up to saturation have been computed using spin-polarized density functional theory and ab initio thermodynamics. The computed hydrogen desorption temperatures and energies on the (100), (110), (111) and (211) surfaces as well as the Fe-H binding energies on the (110) and (111) surfaces agree well with the available experimental data. At typical hydrogen reduction temperature (675 K), the mainly exposed (110) and (310) facets represent the active surfaces, as supported by the transmission electron microscopy study. Our results offer an example in investigating and understanding surface structures and active facets of heterogeneous catalysts under experimental conditions.

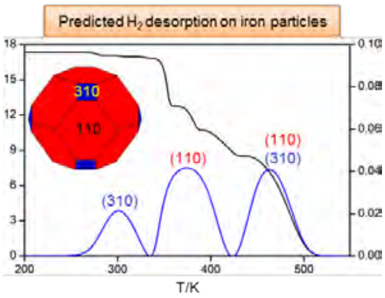

Contributions

In this paper, I planned, performed and analyzed most calculations for this manuscript. I have done the major part of writing of the manuscript. My contribution as co-author of this paper is approximately 80%.

THE JOURNAL OF PHYSICAL CHEMISTRY C
Article
pubs.acs.org/JPCC

Hydrogen Adsorption Structures and Energetics on Iron Surfaces at High Coverage

Tao Wang,[†] Shengguang Wang,[‡] Qiquan Luo,[†] Yong-Wang Li,[‡] Jianguo Wang,[‡] Matthias Beller,[†] and Haijun Jiao*,[†,‡]

[†]Leibniz-Institut für Katalyse e.V. an der Universität Rostock, Albert-Einstein Straße 29a, 18059 Rostock, Germany

[‡]State Key Laboratory of Coal Conversion, Institute of Coal Chemistry, Chinese Academy of Sciences, Taiyuan, Shanxi 030001, China

S *Supporting Information*

ABSTRACT: Hydrogen adsorption structures and energetics on the (100), (110), (111), (210), (211), (310), and (321) iron surfaces up to saturation have been computed using spin-polarized density functional theory and ab initio thermodynamics. The computed hydrogen desorption temperatures and energies on the (100), (110), (111), and (211) surfaces as well as the Fe−H binding energies on the (110) and (111) surfaces agree well with the available experimental data. At typical hydrogen reduction temperature (675 K), the mainly exposed (110) and (310) facets represent the active surfaces, as supported by the transmission electron microscopy study. Our results offer an example of investigating and understanding surface structures and active facets of heterogeneous catalysts under experimental conditions.

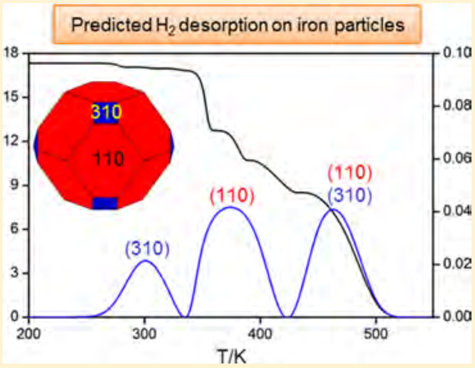

1. INTRODUCTION

Catalysis is a key enabling technology for chemistry, and the world market for catalysts is expected to reach \$19.5 billion in 2016.[1] Nowadays, especially heterogeneous catalysts provide the basis for economically and ecologically improved processes for value-added fine and bulk chemicals as well as life science products.[2] In heterogeneous catalysis, the surface active sites are responsible for the specific activity. However, the absence of precise tools for direct characterization and identification of surface active sites has hindered the rational development of heterogeneous catalysts.[3,4] Despite the past significant improvements,[5−7] the available experimental characterization techniques, e.g., X-ray diffraction (XRD), extended X-ray absorption fine structure (EXAFS), X-ray absorption near edge structure (XANES), low-energy electron diffraction (LEED), ultraviolet photoelectron spectroscopy (UPS), transmission electron microscopy (TEM), scanning transmission electron microscopy (STEM), high-resolution transmission electron microscopy (HRTEM), and scanning tunneling microscopy (STM), cannot yet give the full structural information of real catalysts under working conditions. Hence, identification of individual facets of polycrystalline (or amorphous) materials and rationalization of different catalytic properties of catalysts prepared from the same starting materials but by different methods are not easily possible by using experimental approaches. In investigations of catalytic surface adsorption phenomena and activities, temperature-programmed techniques (TPX) provide useful information about solid surfaces,[8] adsorption properties of gas species, and thermal stability of adsorption states, but TPX can give only indirect information and cannot identify and differentiate individual active sites.

Iron-based heterogeneous catalysts are widely applied in industry. For example, ammonia[9] and Fischer−Tropsch syntheses[10,11] are two of the most important large-scale industrial processes, where hydrogen is used as the principal reactant. Hence, investigating hydrogen adsorption on the surface of iron particles provides an ideal example for understanding structure and reactivity relationships in heterogeneous catalysis. Despite the significant industrial importance of hydrogen interaction with iron surfaces, few systematic experimental and theoretical studies about this system have been reported. Experimentally, Bozso et al.[12] studied hydrogen chemisorption on iron (100), (110), and (111) surfaces by applying LEED, thermal desorption spectroscopy (TDS), UPS, and work-function measurement under UHV conditions and provided the adsorption as well as desorption properties of hydrogen on these surfaces. Equilibration and exchange reaction between H_2 and D_2 on polycrystalline films as well as on the iron (100), (110), and (111) surfaces[13] indicate that hydrogen adsorbs dissociatively. Dissociative hydrogen adsorption was also found by Yoshida et al.[14] in their studies about the chemisorption of CO, CO_2, C, C_2H_4, H_2, and NH_3 on clean iron (100) and (111) surfaces. The ordered overlayer structures were found by Imbihl et al.[15] in their LEED studies about the

Received: October 28, 2013
Revised: February 5, 2014
Published: February 5, 2014

© 2014 American Chemical Society

interaction of hydrogen with the Fe(110) surface. Nichtl-Pecher et al.[16] reported a LEED study of hydrogen adsorption on the Fe(110) surface and found a new 2 × 2-2H superstructure which reversibly transforms to the $c(2 \times 2)$ phase at about 80 K. Schmiedl et al.[17] reported a LEED and TDS study of the interaction of hydrogen with the Fe(211) surface and found the metastable commensurate phase at temperatures less than 200 K and the reconstructed phases at temperatures greater than 200 K. Schmiedl et al.[18] further studied the structural, thermodynamic, and kinetic properties of hydrogen on the Fe(211) surface by using LEED, TDS, and work-function measurement and found that the activation barrier for the transition from the commensurate phase to reconstructed phase is 0.34 ± 0.04 eV and hydrogen desorption energy is 1.05 ± 0.02 eV. High-resolution electron energy loss spectroscopy (HREELS) measurements[19] reveal that hydrogen prefers the 4-fold hollow site on the Fe(100) surface. Suo et al.[20] reported two peaks of hydrogen desorption at about 350 and 425 K on the supported iron catalyst in their studies about the chemical and structural effects of silica in iron-based Fischer−Tropsch synthesis catalysts.

Compared with extensive experimental studies about the interaction of hydrogen with iron, few theoretical calculations are known. Early Hartree−Fock calculations using cluster models by Walch[21] reveal that H prefers the 4-fold hollow site on the Fe(100) surface. Sorescu[22] systematically studied the adsorption and diffusion of hydrogen on the Fe(100) surface by using DFT calculations and found that the site preference depends on hydrogen coverage and that H diffusion from surface to subsurface is more difficult than on the surface. van Steen[23] reported a DFT study about H_2 dissociation on CO and C precovered Fe(100) surface and hydrogen dissociation is found to be blocked by CO and C adsorption. Jiang et al.[24] present a DFT study about the interaction of hydrogen with the Fe(110) surface as a function of coverage and found H to prefer the 3-fold site. Jiang et al.[25] also reported a periodic spin-polarized DFT calculation of hydrogen adsorption, absorption, and dissolution as well as diffusion on and in bcc iron and found that H prefers to stay on the Fe surface instead of subsurfaces or in bulk. Huo et al.[26] performed a spin-polarized DFT calculation to characterize the adsorption and diffusion of hydrogen on the Fe(111) surface and found the top-shallow bridge site to be most favored. Fabiani[27] studied the adsorption properties of hydrogen on the Fe(310) surface by using DFT calculations and compared those on the Fe(100) surface. It revealed that the site preference of hydrogen is different on these two surfaces despite their similar structures. Faglioni et al.[28] reported a systematic DFT study about the coverage-dependent hydrogen adsorption on the closest packed surface of all nine group VIII transition metals (including Fe(110) and Fe(111)), leading to results consistent with the available surface science studies. On the basis of these results, they also developed a simple thermodynamic model useful in estimating the surface coverage under typical heterogeneous catalysis conditions.

For several decades a major goal in catalysis research has been the rational development of state of the art materials. To achieve this goal, not only specific experimental characterization tools but also high-level DFT computations might play a complementary and decisive role.[29] Commonly, DFT computations describe the structures and properties of materials at atomic scales. Ideally, interplay of informative experimental techniques and accurate DFT computations can synergistically provide insights into surface structures of catalysts and rationalize the catalytic activities and in turn facilitate the rational design of novel selective catalysts.[30] On the basis of experimental studies of hydrogen adsorption on several iron single crystal surfaces, we carried out systematic DFT computations on the surface morphology of Fe particles and hydrogen adsorption properties on seven iron surfaces from ab initio thermodynamics.[31,32] Our goal is to characterize and identify the possible active facets of Fe particles from the computed hydrogen adsorption properties on single-crystal surfaces in combination with the experimental temperature-programmed desorption (TPD) data.

2. COMPUTATIONAL DETAILS

2.1. Method and Models. All spin-polarized periodic DFT calculations were carried out using the Perdew−Burke−Ernzerhof (PBE) functional[33] and projector augmented wave potential (PAW)[34,35] as implemented in VASP code.[36,37] Spin polarization was included for iron systems to correctly account for its magnetic properties, and this was found to be essential for an accurate description of adsorption energy.[38] An energy cutoff of 400 eV and a second-order Methfessel−Paxton[39] electron smearing with $\sigma = 0.2$ eV were used to ensure accurate energies with errors less than 1 meV per atom. The geometry optimization was done when forces became smaller than 0.02 eV/Å and the energy difference was lower than 10^{-4} eV. Calculations on α-Fe bulk crystal structure with a k-point mesh of 9 × 9 × 9 give a lattice constant of 2.84 Å and a local spin magnetic moment of 2.214 μ_B, in good agreement with other DFT calculations[40,41] and experiment.[42] For studying hydrogen adsorption, the $p(3 \times 4)$, $p(4 \times 4)$, $p(3 \times 3)$, $p(3 \times 2)$, $p(4 \times 2)$, $p(3 \times 2)$, and $p(2 \times 3)$ super cells were used for the (100), (110), (111), (210), (211), (310), and (321) surfaces, respectively. The 3 × 3 × 1 Monkhorst−Pack k-point grid was used in all the surfaces for sampling the Brillouin zone. The vacuum layer between periodically repeated slabs was set as 12 Å to avoid interactions between slabs. All reported stable adsorption configurations were verified to be energy minima by frequency analysis.

2.2. Ab Initio Thermodynamics. As a convenient tool to solve problems referring to real reaction conditions, atomistic thermodynamics proposed by Scheffler and Reuter have been widely and successfully applied in many systems.[43−50] In this method, the surface free energy γ of a surface can be described as in eq 1, in which G is the Gibbs free energy of a solid surface, A the total surface area of two equilibrium surfaces (top and bottom sides), $\mu_i(T, p)$ the chemical potential of the species i, and n_i the number of the ith type species.

$$\gamma(T, p) = \frac{1}{A}[G - \sum_i n_i\mu_i(T, p)] \tag{1}$$

For describing the adsorption of gas species on surfaces, we define the surface energy of a surface with n_i gas species adsorption as in eq 2, where $G_{hkl}^{ads}(T,p,\{n_{gas}^{ads}\})$is the Gibbs free energy of the (hkl) surface with n adsorbed species and $\mu_i(T, p)$ is the chemical potential of all the species in the system (including the adsorbed species).

$$\gamma_{hkl}^{ads}(T, p, n_i) = \frac{1}{A}[G_{hkl}^{ads}(T, p, \{n_{gas}^{ads}\}) - \sum_i n_i\mu_i(T, p)] \tag{2}$$

For iron surfaces with nH atoms adsorption, eq 2 can be rewritten as

$$\gamma_{\mathrm{Fe}}^{\mathrm{ads}}(T,\ p,\ n\mathrm{H}) = \frac{1}{A}\left[G_{\mathrm{Fe}}^{\mathrm{ads}}(T,\ p,\ \{n\mathrm{H}\}) - n_{\mathrm{Fe}}\mu_{\mathrm{Fe}}(T,\ p) - \frac{1}{2}n_{\mathrm{H}}\mu_{\mathrm{H_2}}(T,\ p)\right] \qquad (3)$$

As for the clean iron surfaces, the surface free energy ($\gamma_{\mathrm{Fe}}^{\mathrm{clean}}(T,\ p)$) is given in eq 4:

$$\gamma_{\mathrm{Fe}}^{\mathrm{clean}}(T,\ p) = \frac{1}{A}[G_{\mathrm{Fe}}^{\mathrm{clean}}(T,\ p) - n_{\mathrm{Fe}}\mu_{\mathrm{Fe}}(T,\ p)] \qquad (4)$$

where $G_{\mathrm{Fe}}^{\mathrm{clean}}(T,\ p)$ represents the Gibbs free energy of the clean Fe surface and $\mu_{\mathrm{Fe}}(T,\ p)$ is the chemical potential of bulk Fe. The surface free energy of the (hkl) surface with n H atoms by inserting eq 4 to eq 3 is given in eq 5.

$$\gamma_{\mathrm{Fe}}^{\mathrm{ads}}(T,\ p,\ nH) = \gamma_{\mathrm{Fe}}^{\mathrm{clean}}(T,\ p) + \frac{1}{A}\left[G_{\mathrm{Fe}}^{\mathrm{ads}}(T,\ p,\ \{n\mathrm{H}\}) - G_{\mathrm{Fe}}^{\mathrm{clean}}(T,\ p) - \frac{1}{2}n_{\mathrm{H}}\mu_{\mathrm{H_2}}(T,\ p)\right] \qquad (5)$$

Considering the adsorption process of H atoms on Fe surface as

$$\mathrm{Fe}(hkl) + n\mathrm{H} \leftrightarrow \mathrm{Fe}(hkl)/\{n\mathrm{H}\}$$

the change of Gibbs free energy for those adsorption processes, $\Delta G_{\mathrm{Fe}}^{\mathrm{ads}}(T,p,n\mathrm{H})$, can be found in eq 6.

$$\Delta G_{\mathrm{Fe}}^{\mathrm{ads}}(T,\ p,\ n\mathrm{H}) = G[\mathrm{Fe}(hkl)/\{n\mathrm{H}\}] - G[\mathrm{Fe}(hkl)] - \frac{1}{2}G_{\mathrm{gas}}(\mathrm{H_2}) \qquad (6)$$

In this equation, $G[\mathrm{Fe}(hkl)/\{n\mathrm{H}\}]$ is the Gibbs free energy of an Fe surface with nH atoms, while $G[\mathrm{Fe}(hkl)]$ is the Gibbs free energy of the clean Fe surface. Compared with the large contribution of vibration to the gases, this contribution to the solid surfaces is negligible because of their large mass differences. Therefore, we apply the DFT-calculated total energy to substitute the Gibbs free energies of solid Fe surfaces, and eq 6 can be rewritten as

$$\Delta G_{\mathrm{Fe}}^{\mathrm{ads}}(T,\ p,\ n\mathrm{H}) = E[\mathrm{Fe}(hkl)/\{n\mathrm{H}\}] - E[\mathrm{Fe}(hkl)] - \frac{1}{2}G_{\mathrm{gas}}(\mathrm{H_2})$$

where $E[\mathrm{Fe}(hkl)/\{n\mathrm{H}\}]$ and $E[\mathrm{Fe}(hkl)]$ are the total energies of corresponding systems. The $G_{\mathrm{gas}}(\mathrm{H_2})$ term equals $n\mu_{\mathrm{H_2}}(T,\ p)$. Then, the chemical potential of $\mathrm{H_2}$($\mu_{\mathrm{H_2}}$) can be described as

$$\mu_{\mathrm{H_2}}(T,\ p) = E_{\mathrm{H_2}}^{\mathrm{total}} + \tilde{\mu}_{\mathrm{H_2}}(T,\ p^0) + k_{\mathrm{B}}T\ln\frac{p_{\mathrm{H_2}}}{p^0}$$

At 0 K, the chemical potential of $\mathrm{H_2}$ can be regarded as the total energy of an isolated $\mathrm{H_2}$ molecule, which can be calculated directly with VASP. The $\tilde{\mu}_{\mathrm{H_2}}(T,\ p^0)$ term includes the contributions from vibration and rotation of the $\mathrm{H_2}$ molecule. It can be calculated or found in thermodynamic tables. In this paper we calculate these data by Gaussian software.[51] The last term of the formula is the contributions of temperature and $\mathrm{H_2}$ partial pressure to the chemical potential. Finally, the change in the Gibbs free energy of the Fe surfaces after the adsorption of n H atoms can be expressed as

$$\Delta G_{\mathrm{Fe}}^{\mathrm{ads}}(T,\ p,\ n\mathrm{H}) = E[\mathrm{Fe}(hkl)/\{n\mathrm{H}\}] - E[\mathrm{Fe}(hkl)] - \frac{1}{2}nE_{\mathrm{H_2}}^{\mathrm{total}} - \frac{1}{2}n\tilde{\mu}_{\mathrm{H_2}}(T,\ p^0) - \frac{1}{2}nk_{\mathrm{B}}T\ln\frac{p_{\mathrm{H_2}}}{p^0} \qquad (7)$$

In this respect, we can plot $\Delta G(T,\ p)$ as a function of T and p. The system (surface with nH atoms adsorption) with the lowest value of $\Delta G(T,\ p)$ will be most stable under the given conditions, and this also provides information about the $\mathrm{H_2}$ equilibrium coverage on the Fe surface under fixed conditions. Furthermore, the $\Delta G_{\mathrm{Fe}}^{\mathrm{ads}}(T,\ p,\ n\mathrm{H})$ part is equal to the second part of eq 5. Finally, we can get the value of the surface free energy of a surface with nH atoms adsorption under different temperatures and pressures by adding the contribution of hydrogen adsorption by using eq 8.

$$\gamma_{\mathrm{Fe}}^{\mathrm{ads}}(T,\ p,\ n\mathrm{H}) = \gamma_{\mathrm{Fe}}^{\mathrm{clean}}(T,\ p) + \frac{1}{A}[\Delta G_{\mathrm{Fe}}^{\mathrm{ads}}(T,\ p,\ \{n\mathrm{H}\})] \qquad (8)$$

The surface energy of clean iron surface (γFe) can be written as

$$\gamma_{\mathrm{Fe}}^{\mathrm{clean}}(T,\ p) = \frac{1}{A}[E_{\mathrm{Fe}(hkl)} - n_{\mathrm{Fe}}E_{\mathrm{Fe\text{-}bulk}}] \qquad (9)$$

where $E_{\mathrm{Fe}(hkl)}$ is the total energy of Fe(hkl) surface and $E_{\mathrm{Fe\text{-}bulk}}$ is the total energy of bulk iron.

3. RESULTS AND DISCUSSION

3.1. Surface Structures and Hydrogen Adsorption.

The morphology of real catalysts plays a key role in heterogeneous catalysis, and it is possible to get a clear picture of a practical catalyst only by considering all possible structures. For Fe particles, the seven body-centered cubic iron surfaces were considered, i.e., low index (100), (110), and (111) surfaces for the basic structures and high index (210), (211), (310), and (321) surfaces for the step and kinked structures (Figure 1).

For obtaining the most stable adsorption sites at any coverage, all adsorption sites and configurations were calculated. To determine the saturated coverage on a specific surface, the stepwise adsorption energy, $\Delta E_{\mathrm{ads}} = E[\mathrm{H}_{n+1}/\mathrm{slab}] - E[\mathrm{H}_n/\mathrm{slab}] - 1/2E[\mathrm{H_2}]$, was used, where a positive ΔE_{ads}

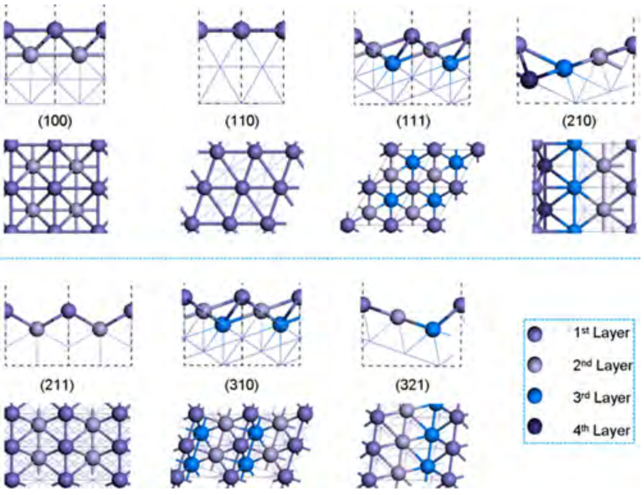

Figure 1. Schematic side and top views of seven iron surfaces (larger sizes are used in calculations).

indicates the saturated adsorption with hydrogen atoms on the surface. It is worth noting that our stepwise adsorption energy defines the change of the adsorption energy by adding one more species to the surface, whereas the differential energy of adsorption defines the change of the average adsorption energy per coverage as the function of coverage.[52] The binding energy (E_b) is defined as the adsorption energy of one H atom. All our reported energetics includes the correction of zero-point energy (ZPE) between the adsorbed surface H atoms and H_2 in the gas phase. As shown in Supporting Information (Table S1), ZPE correction has a maximal effect of only 0.7 kcal/mol (or 0.03 eV) to the binding energies on all surfaces. The contribution of ZPE correction to the stepwise adsorption energies on all seven surfaces (Tables S2−S8 of Supporting Information) has maximal absolute effect of 1.15 kcal/mol (or 0.05 eV). In our calculations, we observed only dissociative hydrogen adsorption up to saturation on all surfaces, in agreement with the experimental results. The structures of the most stable sites for hydrogen atom stepwise adsorption on these surfaces are given in Supporting Information (Figures S1−S7).

3.2. Gibbs Free Energy with Temperature and Pressure. On the basis of the saturated coverage determined by ΔE_{ads}, we want to connect stable hydrogen coverage with experimental conditions (temperature and pressure) by using Gibbs free energy as the criterion. Figure 2 presents the relationship between the stable H coverage with temperatures and hydrogen partial pressure on the Fe(110) surface. It indicates clearly that the stable hydrogen coverage decreases upon temperature increase at given pressures. On the basis of the equilibrium phase diagram of hydrogen coverage, one can directly get the stable hydrogen coverage under any given T and p_{H_2}. The phase diagrams of the other six surfaces are given in Supporting Information (Figure S8). Systematic comparisons reveal that each surface has quite different hydrogen coverage even under the same conditions, which rationalizes the experimentally observed differences in activities of catalysts prepared under different conditions.

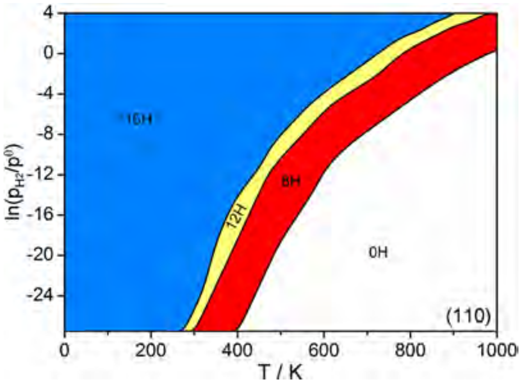

Figure 2. Equilibrium phase diagram of H coverage on the (110) surface.

3.3. Morphology of Iron Particles under Different Conditions. Because Fe particles are usually prepared experimentally from Fe_2O_3 and H_2, the reduction conditions play important roles in the formation of Fe surface morphology. On the basis of surface free energy of the iron surfaces (Tables S9 and S10 in Supporting Information), we modeled the iron crystal shapes at different temperatures and one atmosphere hydrogen pressure using Wulff constructions.[53,54] In addition, those crystal shapes resulting at 675 K reduction temperature and different hydrogen pressures are given in Supporting Information (Figure S9). Because the reduction conditions affect the surface morphology of Fe particles, we chose four temperatures to discuss the change in morphology of the Fe particles. Under ideal conditions, the morphology of iron particles is polycrystalline (Figure 3a). Under hydrogen atmosphere at 0 K, the only exposed surface is (110) (Figure 3b). At 425 K (low reduction temperature), the (310) surface starts to expose apart from the (110) surface (Figure 3c). At 675 K (common reduction temperature), the portion of the (310) surface increases, but the (110) surface still dominates (Figure 3d). These results are in agreement with the recent TEM analysis on Fe particles reduced at 673 K for 30 h under pure H_2.[55] Our analysis shows that the Fe(110) surface is most stable under hydrogen reduction and should be expected to be least active. Indeed, the Fe(110) surface has been proven to have the lowest activity in ammonia synthesis compared to the Fe(100) and Fe(111) surfaces.[56]

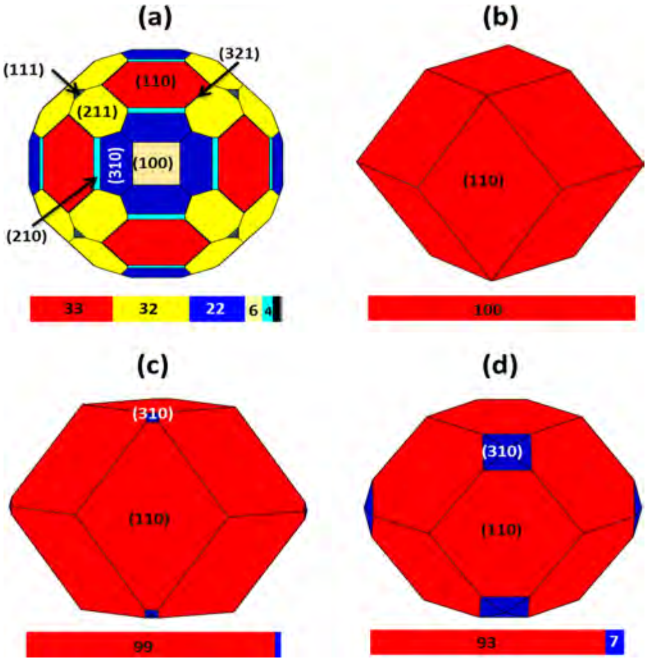

Figure 3. Wulff shapes of clean iron particles at 0 K under vacuum (a) and iron particles under hydrogen atmosphere at (b) 0 K, (c) 425 K, and (d) 675 K.

3.4. Hydrogen Adsorption and Desorption Properties on Iron Surfaces. Because the experimentally synthesized catalyst particles are always polycrystalline with mixed facets and an unambiguous determination of their three-dimensional atomic-scale structures is challenging,[57,58] a clear identification and characterization of the surface active sites is desired. Here, we present the full portrait of Fe particles from the computed hydrogen desorption temperatures and energies on single-crystalline iron surfaces in combination with the experimental TPD results to identify and differentiate the surface active sites.

The equilibrium adsorption configurations depend on coverage and temperature and are dominated by the mutual interactions of adsorbed surface species. Because hydrogen coverage decreases with increasing temperature, each desorption peak at a certain temperature shows the corresponding sharp and sudden change of the equilibrium coverage. On the

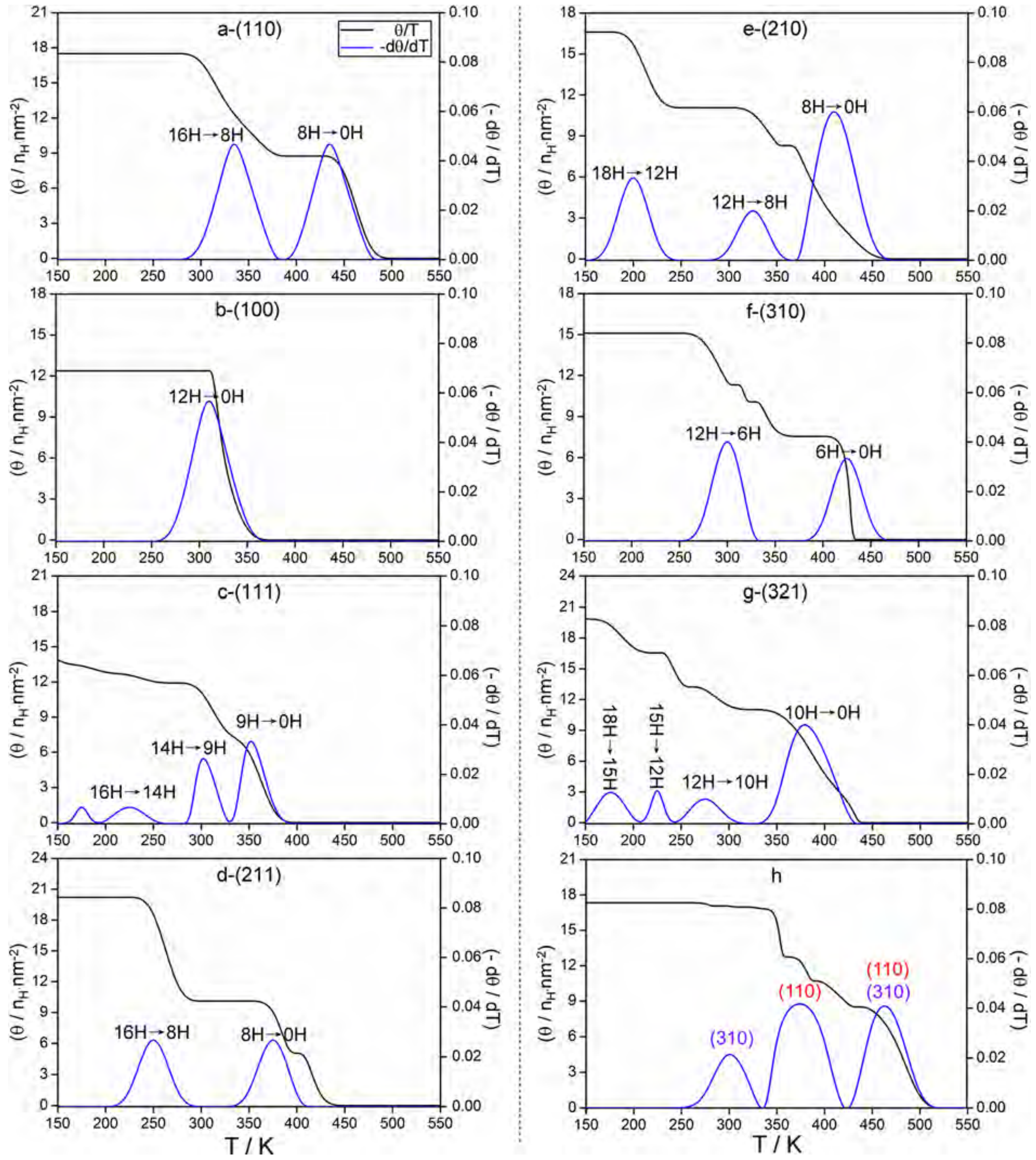

Figure 4. Hydrogen desorption peaks (blue curve) on seven iron surfaces at 10^{-9} atmosphere (a−g) as well as hydrogen desorption peaks on iron particles prepared at 675 K and hydrogen atmosphere pressure (h).

basis of the changes in Gibbs free energies of hydrogen adsorption at different temperatures, the changes in hydrogen coverage on seven iron surfaces at different hydrogen pressures can be obtained. Our results from ultralow (10^{-12} atm) to very high (40 atm) hydrogen pressure show that rising working pressure increases the desorption temperature. Because the available TPD spectra on single iron surfaces were carried out under ultrahigh vacuum (UHV) conditions and different exposures, we used the data at 10^{-9} atm (1 L = 10^{-6} Torr/s means keeping the pressure of hydrogen gas at 10^{-6} Torr for one second; in this respect, the partial pressure of H_2 is 10^{-6} Torr, which is equal to 10^{-9} atm) starting from the saturated coverage for discussion and comparison (Figure 4).

Hydrogen adsorption on the (110), (100), and (111) single crystal planes after H_2 exposures has been studied by using TPD, LEED, UPS, and work function measurements by Bozso et al.[12] On Fe(110), the TPD spectra were recorded with a heating rate of 7 K/sec after H_2 exposures between 0.4 and 3500 L at 140 K. The saturation of the adsorbed layer (1 ML) was formed under the highest exposure. The spectra show two states (β_1 and β_2) in superposition. The temperature maximum of the β_1 state is about 340 K, whereas the β_2 state shifts toward higher temperature (480−430 K) with increasing coverage. Analysis into the total desorption area shows that at saturation of the adsorbed layer both states exist with equal hydrogen concentration on the surface.

These thermal desorption data are excellently reproduced in our calculations. On Fe(110), for example, the totally saturated coverage of 16H atoms (1 ML for $p(4 \times 4)$ unit cell) is stable up to 250 K (Figure 4a). Two desorption peaks are predicated; the first one has a temperature maximum at about 330 K (300–375 K), and the second one has a temperature maximum at about 425 K (400–450 K). The first desorption loses half of the 16 H atoms at saturation (16 H → 8 H), and the second desorption loses all other adsorbed H atoms (8 H → 0 H), indicating the equal concentration of two states. Detailed analysis into the surface structures shows that all adsorbed H atoms in the 3-fold adsorption configuration are fully equivalent and form the ordered "$c(4 \times 4)$-8H" and "$c(4 \times 4)$-16H" surface structures at both 0.5 and 1.0 ML, respectively, in agreement with those from LEED anaylsis.[12] Up to 8 H atoms (0.5 ML), the stepwise adsorption energies are nearly the same, indicating non repulsive lateral interaction. From 9 H to 16 H atoms (1.0 ML), the stepwise adsorption energies are also nearly the same, but lower than those for 8 H atoms, indicating the repulsive interaction of the neighboring hydrogen atoms as coverage increase. All these are in agreement with the experimental findings. Furthermore, the calculated Fe–H binding energy of 67.5 kcal/mol also agrees with the value (65 kcal/mol) from UPS.[12]

On Fe(100), Bozso et al.[12] found two discernible states (β_1 and β_2). The temperature maximum of the β_1 state is about 300 K, whereas the β_2 state shifts toward higher temperature (430–400 K) with increasing coverage. There are no ordered surface structures over the whole range of coverage from LEED analysis. In our calculation we found one broad desorption state with temperature maximum at about 310 K (Figure 4b), which is very close to the experimentally detected β_1 state. However, we could not find the corresponding temperature maximum of the β_2 state. At about 350 K, all 12 H atoms desorb fully. At 1 ML, all 12 H atoms are fully equivalent and have the 4-fold hollow adsorption configuration. As given in Supporting Information (Figure S10), the saturated coverage on the (100) surface has 13 H, and the first desorption temperature at 50 K is below the exposure temperature (140 K). The computed Fe–H bonding energy is 62.5 kcal/mol.

On Fe(111), Bozso et al.[12] found three desorption states (β_1, β_2, and β_3) in the range of 200–450 K. The temperature maximum of the β_1 and β_2 states is about 240 and 310 K, respectively, whereas the β_3 state shifts toward higher temperature (375–400 K) with increasing coverage. There are no ordered surface structures over the whole range of coverage from LEED analysis. Above 200 K, we also found three desorption states, and the corresponding temperature maxima are 225, 300, and 350 K (Figure 4c), respectively, and these are very close to the experimentally detected β_1, β_2, and β_3 states. The first state indicates the coverage change from 16 H to 14 H and the second state indicates the coverage change from 14 H to 9 H. The third state indicates the full desorption. As given in Supporting Information (Figure S10), the saturated coverage on the Fe(111) surface has 23 H and a broad desorption peak with a temperature maximum at 75–100 K, which is below the exposure temperature (140 K). In addition, the calculated Fe–H binding energy (63.8 kcal/mol) agrees also with the value (62 kcal/mol) from UPS.[12]

On the (211) surface[17] there are unreconstructed and reconstructed surfaces induced by hydrogen at different exposures. On the unreconstructed surface at low exposure temperature (40 K), there are two desorption states: a weaker one (α_1, α_2, and α_3) with a temperature maximum at 250 K and a stronger one (β) with a temperature maximum at about 350 K. Our calculations (Figure 4d) also show two desorption states, i.e., at 250 K for the coverage change from 16 H (saturated, 2 ML) to 8 H (1 ML) and at 375 K for the full desorption of the 8 H atoms. The computed zigzag (1 ML) and linear (2 ML) arrangements of the adsorbed H atoms (Figure S11 of Supporting Information) are supported by ordered surface structures deduced from LEED analysis.[17] In addition, the calculated Fe–H binding energy is 65.3 kcal/mol.

Not only desorption temperatures but also the corresponding desorption energies (details in Supporting Information) have been well-reproduced computationally (Table 1). The excellent agreement in hydrogen desorption temperatures and energies on the (100), (110), (111), and (211) surfaces as well as the H binding energies on the (110) and (111) surfaces between experiments and theory validates this computational methodology and rationalizes the results. Moreover, the computed desorption temperatures and energies on those surfaces (Figure 4e–g) allow the prediction of the hydrogen TPD data on other surfaces, e.g., (210), (310), and (321), which are experimentally not yet available. In addition, all three surfaces have practically the same Fe–H binding energies. Indeed, a recent TPD and DFT study by van Helden et al.[59] reported desorption properties of hydrogen on different Co surfaces and also showed the reasonable agreement between computation and experiment.

Table 1. Binding Energies (E_b), Desorption Energies (E_d), and Desorption Temperature (T) from Computation (Including Zero-Point Energies) and Experiments

surface	E_b[a]	E_d (T)[a] (kcal/mol (K))	E_d (T)[c] (kcal/mol (K))
(110)	67.5 (65)[b]	23.7 (330)	24 (β_1, 340)[12]
		28.3 (425)	26 (β_2, 430–480)[12]
(100)	62.5	17.9 (310)	18 (β_1, 300)[12]
(111)	63.8 (62)[b]	15.3 (225)	13 (β_1, 240)[12]
		17.1 (300)	18 (β_2, 310)[12]
		17.8 (350)	21 (β_3, 375–400)[12]
(211)	65.3	18.9 (250)	9–12 (α_{1-3}, 210–270)
		22.1 (350)	19.6–24.2 (β, 350)[18]
(210)	66.7	19.0 (400)	
(310)	66.6	21.7 (425)	
(321)	66.7	18.4 (400)	

[a]Computed data in this work. [b]UPS data from ref 12. [c]Experimental data.

It is worth noting that our methods can be used to model the adsorption and desorption properties not only under UHV conditions but also under practical operations at high temperature and pressure. At high pressure, the adsorption patterns become different and desorption temperatures become higher. Furthermore, our predicted TPD peaks represent the changes of the most stable surface coverage at a given temperature; those from the framework of the Polanyi–Wigner equations show the maximal rates of desorption. Both approaches are related by desorption energies at given coverage and conditions.

3.5. Revealing the Exposed Surfaces of a Crystalline Catalyst. When our approach is followed, it becomes possible to evaluate and identify surface characteristics by a direct comparison between experimentally detected desorption temperatures and energies on the whole particles and the theoretically computed desorption temperatures and energies on individual clean surfaces (each surface has its characteristic desorption peaks which play the role of the fingerprint of the surface) at the same conditions. Hence, one can obtain the whole portrait as well as the exposed surfaces of the prepared catalysts in a straightforward manner.

As an example, a metallic iron catalyst prepared at 675 K under hydrogen atmosphere (Figure 4h), which is related to ammonia synthesis, shows three desorption peaks. Each one corresponds to an adsorption state on the characteristic surface. Our detailed analysis indicates that this Fe catalyst has the exposed (110) and (310) surfaces. On the basis of the individual desorption peaks on the clean (110) and (310) surface (Figure 4a and 4f), desorption peaks at about 300 K can be assigned to that on the (310) surface and the desorption peak at 350−375 K should belong to the (110) surface. The third peak at about 470 K is a result of the overlap of desorption on both (110) and (310) surfaces. The changes in desorption temperatures and energies clearly reflect the changes in exposed facets and in hydrogen coverage, and they reveal the relationship between the different facets of Fe particles and their properties in hydrogen adsorption or desorption. More specifically, the obtained results make clear that in ammonia synthesis the active catalyst site should be the most exposed (110) surface because of its high surface exposure (93%).

4. CONCLUSION

We computed the surface morphology of Fe particles using ab initio thermodynamics. Notably, the experimentally detected hydrogen desorption temperatures and energies on the (100), (110), (111), and (211) surfaces as well as the Fe−H binding energies on (110) and (111) surfaces are well-reproduced. A precise identification of the structure of the active surface centers and amount of hydrogen atoms on the different surfaces at different temperatures provides the basis for micro kinetic modeling[60] of hydro-treating reactions. Such agreements between theory and experiment validate our computational methodology and reveal that commonly prepared Fe catalysts have exposed (110) and (310) facets at typical hydrogen reduction temperature. This interplay of hydrogen TPD between theory and experiment provides a novel characterization tool for investigating surface structures and active facets of catalyst systems. In addition, it will help to reveal the relationship of surface structures and catalyst activities in general and might thereby contribute to a more rational catalyst development in the future.

■ ASSOCIATED CONTENT

Ⓢ Supporting Information

Detailed desorption of energy calculation methods; effects of zero-point energies on binding and desorption energies (Table S1); stepwise H adsorption energies with and without zero-point energy corrections (Tables S2−S8); surface free energy of seven iron surfaces under different condition (Tables S9 and S10); stepwise H adsorption structures (Figures S1−S7); H equilibrium coverage phase diagrams for all iron surfaces (Figure S8); Wulff shapes of iron particles at different pressures (Figure S9); Hydrogen desorption peaks on seven iron surfaces at 10^{-9} atm (Figure S10); structures of ordered hydrogen adsorption on Fe(110) and (211) surfaces (Figure S11). This material is available free of charge via the Internet at http://pubs.acs.org.

■ AUTHOR INFORMATION

Corresponding Author

*E-mail: haijun.jiao@catalysis.de.

Notes

The authors declare no competing financial interest.

■ ACKNOWLEDGMENTS

This work was supported by the National Basic Research Program of China (2011CB201406), National Natural Science Foundation of China (21073218), Chinese Academy of Sciences and Synfuels CHINA. Co., Ltd. We also acknowledge general financial support from the BMBF and the state of Mecklenburg-Western Pommerania.

■ REFERENCES

(1) http://www.freedoniagroup.com/World-Catalysts.html.

(2) Ertl, G.; Knözinger, H.; Schüth, F.; Weitkamp, J. *Handbook of Heterogeneous Catalysis*, 2nd ed; VCH: Weinheim, Germany, 2008.

(3) Thomas, J. M.; Thomas, W. J. *Principles and Practice of Heterogeneous Catalysis*; Wiley-VCH: Weinheim, Germany, 1997.

(4) Somorjai, G. A.; Li, Y. *Introduction to Surface Chemistry and Catalysis*, 2nd ed.; John Wiley: Hoboken, NJ, 2010.

(5) Somorgai, G. A.; Park, J. Y. Evolution of the Surface Science of Catalysis from Single Crystals to Metal Nanoparticles under Pressure. *J. Chem. Phys.* **2008**, *128*, 182504.

(6) Weckhuysen, B. M. In-situ Characterization of Heterogeneous Catalyst. In *Catalysis, From Principles To Applications*; Beller, M., Renken, A., van Santen, R. A., Eds.; Wiley-VCH: Weinheim, Germany, 2012.

(7) Rodriguez, J. A.; Hanson, J. C.; Chupas, P. J. *In-situ Characterization of Heterogeneous Catalysts*, 1st ed.; John Wiley & Sons: Hoboken, NJ, 2013.

(8) Niemantsverdriet, J. W. Temperature Programmed Techniques. In *Spectroscopy in Catalysis: An Introduction*, 3rd ed.; Wiley-VCH: Weinheim, Germany, 2007.

(9) Ertl, G. Reactions at Surfaces: From Atoms to Complexity. *Angew. Chem., Int. Ed.* **2008**, *47*, 3524−3535.

(10) de Smit, E.; Weckhuysen, B. M. The Renaissance of Iron-Based Fischer−Tropsch Synthesis: On the Multifaceted Catalyst Deactivation Behavior. *Chem. Soc. Rev.* **2008**, *37*, 2758−2781.

(11) Thüne, P. C.; Weststrate, C. J.; Moodley, P.; Saib, A. M.; van de Loosdrecht, J.; Miller, J. T.; Niemantsverdriet, J. W. Studying Fischer−Tropsch Catalysts Using Transmission Electron Microscopy and Model Systems of Nanoparticles on Planar Supports. *Catal. Sci. Technol.* **2011**, *1*, 689−697.

(12) Bozso, F.; Ertl, G.; Grunze, M.; Weiss, M. Chemisorption of Hydrogen on Iron Surfaces. *Appl. Surf. Sci.* **1977**, *1*, 103−119.

(13) Cavalier, J. C.; Chornet, E. Hydrogen-Deuterium Exchange on Iron: Kinetic Anisotropies. *Surf. Sci.* **1976**, *60*, 125−146.

(14) Yoshida, K.; Somorjai, G. A. The Chemisorption of CO, CO_2, C_2H_2, C_2H_4, H_2 and NH_3 on the Clean Fe(100) and (111) Crystal Surfaces. *Surf. Sci.* **1978**, *75*, 46−60.

(15) Imbihl, R.; Behm, R. J.; Christmann, K.; Ertl, G.; Matsushima, T. Phase Transitions of a Two-Dimensional Chemisorbed System: H on Fe(110). *Surf. Sci.* **1982**, *117*, 257−266.

(16) Nichtl-Pecher, W.; Gossman, J.; Hammer, L.; Heinz, K.; Müller, K. Adsorption of Hydrogen on Fe(110) at Cryogenic Temperatures Investigated by Low Energy Electron Diffraction. *J. Vac. Sci. Technol., A* **1992**, *10*, 501−507.

(17) Schmiedl, R.; Nichtl-Pecher, W.; Heinz, K.; Müller, K. Hydrogen on Fe(211): Commensurate and Reconstructed Phases. *Surf. Sci.* **1990**, *235*, 186−196.

(18) Schmiedl, R.; Nichtl-Pecher, W.; Hammer, L.; Heinz, K.; Müller, K. Hydrogen Adsorption on Fe(211): Structural, Thermodynamic and Kinetic Properties. *Surf. Sci.* **1995**, *324*, 289−304.

(19) Merrill, P. B.; Madix, R. J. Hydrogen Bonding on Iron: Correlation of Adsorption and Desorption States on Fe(100) and Perturbation of the Fe-H Bond with Coadsorbed CO. *Surf. Sci.* **1996**, *347*, 249−264.

(20) Suo, H. Y.; Wang, S. G.; Zhang, C. H.; Xu, J.; Wu, B. S.; Yang, Y.; Xiang, H. W.; Li, Y. W. Chemical and Structural Effects of Silica in Iron-Based Fischer−Tropsch Synthesis Catalysts. *J. Catal.* **2012**, *286*, 111−123.

(21) Walch, S. P. Model Studies of the Interaction of H Atoms with bcc Iron. *Surf. Sci.* **1984**, *143*, 188−203.

(22) Sorescu, D. C. First Principles Calculations of the Adsorption and Diffusion of Hydrogen on Fe(100) Surface and in the Bulk. *Catal. Today* **2005**, *105*, 44−65.

(23) van Steen, E.; van Helden, P. A DFT Study of Hydrogen Dissociation on CO- and C-Precovered Fe(100) Surfaces. *J. Phys. Chem. C* **2010**, *114*, 5932−5940.

(24) Jiang, D. E.; Carter, E. A. Adsorption and Diffusion Energetics of Hydrogen Atoms on Fe(110) from First Principles. *Surf. Sci.* **2003**, *547*, 85−98.

(25) Jiang, D. E.; Carter, E. A. Diffusion of Interstitial Hydrogen into and through bcc Fe from First Principles. *Phys. Rev. B* **2004**, *70*, 064102.

(26) Huo, C. F.; Li, Y. W.; Wang, J.; Jiao, H. Surface Structure and Energetics of Hydrogen Adsorption on the Fe(111) Surface. *J. Phys. Chem. B* **2005**, *109*, 14160−14167.

(27) Fabiani, F. C.; Fratesi, G.; Brivio, G. P. Adsorption Of H_2S, HS, S, and H on a Stepped Fe(310) Surface. *Eur. Phys. J. B* **2010**, *78*, 455−460.

(28) Faglioni, F.; Goddard, W. A., III Energetics of Hydrogen Coverage on Group VIII Transition Metal Surfaces and a Kinetic Model for Adsorption/Desorption. *J. Chem. Phys.* **2005**, *122*, 014704.

(29) van Santen, R. A.; Neurock, M. *Molecular Heterogeneous Catalysis: A Conceptual and Computational Approach*; Wiley-VCH: Weinheim, Germany, 2006.

(30) Honkala, K.; Hellman, A.; Remediakis, I. N.; Logadottir, A.; Carlsson, A.; Dahl, S.; Christensen, C. H.; Nørskov, J. K. Ammonia Synthesis from First-Principles Calculations. *Science* **2005**, *307*, 555−558.

(31) Reuter, K.; Scheffler, M. Composition, Structure, and Stability of RuO2(110) as a Function of Oxygen Pressure. *Phys. Rev. B* **2001**, *65*, 035406.

(32) Reuter, K.; Scheffler, M. Composition and Structure of the RuO_2(110) Surface in an O_2 and CO Environment: Implications for the Catalytic Formation of CO_2. *Phys. Rev. B* **2003**, *68*, 045407.

(33) Perdew, J. P.; Burke, K.; Ernzerhof, M. Generalized Gradient Approximation Made Simple. *Phys. Rev. Lett.* **1996**, *77*, 3865−3868.

(34) Blochl, P. E. Projector Augmented-Wave Method. *Phys. Rev. B* **1994**, *50*, 17953−17979.

(35) Kresse, G. From Ultrasoft Pseudopotentials to the Projector Augmented-Wave Method. *Phys. Rev. B* **1999**, *59*, 1758−1775.

(36) Kresse, G.; Furthmüller, J. Efficiency of Ab-initio Total Energy Calculations for Metals and Semiconductors Using a Plane-Wave Basis Set. *Comput. Mater. Sci.* **1996**, *6*, 15−50.

(37) Kresse, G.; Furthmüller, J. Efficient Iterative Schemes for Ab initio Total-Energy Calculations Using a Plane-Wave Basis Set. *Phys. Rev. B* **1996**, *54*, 11169−11186.

(38) Kresse, G.; Hafner, J. First-Principles Study of the Adsorption of Atomic H on Ni (111), (100) and (110). *Surf. Sci.* **2000**, *459*, 287−302.

(39) Methfessel, M.; Paxton, A. T. High-Precision Sampling for Brillouin-zone Integration in Metals. *Phys. Rev. B* **1989**, *40*, 3616−3621.

(40) Jiang, D. E.; Carter, E. A. Carbon Dissolution and Diffusion in Ferrite and Austenite from First Principles. *Phys. Rev. B* **2003**, *67*, 214103.

(41) Sorescu, D. C. First-Principles Calculations of the Adsorption and Hydrogenation Reactions of CH_x (x=0−4) Species on a Fe(100) Surface. *Phys. Rev. B* **2006**, *73*, 155420.

(42) Kittel, C. *Introduction to Solid State Physics*; Wiley: New York, 1996.

(43) Li, W. X.; Stampfl, C.; Scheffler, M. Insights into the Function of Silver as an Oxidation Catalyst by Ab Initio Atomistic Thermodynamics. *Phys. Rev. B* **2003**, *68*, 165412.

(44) Rogal, J.; Reuter, K.; Scheffler, M. Thermodynamic Stability of PdO Surfaces. *Phys. Rev .B* **2004**, *69*, 075421.

(45) Zasada, F.; Piskorz, W.; Cristol, S.; Paul, J. F.; Kotarba, A.; Sojka, Z. Periodic Density Functional Theory and Atomistic Thermodynamic Studies of Cobalt Spinel Nanocrystals in Wet Environment: Molecular Interpretation of Water Adsorption Equilibria. *J. Phys. Chem. C* **2010**, *114*, 22245−22253.

(46) Wang, T.; Liu, X. W.; Wang, S. G.; Huo, C. F.; Li, Y. W.; Wang, J.; Jiao, H. Stability of β-Mo_2C Facets from ab Initio Atomistic Thermodynamics. *J. Phys. Chem. C* **2011**, *115*, 22360−22368.

(47) Wang, T.; Wang, S. G.; Li, Y. W.; Wang, J.; Jiao, H. Adsorption Equilibria of CO Coverage on β-Mo_2C Surfaces. *J. Phys. Chem. C* **2012**, *116*, 6340−6348.

(48) Zhao, S.; Liu, X. W.; Huo, C. F.; Li, Y. W.; Wang, J.; Jiao, H. Surface Morphology of Hägg Iron Carbide (χ-Fe_5C_2) from Ab initio Atomistic Thermodynamics. *J. Catal.* **2012**, *294*, 47−53.

(49) Wang, T.; Tian, X. X.; Li, Y. W.; Wang, J.; Beller, M.; Jiao, H. High Coverage CO Activation Mechanisms on Fe(100) from Computations. *J. Phys. Chem. C* **2014**, *118*, 1095−1101.

(50) Wang, T.; Li, Y.-W.; Wang, J.; Beller, M.; Jiao, H. High Coverage CO Adsorption and Dissociation on the Orthorhombic Mo_2C(100) Surface. *J. Phys. Chem. C* **2014**, *118*, **DOI:** 10.1021/jp412067x.

(51) Frisch, M. J. et al. *Gaussian 09*, revision D.01; Gaussian, Inc.: Wallingford, CT, 2009.

(52) Digne, M.; Sautet, P.; Raybaud, P.; Euzen, P.; Toulhoat, H. Use of DFT to Achieve a Rational Understanding of Acid-Basic Properties of γ-Alumina Surfaces. *J. Catal.* **2004**, *226*, 54−68.

(53) WULFFMAN: An Interactive Crystal Shape Constructor. http://www.ctcms.nist.gov/wulffman/.

(54) Geomview. http://www.geomview.org/.

(55) Huo, C. F.; Wu, B. S.; Gao, P.; Yang, Y.; Li, Y. W.; Jiao, H. The Mechanism of Potassium Promoter: Enhancing the Stability of Active Surfaces. *Angew. Chem., Int. Ed.* **2011**, *50*, 7403−7406.

(56) Spencer, N. D.; Schoonmaker, R. C.; Somorjai, G. A. Iron Single Crystals as Ammonia Synthesis Catalysts: Effect of Surface Structure on Catalyst Activity. *J. Catal.* **1982**, *74*, 129−135.

(57) Koga, K.; Ikeshoji, T.; Sugawara, K. Size- and Temperature-Dependent Structural Transitions in Gold Nanoparticles. *Phys. Rew. Lett.* **2004**, *92*, 115507.

(58) Li, Z. Y.; Yang, N. P.; DiVece, M.; Palmer, S.; Bleloch, A. L.; Curley, B. C.; Johnston, R. L.; Jiang, J.; Yuan, J. Three-Dimensional Atomic-Scale Structure of Size-Selected Gold Nanoclusters. *Nature* **2008**, *451*, 46−48.

(59) van Helden, P.; van den Berg, J. A.; Weststrate, C. J. Hydrogen Adsorption on Co Surfaces: A Density Functional Theory and Temperature Programmed Desorption Study. *ACS Cat.* **2012**, *2*, 1097−1107.

(60) Lynggaard, H.; Andreasen, A.; Stegelmann, C.; Stoltze, P. Analysis of Simple Kinetic Models in Heterogeneous Catalysis. *Prog. Surf. Sci.* **2004**, *77*, 71−137.

3.4 Stable Surface Terminations of orthorhombic Mo_2C Catalysts and their CO Activation Mechanisms

Tao Wang, Qiquan Luo, Yong-Wang Li, Jianguo Wang, Matthias Beller, Haijun Jiao*

Applied Catalysis A: General **2014**, *478*, 146-156.

Summary: The structure and stability of all twenty-two terminations of the seven low-Miller index orthorhombic Mo_2C surfaces have been systematically investigated on the basis of the computed surface energies from periodic density functional theory. With the increase of the carbon chemical potential (μ_C), the most stable surface structure and composition change from the metallic (110)-Mo and (100)-Mo terminations to the mixed (111)-Mo/C and strongly reconstructed (110)-Mo/C terminations. The calculated stability order and surface area proportions of the (100), (110) and (111) surfaces agree very well with the available X-ray diffraction data. In addition, CO adsorption and dissociation on these surfaces have been computed and micro-kinetic analysis reveals that CO dissociation is rate-determining on the metallic termination, and CO adsorption is rate-determining on the mixed Mo/C-termination. This might explain the observed catalytic differences of orthorhombic Mo_2C catalysts prepared from different ways.

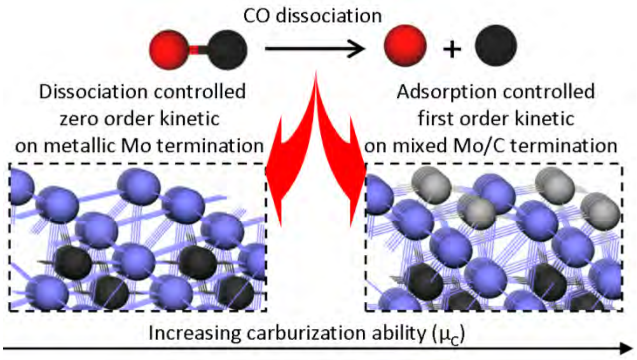
CO dissociation
+
Dissociation controlled
zero order kinetic
on metallic Mo termination
Adsorption controlled
first order kinetic
on mixed Mo/C termination
Increasing carburization ability (μ_C)

Contributions

In this paper, I planned, performed and analyzed most calculations for this manuscript. I have done the major part of writing of the manuscript. My contribution as co-author of this paper is approximately 80%.

Applied Catalysis A: General 478 (2014) 146–156

Contents lists available at ScienceDirect

Applied Catalysis A: General

journal homepage: www.elsevier.com/locate/apcata

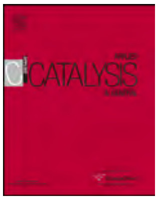

Stable surface terminations of orthorhombic Mo_2C catalysts and their CO activation mechanisms

Tao Wang[a], Qiquan Luo[a], Yong-Wang Li[b], Jianguo Wang[b], Matthias Beller[a], Haijun Jiao[a,b,*]

[a] *Leibniz-Institut für Katalyse e.V. an der Universität Rostock, Albert-Einstein Strasse 29a, 18059 Rostock, Germany*
[b] *State Key Laboratory of Coal Conversion, Institute of Coal Chemistry, Chinese Academy of Sciences, Taiyuan 030001, PR China*

ARTICLE INFO

Article history:
Received 16 January 2014
Received in revised form 14 March 2014
Accepted 31 March 2014
Available online 8 April 2014

Keywords:
DFT
Orthorhombic Mo_2C
Surface energy
Morphology
CO activation

ABSTRACT

The structure and stability of all twenty-two terminations of the seven low-Miller index orthorhombic Mo_2C surfaces have been systematically investigated on the basis of the computed surface energies from periodic density functional theory. With the increase of the carbon chemical potential (μ_C), the most stable surface structure and composition change from the metallic (1 1 0)-Mo and (1 0 0)-Mo terminations to the mixed (1 1 1)-Mo/C and strongly reconstructed (1 1 0)-Mo/C terminations. The calculated stability order and surface area proportions of the (1 0 0), (1 1 0) and (1 1 1) surfaces agree very well with the available X-ray diffraction data. In addition, CO adsorption and dissociation on these surfaces have been computed and micro-kinetic analysis reveals that CO dissociation is rate-determining on the metallic termination, and CO adsorption is rate-determining on the mixed Mo/C-termination. This might explain the observed catalytic differences of orthorhombic Mo_2C catalysts prepared from different ways.

© 2014 Elsevier B.V. All rights reserved.

1. Introduction

On the basis of their extreme hardness and brittleness, high melting points and electrical or thermal conductivities [1–3], transition metal carbides (TMC) have found wide applications as cutting tools [4] and hard-coating materials [5]. TMC also exhibit excellent catalytic activities [6], e.g., in hydrogenation [7–10], dehydrogenation [11], hydrogenolysis [12] and Fischer–Tropsch synthesis [13–17]. As a representative member of TMC, molybdenum carbide (Mo_2C) has been intensively studied experimentally and theoretically. Mo_2C mainly has two crystalline phases with slight distinctions; the orthorhombic [18] and the hexagonal [19] phases.

Mo_2C and WC have been reported to have similar catalytic activities as noble metals [20,21]. The catalytic activities of Mo_2C in water–gas shift (WGS, $CO + H_2O = CO_2 + H_2$) reaction [22,23], alcohol synthesis from CO hydrogenation [24–26], hydrodesulfurization (HDS) [27] and hydrodenitrogenation (HDN) [28] in petroleum refining, hydro-treating [29,30] and hydrogen production [31] as well as the unique catalytic behaviors in the aromatization of CH_4 [32,33] have been widely investigated experimentally. The adsorption and decomposition of small molecules [34–38], like nitrogenous compounds, aromatic hydrocarbons and CO, have been studied on both orthorhombic and hexagonal Mo_2C phases. Liu et al., [39–41] found that surface carbon in Mo_2C plays a key role in the dissociation of sulfur-containing molecules, and emphasized the importance of surface oxygen on Mo_2C in WGS reaction [42]. The hydrogenolysis of thiophene [43] and indole [44] on the clean hexagonal Mo_2C surface was also computed systematically. Pistonesi et al., discussed the chemical properties of methanol [45], methyl iodide [46] and potassium promoting effect on orthorhombic Mo_2C [47] and found that the incorporation of potassium atoms promotes the dissociation ability of the C—I and C—O bonds. Tominaga and Nagai [48] studied the potential energy surface of WGS reaction and concluded that the formation of CO_2 is rate-determining. In order to study the intrinsic WGS activity of Mo_2C, Schweitzer et al., [49] loaded Pt on Mo_2C and found Mo_2C to play the roles of both support and catalyst. Study of the thermodynamics of elementary steps of synthesis gas reactions on Mo_2C(0 0 1) [50] indicates that the Mo-termination exhibits similar activity with transition metals such as Ru and Ir in carbon related reactions. Tominaga et al., [51] studied CO hydrogenation on both clean and cobalt doped hexagonal Mo_2C(1 0 0) surface and they ruled out the possible formation of CH_3OH, and these results are supported by their experimental findings. The

---

* Corresponding author at: Leibniz-Institut für Katalyse e.V. an der Universität Rostock, Albert-Einstein Strasse 29a, 18059 Rostock, Germany.
Tel.: +49 381 1281 135; fax: +48 381 1281 51135.
E-mail address: haijun.jiao@catalysis.de (H. Jiao).

http://dx.doi.org/10.1016/j.apcata.2014.03.042
0926-860X/© 2014 Elsevier B.V. All rights reserved.

mechanism of CO hydrogenation into CH_4 on both orthorhombic Mo_2C(1 0 0) and hexagonal Mo_2C(1 0 1) surfaces was reported by Qi et al., [52] and the orthorhombic Mo_2C(1 0 0) surface was proved to have higher activity in CH_4 formation. A combined experimental and density functional theory (DFT) study showed very high catalytic activity of hexagonal Mo_2C in ammonia dehydrogenation [53]. A recent formic acid decomposition mechanism study [54] revealed that Mo_2C is a promising catalyst for CO-free hydrogen production.

Theoretical attentions have been paid to the adsorptions of simple molecules and reaction mechanisms on hexagonal Mo_2C(0 0 1) and orthorhombic Mo_2C(1 0 0) surfaces, but discussions about other Mo_2C surfaces are less known. Shi et al., [55] and Han et al., [56] calculated the surface energies of the low Miller index surfaces of hexagonal Mo_2C and found the (0 1 1) facet to be most stable. However, calculations of surface free energies of low and high Miller index surfaces of hexagonal Mo_2C using atomistic thermodynamics under the consideration of carburization conditions showed the (1 0 1) surface to be most stable and representative [57], in good agreement with the available X-ray diffraction (XRD) [58,59] and high resolution transmission electron microscopy (HRTEM) [60] results. Recently, dos Santos Politi et al., [61] computed the atomic and electronic structures of the bulk and low Miller-index surfaces of three molybdenum carbide phases (α-MoC, β-Mo_2C and δ-MoC) and found that the Perdew–Burke–Ernzerhof (PBE) functional is particularly suited to study molybdenum carbide and the β-Mo_2C phase has strong metallic character.

The adsorption and activation of CO is of particular importance for understanding the initial steps in many practical industry applications, such as Fischer–Tropsch synthesis [62], alcohol synthesis [63], water–gas sift reaction [64], fuel-cell technology and environment protection [65]. Since the orthorhombic molybdenum carbide has been proposed as potential substitute for the commercially used Cu-based catalysts for WGS reaction [66], it is essential to study the interaction of CO with Mo_2C. Despite of its importance, only few theoretical studies about CO adsorption and activation on Mo_2C were reported. Shi et al., [67] calculated CO adsorption on the hexagonal Mo_2C(0 0 1) surface and found that the Mo-termination can activate CO more strongly than the C-termination. On the basis of the computed Gibbs free energies, we studied the relationship among temperature, CO equilibrium coverage and CO partial pressure on the hexagonal Mo_2C surfaces [68], and found good agreement between the predicated and the experimentally recorded spectra of temperature programmed CO desorption. Our results provide useful information not only for adjusting the equilibrium between temperature and CO partial pressure for stable CO coverage but also for identifying the active surfaces and the initial states under given conditions. Ren et al., [69] calculated CO adsorption on the orthorhombic Mo_2C(1 0 0) surface and found CO preferring the Mo-termination over the C-termination. Pistonesi et al., [70] studied CO adsorption and dissociation on the clean and K-doped orthorhombic Mo_2C(0 0 1) surfaces and found that the incorporation of K strengthens CO adsorption but increases CO dissociation barrier. Apart from the (1 0 0) surface, to the best of our knowledge, the stability of the other low Miller-index surfaces of the orthorhombic Mo_2C phase as well as CO adsorption and dissociation on these surfaces have not been systematically studied. Furthermore, atomistic thermodynamics method [71–74] facilitates the discussion of the relationship of reaction conditions with surface stability and adsorption properties. In this method, the effects of reaction conditions (temperature, pressure and gas contents) can be reflected by the values of chemical potential. In particular, the effect of carbon chemical potential on the stability and composition of different surface terminations is of great relevance in investigating the properties of transition metal carbides for practical applications [75,76].

In this work we present a systematic study on the stability of the (0 0 1), (0 1 0), (0 1 1), (1 0 0), (1 0 1), (1 1 0) and (1 1 1) surfaces of the orthorhombic Mo_2C phase on the basis of periodic DFT calculations. We also present CO adsorption and dissociation properties on those surfaces from the thermodynamic and kinetic points of view. Our goal is to discuss the effect of carbon chemical potential on the stability of different surface terminations and also to build the relationships among surface stability as well as CO adsorption and activation properties.

2. Computational model and method

2.1. Method

All calculations were done by using the plane-wave based periodic DFT method implemented in the Vienna *ab initio* simulation package (VASP) [77,78]. The electron ion interaction is described with the projector augmented wave (PAW) method [79,80]. The electron exchange and correlation energy is treated within the generalized gradient approximation (GGA) in the Perdew–Burke–Ernzerhof formalism (PBE) [81]. Although DFT + U_{eff} is required to clearly describe the properties of Mo oxides [82,83], GGA-PBE is proved to be particularly suitable to describe the properties of Mo_2C catalyst [61]. Moreover, we also tested the effect of different U_{eff} values on the structural parameters. In comparison with the bulk structural parameters from experiment, the best agreement is found for $U_{eff} = 0$; and the larger the U_{eff}, and the worse the agreement (Table S1). To have the energies with errors less than 1 meV per atom, cutoff energy of 400 eV and Gaussian electron smearing method with $\sigma = 0.05$ eV were used. For the bulk optimization, the lattice parameters for orthorhombic Mo_2C were determined by minimizing the total energy of the unit cell on the basis of a conjugated-gradient algorithm to relax the ions, and a 5 × 5 × 5 Monkhorst–Pack *k*-point grid was used for sampling the Brillouin zone. The geometry optimization was done when force difference became smaller than 0.02 eV/Å and the energy difference was lower than 10^{-4} eV. (The test of this parameter is given in Table S2) Adsorption energy (E_{ads}) is calculated by subtracting the energies of gas phase species and the clean surface from the total energy of the adsorbed system; $E_{ads} = E(\text{adsorbate/slab}) - [E(\text{adsorbate}) + E(\text{slab})]$, and a more negative E_{ads} indicates a more stable adsorption. For evaluating the energy barrier, the transitional state (TS) was located using the nudged elastic band (NEB) method [84]. The TS configurations were verified by vibration analyses, and in all cases, only one imaginary frequency is found. The barrier (E_a) and reaction energy (ΔE_r) are calculated according to $E_a = E_{TS} - E_{IS}$ and $\Delta E_r = E_{FS} - E_{IS}$, where E_{IS}, E_{FS} and E_{TS} are the energies of the corresponding initial state (IS), final state (FS) and transition state (TS), respectively. The description of the method for the calculation of surface energy is included in Supporting information.

2.2. Model

We used the orthorhombic Mo_2C phase as unit cell. The calculated lattice parameters for Mo_2C bulk are $a = 4.751$ Å, $b = 6.065$ Å, $c = 5.237$ Å, very close to the experimental values ($a = 4.732$ Å, $b = 6.037$ Å and $c = 5.204$ Å) [85]. When calculating the surface energies, all applied slabs are equivalent in both sides and all the atoms were allowed to fully relax. The slab thickness of different terminations is in the range of 9–14 Å, thick enough to avoid significant influence on the surface energies from our tests in Supporting information. For example (Table S3), the calculated surface energies are 3.11 and 3.08 J/m^2 for 9-layer (1 0 0)-Mo (9.55 Å) and (1 0 0)-C (9.50 Å) slabs, as well as for 17-layer (1 0 0)-Mo (19.05 Å) and (1 0 0)-C (19.00 Å) slabs, respectively. A vacuum layer of 10 Å was set to

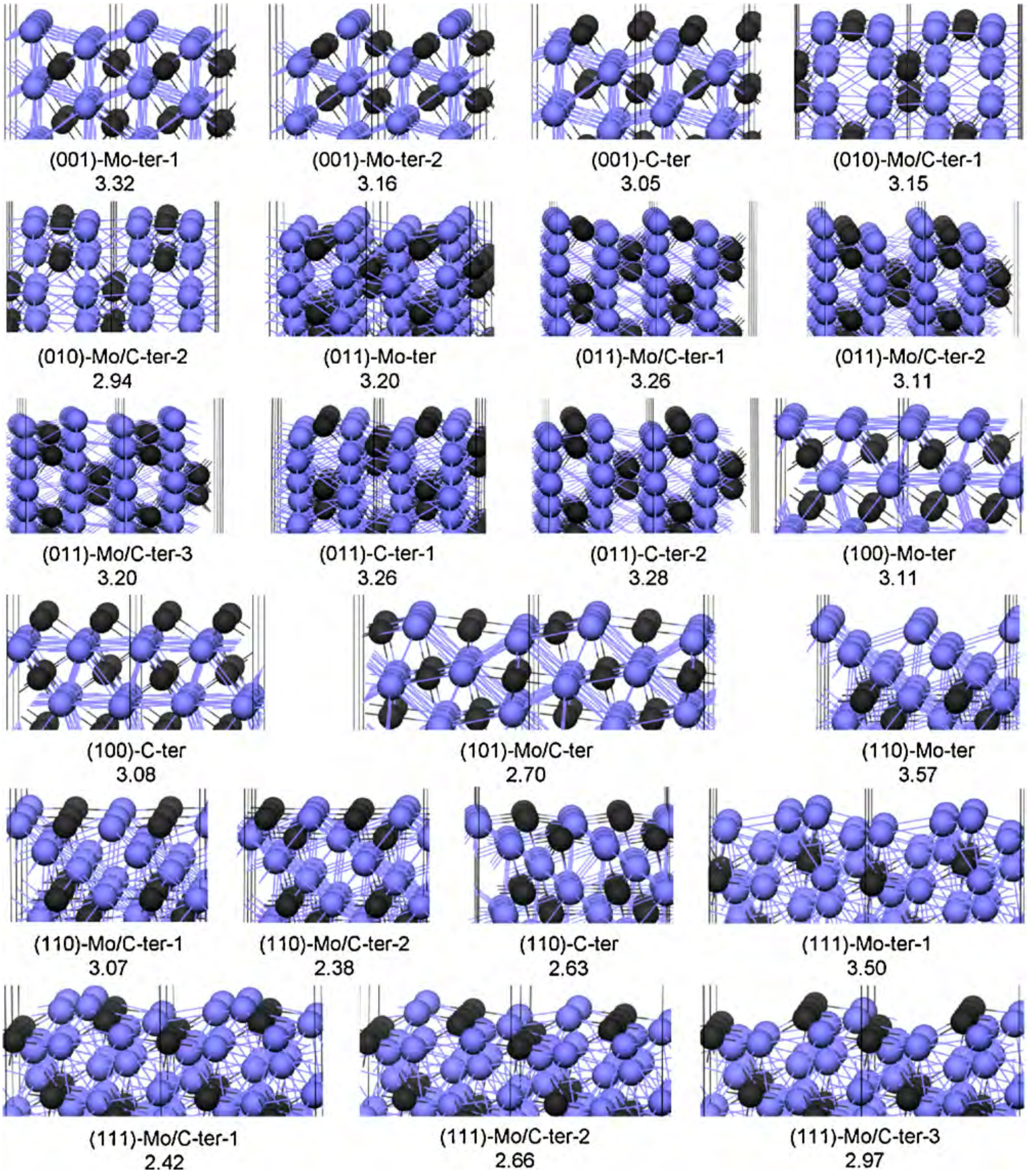

(001)-Mo-ter-1 3.32

(001)-Mo-ter-2 3.16

(001)-C-ter 3.05

(010)-Mo/C-ter-1 3.15

(010)-Mo/C-ter-2 2.94

(011)-Mo-ter 3.20

(011)-Mo/C-ter-1 3.26

(011)-Mo/C-ter-2 3.11

(011)-Mo/C-ter-3 3.20

(011)-C-ter-1 3.26

(011)-C-ter-2 3.28

(100)-Mo-ter 3.11

(100)-C-ter 3.08

(101)-Mo/C-ter 2.70

(110)-Mo-ter 3.57

(110)-Mo/C-ter-1 3.07

(110)-Mo/C-ter-2 2.38

(110)-C-ter 2.63

(111)-Mo-ter-1 3.50

(111)-Mo/C-ter-1 2.42

(111)-Mo/C-ter-2 2.66

(111)-Mo/C-ter-3 2.97

Fig. 1. Structures and surface energies of different terminations of orthorhombic Mo_2C by using graphite bulk energy as standard (μ_C) carbon chemical potential.

exclude the slab interactions. When considering CO adsorption and dissociation, the surfaces were modeled by periodic slabs, which are stoichiometric and thicker than 5 Å from our tests in Supporting information. For example (Table S3), the calculated CO adsorption energy is −2.35, −2.56 and −2.51 eV on the 4-layer (3.59 Å), 6-layer (5.96 Å) and 8-layer (8.33 Å) (1 0 0)-Mo surface, respectively. We also calculated the adsorption energy of H atom to test the effect of thickness. It reveals that the thickness has practically no effect for slab thicker than 5 Å. The detailed information of these applied slabs is listed in Supporting information (Table S4).

3. Results and discussion

3.1. Surface energy and relaxation

Fig. 1 shows the schematic view of seven orthorhombic Mo_2C surfaces in different terminations and their surface energies by using the bulk energy of graphite (which is directly calculated by the VASP on the basis of DFT) as carbon chemical potential (μ_C). The (0 0 1) surface has two Mo and one C terminations. The (0 1 0) surface has two Mo/C mixed terminations. The (0 1 1) surface has

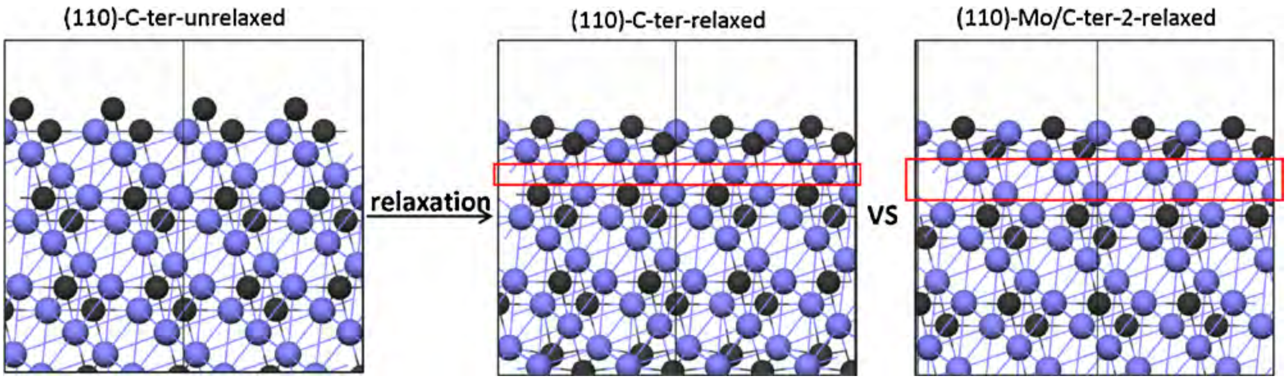

Fig. 2. Relationship of surface energy (γ) with carbon chemical potential (μ_c) of different Mo_2C terminations.

one Mo termination, two C terminations and three Mo/C mixed terminations. The (1 0 0) surface has one flat pure Mo termination and one C termination. The (1 0 1) surface has only one Mo/C mixed termination. The (1 1 0) surface has one Mo termination and three Mo/C mixed terminations. The (1 1 1) surfaces have one pure Mo termination and three Mo/C mixed terminations. Since surface relaxation or reconstruction can lower the surface energy considerably, it is necessary to check the relaxation degree of those surfaces. As listed in the Supporting information (Table S5), most of these surfaces show moderate to strong relaxation without reconstruction (less than 20%), and the strongest relaxation has been found in the C termination of (1 1 0) surface with reconstruction (43%). On the un-constructed (1 1 0)-C termination (Fig. 2), the first layer has only carbon atoms, and the second layer has both Mo/C atoms, while the third and fourth layers contain only Mo atoms. After the relaxation, the carbon atoms in the first and second layers diffuse into the sub-layers and form mixed Mo/C layers, and only one Mo sub-layer remains. This strongly relaxed surface termination, (1 1 0)-Mo/C-relaxed, is comparable to the mixed (1 1 0)-Mo/C-2 termination, but they are obvious different. On the mixed (1 1 0)-Mo/C-2 termination, the first two layers have both Mo/C atoms, and the third and fourth layers have only Mo atoms. Our previous work [69] and recent systematic band structure study of Mo_2C surfaces [61] show that both the bulk and low miller index surfaces of orthorhombic Mo_2C have strong metallic character.

On the basis of the computed surface energies (Fig. 1), the (1 1 0)-Mo/C-2 and (1 1 1)-Mo/C-1 terminations are most stable (2.38 and 2.42 J/m^2). Closer inspection shows that both surface Mo and C atoms on these terminations have higher coordination numbers than on the other surfaces (the saturated coordination number of Mo and C in Mo_2C bulk is three and six, respectively).

3.2. Surface stability and morphology

In heterogeneous catalysis, surface structures of catalysts play very important roles in activities, and the active centers are the coordinatively unsaturated sites [86,87]. The surface stabilities of catalysts are related with the surface structures, and experimental conditions (such as carburization abilities during the preparation of carbide) always affect the surface structures. This is also why that catalysts prepared under different conditions exhibit quite different activities. As the indicator for surface stability, surface energy has an intimate relationship with the value of carbon chemical potentials (μ_C) which can reflect the change of carburization ability (a less negative μ_C indicates stronger carburization ability).

Fig. 3 shows the relationship between surface energies and μ_C in the ranges of −12 to −6 eV. It reveals that different surface terminations present quite diverse trends with μ_C, i.e., the surface energies of Mo-rich terminations increase with increasing μ_C, while those of C-rich terminations decrease, i.e., C-terminated surfaces are more stable under stronger carburization ability (large value of μ_C) than Mo-terminated surfaces. The most stable surface is different at different μ_C. For example, the (1 1 0)-Mo termination is most stable in the μ_C range of −12.0 to −10.7 eV, and the (1 0 0)-Mo termination becomes most stable in the μ_C range of −10.7 to −10.2 eV. In the μ_C range of −10.2 to −9.5 eV, the (1 1 1)-Mo/C-1 termination becomes most stable. In the μ_C range of −9.5 to −8.5 eV, the (1 1 0)-Mo/C-2 termination is most stable, while the (1 1 0)-Mo/C-relaxed termination becomes most stable in the μ_C range of −8.5 to −6.0 eV. In this respect, it should be noted that the choice of surfaces as well as terminations is essential for a clear description of important catalysis reaction mechanisms by using DFT calculations.

On the basis of the computed μ_C in Fig. 3, we plotted the ideal equilibrium crystal shapes by using the standard Wulff construction [88,89]. In the standard Wulff construction, the orientation-dependent surface free energy for a given closed volume is minimized and the exposure of a facet depends not only on its surface free energy but also on its orientation in its crystal. In Supporting Information, the surface energies of all twenty two terminations at five defined μ_C values are listed (Table S6). Each defined μ_C value corresponds to the carburization ability of a given condition. As shown in Fig. 4, different μ_C values have different equilibrium crystal shapes.

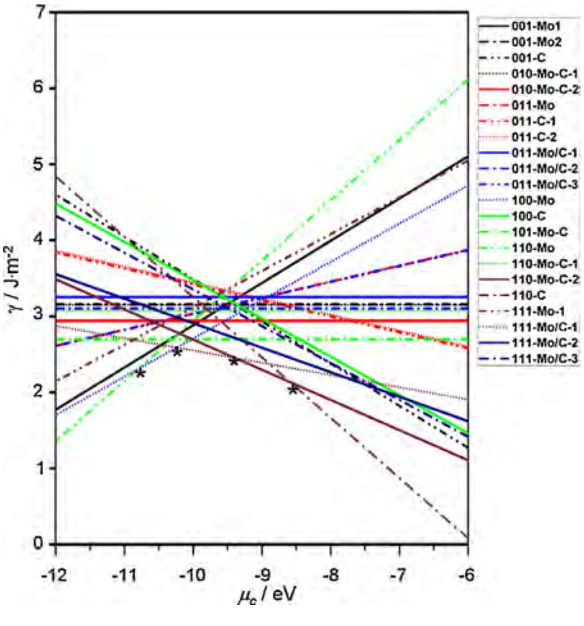

Fig. 3. Surface morphology of orthorhombic Mo_2C from Wulff construction at given carbon chemical potential (μ_c).

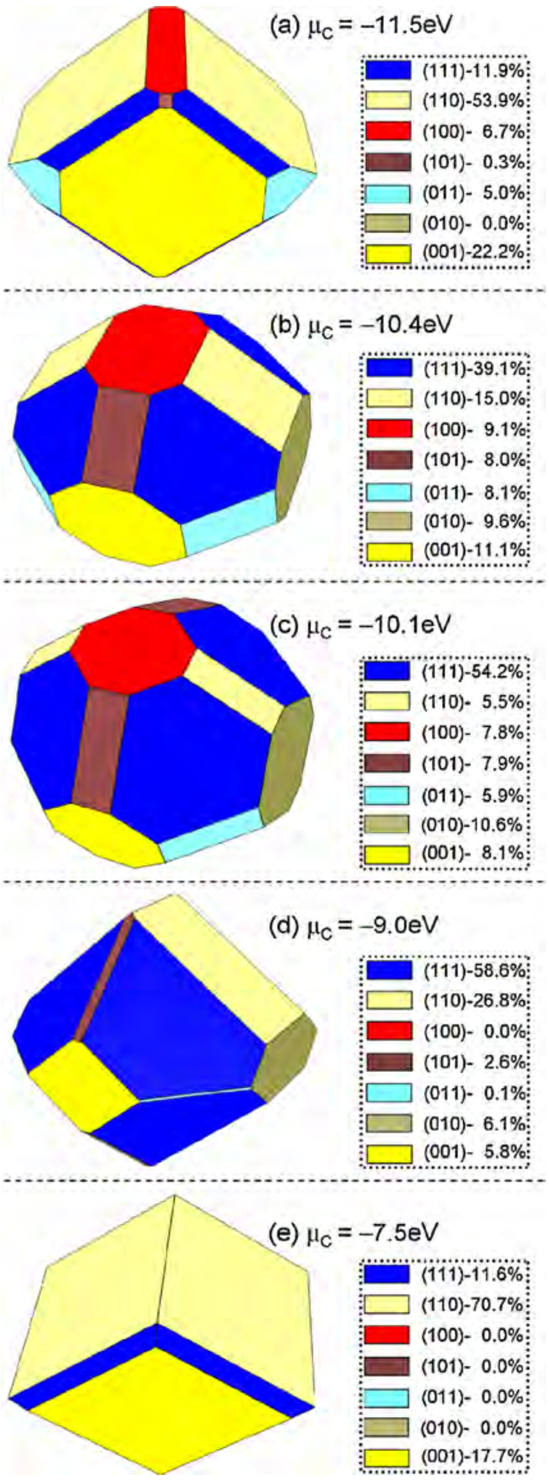

Fig. 4. Side (left) and top (right) views of the most stable Mo_2C terminations.

At very low carburization ability ($\mu_C = -11.5$ eV), there are five exposed Mo terminations, and the (1 1 0)-Mo (53.9%) termination has the largest surface proportion, followed by the (0 0 1)-Mo-1 (22.2%), (1 1 1)-Mo (11.9%), (1 0 0)-Mo (6.7%) and (0 1 1)-Mo (5.0%) terminations.

Increasing the carburization ability to $\mu_C = -10.4$ eV, (1 1 1)-Mo/C-1 has the largest surface proportion (39.1%), followed by (1 1 0)-Mo (15.0%), while (0 0 1)-Mo-1 (11.1%), (0 1 0)-Mo/C-2 (9.6%), (1 0 0)-Mo (9.1%), (0 1 1)-Mo (8.1%) and (1 0 1)-Mo/C (8.0%) have close surface proportions.

At the carburization ability similar to CH_4/H_2 gas mixture ($\mu_C = -10.1$ eV) [57], the surface proportion of (1 1 1)-Mo/C-1 increases to 54.2%, followed by (0 1 0)-Mo/C-2 (10.6%), while (0 0 1)-Mo-1 (8.1%), (1 0 1)-Mo/C-2 (7.9%), (1 0 0)-Mo (7.8%), (0 1 1)-Mo (5.9%) and (1 1 0)-Mo/C-2 (5.5%) have low surface proportions.

At the carburization ability ($\mu_C = -9.0$ eV) similar to graphite, the surface proportion of (1 1 1)-Mo/C-1 increases to 58.6%, followed by (1 1 0)-Mo/C-2 (26.8%), (0 1 0)-Mo/C-2 (6.1%), (0 0 1)-C (5.8%), (1 0 1)-Mo/C (2.6%), while (0 1 1)-Mo/C-2 (0.1%) and (1 0 0)-C disappear.

At very high carburization ability ($\mu_C = -7.5$ eV) similar to CO/CO_2 gas mixture [57], only three surface terminations are exposed, (1 1 0)-Mo/C-relaxed has the largest surface proportion (70.7%), followed by (0 0 1)-C (17.7%) and (1 1 1)-Mo/C-2 (11.6%), while other terminations disappear.

It is now interesting to compare our calculated surface stability and area of individual terminations with the experimental data from X-ray diffraction (XRD). Experimentally, the XRD data of the orthorhombic Mo_2C phase (prepared from TPR method with CH_4/H_2) reveal the exposure of the characteristic crystalline orientations of (1 1 1), (2 0 0), (2 2 0), (3 1 1) and (2 2 2) surfaces [90–93], although their intensities depend on their preparation conditions. These characteristic surfaces are also found to be most stable and representative in our computed surface stabilities and proportions in the range of μ_C from −10.4 to −10.1 eV (carburization ability similar to CH_4/H_2). i.e., the (1 1 1), (1 0 0) and (1 1 0) surfaces together cover the largest surface proportion and the surface stability has the order of (1 0 0) > (1 1 1) > (1 1 0) at $\mu_C = -10.1$ eV (the (2 0 0), (2 2 0) and (2 2 2) surfaces correspond to (1 0 0), (1 1 0) and the (1 1 1) surfaces in DFT calculations).

In Fig. 5, we present the structures of the most stable terminations at five given μ_C (−11.5 eV, −10.4 eV, −10.1 eV, −9.0 eV and −7.5 eV), detailed analysis shows that with the increase of the carburization ability (μ_C) the most stable terminations have interesting surface structures and compositions, i.e., the lower the carburization ability, and the more stable the Mo terminated surface; and the higher the carburization ability, the more stable the Mo/C mixed terminated surfaces. At very low carburization ability, the most stable (1 1 0)-Mo termination (Fig. 5a) is very similar to a metallic Mo surface since the first three layers have only Mo atoms, and the fourth and fifth layers have mixed Mo/C atoms; and these five layers form the repeating unit. With the increase of the carburization ability, the (1 0 0)-Mo termination (Fig. 5b) becomes most stable. Although the first layer of the (1 0 0)-Mo termination still has only Mo atom, the second layer become C atoms, and this is different from the (1 1 0)-Mo termination.

Further increase of the carburization ability results in the formation of mixed Mo/C terminations. The (1 1 1)-Mo/C-1 termination (Fig. 5c) is very open; and the first two layers have mixed Mo/C atoms, and the third layer has only Mo atom; and these layers form the repeating unit. In the (1 1 0)-M/C-2 termination (Fig. 5d), the first two layers have mixed Mo/C atoms, and the third and fourth layers have only Mo atoms, and these four layers form the repeating unit. In the (1 1 0)-Mo/C-relaxed termination (Fig. 5e), the first two layers also have mixed Mo/C atoms, and they are very similar to that of the (1 1 0)-M/C-2 termination, while third layer has only Mo atoms.

It is interesting to note that all these three mixed Mo/C terminations have eight exposed surface C atoms. On the (1 1 1)-Mo/C-1 termination, two carbon atoms have 4-fold coordination (the saturated coordination number of bulk carbon is six), and six carbon atoms have 5-fold coordination. On the (1 1 0)-Mo/C-2 and (1 1 0)-Mo/C-relaxed terminations, four carbon atoms have 4-fold coordination, and the other four carbon atoms have 5-fold coordination.

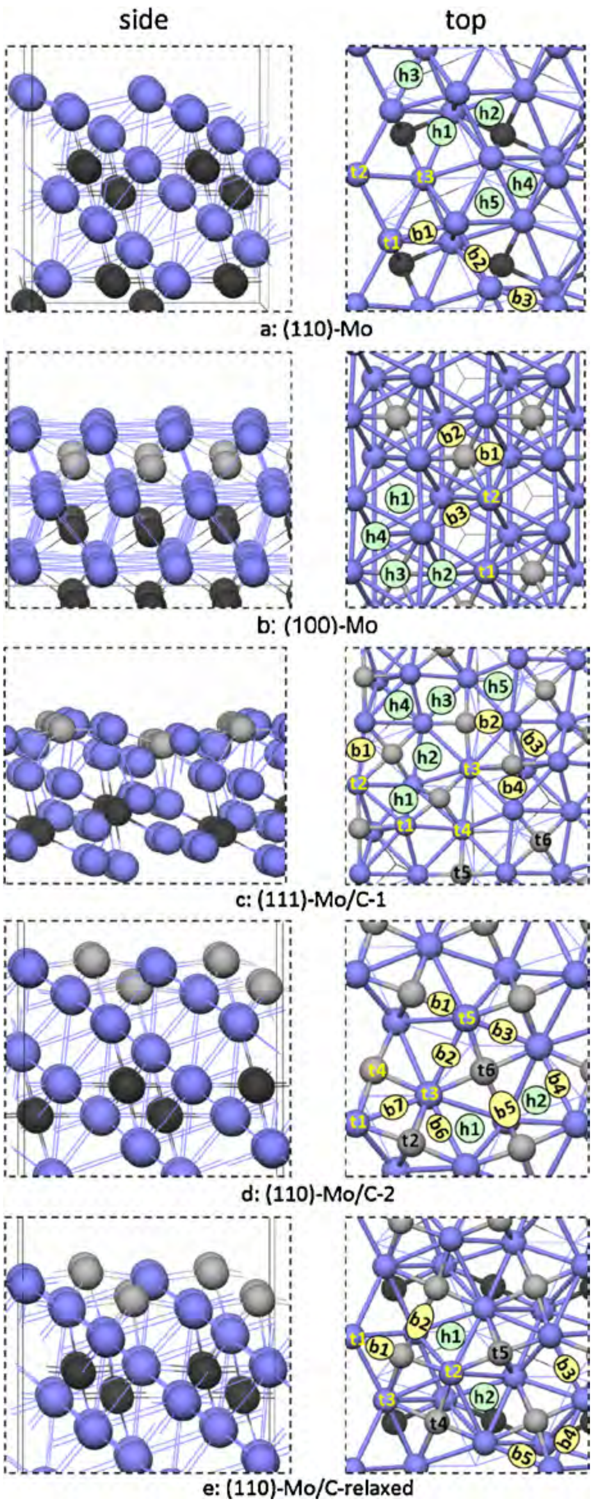

Fig. 5. Selected stable CO adsorption configurations on the five most stable surfaces.

With the increase of the carburization ability (μ_C), the surface structures and composition of the most stable terminations change from the pure metallic ((1 1 0)-Mo and (1 0 0)-Mo) to the mixed and strongly relaxed Mo/C ((1 1 0)-Mo/C-relaxed) terminations. This change in surface structures and composition might explain the observed activity differences in indole HDN by using Mo_2C catalysts from different preparation methods [91]. It is therefore to expect their different structures and energies in CO adsorption and dissociation as discussed below.

3.3. CO adsorption

On the basis of the surface energies and equilibrium crystal shapes, we computed CO adsorption on the five most stable surface terminations in Fig. 5, i.e., (1 1 0)-Mo, (1 0 0)-Mo, (1 1 1)-Mo/C-1, (1 1 0)-Mo/C-2 and (1 1 0)-Mo/C-relaxed. The side and top views of these terminations as well as their possible CO adsorption sites are shown in Fig. 5.

There are eleven possible adsorption sites on the (1 1 0)-Mo termination, i.e., three top sites (**t1–t3**), three bridge sites (**b1–b3**), five hollow sites (**h1–h5**). On the (1 0 0)-Mo termination, nine adsorption sites are possible, i.e., two top sites (**t1–t2**), three bridge sites (**b1–b3**) and four hollow sites (**h1–h4**). These four hollow sites differ in their local arrangements. For example, **h3** has three Mo atoms on the surface and one sub-layer C atom in the hollow, while **h1** has only three surface Mo atoms. In **h2** and **h4**, they have three Mo atoms on the surface in different coordination numbers and one Mo atom in the third layer. The (1 1 1)-Mo/C-1 termination has fifteen possible adsorption sites, i.e., six top sites (**t1–t6**), four bridge sites (**b1**–**b4**) and five hollow sites (**h1–h5**). The (1 1 0)-Mo/C-2 termination has fifteen possible adsorption sites, i.e., six top sites (**t1–t6**), seven bridge sites (**b1–b7**) and two hollow sites (**h1–h2**). On the (1 1 0)-Mo/C-relaxed termination, there are twelve possible adsorption sites, i.e., five top adsorption sites (**t1–t5**) and five bridge adsorption sits (**b1**–**b5**) and two hollow sites (**h1–h2**). However, not all possible sites can form stable adsorption. The computed adsorption energies (E_{ads}), C—O bond length for adsorbed CO (d_{C-O}) and distances of C atom in CO to surface atoms as well as C—O stretching frequencies of the stable adsorptions are given in Table 1 and the structures of all these configurations are given in supporting information (Fig. S1). The adsorption configurations in close energies are shown in Fig. 6.

On the (1 1 0)-Mo termination, there are nine stable adsorption configurations (**t$_1$**, **b$_1$**, **b$_2$**, **b$_3$** and **h$_1$**–h$_5$). The most stable adsorption configuration (Fig. 6a) is **h$_3$** (−2.59 eV), tightly followed by **h$_4$** (-2.53 eV), **h$_1$** (−2.51 eV) and **h$_5$** (−2.50 eV), and the other configurations are higher in energy. In the **h$_1$** and **h$_3$** adsorption configurations, the C atom in CO interacts with four surface Mo atoms while the O atom interacts with two Mo atoms and the C—O bond is elongated to be 1.34 and 1.33 Å, respectively. In the **h$_4$** configuration, the C atom interacts with three surface Mo atoms while the O atom interacts with one surface Mo and the C—O bond is elongated to 1.30 Å. In the h$_5$ configuration, the C atom interacts with four surface Mo atoms while the O atom interacts with one surface Mo and the C—O bond is elongated to 1.33 Å.

On the (1 0 0)-Mo termination, there are mainly 10 stable CO adsorptions configurations (**t$_1$**, **t$_2$**, **b$_1$**, **b$_2$**, **b$_3$**, **h$_{1-1}$**, **h$_{1-2}$** **h$_2$**, **h$_3$** and **h$_4$**). The most stable adsorption configuration (Fig. 6b) is **h$_{1-1}$** (−2.56 eV), followed by **h$_{1-2}$** (−2.51 eV), and the other configurations are less stable. In **h$_{1-1}$**, the C atom of CO adsorbs on the hollow site and the O atom interacts with two surface Mo atoms (one has two bulk C coordination and another has only one bulk C coordination); and the C—O bond is elongated to 1.27 Å. This adsorption configuration is line with the result reported by Ren et al. [69] in studying CO adsorption on the (1 0 0) surface of the orthorhombic Mo_2C phase. In **h$_{1-2}$**, the C atom of CO adsorbs on the same hollow site as **h$_{1-1}$** and the C—O bond of 1.29 Å, however, the O atom interacts with two surface Mo atoms (each coordinates with only one bulk C atom). Although the (1 0 0)-Mo surface has only one surface layer Mo atom, the adsorption energy of **h$_{1-1}$** is close to that of **h$_3$** on the (1 1 0)-Mo termination (−2.59 eV). It is interesting to compare the differences and similarities in their properties between the (1 0 0)-Mo surface of the orthorhombic Mo_2C phase and the (0 0 1) surface of the hexagonal Mo_2C phase since they have very similar surface structures and adsorption sites. The orthorhombic Mo_2C

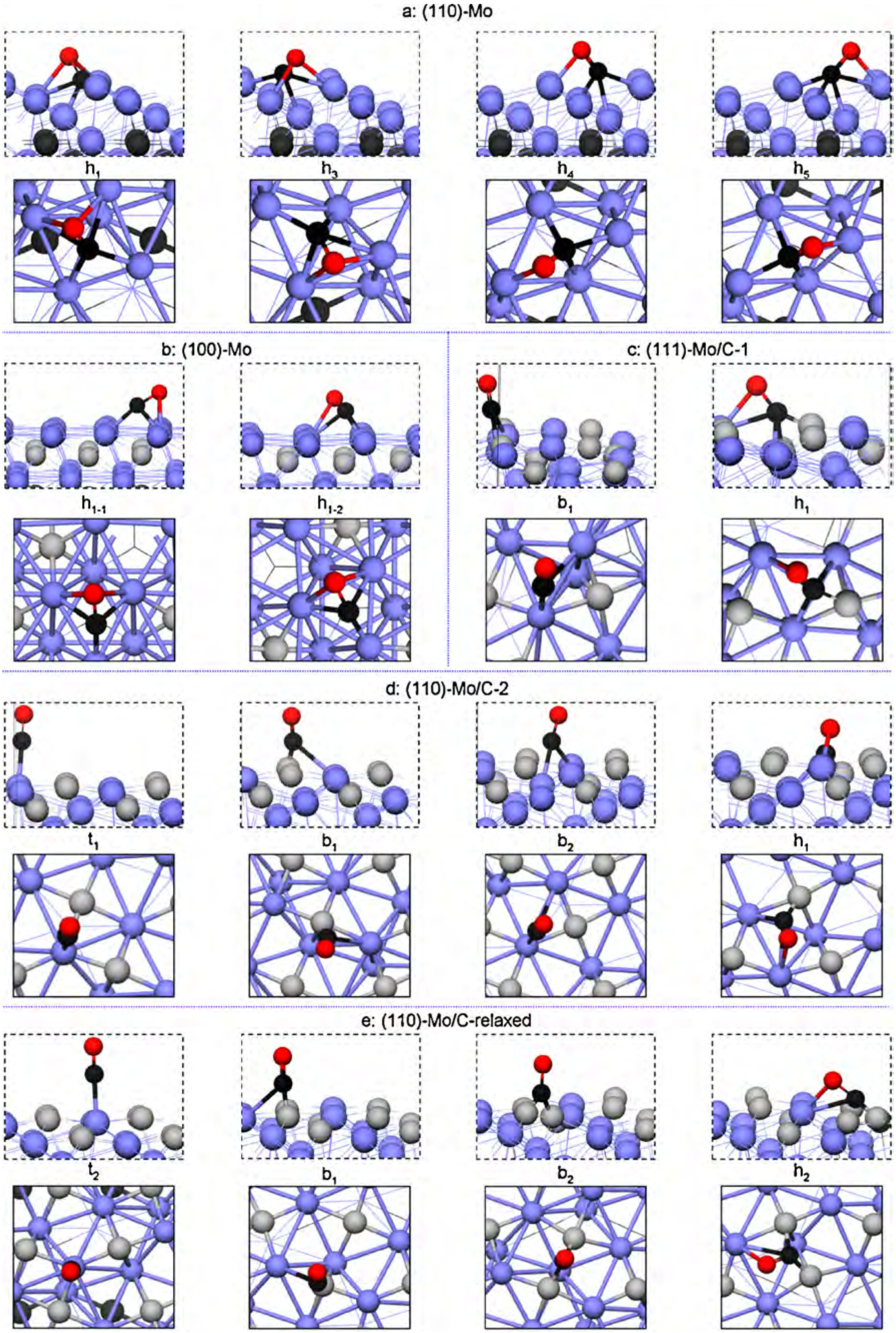
a: (110)-Mo
h1
h3
h4
h5
b: (100)-Mo
h1-1
h1-2
c: (111)-Mo/C-1
b1
h1
d: (110)-Mo/C-2
t1
b1
b2
h1
e: (110)-Mo/C-relaxed
t2
b1
b2
h2

Fig. 6. Selected stable CO adsorption configurations on the five most stable surfaces (surface Mo/blue; surface C/gray; in CO, C/black; O/red). (For interpretation of the references to color in this figure legend, the reader is referred to the web version of this article.)

Table 1
CO adsorption energies (E_{ads}, eV), C—O distances ($d_{C–O}$, Å) and distances of CO to surface Mo atoms ($d_{Mo–C}$ and $d_{Mo–O}$, Å) and to surface C atoms ($d_{Cs–C}$, Å), as well as CO stretching frequency (ν, cm^{-1}) on the most stable Mo_2C terminations under different conditions (**t** for top sites, **b** for bridge sites and **h** for hollow sites).

Site	E_{ads}	$d_{C–O}$	$d_{Mo–C}$	$d_{Mo–O}$	$d_{Cs–C}$	$\nu_{C–O}$
(1 1 0)-Mo						
$\mathbf{t_1}$	−2.22	1.19	2.00			1805
$\mathbf{b_1}$	−1.94	1.23	2.01, 2.19	2.37		1581
$\mathbf{b_2}$	−2.33	1.23	1.96, 2.29	2.27		1554
$\mathbf{b_3}$	−2.35	1.24	1.96, 2.26	2.25		1546
$\mathbf{h_1}$	−2.51	1.34	2.10, 2.33, 2.27, 2.28	2.22, 2.24		1135
$\mathbf{h_2}$	−1.72	1.26	2.02, 2.32, 2.32	2.37		1440
$\mathbf{h_3}$	−2.59	1.33	2.04, 2.19, 2.24, 2.39	2.15, 2.30		1118
$\mathbf{h_4}$	−2.53	1.30	2.07, 2.17, 2.37	2.11		1228
$\mathbf{h_5}$	−2.50	1.33	2.07, 2.23, 2.27, 2.23	2.06		1118
(1 0 0)-Mo						
$\mathbf{t_1}$	−2.08	1.17	2.03			1931
$\mathbf{t_2}$	−1.99	1.17	2.02			1922
$\mathbf{b_1}$	−2.48	1.24	1.98, 2.22	2.32		1535
$\mathbf{b_2}$	−2.20	1.23	2.02,2.28	2.47		1564
$\mathbf{b_3}$	−2.36	1.24	2.00,2.22	2.38		1526
$\mathbf{h_{1-1}}$	−2.56	1.27	1.98, 2.25, 2.29	2.40, 2.47		1409
$\mathbf{h_{1-2}}$	−2.51	1.29	1.98, 2.22, 2.28	2.37, 2.39		1335
$\mathbf{h_2}$	−2.18	1.28	1.97, 2.33, 2.35	2.35, 2.45		1381
$\mathbf{h_3}$	−1.79	1.20	2.26, 2.31, 2.31			1680
$\mathbf{h_4}$	−2.25	1.28	1.98, 2.29, 2.31	2.37, 2.46		1375
(1 1 1)-Mo/C-1						
$\mathbf{t_1}$	−1.45	1.17	2.03			1939
$\mathbf{t_2}$	−1.58	1.19	2.01			1804
$\mathbf{t_3}$	−0.97	1.16	2.03			1959
$\mathbf{b_1}$	−1.59	1.20	2.01, 2.40			1764
$\mathbf{h_1}$	−1.71	1.30	2.17, 2.26, 2.35	2.17	1.40	1379
$\mathbf{h_2}$	−0.09	1.27	2.13, 2.55, 2.27	2.35	1.40	1471
$\mathbf{h_3}$	−0.96	1.29	2.14, 2.24	2.21	1.41	1386
$\mathbf{h_4}$	−1.22	1.26	2.10, 2.15, 2.27	2.27		1397
(1 1 0)-Mo/C-2						
$\mathbf{t_1}$	−1.39	1.16	2.04			1960
$\mathbf{b_1}$	−1.17	1.20	2.37		1.36	1879
$\mathbf{b_2}$	−0.85	1.18	2.03, 2.51			1843
$\mathbf{h_1}$	−0.13	1.27	2.08, 2.36		1.42	1461
(1 1 0)-Mo/C-relaxed						
$\mathbf{t_1}$	−1.26	1.17	2.03			1961
$\mathbf{t_2}$	−1.42	1.16	2.04			1964
$\mathbf{t_3}$	−0.66	1.17	2.03			1939
$\mathbf{b_1}$	−1.14	1.19	2.40		1.42	1928
$\mathbf{b_2}$	−0.43	1.23			1.51, 1.57	1581
$\mathbf{h_1}$	−0.24	1.27	2.10, 2.43	2.34	1.21	1488
$\mathbf{h_2}$	−0.68	1.33	2.42	2.17	1.47, 1.48	1172

Calculated C—O bond length (1.14 Å) and C—O stretching frequency (2124 cm^{-1}).

phase has a structure with Mo atoms slightly distorted from their positions in close-packed planes and carbon atoms orderly occupying one-half of the octahedral interstitial sites. In the hexagonal phase, Mo atoms form a hexagonally close packed structure with carbon atoms randomly filling half of the octahedral interstitial sites. The adsorption of CO on the (0 0 1) surface of the hexagonal Mo_2C phase has been systematically studied by Shi et al. [67] using a cluster model and the most stable adsorption configuration is also located on the 3F hollow site (three surface Mo atoms with a carbon vacancy in the second layer).

On the (1 1 1)-Mo/C-1 termination, there are eight stable CO adsorption configurations ($\mathbf{t_1}$, $\mathbf{t_2}$, $\mathbf{t_3}$, $\mathbf{b_1}$, $\mathbf{h_1}$, $\mathbf{h_2}$, $\mathbf{h_3}$ and $\mathbf{h_4}$) and $\mathbf{h_1}$ (Fig. 6c) has the largest adsorption energy (−1.71 eV), followed by $\mathbf{b_1}$ (−1.59 eV) and $\mathbf{t_2}$ (−1.58 eV). In $\mathbf{h_1}$, the adsorbed CO forms surface ketenylidene (C = C = O), in which the C atom of CO interacts with three surface Mo atoms and one surface C atom, while the O atom interacts with one surface Mo atom. Indeed, an in situ infrared study of CO adsorption on freshly prepared Mo_2C showed the existence of C = C = O [94]. Although the C atom of CO interacts with three surface Mo atoms in $\mathbf{h_1}$ on the (1 1 1)-Mo/C-1, which is similar to those of $\mathbf{h_{1-1}}$ on the (1 0 0)-Mo surface (−2.56 eV), the adsorption energy of $\mathbf{h_1}$ is much lower. In addition, the adsorption energies on the other hollow sites ($\mathbf{h_2}$, $\mathbf{h_3}$, $\mathbf{h_4}$) are much lower (−0.09, −0.96, −1.22 eV, respectively).

On the (1 1 0)-Mo/C-2 termination, there are four stable adsorption configurations ($\mathbf{t_1}$, $\mathbf{b_1}$, $\mathbf{b_2}$ and $\mathbf{h_1}$). The most stable adsorption configuration is $\mathbf{t_1}$ (−1.39 eV, Fig. 6d), followed by $\mathbf{b_1}$ (−1.17 eV), while $\mathbf{b_2}$ (−0.85 eV) and $\mathbf{h_1}$ (−0.13 eV) are higher in energy. On the (1 1 0)-Mo/C-relaxed termination, seven stable adsorption configurations ($\mathbf{t_1}$, $\mathbf{t_2}$, $\mathbf{t_3}$, $\mathbf{b_1}$, $\mathbf{b_2}$, $\mathbf{h_1}$ and $\mathbf{h_2}$) have been located, and the most stable one (Fig. 6e) is $\mathbf{t_2}$ with adsorption energy of −1.42 eV, and the second most stable one is $\mathbf{t_1}$ with adsorption energy of −1.26 eV. Despite of its interesting ketone-like structure of $\mathbf{h_2}$, the adsorption energy is quite low (−0.68 eV).

Due to their surface structures and compositions of these stable terminations, their CO adsorption configurations and energies are also very different. The most stable CO adsorption configuration changes from the 4-fold hollow site and 3-fold hollow site on the metallic termination to the 3-fold hollow site with the formation of surface C═C═O species on the mixed Mo/C termination. With the further expose of surface C atoms on the mixed and strongly relaxed Mo/C terminations, atop adsorption configuration of CO becomes most stable. At the same time, the CO adsorption energy decreases accordingly.

Table 2
CO dissociation barrier (E_a, eV) and dissociation energy (ΔE_r, eV), dissociating C—O distance ($d_{\text{C–O}}$, Å) in transition state and the corresponding imaginary frequency (V_{imag}, cm^{-1}) as well as the calculated adsorption energies of the initial (IS) and transition (TS) states.

Initial state	E_ads (IS)	E_ads (TS)	E_a	ΔE_r[a]	ΔE_r[b]	ΔE_r[c]	$d_{\text{C–O}}$	V_imag
				(1 1 0)-Mo				
h_1	−2.51	−1.92	0.59	−1.24	−1.65	−4.16	1.90	−435
h_3	−2.59	−1.97	0.62	−1.33	−1.57		1.92	−351
h_5	−2.50	−1.81	0.69	−0.58	−1.66		1.87	−440
				(1 0 0)-Mo				
$h_{1\text{-}1}$	−2.56	−1.51	1.05	−1.71	−1.93	−4.49	1.70	−525
				(1 1 1)-Mo/C-1				
h_1	−1.71	−0.45	1.26	−0.50	−0.71	−2.42	1.86	−479
h_2	−0.09	0.97	1.06	0.29	−2.33		1.88	−490
h_3	−0.96	0.20	1.16	−0.92	−1.46		1.82	−503
h_4	−1.22	0.09	1.31	−0.10	−1.21		1.93	−446
				(1 1 0)-Mo/C-2				
b_1	−1.17	1.07	2.24	1.02	−0.22	−1.39	1.87	−503
b_2	−0.85	1.02	1.87	0.98	−0.54		1.91	−443
h_1	−0.13	1.32	1.45	−0.23	−1.26		1.75	−455
				(1 1 0)-Mo/C-relaxed				
b_1	−1.14	0.40	1.54	1.26	−0.49	−1.63	1.91	−444
b_2	−0.43	0.32	0.75	−0.24	−1.20		1.93	−516
h_1	−0.24	1.67	1.91	−0.44	−1.39		1.90	−472
h_2	−0.68	0.12	0.80	−0.84	−0.95		1.86	−517

[a] Final state is the C and O co-adsorption directly from dissociation.
[b] Final state is the most stable C and O co-adsorption after diffusion.
[c] Energy difference between the most stable C and O co-adsorption after diffusion and gaseous CO molecule.

3.4. *CO dissociation*

Since CO dissociation is a critical step in CO hydrogenation processes [95–98], we computed direct CO dissociation on those most stable surfaces into surface C and O on the basis of the most stable adsorption configurations on the metallic surface terminations as well as the adsorption configurations with highly activated CO on the mixed Mo/C terminations. In the dissociated state with surface C and O atoms, we computed not only their co-adsorption directly from dissociation but also the most stable co-adsorption state after diffusion. The computed direct CO dissociation pathway, the activation barrier, the C—O distance in transition state and the imaginary frequencies are given in Table 2. All adsorption structures of the initial states, transition states and final states are given in Supporting information (Fig. S2).

On the (1 1 0)-Mo termination, we used the most stable adsorbed CO as initial state (**h_3**) for CO dissociation because of the highly activated CO with 4-fold coordination of C atom and 2-fold coordination of O atom on the surface. The computed CO dissociation barrier is 0.62 eV, which is much smaller than the CO adsorption energy (−2.59 eV), and the dissociation energy is highly exothermic (−1.65 eV, or −4.16 eV to gaseous CO molecule). In the transition state, the dissociating C—O distance is 1.92 Å, which is much longer than that in the initial state (1.33 Å). In addition, we computed the CO dissociation of the adsorbed **h_1** and **h_5** configurations due to their very similar adsorption configurations to **h_3**, and the CO dissociation barrier is 0.59 and 0.69 eV, respectively; and the dissociation energy is exothermic by 1.57 and 1.66 eV, respectively. These show clearly that very close adsorption configurations have very close energetic parameters.

On the (1 0 0)-Mo termination, the most stable adsorbed CO (**$h_{1\text{-}1}$**) has 3-fold coordination C atom and 2-fold coordinated O atom, which is similar to **h_3** on the (1 1 0)-Mo termination. The computed CO dissociation barrier is 1.05 eV, smaller than the CO adsorption energy (−2.56 eV), and the dissociation energy is highly exothermic (−1.93 eV or −4.49 eV to gaseous CO molecule). In the transition state, the dissociating C—O distance is 1.70 Å, longer than that in the initial state (1.27 Å).

On the mixed (1 1 1)-Mo/C-1 termination, we computed the dissociation of the adsorbed CO on the hollow sites (**h_1** to **h_4**) due to their close C—O distances in the initial states, although they have very different adsorption energies (Table 1). For the most stable adsorption configuration (**h_1**), the computed CO dissociation barrier is 1.26 eV, slightly lower than the CO adsorption energy (−1.71 eV), and the dissociation energy is exothermic (−0.71 eV or −2.42 eV to gaseous CO molecule). In the transition state, the dissociating C—O distance is 1.86 Å, longer than that in the initial state (1.30 Å). This is similar to those on the metallic (1 1 0)-Mo and (1 0 0)-Mo terminations. For the less stable adsorption configurations (**h_2**, **h_3**, **h_4**), the computed CO dissociation barriers (1.06, 1.16 and 1.31 eV, respectively) are higher than their adsorption energies (−0.09, −0.96 and −1.22 eV, respectively), indicating that CO desorption is more favorable than dissociation thermodynamically. However, the CO dissociation energies are exothermic (−2.33, −1.46 eV and −1.21 eV) for **h_2, h_3** and **h_4**.

On the mixed (1 1 0)-Mo/C and (1 1 0)-Mo/C-relaxed terminations, we computed CO dissociation on the less stable bridge and hollow sites instead of the most stable atop sites. This is because that at atop sites CO is much less activated and very difficult to dissociate. As shown in Table 2, the computed CO dissociation barriers on either the bridge or the hollow sites are much larger than their CO adsorption energies, indicating that CO desorption is thermodynamically more favorable than dissociation. The transition states have positive activation barriers compared to gaseous CO molecule. However, the computed CO dissociation energies are exothermic compared to gaseous CO molecules. On the basis of their adsorption energies, the CO dissociation is exothermic for **b_1**, **b_2** and **h_1** on the (1 1 0)-Mo/C-2 termination; and on the (1 1 0)-Mo/C-relaxed termination, the CO dissociation is also exothermic for **b_1**, **b_2**, **h_1** and **h_2**.

3.5. *Micro-kinetics of CO dissociation*

Our computational results show clearly that metallic (1 1 0)-Mo and (1 0 0)-Mo terminations adsorb CO much more strongly than mixed Mo/C termination. It is also found that CO dissociation barriers on the metallic terminations are lower than their respective adsorption energies, while CO dissociation barriers on the mixed Mo/C terminations are higher than their respective adsorption energies. These differences in CO adsorption energies and dissociation barriers imply different CO dissociation mechanisms on different terminations.

Table 3
CO adsorption Gibbs free energies (ΔG_{ads}, eV), adsorption rate constant (k_1, s^{-1}), desorption rate constant (k_{-1}, s^{-1}), CO dissociation rate constant (k_2, s^{-1}) and total rate constant of CO dissociations (K_{total}, s^{-1}) on five surface terminations at 600 K and 40atm.

IS	ΔG_{ads}	k_1	k_{-1}	k_2	K_{total}
(1 1 0)-Mo					
$\mathbf{h}_1$	−1.53	7.33×10^{12}	1.36×10^{-13}	1.03×10^{-5}	1.03×10^{-5}
$\mathbf{h}_3$	−1.61	3.19×10^{13}	3.14×10^{-14}	1.03×10^{-5}	1.03×10^{-5}
$\mathbf{h}_5$	−1.52	5.42×10^{12}	1.85×10^{-13}	1.66×10^{-6}	1.66×10^{-6}
(1 0 0)-Mo					
$\mathbf{h}_{1\text{-}1}$	−1.58	1.79×10^{13}	5.60×10^{-14}	1.55×10^{-9}	1.55×10^{-9}
(1 1 1)-Mo/C-1					
$\mathbf{h}_1$	−0.73	1.39×10^{6}	7.20×10^{-7}	2.80×10^{-11}	2.80×10^{-11}
$\mathbf{h}_2$	0.89	3.22×10^{-8}	3.11×10^{7}	1.28×10^{-9}	1.33×10^{-24}
$\mathbf{h}_3$	0.02	0.69	1.46	1.80×10^{-10}	8.51×10^{-11}
$\mathbf{h}_4$	−0.23	89.12	0.01	1.03×10^{-11}	1.03×10^{-11}
(1 1 0)-Mo/C-2					
$\mathbf{b}_1$	−0.19	40.35	0.03	1.46×10^{-19}	1.46×10^{-19}
$\mathbf{b}_2$	0.13	0.08	12.95	1.87×10^{-16}	1.16×10^{-18}
$\mathbf{h}_1$	0.85	6.76×10^{-8}	1.48×10^{7}	6.81×10^{-13}	3.11×10^{-29}
(1 1 0)-Mo/C-relaxed					
$\mathbf{b}_1$	−0.16	21.23	0.05	1.15×10^{-13}	1.15×10^{-13}
$\mathbf{b}_2$	0.55	2.30×10^{-5}	4.35×10^{4}	4.97×10^{-7}	2.63×10^{-16}
$\mathbf{h}_1$	0.74	5.81×10^{-7}	1.72×10^{6}	9.09×10^{-17}	3.07×10^{-29}
$\mathbf{h}_2$	1.11	4.98×10^{-10}	2.01×10^{9}	1.85×10^{-7}	4.58×10^{-26}

Since the activity of CO dissociation has an intimated relationship with CO concentration, temperature and pressure, it is not plausible to only consider the activation energy barriers. Here, we present a simple micro-kinetic modeling to discuss the CO dissociation activities on the five considered surfaces. For a simple CO dissociation on the surface, the reaction occurs through adsorption and desorption as well as dissociation (Eq. (1)); where S is the adsorption site on the surface and the rate constant for the adsorption, desorption and CO dissociation is k_1, k_{-1} and k_2, respectively. The detailed information for the micro-kinetic models is given in Supporting information.

$$CO(g) + S \leftrightarrow CO(s) \rightarrow C(s) + O(s) \tag{1}$$

The computed k_1, k_{-1} and k_2 values at 600 K and 40 atm in Table 3 facilitate the differentiation of the rate-determining step and reaction order of CO dissociation on these five chosen surface terminations. On the (1 1 0)-Mo and (1 0 0)-Mo terminations, k_1 are much larger than k_2 and k_{-1}, and the reaction rate is $r = k_2 C_s$ (C_s represents the total number of adsorption sites). On the sites $\mathbf{h}_3$ site of (1 1 0)-Mo with the largest adsorption free energy, for example, k_1 ($3.19 \times 10^{13}\ s^{-1}$) is much larger than k_2 and k_{-1} ($1.03 \times 10^{-5}\ s^{-1}$ and $3.14 \times 10^{-14}\ s^{-1}$), and the total reaction rate is determined by k_2 ($1.03 \times 10^{-5}\ s^{-1}$). This indicates that CO dissociation on these metallic terminations is the rate-determining step and the reaction order is zero.

On the (1 1 1)-Mo/C-1, k_1 are much larger than k_2 and k_{-1} on the $\mathbf{h}_1$ and $\mathbf{h}_4$ sites and CO dissociation is the rate-determining step, while the reaction order is zero. On the $\mathbf{h}_2$ site, however, k_{-1} is much larger than k_2 and k_1 ($3.11 \times 10^{7}\ s^{-1}$ vs $1.28 \times 10^{-9}\ s^{-1}$ and $3.22 \times 10^{-8}\ s^{-1}$) and the total reaction rate is $r = k_1 k_2 C_{[CO(g)]} C_s / k_{-1}$ ($1.33 \times 10^{-24}\ s^{-1}$). This indicates that CO adsorption on these mixed terminations is the rate-determining step and the reaction order is first. Similarly, two reaction mechanisms co-exist on the (1 1 0)-Mo/C-2 and (1 1 0)-Mo/C-relaxed terminations, i.e., zero order on the $\mathbf{b}_1$ sites and first order on the other sites.

A representative comparison shows that CO dissociation on the $\mathbf{h}_3$ site of (1 1 0)-Mo rate is much faster than on the $\mathbf{h}_2$ site of (1 1 1)-Mo/C-1 ($1.03 \times 10^{-5}\ s^{-1}$ vs $1.33 \times 10^{-24}\ s^{-1}$).

4. Conclusion

Using periodic density functional theory calculations we have systematically studied the structure and the stability of all twenty-two terminations of the seven low-Miller index orthorhombic Mo_2C surfaces.

Among all these 22 terminations, strong surface reconstruction and relaxation have been found for the (1 1 0)-C termination; and after the optimization, the pure C termination is relaxed to the mixed (1 1 0)-Mo/C termination; while other surface terminations have only moderate relaxations (less than 20% in surface energies) and they are not reconstructed.

An intrinsic and strong correlation between surface energies and carbon chemical potentials (μ_C) has been estimated, where μ_C reflects the carburization ability. It is found that the surface termination and composition depend strongly on the carburization ability. At low carburization ability, terminations with more metallic Mo atoms on the surface are more stable and favorable, while at high carburization ability, terminations with both Mo and C atoms exposed on the surfaces become more stable and auspicious.

The exposed terminations and their surface area proportions in the range of μ_C from −10.4 to −10.1 eV on the basis of the standard Wulff construction are supported by experimentally detected XRD data. The surface stability follows the order of $(1 0 0) > (1 1 1) \approx (1 1 0)$ at $\mu_C = -10.4$ eV, while it changes to $(1 1 1) > (1 0 0) > (1 1 0)$ at $\mu_C = -10.1$ eV. Indeed the experimentally synthesized orthorhombic Mo_2C with different methods present similar XRD peak intensity orders for these three surfaces.

The remarkable and interesting differences among the metallic and the mixed Mo/C surface terminations have also been revealed by CO adsorption and dissociation on these surfaces. On the metallic surface terminations, the most stable CO adsorption configuration prefers the 4-fold and 3-fold sites with titled and strongly activated CO. On the mixed Mo/C surface terminations, the most stable CO adsorption configuration changes from 3-fold site to bridge site as well as to atop sites, and surface ketenylidene (C=C=O) species become possible and stable.

For CO dissociation on these most stable surface terminations, two notable reaction mechanisms have been identified on the basis of the computed CO adsorption energies and dissociation barriers. On the metallic surface terminations, the CO dissociation barriers are lower than the CO adsorption energies, and CO dissociation represents the rate-limiting step. On the mixed Mo/C surface terminations, the CO dissociation barriers are higher than the CO adsorption energies, and therefore, CO adsorption is the rate-limiting step. On the basis of a micro-kinetic model, CO dissociation is zero order reaction on the metallic terminations, and first order reaction on the mixed Mo/C terminations. CO dissociation on the metallic terminations is much faster than on the mixed Mo/C terminations.

Our exciting findings facilitate a deeper understanding into the surface structures and activity, and provide the insights into the different catalytic properties of orthorhombic Mo_2C catalysts prepared from different methods and procedures.

Acknowledgments

This work was supported by National Basic Research Program of China (No. 2011CB201406), Chinese Academy of Science and Synfuels CHINA. Co., Ltd. We also acknowledge general financial support from the BMBF and the state of Mecklenburg-Vorpommern (Germany).

Appendix A. Supplementary data

Supplementary data associated with this article can be found, in the online version, at http://dx.doi.org/10.1016/j.apcata.2014.03.042.

References

[1] J.G. Chen, Chem. Rev. 96 (1996) 1447–1498.
[2] J.G. Chen, J. Eng, S.P. Kelty, Catal. Today 43 (1998) 147–158.
[3] H.H.H. Wu, J.G. Chen, Chem. Rev. 105 (2005) 185–212.
[4] L.E. Toth, Transition Metal Carbides and Nitrides, Academic Press, New York, NY, 1971.
[5] V.A. Gubanov, A.L. Ivanovsky, V.P. Zhukov, Electronic Structure of Refractory Carbides and Nitrides, Cambridge University Press, Cambridge, 1994.
[6] S.T. Oyama, The Chemistry of Transition Metal Carbides and Nitrides, Blackie Academic and Professional, Glasgow, 1996.
[7] C. Moreno-Castilla, M.A. Alvarez-Merino, F. Carrasco-Marin, J.L.G. Fierro, Langmuir 17 (2001) 1752–1756.
[8] Y.F. Zhao, A.C. Dillon, Y.H. Kim, M.J. Heben, S.B. Zhang, Chem. Phys. Lett. 425 (2006) 273–277.
[9] M. Espinoza, J. Cruz-Reyes, M. Del Valle-Granados, E. Flores-Aquino, M. Avalos-Borja, S. Fuentes-Moyado, Catal. Lett. 120 (2008) 137–142.
[10] M.L. Frauwallner, F. Lopez-Linares, J. Lara-Romero, C.E. Scott, V. Ali, E. Hernandez, P. Pereira-Almao, Appl. Catal., A: Gen. 394 (2011) 62–70.
[11] T.J. Zhou, A.M. Liu, Y.R. Mo, H.B. Zhang, J. Phys. Chem. A 104 (2000) 4505–4513.
[12] C.S. Song, W. Wang, S.T. Oyama, V. Schwartz, Am. Chem. Soc. Div. Fuel Chem. Prepr. 48 (2003) 182–184.
[13] S. Weller, L.J.E. Hofer, R.B. Anderson, J. Am. Chem. Soc. 70 (1948) 799–801.
[14] R.W. Joyner, G.R. Darling, J.B. Pendry, Surf. Sci. 205 (1988) 513–522.
[15] Y.G. Wang, B.H. Davis, Appl. Catal., A: Gen. 180 (1999) 277–285.
[16] N. Lohitharn, J.G. Goodwin, E. Lotero, J. Catal. 255 (2008) 104–113.
[17] P.C. Thune, C.J. Weststrate, P. Moodley, A.M. Saib, J. van de Loosdrecht, J.T. Miller, J.W. Niemantsverdriet, Catal. Sci. Technol. 1 (2011) 689–697.
[18] T.P. St Clair, S.T. Oyama, D.F. Cox, S. Otani, Y. Ishizawa, R.L. Lo, K. Fukui, Y. Iwasawa, Surf. Sci. 426 (1999) 187–198.
[19] E. Parthe, V. Sadagopan, Acta Crystallogr. 16 (1963) 202–205.
[20] S.T. Oyama, Catal. Today 15 (1992) 179–200.
[21] R.B. Levy, M. Boudart, Science 181 (1973) 547–549.
[22] M. Nagai, K. Matsuda, J. Catal. 238 (2006) 489–496.
[23] J.A. Schaidle, A.C. Lausche, L.T. Thompson, J. Catal. 272 (2010) 235–245.
[24] M.L. Xiang, D.B. Li, W.H. Li, B. Zhong, Y.H. Sun, Fuel 85 (2006) 2662–2665.
[25] M.L. Xiang, D.B. Li, H.C. Xiao, J.L. Zhang, W.H. Li, B. Zhong, Y.H. Sun, Catal. Today 131 (2008) 489–495.
[26] S. Zaman, K.J. Smith, Catal. Rev.: Sci. Eng. 54 (2012) 41–132.
[27] V. Sundaramurthy, A.K. Dalai, J. Adjaye, Appl. Catal., B: Environ. 68 (2006) 38–48.
[28] H.A. Al-Megren, S.L. Gonzalez-Cortes, T.C. Xiao, M.L.H. Green, Appl. Catal., A: Gen. 329 (2007) 36–45.
[29] M.K. Neylon, S. Choi, H. Kwon, K.E. Curry, L.T. Thompson, Appl. Catal., A: Gen. 183 (1999) 253–263.
[30] S.J. Ardakani, X.B. Liu, K.J. Smith, Appl. Catal., A: Gen. 324 (2007) 9–19.
[31] R. Barthos, F. Solymosi, J. Catal. 249 (2007) 289–299.
[32] F. Solymosi, J. Cserenyi, A. Szöke, T. Bansagi, A. Qszko, J. Catal. 165 (1997) 150–161.
[33] K. Oshikawa, M. Nagai, S. Omi, J. Phys. Chem. B 105 (2001) 9124–9131.
[34] M. Nagai, H. Tominaga, S. Omi, Langmuir 16 (2000) 10215–10220.
[35] J. Ren, C.F. Huo, J.G. Wang, Z. Cao, Y.W. Li, H.J. Jiao, Surf. Sci. 600 (2006) 2329–2337.
[36] J. Ren, J.G. Wang, C.F. Huo, X.D. Wen, Z. Cao, S.P. Yuan, Y.W. Li, H.J. Jiao, Surf. Sci. 601 (2007) 1599–1607.
[37] A.S. Rocha, A.B. Rocha, V.T. Silva, Appl. Catal., A: Gen. 379 (2010) 54–60.
[38] X.C. Liu, A. Tkalych, B.J. Zhou, A.M. Köster, D.R. Salahub, J. Phys. Chem. C 117 (2013) 7069–7080.
[39] P. Liu, J.A. Rodriguez, J.T. Muckerman, J. Phys. Chem. B 108 (2004) 15662–15670.
[40] P. Liu, J.A. Rodriguez, T. Asakura, J. Gomes, K. Nakamura, J. Phys. Chem. B 109 (2005) 4575–4583.
[41] P. Liu, J.A. Rodriguez, J.T. Muckerman, J. Mol. Catal. A: Chem. 239 (2005) 116–124.
[42] P. Liu, J.A. Rodriguez, J. Phys. Chem. B 110 (2006) 19418–19425.
[43] H. Tominaga, M. Nagai, Appl. Catal., A: Gen. 343 (2008) 95–103.
[44] W. Piskorz, G. Adamski, A. Kotarba, Z. Sojka, C. Sayag, G. Djega-Mariadassou, Catal. Today 119 (2007) 39–43.
[45] C. Pistonesi, A. Juan, A.P. Farkas, F. Solymosi, Surf. Sci. 602 (2008) 2206–2211.
[46] M.E. Pronsato, C. Pistonesi, A. Juan, A.P. Farkas, L. Bugyi, F. Solymosi, J. Phys. Chem. C 115 (2011) 2798–2804.
[47] C. Pistonesi, A. Juan, A.P. Farkas, F. Solymosi, Surf. Sci. 604 (2010) 914–919.
[48] H. Tominaga, M. Nagai, J. Phys. Chem. B 109 (2005) 20415–20423.
[49] N.M. Schweitzer, J.A. Schaidle, O.K. Ezekoye, X.Q. Pan, S. Linic, L.T. Thompson, J. Am. Chem. Soc. 133 (2011) 2378–2381.
[50] A.J. Medford, A. Vojvodic, F. Studt, F. Abild-Pedersen, J.K. Nørskov, J. Catal. 290 (2012) 108–117.
[51] H. Tominaga, Y. Aoki, M. Nagai, Appl. Catal., A: Gen. 423 (2012) 192–204.
[52] K.Z. Qi, G.C. Wang, W.J. Zheng, Surf. Sci. 614 (2013) 53–63.
[53] W. Zheng, T.P. Cotter, P. Kaghazchi, T. Jacob, B. Frank, K. Schlichte, W. Zhang, D.S. Su, F. Schüth, R. Schlögl, J. Am. Chem. Soc. 135 (2013) 3458–3464.
[54] Q.Q. Luo, T. Wang, G. Walther, M. Beller, H. Jiao, J. Power Sources 246 (2014) 548–555.
[55] X.R. Shi, S.G. Wang, H. Wang, C.M. Deng, Z.F. Qin, J.G. Wang, Surf. Sci. 603 (2009) 852–859.
[56] J.W. Han, L. Li, D.S. Sholl, J. Phys. Chem. C 115 (2011) 6870–6876.
[57] T. Wang, X.W. Liu, S.G. Wang, C.F. Huo, Y.W. Li, J.G. Wang, H.J. Jiao, J. Phys. Chem. C 115 (2011) 22360–22368.
[58] T. Miyao, I. Shishikura, M. Matsuoka, M. Nagai, S.T. Oyama, Appl. Catal., A: Gen. 165 (1997) 419–428.
[59] A. Kotarba, G. Adamski, W. Piskorz, Z. Sojka, C. Sayag, G.D. Mariadassou, J. Phys. Chem. B 108 (2004) 2885–2892.
[60] M. Nagai, A.M. Zahidul, K. Matsuda, Appl. Catal., A: Gen. 313 (2006) 137–145.
[61] J.R.d.S. dos Santos Politi, F. Vines, J.A. Rodriguez, F. IIlas, Phys. Chem. Chem. Phys. 15 (2013) 12617–12625.
[62] F. Fischer, H. Tropsch, Brennstoff Chem. 7 (1926) 97–116.
[63] K.G. Fang, D.B. Li, M.G. Lin, M.L. Xiang, W. Wei, Y.H. Sun, Catal. Today 147 (2009) 133–138.
[64] D.S. Newsome, Catal. Rev.: Sci. Eng. 21 (1980) 275–318.
[65] C.S. Song, Catal. Today 77 (2002) 17–49.
[66] F. Vines, J.A. Rodriguez, P. Liu, F. Illas, J. Catal. 260 (2008) 103–112.
[67] X.R. Shi, J.G. Wang, K. Hermann, J. Phys. Chem. C 114 (2010) 13630–13641.
[68] T. Wang, S.G. Wang, Y.W. Li, J.G. Wang, H.J. Jiao, J. Phys. Chem. C 116 (2012) 6340–6348.
[69] J. Ren, C.F. Huo, J.G. Wang, Y.W. Li, H.J. Jiao, Surf. Sci. 596 (2005) 212–221.
[70] C. Pistonesi, M.E. Pronsato, L. Bugyi, A. Juan, J. Phys. Chem. C 116 (2012) 24573–24581.
[71] K. Reuter, M. Scheffler, Phys. Rev. B: Condens. Matter 65 (2001) 035406.
[72] K. Reuter, M. Scheffler, Phys. Rev. B: Condens. Matter 68 (2003) 045407.
[73] T. Wang, X.X. Tian, Y.W. Li, J. Wang, M. Beller, H. Jiao, J. Phys. Chem. C 118 (2014) 1095–1101.
[74] T. Wang, Y.W. Li, J. Wang, M. Beller, H. Jiao, J. Phys. Chem. C 118 (2014) 3162–3171.
[75] E. de Smit, F. Cinquini, A.M. Beale, O.V. Safonova, W. van Beek, P. Sautet, B.M. Weckhuysen, J. Am. Chem. Soc. 132 (2010) 14928–14941.
[76] S. Zhao, X.W. Liu, C.F. Huo, Y.W. Li, J. Wang, H. Jiao, J. Catal. 294 (2012) 47–53.
[77] G. Kresse, J. Furthmüller, Comput. Mater. Sci. 6 (1996) 15–50.
[78] G. Kresse, J. Furthmüller, Phys. Rev. B: Condens. Matter 54 (1996) 11169–11186.
[79] P.E. Blochl, Phys. Rev. B: Condens. Matter 50 (1994) 17953–17979.
[80] G. Kresse, Phys. Rev. B: Condens. Matter 59 (1999) 1758–1775.
[81] J.P. Perdew, K. Burke, M. Ernzerhof, Phys. Rev. Lett. 77 (1996) 3865–3868.
[82] R. Coquet, D.J. Willock, Phys. Chem. Chem. Phys. 7 (2005) 3819–3828.
[83] D.O. Scanlon, G.W. Watson, D.J. Payne, G.R. Atkinson, R.G. Egdell, D.S.L. Law, J. Phys. Chem. C 114 (2010) 4636–4645.
[84] G. Henkelman, H. Jónsson, J. Chem. Phys. 113 (2000) 9978–9985.
[85] A.N. Christensen, Acta Chem. Scand. Ser. A: Phys. Inorg. Chem. 31 (1977) 509–511.
[86] R.L. Burwell, G.L. Haller, K.C. Taylor, J.F. Read, Adv. Catal. 20 (1969) 1–96.
[87] F. Dumeignil, J.F. Paul, E. Veilly, E.W. Qian, A. Ishihara, E. Payen, T. Kabe, Appl. Catal., A: Gen. 289 (2005) 51–58.
[88] ⟨http://www.ctcms.nist.gov/wulffman/⟩.
[89] ⟨http://www.geomview.org/⟩.
[90] J.S. Lee, L. Volpe, F.H. Ribeiro, M. Boudart, J. Catal. 112 (1988) 44–53.
[91] S.Z. Li, J.S. Lee, T. Hyeon, K.S. Suslick, Appl. Catal., A: Gen. 184 (1999) 1–9.
[92] R. Kojima, K.I. Aika, Appl. Catal., A: Gen. 219 (2001) 141–147.
[93] P.M. Patterson, T.K. Da, B.H. Davis, Appl. Catal., A: Gen. 251 (2003) 449–455.
[94] W. Wu, Z. Wu, C. Liang, X. Chen, P. Ying, C. Li, J. Phys. Chem. B 107 (2003) 7088–7094.
[95] G.S. Ranhotra, A.T. Bell, J.A. Reimer, J. Catal. 108 (1987) 40–49.
[96] Z.P. Liu, P. Hu, J. Chem. Phys. 114 (2001) 8244–8247.
[97] Z.P. Liu, P. Hu, J. Am. Chem. Soc. 123 (2001) 12596–12604.
[98] A. Michaelides, Z.P. Liu, C.J. Zhang, A. Alavi, D.A. King, P. Hu, J. Am. Chem. Soc. 125 (2003) 3704–3705.

3.5 High Coverage CO Adsorption and Dissociation on the Orthorhombic $Mo_2C(100)$ Surface

Tao Wang, Yong-Wang Li, Jianguo Wang, Matthias Beller, Haijun Jiao*

Journal of Physical Chemistry C **2014**, *118*, 3162-3171.

Summary: CO adsorption and dissociation on the Mo- and C- terminations of the orthorhombic $Mo_2C(100)$ surface at different coverage were systematically investigated on the basis of density functional theory. On the Mo-termination, only molecular adsorption is likely for n_{CO} = 9-16, and mixed molecular and dissociative adsorption becomes possible for n_{CO} = 8, while only dissociative adsorption is favorable for n_{CO} = 1-7. This indicates the coverage dependent CO dissociation and equilibrium between dissociation and desorption. On the C-termination, there is no dissociative adsorption and only molecular adsorption is favorable at all coverage (n_{CO} = 1-16). The computed CO stretching frequencies as well as the predicted desorption states from ab initio thermodynamic analysis agree well with the available experimental findings. The stable coverage as function of temperature and partial pressure provide useful information not only for surface science studies at ultra-high vacuum condition but also for practical applications at high temperature and pressure in exploring reactions.

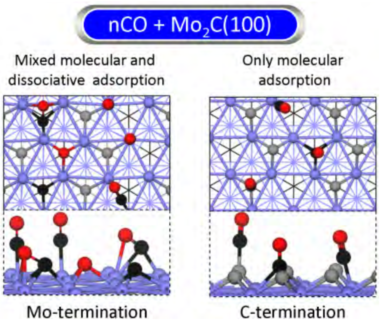
nCO + Mo$_2$C(100)
Mixed molecular and dissociative adsorption
Only molecular adsorption
Mo-termination
C-termination

Contributions

In this paper, I planned, performed and analyzed most calculations for this manuscript. I have done the major part of writing of the manuscript. My contribution as co-author of this paper is approximately 80%.

THE JOURNAL OF
PHYSICAL CHEMISTRY C

Article

pubs.acs.org/JPCC

High Coverage CO Adsorption and Dissociation on the Orthorhombic $Mo_2C(100)$ Surface

Tao Wang,[†] Yong-Wang Li,[‡] Jianguo Wang,[‡] Matthias Beller,[†] and Haijun Jiao*[,†,‡]

[†]Leibniz-Institut für Katalyse e.V. an der Universität Rostock, Albert-Einstein Strasse 29a, 18059 Rostock, Germany

[‡]State Key Laboratory of Coal Conversion, Institute of Coal Chemistry, Chinese Academy of Sciences, Taiyuan 030001, PR China

Supporting Information

ABSTRACT: CO adsorption and dissociation on the Mo and C terminations of the orthorhombic $Mo_2C(100)$ surface at different coverage were systematically investigated on the basis of density functional theory. On the Mo termination, only molecular adsorption is likely for $n_{CO} = 9-16$. Mixed molecular and dissociative adsorption becomes possible for $n_{CO} = 8$, while only dissociative adsorption is favorable for $n_{CO} = 1-7$. This indicates the coverage-dependent CO dissociation and equilibrium between dissociation and desorption. On the C termination, there is no dissociative adsorption, and only molecular adsorption is favorable at all coverages ($n_{CO} = 1-16$). The computed CO stretching frequencies as well as the predicted desorption states from ab initio thermodynamic analysis agree well with the available experimental findings. The stable coverage as a function of temperature and partial pressure provides useful information not only for surface science studies at ultrahigh vacuum conditions but also for practical applications at high temperature and pressure in exploring reactions.

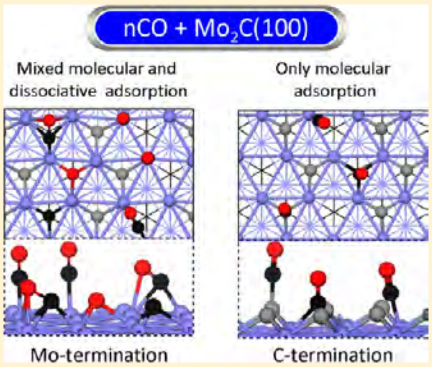
nCO + Mo2C(100)
Mixed molecular and dissociative adsorption
Only molecular adsorption
Mo-termination
C-termination

1. INTRODUCTION

The outstanding physical[1,2] and chemical[3−6] properties of transition metal carbides (TMCs) have attracted great attention from academic researchers and for industrial applications, especially their promising activities in heterogeneous catalysis. As the important and representative members of TMCs, molybdenum (Mo_2C) and tungsten (W_2C) carbides were regarded as the potential substitutes of noble metals as catalysts as shown by the pioneering work of Levy and Boudart in 1973.[7] Since then the catalytic properties of Mo_2C have been intensively investigated experimentally in those reactions initially catalyzed by noble metals, e.g., in water−gas shift (WGS, $CO + H_2O = CO_2 + H_2$) reaction,[8,9] CO hydrogenation to alcohols,[10,11] hydrodesulfurization (HDS),[12] and hydrodenitrogenation (HDN)[13] in petroleum refining, hydrotreating,[14−16] as well as hydrogen production.[17] The Mo termination of the $Mo_2C(001)$ surface[18] has been found to have similar activity in carbon-related reactions as transition metals such as Ru and Ir.

Mo_2C mainly has two crystalline structures with slight distinctions: the orthorhombic[19] and the hexagonal[20] phases. Systematic theoretical studies on these two phases were reported.[21−28] On the related reactions involving CO, Tominaga and Nagai[29] studied the potential energy surface of the WGS reaction and concluded that the formation of CO_2 from O and CO is rate determining. Liu et al. emphasized the importance of surface oxygen on Mo_2C in the WGS reaction.[30] Tominaga et al.[31] studied CO hydrogenation on both clean and cobalt-doped hexagonal $Mo_2C(100)$ surfaces and ruled out the possible formation of CH_3OH on both catalysts. The CO hydrogenation mechanism into CH_4 on both orthorhombic $Mo_2C(100)$ and hexagonal $Mo_2C(101)$ surfaces was reported by Qi et al.,[32] and the orthorhombic $Mo_2C(100)$ surface was proved to have higher activity in CH_4 formation. A recent theoretical study[33] revealed that Mo_2C is a promising catalyst for CO-free hydrogen production from formic acid decomposition. A combined experimental and density functional theory (DFT) study showed very high catalytic activity of hexagonal Mo_2C in ammonia dehydrogenation.[34]

Although CO plays the key role in Fischer−Tropsch synthesis and alcohol synthesis, only a few theoretical studies about CO adsorption and activation on Mo_2C were reported. Ren et al.[35] and Shi et al.[36] calculated CO adsorption on the orthorhombic $Mo_2C(100)$ and hexagonal $Mo_2C(001)$ surfaces, respectively, and they found that the Mo termination can adsorb and activate CO more strongly than the C termination. Pistonesi et al.[37] studied CO adsorption and dissociation on the clean and K-doped orthorhombic $Mo_2C(001)$ surfaces and found that K incorporation strengthens CO adsorption but increases CO dissociation barrier. On the basis of the computed Gibbs free energies, we studied the relationship among temperature, CO equilibrium coverage, and CO partial pressure on the hexagonal Mo_2C surfaces,[38] and found good agreement between the theoretically predicated and experimentally recorded spectra of temperature-programmed CO desorption at low temperature.

Received: December 10, 2013
Revised: January 17, 2014
Published: January 21, 2014

ACS Publications © 2014 American Chemical Society

dx.doi.org/10.1021/jp412067x | *J. Phys. Chem. C* 2014, 118, 3162−3171

Despite the above-mentioned studies, no available work about the adsorption and dissociation of CO at high coverage on the Mo_2C surfaces was reported within the scope of our knowledge. Since experimental studies[39−42] have revealed that catalyst surfaces are always covered by CO molecules before hydrogenation under practical Fischer−Tropsch processes, we have performed systematic DFT studies on the adsorption and dissociation of CO at different coverages on the Mo and C terminations of the orthorhombic $Mo_2C(100)$ surface. Our goal is to probe the effects of CO coverage on adsorption structures and energies as well as activation mechanisms in the initial stage of CO hydrogenation.

2. COMPUTATIONAL MODEL AND METHOD

(a). Model. In computational studies, the choice of appropriate slab surface models is very important for understanding the adsorption properties of molecules and their catalytic mechanisms on the surfaces. Shi et al.[43] and Han et al.[44] calculated the surface energies of the low Miller index surfaces of the hexagonal Mo_2C phase and found the (011) facet to be most stable. The calculated surface free energies of low and high Miller index surfaces of the hexagonal Mo_2C phase using atomistic thermodynamics under the consideration of temperature and gas condition identified the (101) surface to be most stable and representative,[45] in agreement with the available X-ray diffraction (XRD)[46] and high-resolution transmission electron microscopy (HRTEM)[47] results. Recently, Politi et al.[48] computed the atomic and electronic structures of the bulk and low Miller index surfaces of three molybdenum carbide phases (hexagonal and orthorhombic Mo_2C as well as face-centered cubic MoC) and found that the Perdew−Burke−Ernzerhof (PBE) functional is particularly suitable to study molybdenum carbides and that the orthorhombic Mo_2C phase has stronger metallic character.

We used the orthorhombic Mo_2C phase as the unit cell. The calculated lattice parameters for Mo_2C bulk are $a = 4.751$ Å, $b = 6.065$ Å, and $c = 5.237$ Å, very close to the experimental values ($a = 4.732$ Å, $b = 6.037$ Å, and $c = 5.204$ Å).[49] For studying CO adsorption and dissociation, the Mo and C terminations of the orthorhombic $Mo_2C(100)$ surface were modeled by a periodic slab with a thickness of 5.96 and 5.96 Å, which is thick enough based on the tests in our benchmark work. A vacuum layer of 12 Å was set to exclude the slab interactions. The orthorhombic $Mo_2C(100)$ surface is stable and representative and has been prepared and widely investigated by surface science techniques[19,50−52] as well as by theoretical studies.[22,23,26,35] These experimental results can be used for direct comparison with our computed values. Although both orthorhombic and hexagonal Mo_2C phases are available, the former has been found to have higher surface area than the latter from their experimental preparation.[53] In this work, we applied a $p(2 \times 2)$-6L supercell with 16 surface Mo atoms to model the Mo termination and a $p(2 \times 2)$-6L supercell with 8 surface C atoms and 16 exposed Mo atoms for the C termination.

(b). Method. All calculations were done by using the plane-wave-based periodic DFT method implemented in the Vienna ab initio simulation package (VASP).[54,55] The electron ion interaction is described with the projector augmented wave (PAW) method.[56,57] The electron exchange and correlation energy is treated within the generalized gradient approximation in the Perdew−Burke−Ernzerhof formalism (GGA-PBE).[58] To have accurate energies with errors less than 1 meV per atom, a cutoff energy of 400 eV and Gaussian electron smearing method with $\sigma = 0.05$ eV were used. For the bulk optimization, the lattice parameters for the orthorhombic Mo_2C phase were determined by minimizing the total energy of the unit cell on the basis of a conjugated-gradient algorithm to relax the ions, and a $5 \times 5 \times 5$ Monkhorst−Pack k-point grid was used for sampling the Brillouin zone. The geometry optimization was done when forces became smaller than 0.02 eV/Å, and the energy difference was lower than 10^{-4} eV. Adsorption energy (E_{ads}) is calculated by subtracting the energies of gas-phase species and the clean surface from the total energy of the adsorbed system, $E_{ads} = E(\text{adsorbate/slab}) - [E(\text{adsorbate}) + E(\text{slab})]$, and more negative E_{ads} indicate stronger adsorptions. To get the saturated coverage, we used the stepwise adsorption energy, $\Delta E_{ads} = E_{(CO)n+1/slab} - [E_{(CO)n/slab} + E_{CO}]$, where a positive ΔE_{ads} for $n + 1$ adsorbed CO molecules indicates the saturated adsorption with n adsorbed CO molecules.

For evaluating the energy barrier, the transitional state (TS) was located using the nudged elastic band (NEB) method.[59] The TS configurations were verified by vibration analyses, and in all cases, only one imaginary frequency is found. The barrier (E_a) and reaction energy (ΔE_r) are calculated according to $E_a = E_{TS} - E_{IS}$ and $\Delta E_r = E_{FS} - E_{IS}$, where E_{IS}, E_{FS}, and E_{TS} are the energies of the corresponding initial state (IS), final state (FS), and transition state (TS), respectively.

(c). Thermodynamics. As a convenient tool to solve problems referring to real reaction conditions, the ab initio atomistic thermodynamics method, proposed by Scheffler and Reuter,[60,61] has been widely and successfully applied in many other systems.[62−66] The detailed description of the method can be found in the Supporting Information.

3. RESULTS AND DISCUSSION

3.1. Structures and Adsorption Sites of Mo and C Terminations.

The $Mo_2C(100)$ surface consists of alternating Mo and C layers. The schematic side and top views of the Mo and C terminations of the orthorhombic $Mo_2C(100)$ surface and possible adsorption sites are shown in Figure 1. On the Mo termination, there are 16 surface Mo atoms and 9 possible adsorption sites, i.e., two top sites ($\mathbf{t}_1$ and $\mathbf{t}_2$), three bridge sites ($\mathbf{b}_1$, $\mathbf{b}_2$, and $\mathbf{b}_3$), and four 3-fold hollow sites ($\mathbf{h}_1$, $\mathbf{h}_2$, $\mathbf{h}_3$, and $\mathbf{h}_4$). More specifically, there are two types of Mo atoms with different coordination numbers (the saturated bulk Mo coordinates with three C atoms, while that of the C atom coordinates with six Mo atoms). For example, on the $\mathbf{t}_1$ site, the Mo_1 atom coordinates with two C atoms in the second layer and has only one free coordination site. On the $\mathbf{t}_2$ site, the Mo_2 atom coordinates with only one C atom in the second layer and has two free coordination sites. Similarly, the other adsorption sites are also divided by the differences in the coordination numbers of Mo atoms. For those three bridge sites, the $\mathbf{b}_1$ site has one Mo_1 and one Mo_2 atom, the $\mathbf{b}_2$ site two Mo_1 atoms, and the $\mathbf{b}_1$ site two Mo_2 atoms. For the 3-fold hollow sites, they distinguished each other not only by the coordination numbers of three Mo atoms but also the differences of the sublayer atoms. The $\mathbf{h}_1$ site has one surface Mo_1 atom and two Mo_2 atoms as well as a carbon vacancy in the second layer. The $\mathbf{h}_2$ site has two surface Mo_1 atoms as well as one Mo_2 atom and is above a Mo atom in the third layer. The $\mathbf{h}_3$ site has two Mo_1 surface atoms and one Mo_2 atom as well as a carbon atom in the second layer. The $\mathbf{h}_4$ site has one surface Mo_1 atom as well as two Mo_2 atoms and is above a Mo atom in the third layer.

On the C termination, there are 8 surface C atoms as well as 16 exposed Mo atoms and 9 possible adsorption sites, i.e., three

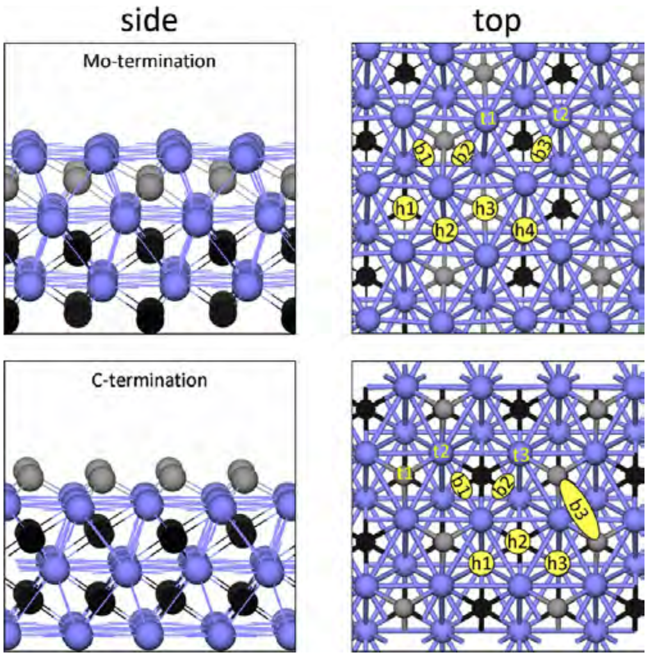

Figure 1. Schematic side and top views of Mo and C terminations of orthorhombic $Mo_2C(100)$ and possible adsorption sites (blue balls for Mo atoms, gray balls for first layer C atoms, and black balls for C atoms in other layers, t for top, b for bridge, and h for hollow).

top sites (**t**$_1$, **t**$_2$, and **t**$_3$), three bridge sites (**b**$_1$, **b**$_2$, and **b**$_3$), and three 3-fold hollow sites (**h**$_1$, **h**$_2$, and **h**$_3$). The coordination numbers of surface atoms on the C termination are quite different from those on the Mo termination. For example, all the surface Mo atoms are saturated and coordinated with three carbon atoms; while surface C atoms only coordinate with three Mo atoms; and each surface C atom has three free coordination sites. For the top adsorption sites, the **t**$_1$ site is located on the surface C atom, while **t**$_2$ and **t**$_3$ are located on the surface Mo atoms. However, these two Mo atoms on the **t**$_2$ and **t**$_3$ sites have a slight difference; i.e., the Mo_{2s} atom in the **t**$_2$ site coordinates with two surface C atoms and one bulk C atom, while that the Mo_{1s} atom in the **t**$_3$ site coordinates with one surface C atom and two bulk C atoms. For the bridge sites, the **b**$_1$ site has one Mo_{1s} atom and one Mo_{2s} atom, the **b**$_2$ site two Mo_{1s} atoms, and the **b**$_3$ site two surface C atoms. For the 3-fold hollow sites, the **h**$_1$ site is above a sublayer Mo atom and has two Mo_{1s} atoms as well as one Mo_{2s} atom. The **h**$_2$ site is above a sublayer C atom and has two Mo_{1s} atoms as well as one Mo_{2s} atom. The **h**$_3$ site is above a sublayer Mo atom and has one Mo_{1s} atom as well as two Mo_{2s} atoms.

3.2. Molecular CO Adsorption on the Mo and C Terminations at Different Coverage. Among the nine possible sites on the Mo termination for one CO adsorption, the **h**$_1$ site has the largest adsorption energy (−2.56 eV). For studying CO adsorption at higher coverage we further increased the numbers of CO molecules one by one and found the most stable adsorption structures at individual

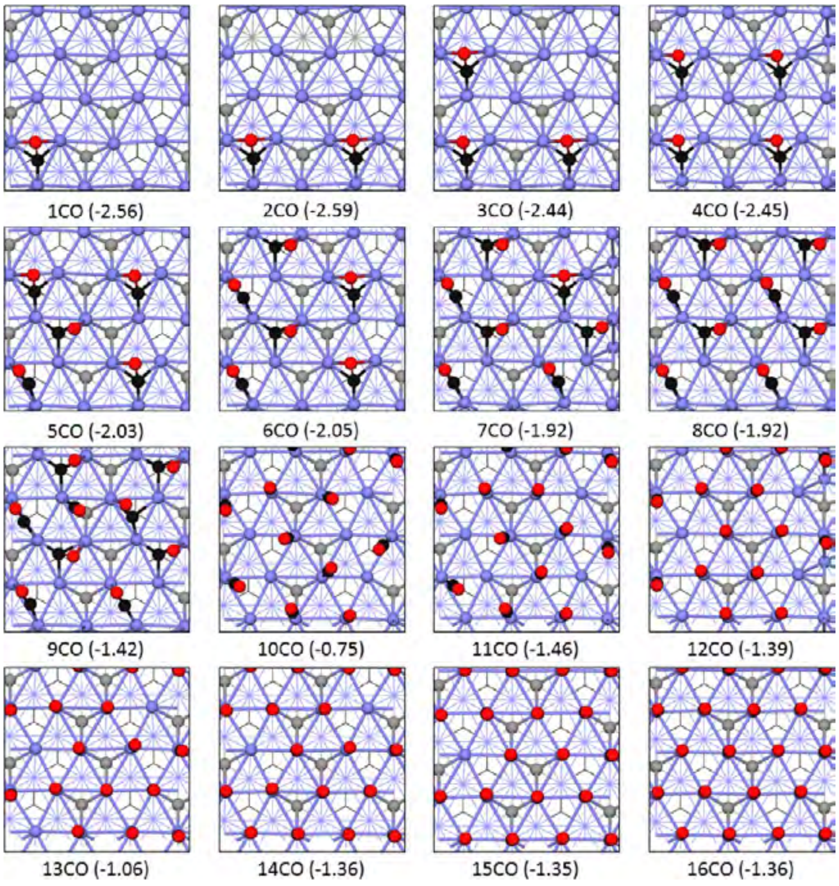

Figure 2. Structures and energies (ΔE_{ads}/eV) of the most stable adsorption sites for stepwise CO adsorption on the Mo termination (gray balls for the first layer C atoms below surface Mo atoms, black ball for the C atom in CO, red ball for O, and the blue balls for Mo atoms).

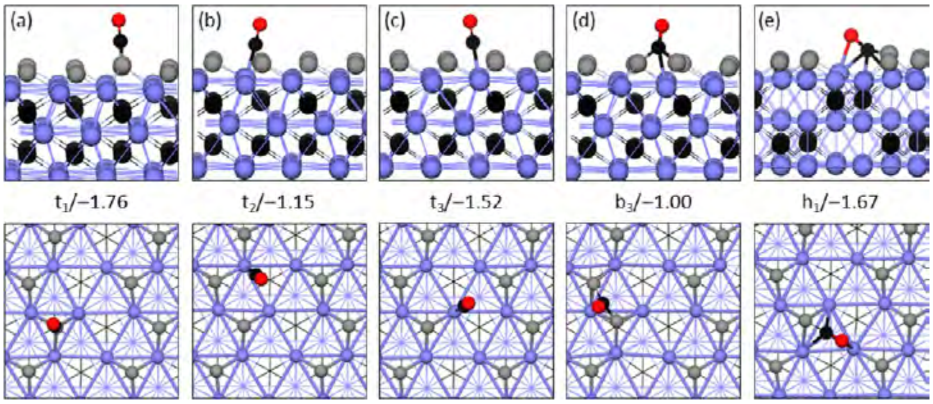

Figure 3. Structures and energies (eV) of five stable adsorption configurations with one CO molecule on the C termination. (Above for side view, below for top view, blue balls for Mo atoms, gray balls for surface C atoms, and black balls for bulk C and C in CO).

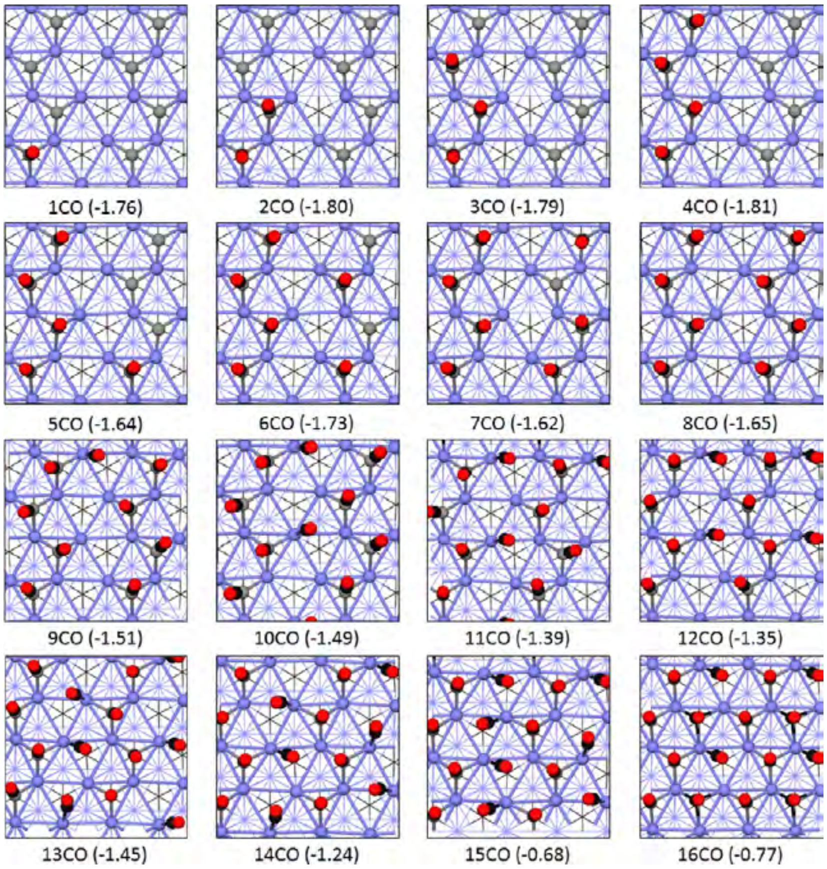

Figure 4. Structures and energies (ΔE_{ads}/eV) of the most stable adsorption sites for stepwise CO adsorption on the C termination (gray balls for the surface C atoms, black ball for the C atom in CO, red ball for O, and the blue balls for Mo atoms).

coverage by considering different possibilities. The structures and energies (ΔE_{ads}) of those most stable configurations of stepwise CO adsorption are given in Figure 2.

For n_{CO} = 1−4, four adsorbed CO molecules are located on the $\mathbf{h}_1$ sites with very similar adsorption structures and energies, indicating their negligible lateral repulsive interactions. In this adsorption configuration, the C atom of CO interacts with three surfaces Mo atoms, while the O atom interacts with two surface Mo atoms. For n_{CO} = 5−8, the repulsive interaction affects the structures and energies of the adsorbed CO molecules, although they have similar ΔE_{ads}. For example, for n_{CO} = 5, three adsorbed CO molecules maintain the same structures as those for n_{CO} = 1−4, while two new adsorption configurations appear; i.e., one CO molecule is located on the $\mathbf{b}_1$ site, while another one is located on the $\mathbf{h}_1$ site but with different configurations (C atom in CO interacting with three surfaces Mo atoms and that of the O atom interacting with only one surface Mo atom). For n_{CO} = 8, only two adsorption configurations ($\mathbf{b}_1$ site and $\mathbf{h}_1$ site with the O atom in CO coordinating with only one surface Mo atom) coexist, and the adsorbed CO molecules tend to avoid lateral repulsive interaction by decreasing coordination numbers with the surfaces. For n_{CO} = 9, the top adsorption configuration appears on the surface. For $n_{CO} \geq 10$, all adsorbed CO molecules have the atop configurations to reduce the lateral repulsive interaction. Finally, the saturated coverage has n_{CO} = 16 since a positive value ΔE_{ads} is found for n_{CO} = 17 with only top adsorption configuration.

Apart from the Mo termination, CO adsorption at different coverage on the C termination was also systematically studied. Among the nine possible sites on the C termination for one CO adsorption, only five stable configurations are located ($\mathbf{t}_1$, $\mathbf{t}_2$, $\mathbf{t}_3$, $\mathbf{b}_3$, and $\mathbf{h}_1$), and the $\mathbf{t}_1$ site has the largest adsorption energy (−1.76 eV). In this adsorption configuration (Figure 3a), the C atom of CO coordinates with the surface C atom. In the $\mathbf{t}_2$ (Figure 3b) and $\mathbf{t}_3$ (Figure 3c) configurations, the CO molecule adsorbs on the top sites with the surface Mo atom. In the $\mathbf{b}_3$ configuration (Figure 3d), the C atom in CO coordinates with two surface C atoms (C_s) and one surface Mo atom. In the $\mathbf{h}_1$ configuration (Figure 3e), the C atom in CO coordinates with one surface C atom and three surface Mo atoms, while the O atom coordinates with one surface Mo atom. This shows the possibility of the formation of a surface ketenylidene (C═C═O) species on the C termination. Actually, an in situ infrared study of CO adsorption on freshly prepared Mo_2C catalyst has found the existence of C═C═O species.[67]

On the basis of the most stable adsorption configuration of one CO adsorption, we further increased the number of CO molecules and found the most stable configurations at given coverage by considering different possibilities. The structures and energies (ΔE_{ads}) of those most stable configurations for stepwise CO adsorption are given in Figure 4. For n_{CO} = 1−8, all adsorbed CO molecules are located on surface C atoms, and they have very similar stepwise adsorption energies, indicating their negligible lateral repulsive interactions. With n_{CO} = 9−15, two adsorption configurations on the $\mathbf{t}_1$ and $\mathbf{t}_3$ sites coexist on the surface, and lateral repulsive interaction affects the ΔE_{ads}. Finally, the saturated coverage has n_{CO} = 16 since a positive ΔE_{ads} is found for n_{CO} = 17. At the saturated coverage, $\mathbf{t}_1$, $\mathbf{t}_3$, and $\mathbf{h}_2$ adsorption configurations coexist on the surface.

In this respect, it is necessary to compare the similarities and differences in CO adsorptions between the Mo and C terminations of the orthorhombic $Mo_2C(100)$ surface. At low coverage the favored CO adsorption configuration is located on the hollow site with high coordination numbers on the Mo termination, and the top site has low coordination numbers on the C termination. At high coverage on both terminations, due to the increase of the lateral repulsive interaction, mixed adsorption configurations coexist, and top adsorption configurations become favorable. At saturated coverage, both terminations have 16 CO molecules in different adsorption configurations, i.e., top site on the Mo termination and the $\mathbf{t}_1$, $\mathbf{t}_3$, and $\mathbf{h}_2$ sites on the C termination. At given coverage, the Mo termination has higher CO adsorption energies than the C termination.

3.3. Stretching Frequencies of C−O on the Mo and C Terminations.

Although it is very challenging experimentally,[68,69] unambiguous characterization of surface structure and active sites of the catalyst is essential for understanding the catalytic properties. A comparison between theoretically calculated and experimentally detected CO stretching frequencies (ν_{CO}) can identify the possible adsorption sites on the practical catalyst surfaces since theoretical calculations can provide more detailed structural information at the atomic scale. On the basis of the most stable adsorption configurations at a given coverage, we analyzed the C−O stretching frequencies on both terminations and present a direct comparison with available high-resolution electron energy loss spectroscopy (HREELS) results. The computed CO vibrational frequencies for Mo and C terminations (n = 1−16) are given in the Supporting Information. Table 1 lists the possible vibrational range for all adsorbed CO molecules on the surfaces from the lowest to the saturated coverage, and these data do not show their possible populations at equilibrium coverage. Detailed analysis into the CO vibrational frequencies at all coverages shows that the computed frequencies are higher than the experimentally detected numbers, and an empirical scaling factor of about 0.96−0.98 can be obtained.

Table 1. Computed and experimentally Detected C−O Vibration Frequencies (cm^{-1}) on Mo_2C Catalysts

	top	bridge	hollow
theory[a]			
Mo termination	1888−2081	1537−1656	1361−1562
C termination	1835−2123		1758−1765
experiment			
Mo(110)[b]	1920−2055	1500	1345
C-covered Mo(110)[c]	2043−2085		
carburized Mo(100)[d]	2060−2100		
Mo_2C[e]	2057−2072		

[a] Possible vibrational range for all adsorbed CO molecules on the surfaces from the lowest to the saturated coverage. [b] Ref 70. [c] Ref 71. [d] Ref 72. [e] Ref 73

On the Mo termination, C−O bonds have low stretching frequencies in the range of 1411−1459 cm^{-1} for n_{CO} = 1−4 since all CO molecules are adsorbed on the 3-F hollow sites. For n_{CO} = 5−8, new adsorption configurations located in the bridge sites have C−O stretching frequencies in the range of 1537−1651 cm^{-1}, while those configurations on the 3-fold hollow sites have C−O stretching frequencies in the range of 1376−1511 cm^{-1}. For n_{CO} = 9, three adsorption configurations coexist, and C−O stretching frequencies are 1929 cm^{-1} for the top sites, 1628−1656 cm^{-1} for bridge sites, as well as 1361−1560 cm^{-1} for 3-fold hollow sites. For $n_{CO} \geq 10$, the C−O stretching frequencies shift to 1888−2081 cm^{-1} since all the CO molecules have the top adsorption configurations. Generally, there are mainly three types of CO adsorption configurations with distinct vibrational frequencies at 1361−1562, 1537−1656, and 1888−2081 cm^{-1} on the Mo termination depending on coverage.

In this respect, it is interesting to compare our theoretically calculated C−O stretching frequencies with the available experimental IR data. Since the Mo termination is metallic, similar CO adsorption properties can be expected with those on metal Mo surfaces. Actually, early electron energy loss spectroscopy study[70] of CO adsorption on the Mo(110) surface also reported three ranges of C−O vibrational frequencies at about 1345, 1500, and 1920−2055 cm^{-1} at different CO exposure and low temperature.

On the C termination, the C−O stretching frequencies present different shift manners with increasing coverage from those on the Mo termination. For n_{CO} = 1−8, the C−O stretching frequencies range from 2015 to 2104 cm^{-1} since all the CO molecules are adsorbed on the $\mathbf{t}_1$ sites with the top adsorption configurations. For n_{CO} = 9−15, the C−O stretching frequencies of the eight CO molecules on the $\mathbf{t}_1$ sites are shifted to the range of 2009−2122 cm^{-1}, while those on the surface $\mathbf{t}_3$ sites are in the range of 1835−1915 cm^{-1}. At saturated coverage, the C−O stretching frequencies of the eight

Table 2. CO Step Desorption Energies (ΔE_{des}, eV) and Dissociation Barriers (E_a, eV) As Well As Dissociation Energies (ΔE_{dis}, eV) at Different Coverage

n_{CO}	pathways	E_a	ΔE_{des}	ΔE_{dis}
1CO	1CO → 1C + 1O	1.05	2.56	−1.64
2CO	2CO → 1CO + 1C + 1O	1.04	2.59	−1.61
	1CO + 1C + 1O → 2C + 2O	1.11	2.51	−1.60
3CO	3CO → 2CO + 1C + 1O	1.02	2.44	−1.62
	2CO + 1C + 1O → 1CO + 2C + 2O	1.17	2.25	−1.31
	1CO + 2C + 2O → 3C + 3O	1.16	1.94	−1.24
4CO	4CO → 3CO + 1C+1O	1.08	2.45	−1.38
	3CO + 1C + 1O → 2CO + 2C + 2O	1.10	2.43	−1.20
	2CO + 2C + 2O → 1CO + 3C + 3O	1.17	2.41	−1.27
	1CO + 3C + 3O → 4C + 4O	1.15	2.13	−1.23
5CO	5CO → 4CO + 1C + 1O	1.11	2.03	−1.31
	4CO + 1C + 1O → 3CO + 2C + 2O	1.16	2.24	−1.24
	3CO + 2C + 2O → 2CO + 3C + 3O	1.22	2.20	−1.25
	2CO + 3C + 3O → 1CO + 4C + 4O	1.33	2.06	+0.11
	1CO + 4C + 4O → 5C + 5O	1.81	2.12	+0.39
6CO	6CO → 5CO + 1C + 1O	1.17	2.05	−1.30
	5CO + 1C + 1O → 4CO + 2C + 2O	1.12	2.25	−1.25
	4CO + 2C + 2O → 3CO + 3C + 3O	1.41	2.18	+0.23
	3CO + 3C + 3O → 2CO + 4C + 4O	1.40	2.10	+0.11
	2CO + 4C + 4O → 1CO + 5C + 5O	1.80	2.03	+0.19
	1CO + 5C + 5O → 0CO + 6C + 6O	1.85	1.99	+0.24
7CO	7CO → 6CO + 1C + 1O	1.12	1.92	−1.26
	6CO + 1C + 1O → 5CO + 2C + 2O	1.34	1.90	+0.53
	5CO + 2C + 2O → 4CO + 3C + 3O	1.32	1.74	−0.14
	4CO + 3C + 3O → 3CO + 4C + 4O	1.46	1.95	+0.41
	3CO + 4C + 4O → 2CO + 5C + 5O	1.40	1.92	−0.37
	2CO + 5C + 5O → 1CO + 6C + 6O	1.90	1.92	−0.22
	1CO + 6C + 6O → 0CO + 7C + 7O	1.76	1.97	+0.74
8CO	8CO → 7CO + 1C + 1O	1.45	1.92	−0.30
	7CO + 1C + 1O → 6CO + 2C + 2O	1.47	1.57	+0.05
	6CO + 2C + 2O → 5CO + 3C + 3O	1.55	1.57	+0.15
	5CO + 3C + 3O → 4CO + 4C + 4O	1.62	1.56	+0.19
	4CO + 4C + 4O → 3CO + 5C + 5O	1.39	1.33	+0.07
	3CO + 5C + 5O → 2CO + 6C + 6O	1.94	1.44	+0.18
9CO	9CO → 8CO + 1C + 1O	1.52	1.42	+0.09

CO molecules on the $\mathbf{t}_1$ sites are shifted to the range of 2042−2123 cm^{-1}; those on the $\mathbf{t}_3$ sites are in the range of 1890−1898 cm^{-1}; and those on the $\mathbf{h}_2$ sites are in the range of 1758−1765 cm^{-1}. Compared with the Mo termination, the C−O stretching frequencies are mainly in the high wavenumber range on the C termination, which indicates a lower activation degree of the C−O bonds.

To deeply understand the adsorption properties of CO on the Mo_2C catalysts, many pioneering works studied the interaction of CO with C precovered or carburized Mo surfaces. On the C precovered Mo(110) surface, He et al.[71] reported two IR spectra signals at about 2043 and 2085 which are assigned to CO adsorbed on the Mo and C islands, respectively. On the carburized Mo(100) surface,[72] HREELS result at 140 K shows the range of 2060−2100 cm^{-1} for C−O vibration. Wang et al.[73] reported a single C−O vibration peak at 2057−2072 cm^{-1} in the reflectance absorbance infrared spectroscopy (RAIRS) study of CO adsorption on Mo_2C. Close inspections reveal that our theoretically predicted C−O stretching frequencies on the C termination are all within the range of experimentally detected IR results.

3.4. Dissociation of CO at Different Coverage on Mo and C Termination.

Apart from the studies about CO molecular adsorption on Mo_2C, CO dissociation also attracted great attention. An early study by Ko et al.[74] suggested that the deposition of carbon on the Mo(100) surface strongly suppressed CO dissociation. Temperature-programmed desorption (TPD) studies of CO on the C-precovered Mo(110) surface[75] and Mo_2C[73] revealed that the recombinative thermal desorption state of C and O is present at high temperature which indicates the dissociation of CO on Mo_2C.

The dissociation of one CO on the hexagonal[36] and orthorhombic[37] Mo_2C surface has been investigated by early DFT calculations. However, those works ignored the effect of coverage as well as the equilibrium between CO dissociation and desorption. To deeply understand the interaction of CO with Mo_2C catalysts, for the first time, we calculated CO dissociation on the Mo and C terminations of the orthorhombic $Mo_2C(100)$ surface at high coverage. Our goal is to reveal the coverage-dependent CO dissociation and the equilibrium between dissociation and desorption.

On the Mo termination, the calculated dissociation barriers of all adsorbed CO molecules based on the most stable adsorption configurations in Figure 2 as the initial states at individual coverage are listed in Table 2, and the corresponding structures of initial states (ISs), transition states (TSs), and final states (FSs) are given in the Supporting Information (Figure S1). For a direct and convenient comparison, we converted the calculated stepwise adsorption energies approximately to the reversed stepwise desorption energies. The potential energy surfaces at coverage of n_{CO} = 1−9 are shown in the Supporting Information (Figure S2).

For n_{CO} = 1, the computed CO dissociation barrier is much lower than its desorption energy (1.05 vs 2.56 eV), and CO dissociation is exothermic by 1.64 eV, indicating that CO dissociation is favorable both kinetically and thermodynamically. For n_{CO} = 2, the dissociation barriers of these two CO molecules (1.04 and 1.11 eV) are still very low, and the stepwise dissociation is exothermic by 1.61 and 1.60 eV, respectively. This shows that CO dissociation at this coverage is also very favorable both kinetically and thermodynamically. For n_{CO} = 3, the dissociation barriers (1.02, 1.17, and 1.16 eV) of these three CO molecules are lower than their corresponding desorption energies, and their dissociations are exothermic by 1.62, 1.31, and 1.24 eV, respectively. For n_{CO} = 4, the dissociation barriers of these four CO molecules (1.08, 1.10, 1.17, and 1.15 eV) are lower than their corresponding desorption energies, and their dissociations are exothermic by 1.38, 1.20, 1.27, and 1.23 eV, respectively. For n_{CO} = 1−4, all final states have adsorbed surface C and O atoms (nC + nO), and the dissociation of CO at these coverages is very favorable both kinetically and thermodynamically.

For n_{CO} = 5, the dissociation barriers of the first three CO molecules (1.11, 1.16, and 1.22 eV) are lower than their desorption energies, and their dissociations are exothermic by 1.31, 1.24, and 1.25 eV, respectively. This indicates that the dissociation of these three CO molecules is favorable both kinetically and thermodynamically. The dissociation barrier of the fourth and fifth CO molecules (1.33 and 1.81 eV) is higher than the first three CO molecules but still lower than their corresponding desorption energies which indicates that their dissociation is more favorable than desorption. However, the dissociation of these two CO molecules becomes endothermic by 0.11 and 0.39 eV, respectively. This indicates that at this coverage it is possible to dissociate all five CO molecules on the surface. The final adsorption state has five C and five O atoms (5C + 5O) on the surface. Similarly, for n_{CO} = 6 and 7, the dissociation of all the CO molecules is more favorable than desorption, despite that the dissociation of some CO molecules becomes thermodynamically less favorable. Nevertheless, at the coverage of 6CO and 7CO the final adsorption states have 6C + 6O and 7C + 7O on the surface, respectively.

For n_{CO} = 8, the dissociation barriers of the first three CO molecules (1.45, 1.47, and 1.55 eV) are lower than their desorption energies, and their dissociation is more favorable than desorption. For the dissociation of the other CO molecules, the energy barriers are higher than desorption energies which indicates that desorption becomes more favorable. At this coverage, it is only possible to dissociate three CO molecules on the surface, while the other five CO molecules prefer desorption from the surface and the final adsorption state has five CO molecules as well as three C and three O atoms (5CO + 3C + 3O) on the surface.

For n_{CO} = 9, the dissociation barrier of the first CO (1.52 eV) is higher than its desorption energy (1.42 eV), indicating that CO desorption is the first step instead of CO dissociation. The final adsorption state has nine adsorbed CO molecules. It is to be expected that at the coverage of n_{CO} > 9 only desorption is possible because of the much lower desorption energies. The final adsorption states have only adsorbed CO molecules.

On the basis of the above discussion, it clearly reveals mainly three types of CO activation mechanisms with increasing coverage on the Mo termination. At a coverage of n_{CO} = 1−7, all adsorbed CO molecules can dissociate on the surface, and the final state has only adsorbed C and O atoms. At a coverage of n_{CO} = 8, both CO desorption from the surface and dissociation on the surface are possible, and they might form an equilibrium. With $n_{CO} \geq 9$, the first step of the reaction is desorption of some adsorbed CO molecules from the surface. Moreover, CO dissociation becomes less favorable both kinetically and thermodynamically with increasing coverage. A general trend shows that the adsorbed CO molecules prefer dissociation on the surface at low coverage and desorption from the surface at high coverage, and both CO desorption and dissociation can form equilibrium at coverage in between.

On the C termination, the dissociation of CO was also considered. For n_{CO} = 1, the CO dissociation barrier is 1.91 eV which is higher than its desorption energy (1.76 eV). This indicates that the first step is CO desorption instead of dissociation. Since CO dissociation becomes much more difficult with increasing coverage, it is to be expected that at the coverage of n_{CO} > 1 only CO desorption is possible on the C termination. The structures and energies of CO dissociation on the C termination are given in the Supporting Information (Figure S3).

3.5. Equilibrium Phase Diagrams of Molecular and Dissociative CO Adsorption on Mo and C Terminations.

On the basis of the above-discussed CO adsorption, desorption, and dissociations energies, equilibrium between dissociation and desorption can be found at different coverage, and the final adsorption states on the surface can be estimated. The equilibrium phase diagrams can be built to consider the effects of temperature and pressure from ab initio thermodynamics method.

On the Mo termination (Figure 5a), there are four regions: one only molecular adsorption region (16CO) and two dissociative adsorption CO regions (4C + 4O and 2C + 2O) as well as one CO free region (0CO). This clearly reveals that at given CO partial pressure CO dissociative adsorption becomes favorable with increasing temperature. Under the ultrahigh vacuum experimental conditions (10^{-12} to 10^{-9} atm; $\ln(p_{CO}/p^{\theta}) = -27.6$ to -20.7), the molecularly adsorbed CO starts to desorb in the temperature of 275−325 K, while the recombinative desorption of the dissociative adsorbed C + O occurs in the temperature range of 850−1175 K.

On the carburized Mo(100) surface, Frühberger et al.[75] reported one molecular CO desorption at 300−400 K and one recombinative desorption of C + O at 948−1023 K. Wang et al.[73] also reported two CO desorption peaks at 325−360 K and 1200 K for both molecular and recombinative desorption on synthesized Mo_2C catalyst. All these experimental data fully support our theoretical results.

On the C termination (Figure 5b), there are three molecular adsorption regions and one CO free region, and only molecular CO desorption is possible with increasing temperature at given pressure. Under the ultrahigh vacuum experimental conditions, the molecularly adsorbed CO starts to desorb in a broad temperature range of 200−500 K.

Indeed, a detailed study on CO adsorption on the prepared Mo and C terminations of the orthorhombic $Mo_2C(0001)$ surface (the same as our (100) surface) in the temperature

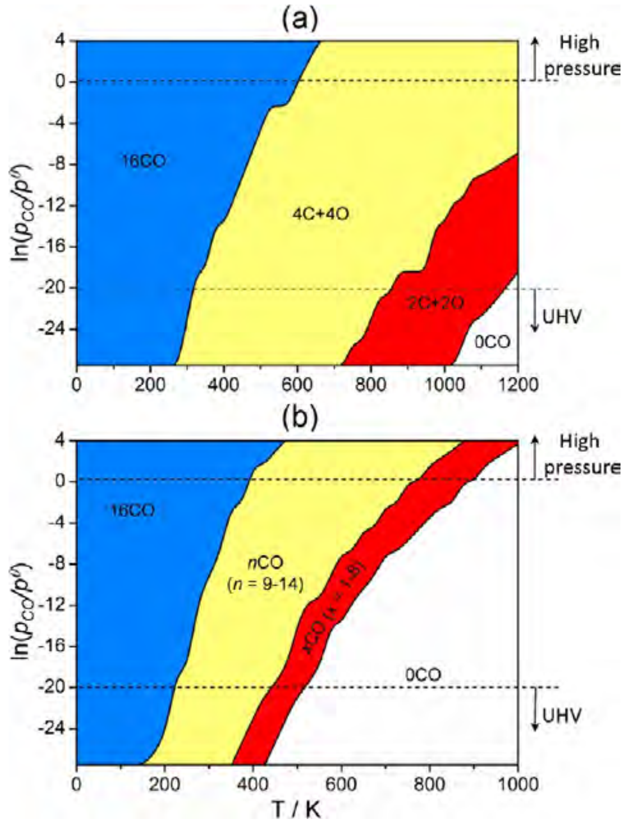

Figure 5. Phase diagrams of CO coverage on Mo (a) and C (b) terminations of orthorhombic $Mo_2C(100)$ surface.

range of 150−600 K at different exposures by Clair et al.[50] reveals desorption peaks at 345−440 K on the Mo termination. Detailed comparison shows that these peaks at 345−440 K also agree with our computed data for molecular CO desorption on the C termination, where the desorption starts at the coverage of n_{CO} = 14 at 350 K to full desorption at 425 K.

On the basis of this agreement, one can conclude that the C termination instead of the Mo termination is indeed applied in the experiment by Clair et al., since they did not observe recombinative desorption of C + O on the surface. Our computed results along with the experimental data from Frühberger et al.[75] and Wang et al.[73] show that recombinative desorption of C + O is characteristic for the Mo termination.

At high temperature and pressure (600 K, 1 atm), the Mo termination should have four dissociatively adsorbed CO (4C + 4O), while there are 9 to 14 adsorbed CO molecules on the C termination. These results might provide the insight into the different mechanisms of hydrogenation reaction under practical conditions.

■ CONCLUSION

Density functional theory computations have been carried out to study the adsorption, dissociation, and desorption of CO on the Mo and C terminations of the orthorhombic $Mo_2C(100)$ surface at different coverage. On the Mo termination using a $p(2 \times 2)$ super cell containing 16 surface Mo atoms, the most stable adsorption configuration changes from the 3-fold hollow site at low coverage (n_{CO} = 1−4) to the coexisted bridge and 3-fold hollow sites at the coverage of n_{CO} = 5−9, as well as to the atop site up to saturated coverage (n_{CO} = 10−16). On the C termination using a $p(2 \times 2)$ super cell having 8 surface C atoms and 16 exposed Mo atoms, the top adsorption configurations are most favorable at all CO coverages (n_{CO} = 1−16). Diverse molecular CO adsorption configurations at different coverage and the respective stretching frequencies are in good agreement with the available experimental data from high-resolution electron energy loss spectroscopy studies.

On the basis of the computed stepwise CO adsorption energies and dissociation barriers, equilibriums between molecular and dissociative adsorption have been found on the Mo termination. At high coverage (n_{CO} = 9−16), only molecular CO adsorption is found. For n_{CO} = 8, mixed molecular and dissociative CO adsorption becomes possible. At low coverage (n_{CO} = 1−7), only dissociative CO adsorption is favorable. In contrast, the C termination favors only molecular CO adsorption at all coverages, and it is not possible for dissociative adsorption.

Ab initio thermodynamic analysis reveals two desorption states from adsorbed CO molecules and dissociatively adsorbed C + O species on the Mo termination and only desorption from adsorbed CO molecules on the C termination. Not only desorption states but also desorption temperatures agree with the available experimental findings at ultrahigh vacuum conditions. Furthermore, the adsorption states and stable coverage at high temperature and pressure deduced from the phase diagram can be used to explore chemical reactions involving CO under practical conditions.

■ ASSOCIATED CONTENT

Ⓢ Supporting Information

Ab inito thermodynamics method, CO vibrational frequencies at different coverage on the Mo and C terminations (Table S1 and S2), structures of IS, TS, FS (Figure S1) as well as potential energy surfaces (Figure S2) of CO dissociation at different coverage on the MO termination, and structures and energies of CO dissociation on C termination (Figure S3) are included. This material is available free of charge via the Internet at http://pubs.acs.org.

■ AUTHOR INFORMATION

Corresponding Author

*E-mail: haijun.jiao@catalysis.de.

Notes

The authors declare no competing financial interest.

■ ACKNOWLEDGMENTS

This work was supported by National Natural Science Foundation of China (No. 21273262), National Basic Research Program of China (No. 2011CB201406), and Chinese Academy of Sciences and Synfuels CHINA. Co., Ltd. We also acknowledge general finical support from the BMBF and the state of Mecklenburg-Western Pommerania.

■ REFERENCES

(1) Toth, L. E. *Transition Metal Carbides and Nitrides*; Academic Press: New York, 1971.

(2) Gubanov, V. A.; Ivanovsky, A. L.; Zhukov, V. P. *Electronic Structure of Refractory Carbides and Nitrides*; Cambridge University Press: Cambridge, 1994.

(3) Oyama, S. T. *The Chemistry of Transition Metal Carbides and Nitrides*; Blackie Academic and Professional: Glasgow, 1996.

(4) Chen, J. G. Carbide and Nitride Overlayers on Early Transition Metal Surfaces: Preparation, Characterization, and Reactivities. *Chem. Rev.* **1996**, *96*, 1447−1498.

(5) Chen, J. G.; Eng, J.; Kelty, S. P. NEXAFS Determination of Electronic and Catalytic Properties of Transition Metal Carbides and Nitrides: From Single Crystal Surfaces to Powder Catalysts. *Catal. Today* **1998**, *43*, 147−158.

(6) Wu, H. H. H.; Chen, J. G. Surface Chemistry of Transition Metal Carbides. *Chem. Rev.* **2005**, *105*, 185−212.

(7) Levy, R. B.; Boudart, M. Platinum-Like Behavior of Tungsten Carbide in Surface Catalysis. *Science* **1973**, *181*, 547−549.

(8) Nagai, M.; Matsuda, K. Low-Temperature Water−Gas Shift Reaction over Cobalt-Molybdenum Carbide Catalyst. *J. Catal.* **2006**, *238*, 489−496.

(9) Schaidle, J. A.; Lausche, A. C.; Thompson, L. T. Effects of Sulfur on Mo_2C and Pt/Mo_2C Catalysts: Water Gas Shift Reaction. *J. Catal.* **2010**, *272*, 235−245.

(10) Xiang, M. L.; Li, D. B.; Li, W.-H.; Zhong, B.; Sun, Y. H. Performances of Mixed Alcohols Synthesis over Potassium Promoted Molybdenum Carbides. *Fuel* **2006**, *85*, 2662−2665.

(11) Zaman, S.; Smith, K. J. A Review of Molybdenum Catalysts for Synthesis Gas Conversion to Alcohols: Catalysts, Mechanisms and Kinetics. *Catal. Rev.: Sci. Eng.* **2012**, *54* (1), 41−132.

(12) Sundaramurthy, V.; Dalai, A. K.; Adjaye, J. HDN and HDS of Different Gas Oils Derived from Athabasca Bitumen over Phosphorus Doped NiMo/γ-Al_2O_3 Carbides. *Appl. Catal., B* **2006**, *68*, 38−48.

(13) Al-Megren, H. A.; Gonzalez-Cortes, S. L.; Xiao, T. C.; Green, M. L. H. A Comparative Study of the Catalytic Performance of Co-Mo and Co(Ni)-W Carbide Catalysts in the Hydrodenitrogenation (HDN) Reaction of Pyridine. *Appl. Catal., A* **2007**, *329*, 36−45.

(14) Oyama, S. T. Preparation and Catalytic Properties of Transition Metal Carbides and Nitrides. *Catal. Today* **1992**, *15*, 179−200.

(15) Neylon, M. K.; Choi, S.; Kwon, H.; Curry, K. E.; Thompson, L. T. Catalytic Properties of Early Transition Metal Nitrides and Carbides: n-butane Hydrogenolysis, Dehydrogenation and Isomerization. *Appl. Catal., A* **1999**, *183*, 253−263.

(16) Ardakani, S. J.; Liu, X. B.; Smith, K. J. Hydrogenation and Ring Opening of Naphthalene on Bulk and Supported Mo_2C Catalysts. *Appl. Catal., A* **2007**, *324*, 9−19.

(17) Barthos, R.; Solymosi, F. Hydrogen Production in the Decomposition and Steam Reforming of Methanol on Mo_2C/Carbon Catalysts. *J. Catal.* **2007**, *249*, 289−299.

(18) Medford, A. J.; Vojvodic, A.; Studt, F.; Abild-Pedersen, F.; Nørskov, J. K. Elementary Steps of Syngas Reactions on $Mo_2C(001)$: Adsorption Thermochemistry and Bond Dissociation. *J. Catal.* **2012**, *290*, 108−117.

(19) Clair, T. P., St; Oyama, S. T.; Cox, D. F.; Otani, S.; Ishizawa, Y.; Lo, R. L.; Fukui, K.; Iwasawa, Y. Surface Characterization of α-Mo_2C (0001). *Surf. Sci.* **1999**, *426*, 187−198.

(20) Parthe, E.; Sadagopan, V. The Structure of Dimolybdenum Carbide by Neutron Diffraction Technique. *Acta Crystallogr.* **1963**, *16*, 202−205.

(21) Nagai, M.; Tominaga, H.; Omi, S. CO Adsorption on Molybdenum Carbides and Molecular Simulation. *Langmuir* **2000**, *16*, 10215−10220.

(22) Ren, J.; Huo, C. F.; Wang, J. G.; Cao, Z.; Li, Y. W.; Jiao, H. J. Density Functional Theory Study into the Adsorption of CO_2, H and CH_x (x = 0−3) as well as C_2H_4 on α-$Mo_2C(0001)$. *Surf. Sci.* **2006**, *600*, 2329−2337.

(23) Ren, J.; Wang, J. G.; Huo, C. F.; Wen, X. D.; Cao, Z.; Yuan, S. P.; Li, Y. W.; Jiao, H. J. Adsorption of NO, NO_2, Pyridine and Pyrrole on α-$Mo_2C(0001)$: A DFT Study. *Surf. Sci.* **2007**, *601*, 1599−1607.

(24) Rocha, A. S.; Rocha, A. B.; Silva, V. T. Benzene Adsorption on Mo_2C: A Theoretical and Experimental Study. *Appl. Catal., A* **2010**, *379*, 54−60.

(25) Liu, X. C.; Tkalych, A.; Zhou, B. J.; Köster, A. M.; Salahub, D. R. Adsorption of Hexacyclic C_6H_6, C_6H_8, C_6H_{10}, and C_6H_{12} on a Mo-Terminated α-Mo_2C (0001) Surface. *J. Phys. Chem. C* **2013**, *117*, 7069−7080.

(26) Liu, P.; Rodriguez, J. A.; Muckerman, J. T. Desulfurization of SO_2 and Thiophene on Surfaces and Nanoparticles of Molybdenum Carbide: Unexpected Ligand and Steric Effects. *J. Phys. Chem. B* **2004**, *108*, 15662−15670.

(27) Liu, P.; Rodriguez, J. A.; Asakura, T.; Gomes, J.; Nakamura, K. Desulfurization Reactions on $Ni_2P(001)$ and α-$Mo_2C(001)$ Surfaces: Complex Role of P and C Sites. *J. Phys. Chem. B* **2005**, *109*, 4575−4583.

(28) Liu, P.; Rodriguez, J. A.; Muckerman, J. T. Sulfur Adsorption and Sulfidation of Transition Metal Carbides as Hydrotreating Catalysts. *J. Mol. Catal. A* **2005**, *239*, 116−124.

(29) Tominaga, H.; Nagai, M. Density Functional Theory of Water-Gas Shift Reaction on Molybdenum Carbide. *J. Phys. Chem. B* **2005**, *109*, 20415−20423.

(30) Liu, P.; Rodriguez, J. A. Water-Gas-Shift Reaction on Molybdenum Carbide Surfaces: Essential Role of the Oxycarbide. *J. Phys. Chem. B* **2006**, *110*, 19418−19425.

(31) Tominaga, H.; Aoki, Y.; Nagai, M. Hydrogenation of CO on Molybdenum and Cobalt Molybdenum Carbides. *Appl. Catal., A* **2012**, *423*, 192−204.

(32) Qi, K. Z.; Wang, G. C.; Zheng, W. J. A First-Principles Study of CO Hydrogenation into Methane on Molybdenum Carbides Catalysts. *Surf. Sci.* **2013**, *614*, 53−63.

(33) Luo, Q. Q.; Wang, T.; Walther, G.; Beller, M.; Jiao, H. Molybdenum Carbide Catalysed Hydrogen Production from Formic Acid - A Density Functional Theory Study. *J. Power Sources* **2014**, *246*, 548−555.

(34) Zheng, W.; Cotter, T. P.; Kaghazchi, P.; Jacob, T.; Frank, B.; Schlichte, K.; Zhang, W.; Su, D. S.; Schüth, F.; Schlögl, R. Experimental and Theoretical Investigation of Molybdenum Carbide and Nitride as Catalysts for Ammonia Decomposition. *J. Am. Chem. Soc.* **2013**, *135*, 3458−3464.

(35) Ren, J.; Huo, C. F.; Wang, J. G.; Li, Y. W.; Jiao, H. J. Surface Structure and Energetics of Oxygen and CO Adsorption on α-$Mo_2C(0001)$. *Surf. Sci.* **2005**, *596*, 212−221.

(36) Shi, X. R.; Wang, J. G.; Hermann, K. CO and NO Adsorption and Dissociation at the β-$Mo_2C(0001)$ Surface: A Density Functional Theory Study. *J. Phys. Chem. C* **2010**, *114*, 13630−13641.

(37) Pistonesi, C.; Pronsato, M. E.; Bugyi, L.; Juan, A. Theoretical Model for CO Adsorption and Dissociation on Clean and K-Doped β-Mo_2C Surfaces. *J. Phys. Chem. C* **2012**, *116*, 24573−24581.

(38) Wang, T.; Wang, S. G.; Li, Y. W.; Wang, J. G.; Jiao, H. J. Adsorption Equilibria of CO Coverage on β-Mo_2C Surfaces. *J. Phys. Chem. C* **2012**, *116*, 6340−6348.

(39) Mims, C. A.; McCandlish, L. E. Evidence for Rapid Chain Growth in the Fischer−Tropsch Synthesis over Iron and Cobalt Catalysts. *J. Phys. Chem.* **1987**, *91*, 929−937.

(40) Yates, I. C.; Satterfield, C. N. Intrinsic Kinetics of the Fischer−Tropsch Synthesis on a Cobalt Catalyst. *Energy Fuels* **1991**, *5*, 168−173.

(41) Ojeda, M.; Nabar, R.; Nilekar, A. U.; Ishikawa, A.; Mavrikakis, M.; Iglesia, E. CO Activation Pathways and the Mechanism of Fischer - Tropsch Synthesis. *J. Catal.* **2010**, *272*, 287−297.

(42) Loveless, B. T.; Buda, C.; Neurock, M.; Iglesia, E. CO Chemisorption and Dissociation at High Coverages during CO Hydrogenation on Ru Catalysts. *J. Am. Chem. Soc.* **2013**, *135*, 6107−6121.

(43) Shi, X. R.; Wang, S. G.; Wang, H.; Deng, C. M.; Qin, Z. F.; Wang, J. G. Structure and Stability of β-Mo_2C Bulk and Surfaces: A Density Functional Theory Study. *Surf. Sci.* **2009**, *603*, 852−859.

(44) Han, J. W.; Li, L.; Sholl, D. S. Density Functional Theory Study of H and CO Adsorption on Alkali-Promoted Mo_2C Surfaces. *J. Phys. Chem. C* **2011**, *115*, 6870−6876.

(45) Wang, T.; Liu, X. W.; Wang, S. G.; Huo, C. F.; Li, Y. W.; Wang, J. G.; Jiao, H. Stability of β-Mo_2C Facets from ab Initio Atomistic Thermodynamics. *J. Phys. Chem. C* **2011**, *115*, 22360−22368.

(46) Miyao, T.; Shishikura, I.; Matsuoka, M.; Nagai, M.; Oyama, S. T. Preparation and Characterization of Alumina-Supported Molybdenum Carbide. *Appl. Catal., A* **1997**, *165*, 419−428.

(47) Nagai, M.; Zahidul, A. M.; Matsuda, K. Nano Structured Nickel-Molybdenum Carbide Catalyst for Low-Temperature Water-Gas Shift Reaction. *Appl. Catal., A* **2006**, *313*, 137−145.

(48) Politi, J. R. d. S.; Vines, F.; Rodriguez, J. A.; IIlas, F. Atomic and Electronic Structure of Molybdenum Carbide Phases: Bulk and Low Miller-Index Surfaces. *Phys. Chem. Chem. Phys.* **2013**, *15*, 12617−12625.

(49) Christensen, A. N. A Neutron Diffraction Investigation on a Crystal of α-Mo_2C. *Acta Chem. Scand. A* **1977**, *31*, 509−511.

(50) Clair, T. P., St.; Oyama, S. T.; Cox, D. F. CO and O_2 Adsorption on α-Mo_2C (0001). *Surf. Sci.* **2000**, *468*, 62−76.

(51) Sugihara, M.; Ozawa, K.; Edamoto, K.; Otani, S. Photoelectron Spectroscopy Study of Mo_2C(0001). *Solid State Commun.* **2002**, *121*, 1−5.

(52) Clair, T. P., St.; Oyama, S. T.; Cox, D. F. Adsorption and Reaction of Thiophene on α-Mo_2C(0001). *Surf. Sci.* **2002**, *511*, 294−302.

(53) Rantotra, G. S.; Haddix, G. W.; Bell, A. T.; Reimer, J. A. Catalysis over Molybdenum Carbides and Nitrides I. Catalyst Characterization. *J. Catal.* **1987**, *108*, 24−39.

(54) Kresse, G.; Furthmüller, J. Efficiency of Ab-initio Total Energy Calculations for Metals and Semiconductors Using a Plane-Wave Basis Set. *Comput. Mater. Sci.* **1996**, *6*, 15−50.

(55) Kresse, G.; Furthmüller, J. Efficient Iterative Schemes for Ab initio Total-Energy Calculations Using a Plane-Wave Basis Set. *Phys. Rev. B* **1996**, *54*, 11169−11186.

(56) Blochl, P. E. Projector Augmented-Wave Method. *Phys. Rev. B* **1994**, *50*, 17953−17979.

(57) Kresse, G. From Ultrasoft Pseudopotentials to the Projector Augmented-Wave Method. *Phys. Rev. B* **1999**, *59*, 1758−1775.

(58) Perdew, J. P.; Burke, K.; Ernzerhof, M. Generalized Gradient Approximation Made Simple. *Phys. Rev. Lett.* **1996**, *77*, 3865−3868.

(59) Henkelman, G.; Jónsson, H. Improved Tangent Estimate in the Nudged Elastic Band Method for Finding Minimum Energy Paths and Saddle Points. *J. Chem. Phys.* **2000**, *113*, 9978−9985.

(60) Reuter, K.; Scheffler, M. Composition, Structure, and Stability of RuO_2(110) as a Function of Oxygen Pressure. *Phys. Rev. B* **2001**, *65*, 035406.

(61) Reuter, K.; Scheffler, M. Composition and Structure of the RuO_2(110) Surface in an O_2 and CO Environment: Implications for the Catalytic Formation of CO_2. *Phys. Rev. B* **2003**, *68*, 045407.

(62) Li, W. X.; Stampfl, C.; Scheffler, M. Insights into the Function of Silver as an Oxidation Catalyst by Ab Initio Atomistic Thermodynamics. *Phys. Rev. B* **2003**, *68*, 165412.

(63) Rogal, J.; Reuter, K.; Scheffler, M. Thermodynamic Stability of PdO Surfaces. *Phys. Rev. B* **2004**, *69*, 075421.

(64) Grillo, M. E.; Ranke, W.; Finnis, M. W. Surface Structure and Water adsorption on Fe_3O_4(111): Spin-Density Functional Theory and on-site Coulomb Interactions. *Phys. Rev. B* **2008**, *77*, 075407.

(65) Aray, Y.; Vidal, A. B.; Rodriguez, J.; Grillo, M. E.; Vega, D.; Coll, D. S. First Principles Study of Low Miller Index RuS_2 Surfaces in Hydrotreating Conditions. *J. Phys. Chem. C* **2009**, *113*, 19545−19557.

(66) Zasada, F.; Piskorz, W.; Cristol, S.; Paul, J. F.; Kotarba, A.; Sojka, Z. Periodic Density Functional Theory and Atomistic Thermodynamic Studies of Cobalt Spinel Nanocrystals in Wet Environment: Molecular Interpretation of Water Adsorption Equilibria. *J. Phys. Chem. C* **2010**, *114*, 22245−22253.

(67) Wu, W.; Wu, Z.; Liang, C.; Chen, X.; Ying, P.; Li, C. In Situ FT-IR Spectroscopic Studies of CO Adsorption on Fresh Mo_2C/Al_2O_3 Catalyst. *J. Phys. Chem. B* **2003**, *107*, 7088−7094.

(68) Thomas, J. M.; Thomas, W. J. *Principles and Practice of Heterogeneous Catalysis*; Wiley-VCH: Weinheim, 1997.

(69) Somorjai, G. A.; Li, Y. *Introduction to Surface Chemistry and Catalysis*, 2nd ed.; John Wiley: NJ, 2010.

(70) Chen, J. G.; Colaianni, M. L.; Weinberg, W. H.; Yates-Jr, J. T. Direct Vibrational Detection of Surface Reaction Channels Leading to CO Dissociation and to Its Inhibition on Mo(110). *Chem. Phys. Lett.* **1991**, *177*, 113−117.

(71) He, J. W.; Kuhn, W. K.; Goodman, D. W. CO Adsorption on Clean and C-, O- and H-Covered Mo(110) Surfaces: an IRAS Study. *Surf. Sci.* **1992**, *262*, 351−358.

(72) Bugyi, L.; Solymosi, F. Effects of Potassium on the Chemisorption of CO on the Mo_2C/Mo(100) Surface. *J. Phys. Chem. B* **2001**, *105*, 4337−4342.

(73) Wang, J.; Castonguay, M.; Deng, J.; McBreen, P. H. RAIRS and TPD Study of CO and NO on β-Mo_2C. *Surf. Sci.* **1997**, *374*, 197−207.

(74) Ko, E. I.; Madix, R. J. Effects of Adsorbed Carbon and Oxygen on the Chemisorption of H_2 and CO on Mo(100). *Surf. Sci.* **1981**, *109*, 221−238.

(75) Frühberger, B.; Chen, J. G. Modification of the Surface Reactivity of Mo(110) upon Carbide Formation. *Surf. Sci.* **1995**, *342*, 38−46.

3.6 Dissociative Hydrogen Adsorption on the Hexagonal Mo_2C Phase at High Coverage

Tao Wang, Yong-Wang Li, Jianguo Wang, Matthias Beller, Haijun Jiao*

Journal of Physical Chemistry C **2014**, *118*, 8079-8089.

Summary: Hydrogen adsorption on the primarily exposed (001), (100), (101) and (201) surfaces of the hexagonal Mo_2C phase at different coverage has been investigated at the level of density functional theory and using ab initio thermodynamics. On the Mo terminated (001) and (100) as well as mixed Mo/C terminated (101) and (201) surfaces, dissociative H_2 adsorption is favored both kinetically and thermodynamically. At high coverage, each surface can have several types of adsorption configurations coexisting and these types are different from surface to surface. The stable coverage as function of temperature and partial pressure provide useful information not only for surface science studies at ultra-high vacuum condition but also for practical applications at high temperature and pressure in monitoring reactions. The differences in the adsorbed H atom numbers and energies of these surfaces indicate their different potential hydro-treating abilities. The relationship between surface stability and stable hydrogen coverage has been discussed.

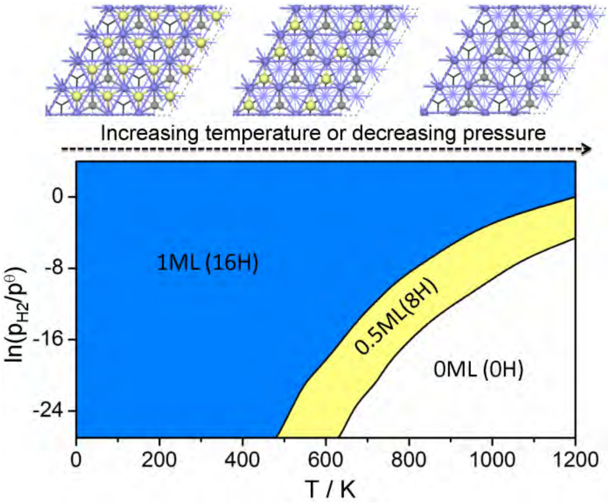

Contributions

In this paper, I planned, performed and analyzed most calculations for this manuscript. I have done the major part of writing of the manuscript. My contribution as co-author of this paper is approximately 80%.

THE JOURNAL OF
PHYSICAL CHEMISTRY C

Article

pubs.acs.org/JPCC

Dissociative Hydrogen Adsorption on the Hexagonal Mo_2C Phase at High Coverage

Tao Wang,[†] Yong-Wang Li,[‡] Jianguo Wang,[‡] Matthias Beller,[†] and Haijun Jiao*[,†,‡]

[†]Leibniz-Institut für Katalyse e.V., an der Universität Rostock, Albert-Einstein Strasse 29a, 18059 Rostock, Germany

[‡]State Key Laboratory of Coal Conversion, Institute of Coal Chemistry, Chinese Academy of Sciences, Taiyuan, Shanxi 030001, P. R. China

Ⓢ *Supporting Information*

ABSTRACT: Hydrogen adsorption on the primarily exposed (001), (100), (101), and (201) surfaces of the hexagonal Mo_2C phase at different coverage has been investigated at the level of density functional theory and using ab initio thermodynamics. On the Mo-terminated (001) and (100) as well as mixed Mo/C-terminated (101) and (201) surfaces, dissociative H_2 adsorption is favored both kinetically and thermodynamically. At high coverage, each surface can have several types of adsorption configurations coexisting, and these types are different from surface to surface. The stable coverage as a function of temperature and partial pressure provides useful information not only for surface science studies at ultrahigh vacuum condition but also for practical applications at high temperature and pressure in monitoring reactions. The differences in the adsorbed H atom numbers and energies of these surfaces indicate their different potential hydrotreating abilities. The relationship between surface stability and stable hydrogen coverage has been discussed.

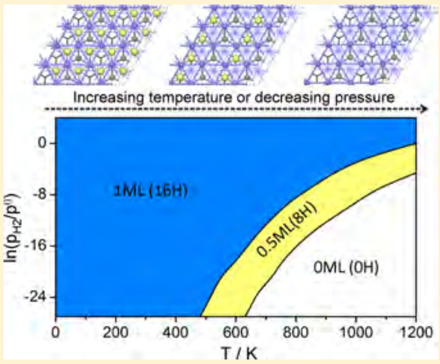

INTRODUCTION

As an important member of transition metal carbides (TMC),[1] molybdenum carbide (Mo_2C) has attracted great attention from academic research and industrial applications. Apart from their high hardness and melting point as well as good thermal stability which are suitable for cutting tools and protection materials,[2−4] TMC also present promising activities in heterogeneous catalysis.[5] For example, Mo_2C and W_2C are proved to have noble metal properties[6] and can substitute noble metal catalysts. The noble-metal-like activities of Mo_2C are proved in many catalytic reactions,[7] e.g., water-gas shift reaction,[8−10] alcohol synthesis from CO hydrogenation,[11−13] hydrodesulfurization,[14] and hydrodenitrogenation[15] in petroleum refining, hydrotreating,[16,17] and H_2 production[18] as well as the unique catalytic behaviors in the aromatization of CH_4.[19,20]

Mo_2C primarily has two crystalline structures with slight distinctions, i.e., the orthorhombic[21] and the hexagonal[22] phases. In the orthorhombic Mo_2C phase, the Mo atoms are hexagonally close-packed in an orthorhombic symmetry, and the carbon atoms orderly occupy half of the octahedral holes (the number of holes is twice the number of C atoms). In the hexagonal Mo_2C phase, the Mo atoms are hexagonally close-packed, and the carbon atoms are located statistically in half of the octahedral holes. Thermodynamic analysis of some elementary steps in synthesis gas reactions on the $Mo_2C(001)$ surface[23] indicates that the Mo termination exhibits similar activities in carbon related reactions to transition metals such as Ru and Ir.

In addition to the experimental investigations, there are also theoretical studies on the catalytic properties of Mo_2C. Liu et al.[24−26] demonstrated the key role of the surface carbon atoms on the orthorhombic Mo_2C in the catalytic dissociation of sulfur containing compounds based on density functional theory (DFT) calculations. Theoretical studies on the adsorption and decomposition of methanol,[27,28] methyl iodide,[29] and CO[30] as well as potassium promoting effect on the orthorhombic Mo_2C were systematically reported by Pistonesi et al., and they found that the incorporation of potassium atoms enhances the dissociation ability of the C−I and C−O bonds in CH_3I and CH_3OH but increases the CO dissociation barrier.

The hydrogenolysis mechanism of thiophene[31] and indole[32,33] on the hexagonal Mo_2C also was systematically investigated on the basis of DFT calculations. The stable CO coverage on the hexagonal Mo_2C under different conditions was also discussed by applying atomistic thermodynamics,[34] and the computed CO desorption is in agreement with the experiment.[35,36] DFT study of the Co promoting effect on CO hydrogenation on hexagonal Mo_2C[37] revealed different reaction mechanisms and surface species compared with the pure hexagonal Mo_2C. A combined catalytic experiments and DFT calculations showed the very high catalytic activity of the hexagonal Mo_2C in NH_3 decomposition.[38] The adsorption and

Received: February 11, 2014
Revised: March 20, 2014
Published: March 24, 2014

ACS Publications © 2014 American Chemical Society

dx.doi.org/10.1021/jp501471u | *J. Phys. Chem. C* 2014, 118, 8079−8089

decomposition of small molecules,[39−44] such as nitrogenous compounds, aromatic hydrocarbons, and CO, on both orthorhombic and hexagonal Mo_2C were also systematically examined. The mechanism of CO hydrogenation into CH_4 on both orthorhombic $Mo_2C(100)$ and hexagonal $Mo_2C(101)$ surfaces was reported by Qi et al.,[45] and the orthorhombic $Mo_2C(100)$ surface was proved to have higher activity for CH_4 formation.

For those hydrogen involving chemical issues, many DFT studies were also reported. On the hexagonal $Mo_2C(001)$ surface with the Mo−C−Mo−Mo−C layer structure, Tominaga and Nagai[46] computed the water-gas shift reaction mechanism and found CO_2 formation from CO oxidation by surface O to be rate determining. Liu et al.[47] calculated the water-gas shift mechanism on different terminations of the orthorhombic Mo_2C and H_2O was found to dissociate very easily. Ren et al.[48] reported the adsorption of H atom on the orthorhombic $Mo_2C(100)$ surface when studying the adsorption properties of many species. The favored reaction route of CO-free hydrogen production from the hexagonal $Mo_2C(101)$ surface catalyzed formic acid dissociation has been identified in a recent DFT study.[49]

Since hydrogen is involved in most of the above-mentioned catalytic reactions, we performed systematic DFT investigations into H_2 adsorption and dissociation on the (001), (100), (101), and (201) surfaces of the hexagonal Mo_2C at different stable coverage. Our goal is the understanding into the initial stages for Mo_2C-catalyzed reactions involving hydrogen, i.e., water-gas shift reaction, Fischer−Tropsch synthesis, and alcohol synthesis from CO hydrogenation.

■ COMPUTATIONAL MODEL AND METHOD

Model. In computational studies, the choice of appropriate slab surface models is very important for understanding the adsorption properties of molecules and their catalytic mechanisms on the surfaces. For the hexagonal Mo_2C phase, there are several studies of the surface terminations. Shi et al.[50] and Han et al.[51] calculated the surface energies of low Miller index surfaces of the hexagonal Mo_2C phase to compare their stabilities and concluded that the (011) facet is most stable. The calculated surface free energies of both low and high Miller index surfaces of the hexagonal Mo_2C phase using atomistic thermodynamics under the consideration of reaction conditions showed the (101) facet is dominant,[52] in agreement with the experiments.[53−55] A recent work by dos Santos Politi et al.[56] computed the atomic and electronic structures of both the bulk and low Miller index surfaces of three molybdenum carbide phases (hexagonal and orthorhombic Mo_2C and face-centered cubic MoC) and revealed that the PBE functional is particularly suited to study molybdenum carbide and the orthorhombic Mo_2C has stronger metallic character.

In this paper, we used the hexagonal Mo_2C phase with an eclipsed configuration as the unit cell, which is the same as in our previous work.[52] The calculated lattice parameters for the hexagonal Mo_2C bulk are a = 6.075 Å, b = 6.069 Å, and c = 4.722 Å, in good agreement with the experiment ($a = b = 2 \times 3.002$ Å and c = 4.724 Å).[57] On the basis of our previous work on the stabilities of different hexagonal Mo_2C surfaces, the four most stable surface terminations, (001), (100), (101), and (201), have been chosen, and they were modeled by periodic slabs with $p(2 \times 2)$, $p(2 \times 2)$, $p(2 \times 1)$, and $p(2 \times 2)$ supercell while the surface area are 12.2 Å × 12.1 Å, 12.1 Å × 9.4 Å, 12.1 Å × 7.7 Å, and 12.1 Å × 11.1 Å, respectively. The thicknesses of these four slabs are 3.6, 4.4, 5.9, and 3.6 Å with the top two layers relaxed and the bottom layers fixed in the bulk positions. The vacuum layer between periodically repeated slabs was set as 10 Å to avoid interactions between slabs. Dipole correction was applied to decouple the slabs and to avoid the effect of dipolar interaction on the total energy.

Method. All calculations were done by using the plane-wave based periodic density functional theory (DFT) method implemented in the Vienna ab initio simulation package (VASP).[58,59] The electron ion interaction was described with the projector augmented wave (PAW) method.[60,61] The electron exchange and correlation energies were treated within the generalized gradient approximation in the Perdew−Burke−Ernzerhof formalism (GGA-PBE).[62] To ensure accurate energies with errors less than 1 meV per unit atom, the cutoff energy of 400 eV and Gaussian electron smearing method with σ = 0.05 eV were used. For the bulk optimization, the lattice parameters for the hexagonal Mo_2C phase were determined by minimizing the total energy of the unit cell using a conjugated-gradient algorithm to relax the ions and a 5 × 5 × 5 Monkhorst−Pack k-point grid (benchmark calculation in Table S0) was used for sampling the Brillouin zone while the 3 × 3 × 1 k-points grid was applied for the periodic slabs. The geometry optimization was done with the changes of forces smaller than 0.02 eV/Å, while the energy difference is lower than 10^{-4} eV. Adsorption energy (E_{ads}) is calculated by subtracting the energies of gas phase H_2 and the clean surface from the total energy of the adsorbed system, $E_{ads} = E(H_2/slab) - E(H_2) - E(slab)$, and a more negative E_{ads} indicates a stronger adsorption. For evaluating the energy barrier, the transition state (TS) was located using the nudged elastic band (NEB) method.[63] All reported stable adsorption configurations were verified to be energy minima without imaginary frequency by frequency analysis, while those transition states have only one imaginary frequency. All reported relative energy data include the corrections of zero-point energies.

Thermodynamics. As a convenient tool to solve problems referring to reaction conditions, atomistic thermodynamics[64,65] has been widely and successfully applied to many systems.[66−72] In this paper, we applied this method to include the effects of temperature (T) and pressure (p) on stable hydrogen coverage. Here, we connected the change of Gibbs free energy during H_2 adsorption with T and p by using the following equations, where $E[Mo_2C(slab)/(nH_2)]$, $E[Mo_2C(slab)]$, and E_{H2} are the total energies of the corresponding systems. The chemical potential of hydrogen in the gas phase includes electronic energy and $\tilde{\mu}_{H2}(T,p^{\theta})$ which includes the contribution from vibration and rotation as well as the ideal gas entropy at 1 atm. The detailed description of the method can be found in our previous work.[34]

$$\Delta G(T, p, nH_2) = E[Mo_2C(slab)/(nH_2)] - E[Mo_2C(slab)] - nE_{H2} - n\tilde{\mu}_{H2}(T, p^{\theta}) - nk_BT \ln(p_{H2}/p^{\theta})$$

■ RESULTS AND DISCUSSION

Molecular and Dissociative H_2 Adsorption at Lowest Coverage. For discussing hydrogen adsorption on the hexagonal Mo_2C phase, the (001), (100), (101), and (201) surfaces with different terminations are applied. These surface terminations have been proved to be stable and representative

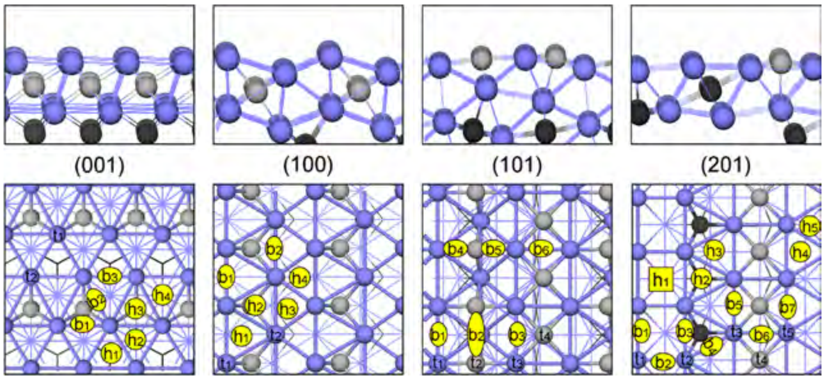

Figure 1. Structures and possible adsorption sites of the (001), (100), (101), and (201) surfaces (surface Mo/blue; surface C/gray; bulk C/black, **h** for hollow sites, **b** for bridge sites, and **t** for top sites) from side (above) and top (below) views.

from theoretical[52] and experimental[53,73,74] studies. The side and top views as well as the possible top (**t**), bridge (**b**), and hollow (**h**) adsorption sites of these surfaces are given in Figure 1, and quite different surface structures and compositions are revealed. For example, the (001) and (100) surfaces have pure metallic Mo terminations and sublayers C atoms, while the (101) and (201) surfaces have mixed Mo/C terminations. The structures and energies of the stable H_2 adsorption are given in the Supporting Information (Figure S1).

Generally, there are many strict definitions of active sites in the field of material and catalysis. For example, a crystal surface always exhibits terraces (T) separated by ledges (L) which may have kinks (K) and a terrace between two ledges is a step (S), while defects on terraces consist of vacancies. Furthermore, coordinatively unsaturated sites (CUS), which also mean dangling bonds, are always regarded as active sites in catalysis.[75] On the Mo termination of the (001) surface, there are 16 surface Mo atoms and nine possible adsorption sites ($\mathbf{t}_1$, $\mathbf{t}_2$, $\mathbf{b}_1$−$\mathbf{b}_3$, and $\mathbf{h}_1$−$\mathbf{h}_4$). On the $\mathbf{t}_1$ site, the Mo_1 atom coordinates with two C atoms in the second layer and has one dangling bond (the saturated bulk Mo coordinates with three C atoms, while that of C atom coordinating with six Mo atoms). On the $\mathbf{t}_2$ site, the Mo_2 atom coordinates with only one C atom in the second layer and has two dangling bonds. For the bridge sites, the $\mathbf{b}_1$ site links two Mo_1 atoms; the $\mathbf{b}_2$ site links one Mo_1 and one Mo_2 atom, while the $\mathbf{b}_3$ site links two Mo_1 atoms. For the 3-fold hollow sites ($\mathbf{h}_1$−$\mathbf{h}_4$), they differ in not only the surface Mo atoms but also the sublayer atoms. The $\mathbf{h}_1$ site has one Mo_1 atom and two Mo_2 atoms as well as one carbon vacancy in the second layer. The $\mathbf{h}_2$ site has two Mo_1 atoms as well as one Mo_2 atom and one third-layer Mo atom. The $\mathbf{h}_3$ site has two Mo_1 atoms and one Mo_2 atom as well as one second-layer carbon atom. The $\mathbf{h}_4$ site has one Mo_1 atom and two Mo_2 atoms as well as one third-layer Mo atom. On (001), all attempts to locate molecular H_2 adsorption result in dissociative H_2 adsorption, and therefore, H_2 dissociation is barrier-less.

On the Mo termination of the (100) surface, there are 16 exposed surface Mo atoms and 8 possible sites ($\mathbf{t}_1$, $\mathbf{t}_2$, $\mathbf{b}_1$, $\mathbf{b}_2$, $\mathbf{h}_1$−$\mathbf{h}_4$). There are two kinds of exposed Mo atoms on the surface; i.e., the Mo_2 atom on the $\mathbf{t}_1$ site in the first layer coordinates with only one bulk C atom, and the Mo_1 atom on the $\mathbf{t}_2$ site in the second layer coordinates with two bulk C atoms. The $\mathbf{b}_1$ site has two Mo_2 atoms while the $\mathbf{b}_2$ site has two Mo_1 atoms. For the 3-fold hollow sites, the $\mathbf{h}_1$ site has one Mo_1 atom and two Mo_2 atoms as well as two neighbor carbon atoms in the third layer (the sublayer carbon atom of the $\mathbf{h}_2$ site); the $\mathbf{h}_2$ site has two Mo_1 atoms and one Mo_2 atom as well as one sublayer carbon atom; the $\mathbf{h}_3$ site also has two Mo_1 atoms and one Mo_2 atom; the $\mathbf{h}_4$ site has one Mo_1 atom and two Mo_2 atoms. On (100), only the $\mathbf{t}_1$ site forms stable molecular H_2 adsorption (−0.82 eV).

On the Mo/C-mixed (101) surface, there are eight surface Mo and eight surface C atoms as well as ten possible adsorption sites ($\mathbf{t}_1$−$\mathbf{t}_4$ and $\mathbf{b}_1$−$\mathbf{b}_6$). Four types of surface atoms with different coordination patterns are exposed on this surface; i.e., the surface C_2 atom on the $\mathbf{t}_2$ site coordinates with four Mo atoms and has two dangling bonds, and the surface C_1 atom on the $\mathbf{t}_4$ site coordinates with five Mo atoms and has one dangling bond. The Mo atoms on the $\mathbf{t}_1$ and $\mathbf{t}_3$ sites coordinate with three C atoms to form saturated coordination and differ in the numbers of their coordinated Mo atoms. On the $\mathbf{t}_1$ site, the Mo_a atom coordinates with eight Mo atoms, while the Mo_b atom on the $\mathbf{t}_3$ site coordinates with seven Mo atoms. For the bridge sites, the $\mathbf{b}_1$ site has two Mo_a atoms; the $\mathbf{b}_2$ site has two C_2 atoms; the $\mathbf{b}_3$ site has two Mo_b atoms; the $\mathbf{b}_4$ site has one Mo_a atom and one C_2 atom; the $\mathbf{b}_5$ site has one Mo_b and one C_2 atom while the b_6 site has two Mo_b atoms. On (101), there are two stable molecular adsorption configurations ($\mathbf{t}_{3-1}$ and $\mathbf{t}_{3-2}$) on the $\mathbf{t}_3$ site with similar adsorption energies (−0.42 and −0.46 eV) but in different orientations.

The Mo/C mixed (201) surface has 16 surface Mo atoms and four surface C atoms as well as 17 possible adsorption sites ($\mathbf{t}_1$−$\mathbf{t}_5$, $\mathbf{b}_1$−$\mathbf{b}_7$ and $\mathbf{h}_1$−$\mathbf{h}_5$). There are five types of surface atoms with different coordination patterns; i.e., the Mo_2 atom on the $\mathbf{t}_1$ site coordinates with one bulk C atom and has two free coordination sites, the Mo_1 atom on the $\mathbf{t}_2$ site coordinates with two bulk C atoms and has one dangling bond, the Mo_3 atom on the $\mathbf{t}_3$ site coordinates with two surface C atoms and one bulk C atom to form saturated coordination, and the Mo_{1s} atom on the $\mathbf{t}_5$ site coordinates with two bulk C atoms and has one dangling bond while the C_1 atom on the $\mathbf{t}_4$ site coordinates with five Mo atoms and has one dangling bond. For the bridge sites, the $\mathbf{b}_1$ site has two Mo_2 atoms; the $\mathbf{b}_2$ site has one Mo_1 atom and one Mo_2 atom; the $\mathbf{b}_3$ site has two Mo_1 atoms; the $\mathbf{b}_4$ site has one Mo_1 atom and one Mo_3 atom; the $\mathbf{b}_5$ site has two Mo_3 atoms; the $\mathbf{b}_6$ site has one Mo_{1s} atom and one Mo_3 atom; while the $\mathbf{b}_7$ site has two Mo_{1s} atoms. For the hollow sites, the 4-fold $\mathbf{h}_1$ site has two Mo_1 atoms and two Mo_2 atoms; the 3-fold $\mathbf{h}_2$ site has two Mo_1 atoms and one Mo_3 atom as well as a bulk carbon atom below; the 3-fold $\mathbf{h}_3$ site has one Mo_1 atom and two Mo_3 atoms; the 3-fold $\mathbf{h}_4$ site has two Mo_{1s} atoms and one Mo_2 atom; while the 3-fold $\mathbf{h}_5$ site has one Mo_{1s} atom and two Mo_2

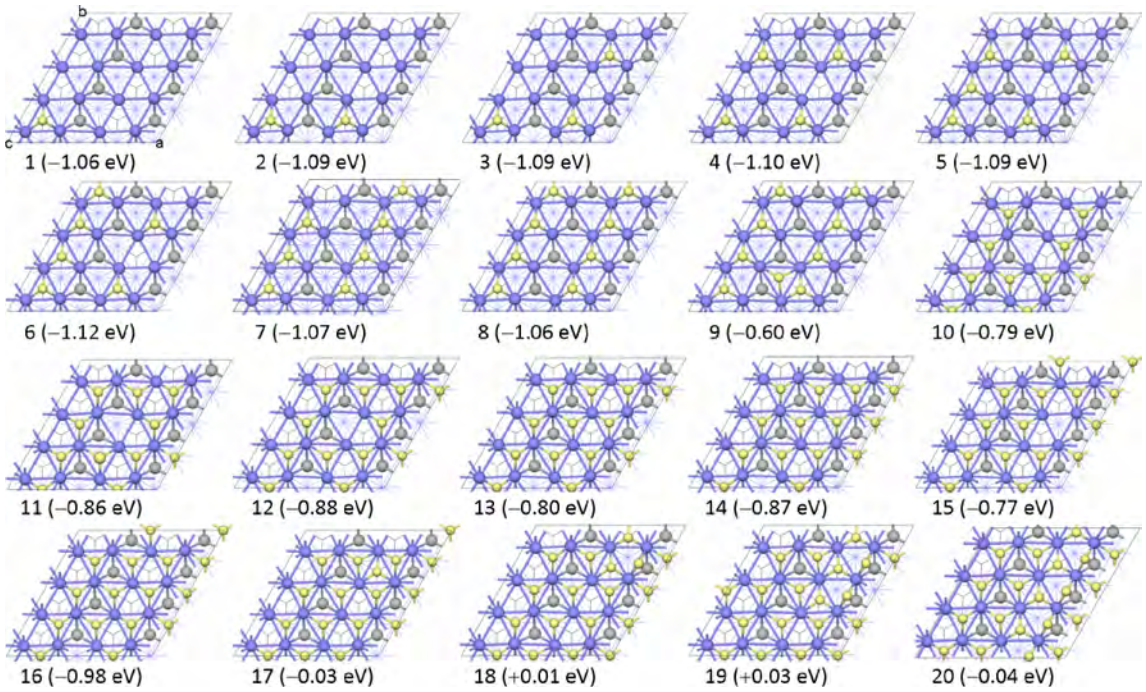

1 (−1.06 eV) 2 (−1.09 eV) 3 (−1.09 eV) 4 (−1.10 eV) 5 (−1.09 eV)
6 (−1.12 eV) 7 (−1.07 eV) 8 (−1.06 eV) 9 (−0.60 eV) 10 (−0.79 eV)
11 (−0.86 eV) 12 (−0.88 eV) 13 (−0.80 eV) 14 (−0.87 eV) 15 (−0.77 eV)
16 (−0.98 eV) 17 (−0.03 eV) 18 (+0.01 eV) 19 (+0.03 eV) 20 (−0.04 eV)

Figure 2. Structures and stepwise adsorption energies of hydrogen at different coverage (n_H = 1−20) on the (001) surface (surface Mo/blue; surface C/gray; bulk C/black, hydrogen/yellow).

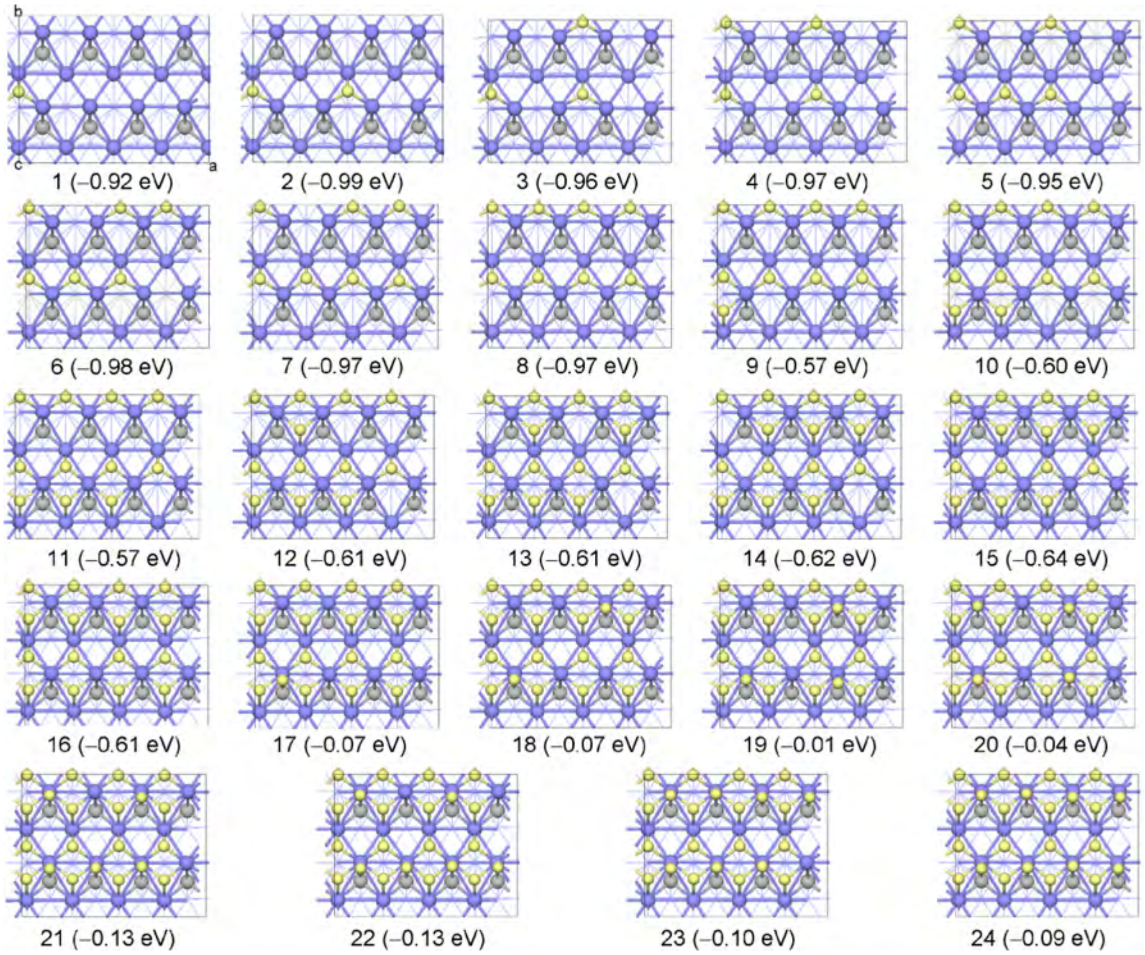

1 (−0.92 eV) 2 (−0.99 eV) 3 (−0.96 eV) 4 (−0.97 eV) 5 (−0.95 eV)
6 (−0.98 eV) 7 (−0.97 eV) 8 (−0.97 eV) 9 (−0.57 eV) 10 (−0.60 eV)
11 (−0.57 eV) 12 (−0.61 eV) 13 (−0.61 eV) 14 (−0.62 eV) 15 (−0.64 eV)
16 (−0.61 eV) 17 (−0.07 eV) 18 (−0.07 eV) 19 (−0.01 eV) 20 (−0.04 eV)
21 (−0.13 eV) 22 (−0.13 eV) 23 (−0.10 eV) 24 (−0.09 eV)

Figure 3. Structures and stepwise adsorption energies of hydrogen at different coverage (n_H = 1−24) on the (100) surface (surface Mo/blue; surface C/gray; bulk C/black, hydrogen/yellow).

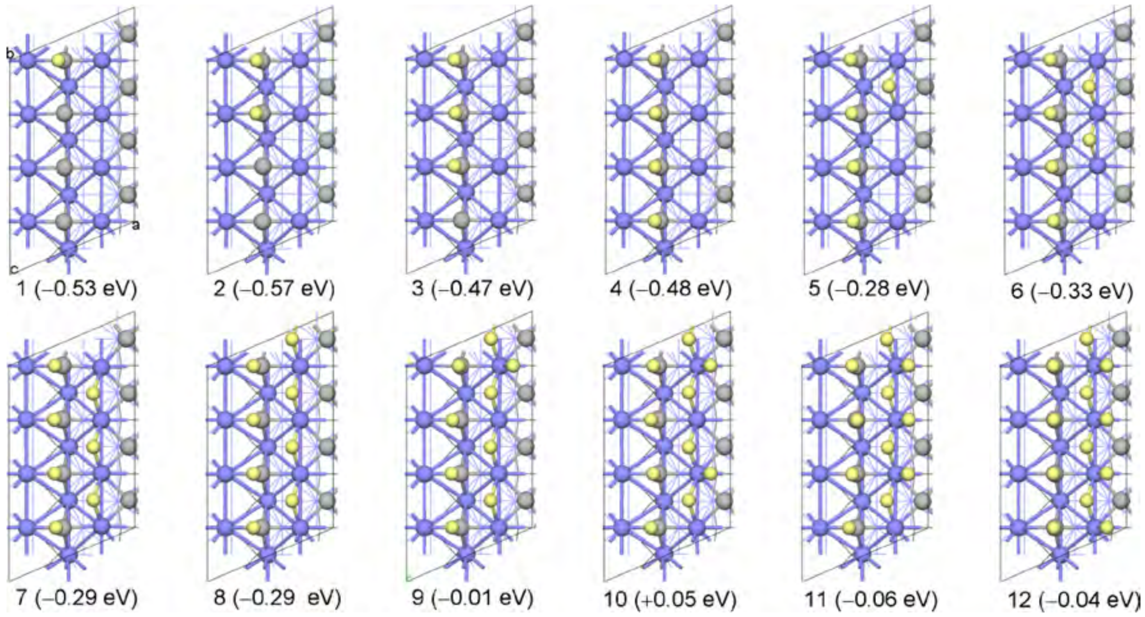

Figure 4. Structures and stepwise adsorption energies of hydrogen at different coverage (n_H = 1−12) on the (101) surface (surface Mo/blue; surface C/gray; bulk C/black, hydrogen/yellow).

atoms. On (201), only four top sites ($\mathbf{t}_1$, $\mathbf{t}_2$, $\mathbf{t}_3$, and $\mathbf{t}_4$) can form molecular H_2 adsorption and the $\mathbf{t}_2$ site is most stable (−0.84 eV).

On the basis of their most stable adsorption configurations in Figure S1, we computed the dissociation barriers and energies for H_2 dissociative adsorption on other three surfaces. The energies of transition states and final states are given in the Supporting Information (Figure S2). Apart from the barrier-less H_2 dissociative adsorption on (001) surface, the calculated dissociation barrier on (100), (101), and (201) is 0.14, 0.34, and 0.20 eV, respectively, and they are smaller in magnitude than their adsorption energy of −0.82, −0.46, and −0.84 eV, respectively. This indicates that H_2 prefers dissociation on the surface instead of desorption from the surface. All H_2 dissociative adsorption is exothermic, i.e., −2.15 eV on (001), −1.09 eV on (100), −0.64 eV on (101), and −1.14 eV on (201). It is noted that H_2 dissociative adsorption on these surfaces is very favorable, and high coverage adsorption is likely.

Hydrogen Adsorption at Higher Coverage. In order to find the most stable adsorption structures at different coverage, we increased the total number of H atoms one by one based on the most stable structure of one H atom on the surfaces. In this way, one additional H was added to the previous most stable one to get the next most stable one by considering many different possibilities. For determining the saturated coverage, we used the stepwise adsorption energy, $\Delta E_{ads} = E[(H)_{n+1}/\text{slab}] - E[(H)_n/\text{slab}] - E[H_2]/2$, where a positive ΔE_{ads} indicates the saturated adsorption with nH atoms. On the basis of these most stable adsorption configurations at given coverage, the actual equilibrium coverage under different conditions can be obtained from atomistic thermodynamics. It is worthy to note that our stepwise adsorption energy defines the change of the adsorption energy by adding one more species to the surface, while the differential energy of adsorption defines the change of the average adsorption energy per coverage as the function of coverage.[76] All our reported energetics includes the correction of zero-point energy (ZPE) between the adsorbed surface H atoms and H_2 in gas phase. The contribution of ZPE correction to the stepwise adsorption energies on all four surfaces (Tables S1−S4) has an average absolute effect of 0.04, 0.03, 0.10, and 0.03 eV on the (001), (100), (101), and (201) surfaces, respectively. The structures and stepwise adsorption energies of hydrogen at different coverage on the (001), (100), (101), and (201) surfaces are given in Figures 2−5.

On the (001) surface (Figure 2), the first eight H atoms (n_H = 1−8) are located at the $\mathbf{h}_1$ site, and they also have very close ΔE_{ads} (−1.15 to −1.06 eV), indicating their negligible lateral repulsive interaction. With n_H = 9, a new adsorption configuration at the $\mathbf{h}_4$ site appears along with the eight hydrogen atoms at the $\mathbf{h}_1$ site, and the ΔE_{ads} (−0.60 eV) is much smaller. With n_H = 10, the most stable adsorption configurations change from $\mathbf{h}_1$ and $\mathbf{h}_4$ sites to $\mathbf{h}_2$ and $\mathbf{h}_4$ sites, and this is also the same for n_H = 11−16. For n_H = 9−16, the ΔE_{ads} are also close, and they are apparently smaller than those for n_H = 1−8, indicating the increased lateral repulsive interaction among the first eight adsorbed hydrogen (n_H = 1−8) atoms with the afterward adsorbed eight hydrogen atoms (n_H = 9−16). However, the lateral repulsive interaction among the afterward adsorbed eight hydrogen (n_H = 9−16) is rather small. For n_H = 17−20, the ΔE_{ads} become very small and positive but are also close. At the coverage of n_H = 18−20, four adsorption configurations ($\mathbf{b}_1$, $\mathbf{h}_1$, $\mathbf{h}_2$, and $\mathbf{h}_4$) coexist. On the basis of the calculated ΔE_{ads}, it is easy to conclude that there are three types of adsorbed hydrogen atoms: the first eight (n_H = 1−8), the second eight (n_H = 9−16), and the third four (n_H = 17−20) hydrogen atoms. It is noted that at saturated coverage the dissociative adsorption of eight H_2 is thermodynamically very favorable than the molecular adsorption by 9.11 eV. Since the H−H distances of these adsorbed H_2 molecules are much longer than that in gas phase (0.994−1.003 Å vs 0.75 Å), H_2 dissociation at the saturated coverage should have very low barriers.

The most stable adsorption configuration on the (100) surface is located on the $\mathbf{h}_4$ site at low coverage (Figure 3). For n_H = 1−8, all hydrogen atoms have the same adsorption

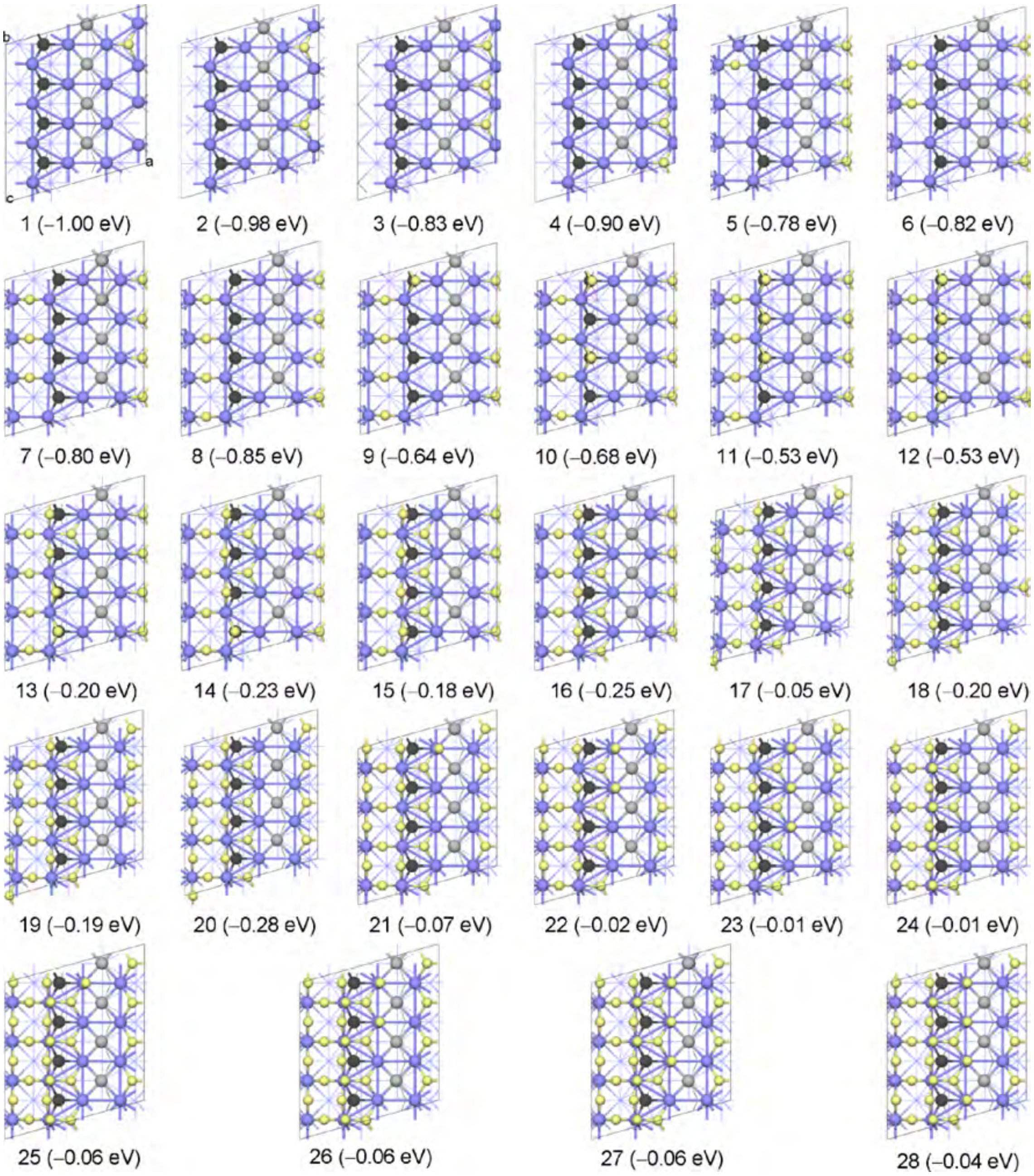

1 (−1.00 eV) 2 (−0.98 eV) 3 (−0.83 eV) 4 (−0.90 eV) 5 (−0.78 eV) 6 (−0.82 eV)
7 (−0.80 eV) 8 (−0.85 eV) 9 (−0.64 eV) 10 (−0.68 eV) 11 (−0.53 eV) 12 (−0.53 eV)
13 (−0.20 eV) 14 (−0.23 eV) 15 (−0.18 eV) 16 (−0.25 eV) 17 (−0.05 eV) 18 (−0.20 eV)
19 (−0.19 eV) 20 (−0.28 eV) 21 (−0.07 eV) 22 (−0.02 eV) 23 (−0.01 eV) 24 (−0.01 eV)
25 (−0.06 eV) 26 (−0.06 eV) 27 (−0.06 eV) 28 (−0.04 eV)

Figure 5. Structures and stepwise adsorption energies of hydrogen at different coverage ($n_H = 1-28$) on the (201) surface (surface Mo/blue; surface C/gray; bulk C/black, hydrogen/yellow).

configuration in the $\mathbf{h}_4$ site and very close stepwise adsorption energies, indicating the negligible lateral repulsive interaction among these adsorbed hydrogen atoms. For $n_H = 9-16$, the second eight hydrogen atoms have the same adsorption configuration at the $\mathbf{h}_1$ site and close ΔE_{ads}, while the first eight adsorbed hydrogen atoms are at the $\mathbf{h}_4$ site. These show that lateral repulsive interaction can only be found among the first eight and the second eight absorbed hydrogen atoms, and the lateral repulsive interaction among the second eight hydrogen atoms are apparently negligible. For $n_H = 17-24$, top adsorption configuration appears and the calculated ΔE_{ads} drops sharply, and the most stable adsorption configurations have hydrogen atoms on the $\mathbf{h}_4$, $\mathbf{h}_1$, and $\mathbf{t}_1$ sites. There are also three types of adsorbed hydrogen atoms: the first eight ($n_H =$ 1−8), the second eight ($n_H = 9-16$), and the third eight ($n_H =$ 17−24) hydrogen atoms.

On the (101) surface the most stable adsorption configuration is located on the surface carbon atom ($\mathbf{t}_2$) at low coverage (Figure 4). With $n_H = 1-4$, four H atoms have the same adsorption configurations and also very similar ΔE_{ads}, indicating the negligible lateral repulsive interaction among these adsorbed hydrogen atoms. It should be noted that H atoms tend to adsorb on the surface carbon atoms at low coverage (C−H) while both C−H and Mo−H are possible at high coverage and form the $Mo_2C_xH_y$ species on the surface. With $n_H = 5-8$, all these four H atoms form stable adsorption configurations on the bridge ($\mathbf{b}_3$) site and have very similar stepwise adsorption energies. With $n_H = 9-12$, the top adsorption configuration on $\mathbf{t}_3$ site appears and the saturated coverage is reached at $n_H = 12$. Three groups of H atoms with $\mathbf{t}_2$, $\mathbf{t}_3$, and $\mathbf{b}_3$ configurations coexist on (101) surface.

On the (201) surface, the most stable adsorption configuration is located on the 3-fold $\mathbf{h}_5$ site at low coverage (Figure 5). With n_H = 1−4, four H atoms have the same adsorption configurations at the $\mathbf{h}_5$ site and very similar ΔE_{ads}. With n_H = 5−8, these four H atoms form the same adsorption configurations on the $\mathbf{b}_2$ sites and also have similar ΔE_{ads}. Despite the changes of adsorption configurations for the four H atoms at n_H = 1−4 and 5−8, these eight H atoms have very similar ΔE_{ads}, which indicates their negligible lateral repulsive interaction. With n_H = 9−12, four H atoms form the same adsorption configurations on the $\mathbf{b}_3$ sites and have very similar ΔE_{ads}. With n_H = 13−16, four H atoms have the same adsorption configurations on the $\mathbf{h}_3$ sites and very similar ΔE_{ads}. With n_H = 17−20, the adsorbed H atoms on the $\mathbf{h}_5$ sites are transferred to the $\mathbf{h}_4$ and $\mathbf{b}_1$ sites. Close inspections reveals that eight H atoms with n_H = 13−20 have very similar stepwise adsorption energies since all of them form stable adsorptions on the 3-fold hollow sites. With n_H = 21−28, adsorption configurations on the top sites appear, but the values of ΔE_{ads} decrease sharply. Finally, the saturated coverage is reached at $n_H = 28$ with seven different adsorption configurations ($\mathbf{t}_2$, $\mathbf{t}_3$, $\mathbf{b}_1$, $\mathbf{b}_2$, $\mathbf{b}_3$, $\mathbf{h}_3$, and $\mathbf{h}_4$) coexist on the surface.

On the basis of the above energetic and structural information, it is interesting to compare their differences in hydrogen adsorption properties among these surfaces. The monolayer (1 ML) coverage on the (001), (100), (101), and (201) surfaces might have 16H, 16H, 16H, and 20H atoms, respectively. However, the DFT predicted saturated coverage on the (001), (100), (101), and (201) surfaces are 1.25, 1.50, 0.75, and 1.40 ML, respectively. Since each surface at the saturated coverage has different types of adsorbed H atoms and each type of adsorbed hydrogen atoms has the same adsorption configuration as well as close stepwise adsorption energies, different desorption properties can be expected.

Stable Hydrogen Coverage Depending on Temperature and Pressure. Since the stable coverage of adsorbed surface species depends strongly on temperature and pressure, it is desired to consider their influences for studying the adsorption properties. Consequently, we applied ab initio thermodynamics to discuss the effects of temperature and hydrogen partial pressure on the stable hydrogen coverage on each surface. It is noted that high pressure H_2 will not change the surface composition of clean surfaces, since these clean surfaces are generated experimentally from hydrogen pretreatment of the freshly synthesized Mo_2C catalysts with polymeric carbons.[77] Furthermore, Mo_2C reduction into metallic Mo has been found only to occur at higher than 1200 K under experimental conditions. As the result, the up limit of the temperature is chosen as 1200 K in this work where the surface composition will not be changed.

Stepwise adsorption Gibbs free energy (ΔG) is used to determine the stable coverage of H atoms on the surfaces under different conditions, and a more negative ΔG indicates a more stable adsorption. On the basis of the calculated total energies of different stable structures and H_2 chemical potentials under different conditions, we plotted ΔG as a function of T and p_{H2} in Figure 6.

As shown in Figure 6, each phase diagram has several stable adsorption regions, and each region represents the possibility for the stable hydrogen coverage within the range of both temperature and H_2 partial pressure. On the (001) surface (Figure 6a), there are three regions, and the first region represents the coverage with n_H = 16 (1 ML), the second region shows the stable adsorption with n_H = 8, and the third region is free from hydrogen. Similar phase diagrams have been found on the (100) and (101) surfaces (Figure 6b,c). On the (201) surface, there are seven possible stable adsorption regions (Figure 6d). Close inspections shows that each stable adsorption region has an intimate relationship with the types of adsorbed H atoms as shown in Figures 2−5.

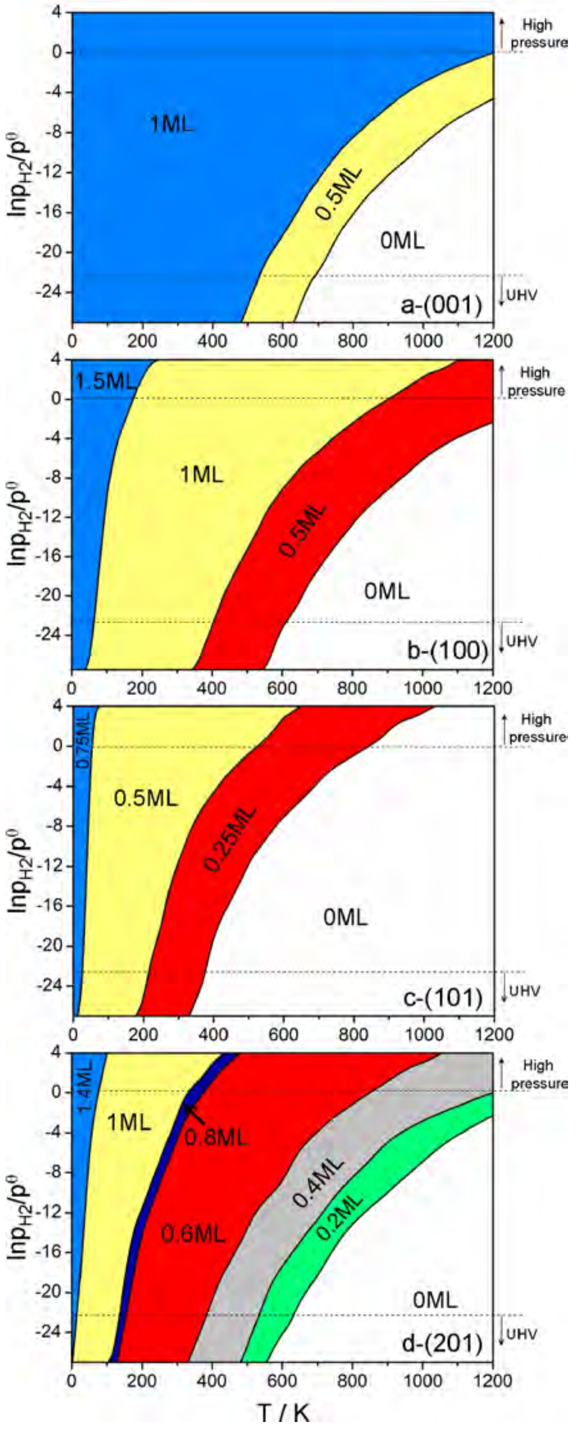

Figure 6. Equilibrium phase diagrams of hydrogen coverage on a-(001), b-(100), c-(101), and d-(201) surfaces.

On the basis of the phase diagrams in Figure 6, it is easy to get the stable hydrogen coverage at any given conditions. It can provide the information on hydrogen adsorption under ultrahigh vacuum (UHV) condition for surface science studies or at high temperature and pressures for practical application, like alcohol synthesis from CO hydrogenation. At $p_{H2} = 10^{-9}$ atm ($\ln p_{H2}/p^{\theta} = -21$) and 200 K, for example, the stable hydrogen coverage on the (001), (100), (101), and (201) surfaces has 16H (1 ML), 16H (1 ML), 8H (0.5 ML), and 12H (0.6 ML), respectively, and they are lower than their saturated coverage, demonstrating their differences in surface structures and active sites. These phase diagrams show that hydrogen desorption from these Mo_2C surfaces generally occurs at the temperature ranges of 300−400 and 550−700 K under UHV condition (10^{-10}−10^{-13} atm). Indeed, our computed results agree well with the experimental observations of UHV studies of $C_xH_yO_z$ decompositions on Mo_2C by Solymosi et al.,[78−80] where that desorption of the formed H_2 occurs at the ranges of 330−400 and 600−640 K.

It is also interesting to compare the energetics of hydrogen adsorption on these surfaces with their surface structures and stabilities. On the basis of the calculated surface Gibbs free energies,[52] the (101) surface is most stable (1.75 J/m^2), followed by the (201) surface (1.95 J/m^2) and the (001) surface (2.02 J/m^2), while the (100) surface is least stable (2.07 J/m^2). The most stable (101) surface has eight Mo and eight C atoms (Mo/C = 1/1) exposed; the second stable (201) surface has 16 Mo and four C atoms (Mo/C = 4/1). On the (001) surface, the first layer has 16 Mo atoms and the second layer has eight C atoms (Mo/C = 2/1); while the open (100) surface has both first and second layer 16 Mo atoms exposed and the third layer has eight C atoms (Mo/C = 2/1).

The weakest dissociative H_2 adsorption is found on the most stable (101) surface (−1.10 eV), followed by the (100) surface (−1.91 eV) and the (201) surface (−1.98 eV), while the strongest dissociative H_2 adsorption is found on the (001) surface. This energetic order differs from their surface stability order on the basis of surface Gibbs free energies. Furthermore, the full hydrogen desorption temperature is the lowest on the (101) surface (425 K), followed by the (100) surface (625 K) and (201) surface (650 K), while the highest on the (001) surface (750 K) at $p_{H2} = 10^{-9}$ atm. The desorption properties of H_2 with increasing temperature is of great relevance to the experimental characterization tool of hydrogen temperature-programmed desorption (TPD), where the desorption states and temperatures of H_2 can provide useful information about the surfaces structures and active sites of catalysts. The difference in hydrogen desorption temperatures can be used to differentiate their hydrogen binding number and strength for hydrotreating ability.

On the basis of our previous study on CO adsorption[34] and current results on H_2 adsorption on the hexagonal Mo_2C surfaces at different coverage, it is interesting to compare their adsorption properties and discuss their chemical consequences for reactions involving synthesis gas (CO/H_2) on catalysts, where CO adsorption and activation as well as H_2 adsorption and activation are the initial and elementary steps. On the hexagonal Mo_2C surfaces, the adsorption energies of CO are much stronger than those of H_2. Under synthesis gas (CO/H_2) condition, it is therefore to expect that the catalysts surfaces will be predominately covered by CO instead of by H_2, as found experimentally.[81−83] Consequently, the adsorbed surface CO/H_2 ratio must be different from that in gas phase. This will raise the questions about the mechanisms of CO activation and surface intermediates ($C_xH_yO_z$) formation as well as products formation. Depending on the differences in adsorption energies of CO and H_2 as well as under different temperature and pressure, two mechanisms can be proposed: one will be the mechanism from CO and H_2 coadsorption, and another one will be the mechanism from adsorbed CO and gas phase H_2. Our recent study on CO adsorption and dissociation on the Fe(100) surface shows clearly the coverage dependence of CO adsorption energy and dissociation barrier,[84] i.e., only molecular adsorption at very high coverage (n_{CO} = 8−11), mixed molecular and dissociative adsorption at medium coverage (n_{CO} = 5−7), and only dissociative adsorption at low coverage (n_{CO} = 1−4). On the basis of very different CO activation on catalysts surfaces, the reaction mechanisms will be totally different from those obtained at low coverage. These results will be very important for understanding the initial stages of reactions involving synthesis gas (CO/H_2), for example, water-gas shift reaction, Fischer−Tropsch synthesis, and alcohol synthesis from CO hydrogenation.

■ CONCLUSION

For understanding the promising hydrotreating activity of molybdenum carbides, the adsorption properties of hydrogen on the mainly exposed (001), (100), (101), and (201) surfaces of the hexagonal Mo_2C phase have been systematically studied on the basis of density functional theory calculations. The (001) and (100) terminations have only Mo atoms on the surface, while the (101) and (201) terminations have mixed metal and carbon atom on the surfaces. The effects of temperature and pressure on the stable hydrogen coverage were considered by applying *ab initio* atomistic thermodynamics method.

On the (001) surface, only dissociative H_2 adsorption is obtained, while molecular H_2 adsorption has been found on the (100), (101), and (201) surfaces. Dissociation of H_2 on these surfaces has very low energy barrier and is very exothermic, indicating their ability of H_2 activation. Because of their different surface structures and composition, they can have different hydrogen adsorption configurations coexisting at very high coverage. At the saturated coverage, the (001) surface has one bridge ($\mathbf{b}_1$) and three hollow ($\mathbf{h}_1$, $\mathbf{h}_2$, and $\mathbf{h}_4$) adsorption configurations, the (100) surface has one top ($\mathbf{t}_1$) and two hollow ($\mathbf{h}_1$ and $\mathbf{h}_4$) adsorption configurations, the (101) surface has three adsorption configurations ($\mathbf{t}_2$, $\mathbf{t}_3$, and $\mathbf{b}_3$), and the (201) surface has seven adsorption configurations ($\mathbf{t}_2$, $\mathbf{t}_3$, $\mathbf{b}_1$, $\mathbf{b}_2$, $\mathbf{b}_3$, $\mathbf{h}_3$, and $\mathbf{h}_4$).

The stable hydrogen coverage on the surfaces depends on temperature and pressure. At given H_2 partial pressure, raising temperature will lower the stable coverage, while at given temperature, raising partial pressure will increase the stable coverage. The phase diagrams reveal that stable hydrogen coverage can be obtained within a range of temperature and partial pressure, and different surfaces can have different coverage under the same conditions. Those phase diagrams provide useful information not only for surface science studies at ultrahigh vacuum conditions but also for practical applications at high temperature and pressure in monitoring surface reactions. Three stable hydrogen regions for the (001) surface as well as four regions for the (100) and (101) surfaces were found, while the (201) surface has seven stable hydrogen regions. The differences in hydrogen adsorption number and strength indicate their characteristic surface active sites and hydrotreating abilities.

ASSOCIATED CONTENT

Supporting Information

Benchmark calculation for k-point grid (Table S0); stepwise H adsorption energies with and without zero-point energy corrections (Tables S1−S4); stable adsorption configuration for molecular hydrogen (Figure S1); and energy profiles for molecular H_2 dissociation (Figure S2). This material is available free of charge via the Internet at http://pubs.acs.org.

AUTHOR INFORMATION

Corresponding Author

*E-mail: haijun.jiao@catalysis.de (H.J.).

Notes

The authors declare no competing financial interest.

ACKNOWLEDGMENTS

This work was supported by National Basic Research Program of China (No. 2011CB201406), Chinese Academy of Science and Synfuels CHINA. Co., Ltd. We also acknowledge general finical support from the BMBF and the state of Mecklenburg-Western Pomerania.

REFERENCES

(1) Toth, L. E. *Transition Metal Carbides and Nitrides*; Academic Press: New York, 1971.

(2) Gubanov, V. A.; Ivanovsky, A. L.; Zhukov, V. P. *Electronic Structure of Refractory Carbides and Nitrides*; Cambridge University Press: Cambridge, 1994.

(3) Chen, J. G. Carbide and Nitride Overlayers on Early Transition Metal Surfaces: Preparation, Characterization, and Reactivities. *Chem. Rev.* **1996**, *96*, 1447−1498.

(4) Wu, H. H. H.; Chen, J. G. Surface Chemistry of Transition Metal Carbides. *Chem. Rev.* **2005**, *105*, 185−212.

(5) Oyama, S. T. *The Chemistry of Transition Metal Carbides and Nitrides*; Blackie Academic and Professional: Glasgow, 1996.

(6) Levy, R. B.; Boudart, M. Platinum-Like Behavior of Tungsten Carbide in Surface Catalysis. *Science* **1973**, *181*, 547−549.

(7) Oyama, S. T. Preparation and Catalytic Properties of Transition Metal Carbides and Nitrides. *Catal. Today* **1992**, *15*, 179−200.

(8) Nagai, M.; Matsuda, K. Low-Temperature Water−Gas Shift Reaction over Cobalt-Molybdenum Carbide Catalyst. *J. Catal.* **2006**, *238*, 489−496.

(9) Schaidle, J. A.; Lausche, A. C.; Thompson, L. T. Effects of Sulfur on Mo_2C and Pt/Mo_2C Catalysts: Water Gas Shift Reaction. *J. Catal.* **2010**, *272*, 235−245.

(10) Namiki, T.; Yamashita, S.; Tominaga, H.; Nagai, M. Dissociation of CO and H_2O during Water−Gas Shift Reaction on Carburized Mo/Al_2O_3 Catalyst. *Appl. Catal., A* **2011**, *398*, 155−160.

(11) Xiang, M. L.; Li, D. B.; Li, W. H.; Zhong, B.; Sun, Y. H. Synthesis of Higher Alcohols from Syngas over K/Co/β-Mo_2C Catalysts. *Catal. Commun.* **2007**, *8*, 503−507.

(12) Xiang, M. L.; Li, D. B.; Xiao, H. C.; Zhang, J. L.; Li, W. H.; Zhong, B.; Sun, Y. H. K/Ni/β-Mo_2C: A Highly Active and Selective Catalyst for Higher Alcohols Synthesis from CO Hydrogenation. *Catal. Today* **2008**, *131*, 489−495.

(13) Zaman, S.; Smith, K. J. A Review of Molybdenum Catalysts for Synthesis Gas Conversion to Alcohols: Catalysts, Mechanisms and Kinetics. *Catal. Rev.: Sci. Eng.* **2012**, *54* (1), 41−132.

(14) Sundaramurthy, V.; Dalai, A. K.; Adjaye, J. HDN and HDS of Different Gas Oils Derived from Athabasca Bitumen over Phosphorus Doped NiMo/γ-Al_2O_3 Carbides. *Appl. Catal., B* **2006**, *68*, 38−48.

(15) Al-Megren, H. A.; Gonzalez-Cortes, S. L.; Xiao, T. C.; Green, M. L. H. A Comparative Study of the Catalytic Performance of Co-Mo and Co(Ni)-W Carbide Catalysts in the Hydrodenitrogenation (HDN) Reaction of Pyridine. *Appl. Catal., A* **2007**, *329*, 36−45.

(16) Neylon, M. K.; Choi, S.; Kwon, H.; Curry, K. E.; Thompson, L. T. Catalytic Properties of Early Transition Metal Nitrides and Carbides: n-Butane Hydrogenolysis, Dehydrogenation and Isomerization. *Appl. Catal., A* **1999**, *183*, 253−263.

(17) Ardakani, S. J.; Liu, X. B.; Smith, K. J. Hydrogenation and Ring Opening of Naphthalene on Bulk and Supported Mo_2C Catalysts. *Appl. Catal., A* **2007**, *324*, 9−19.

(18) Barthos, R.; Solymosi, F. Hydrogen Production in the Decomposition and Steam Reforming of Methanol on Mo_2C/Carbon Catalysts. *J. Catal.* **2007**, *249*, 289−299.

(19) Solymosi, F.; Cserenyi, J.; Szöke, A.; Bansagi, T.; Qszko, A. Aromatization of Methane over Supported and Unsupported Mo-Based Catalysts. *J. Catal.* **1997**, *165*, 150−161.

(20) Oshikawa, K.; Nagai, M.; Omi, S. Characterization of Molybdenum Carbides for Methane Reforming by TPR, XRD, and XPS. *J. Phys. Chem. B* **2001**, *105*, 9124−9131.

(21) St Clair, T. P.; Oyama, S. T.; Cox, D. F.; Otani, S.; Ishizawa, Y.; Lo, R. L.; Fukui, K.; Iwasawa, Y. Surface Characterization of -Mo_2C (0001). *Surf. Sci.* **1999**, *426*, 187−198.

(22) Parthe, E.; Sadagopan, V. The Structure of Dimolybdenum Carbide by Neutron Diffraction Technique. *Acta Crystallogr.* **1963**, *16*, 202−205.

(23) Medford, A. J.; Vojvodic, A.; Studt, F.; Abild-Pedersen, F.; Nørskov, J. K. Elementary Steps of Syngas Reactions on Mo_2C(001): Adsorption Thermochemistry and Bond Dissociation. *J. Catal.* **2012**, *290*, 108−117.

(24) Liu, P.; Rodriguez, J. A.; Muckerman, J. T. Desulfurization of SO_2 and Thiophene on Surfaces and Nanoparticles of Molybdenum Carbide: Unexpected Ligand and Steric Effects. *J. Phys. Chem. B* **2004**, *108*, 15662−15670.

(25) Liu, P.; Rodriguez, J. A.; Asakura, T.; Gomes, J.; Nakamura, K. Desulfurization Reactions on Ni_2P(001) and α-Mo_2C(001) Surfaces: Complex Role of P and C Sites. *J. Phys. Chem. B* **2005**, *109*, 4575−4583.

(26) Liu, P.; Rodriguez, J. A.; Muckerman, J. T. Sulfur Adsorption and Sulfidation of Transition Metal Carbides as Hydrotreating Catalysts. *J. Mol. Catal. A: Chem.* **2005**, *239*, 116−124.

(27) Pistonesi, C.; Juan, A.; Farkas, A. P.; Solymosi, F. DFT Study of Methanol Adsorption and Dissociation on β-Mo_2C(001). *Surf. Sci.* **2008**, *602*, 2206−2211.

(28) Pistonesi, C.; Juan, A.; Farkas, A. P.; Solymosi, F. Effects of Potassium on the Adsorption of Methanol on β-Mo_2C(001) Surface. *Surf. Sci.* **2010**, *604*, 914−919.

(29) Pronsato, M. E.; Pistonesi, C.; Juan, A.; Farkas, A. P.; Bugyi, L.; Solymosi, F. Density Functional Theory Study of Methyl Iodide Adsorption and Dissociation on Clean and K-Promoted β-Mo_2C Surfaces. *J. Phys. Chem. C* **2011**, *115*, 2798−2804.

(30) Pistonesi, C.; Pronsato, M. E.; Bugyi, L.; Juan, A. Theoretical Model for CO Adsorption and Dissociation on Clean and K-Doped β-Mo_2C Surfaces. *J. Phys. Chem. C* **2012**, *116*, 24573−24581.

(31) Tominaga, H.; Nagai, M. Mechanism of Thiophene Hydrodesulfurization on Clean/Sulfided -Mo_2C(001) Based on Density Functional Theory-Cis- and Trans-2-Butene Formation at the Initial Stage. *Appl. Catal., A* **2008**, *343*, 95−103.

(32) Piskorz, W.; Adamski, G.; Kotarba, A.; Sojka, Z.; Sayag, C.; Djéga-Mariadassou, G. Hydrodenitrogenation of Indole over Mo2C Catalyst: Insights into Mechanistic Events Through DFT Modeling. *Catal. Today* **2007**, *119*, 39−43.

(33) Kotarba, A.; Adamski, G.; Piskorz, W.; Sojka, Z.; Sayag, C.; Djéga-Mariadassou, G. Modification of Electronic Properties of Mo_2C Catalyst by Potassium Doping: Impact on the Reactivity in Hydrodenitrogenation Reaction of Indole. *J. Phys. Chem. B* **2004**, *108*, 2885−2892.

(34) Wang, T.; Wang, S. G.; Li, Y. W.; Wang, J. G.; Jiao, H. J. Adsorption Equilibria of CO Coverage on β-Mo_2C Surfaces. *J. Phys. Chem. C* **2012**, *116*, 6340−6348.

(35) Wang, J.; Castonguay, M.; Deng, J.; McBreen, P. H. RAIRS and TPD Study of CO and NO on β-Mo_2C. *Surf. Sci.* **1997**, *374*, 197−207.

(36) Bugyi, L.; Solymosi, F. Effects of Potassium on the Chemisorption of CO on the Mo_2C/Mo(100) Surface. *J. Phys. Chem. B* **2001**, *105*, 4337−4342.

(37) Tominaga, H.; Aoki, Y.; Nagai, M. Hydrogenation of CO on Molybdenum and Cobalt Molybdenum Carbides. *Appl. Catal., A* **2012**, *423*, 192−204.

(38) Zheng, W.; Cotter, T. P.; Kaghazchi, P.; Jacob, T.; Frank, B.; Schlichte, K.; Zhang, W.; Su, D. S.; Schüth, F.; Schlögl, R. Experimental and Theoretical Investigation of Molybdenum Carbide and Nitride as Catalysts for Ammonia Decomposition. *J. Am. Chem. Soc.* **2013**, *135*, 3458−3464.

(39) Nagai, M.; Tominaga, H.; Omi, S. CO Adsorption on Molybdenum Carbides and Molecular Simulation. *Langmuir* **2000**, *16*, 10215−10220.

(40) Ren, J.; Huo, C. F.; Wang, J.; Li, Y. W.; Jiao, H. J. Surface Structure and Energetics of Oxygen and CO Adsorption on -Mo_2C(0001). *Surf. Sci.* **2005**, *596*, 212−221.

(41) Ren, J.; Wang, J.; Huo, C. F.; Wen, X. D.; Cao, Z.; Yuan, S. P.; Li, Y. W.; Jiao, H. J. Adsorption of NO, NO_2, Pyridine and Pyrrole on -Mo_2C(0001): A DFT Study. *Surf. Sci.* **2007**, *601*, 1599−1607.

(42) Rocha, A. S.; Rocha, A. B.; Silva, V. T. Benzene Adsorption on Mo_2C: A Theoretical and Experimental Study. *Appl. Catal., A* **2010**, *379*, 54−60.

(43) Shi, X. R.; Wang, J.; Hermann, K. CO and NO Adsorption and Dissociation at the β-Mo_2C(0001) Surface: A Density Functional Theory Study. *J. Phys. Chem. C* **2010**, *114*, 13630−13641.

(44) Liu, X. C.; Tkalych, A.; Zhou, B. J.; Köster, A. M.; Salahub, D. R. Adsorption of Hexacyclic C_6H_6, C_6H_8, C_6H_{10}, and C_6H_{12} on a Mo-Terminated α-Mo_2C (0001) Surface. *J. Phys. Chem. C* **2013**, *117*, 7069−7080.

(45) Qi, K. Z.; Wang, G. C.; Zheng, W. J. A First-Principles Study of CO Hydrogenation into Methane on Molybdenum Carbides Catalysts. *Surf. Sci.* **2013**, *614*, 53−63.

(46) Tominaga, H.; Nagai, M. Density Functional Theory of Water-Gas Shift Reaction on Molybdenum Carbide. *J. Phys. Chem. B* **2005**, *109*, 20415−20423.

(47) Liu, P.; Rodriguez, J. A. Water-Gas-Shift Reaction on Molybdenum Carbide Surfaces: Essential Role of the Oxycarbide. *J. Phys. Chem. B* **2006**, *110*, 19418−19425.

(48) Ren, J.; Huo, C. F.; Wang, J.; Cao, Z.; Li, Y. W.; Jiao, H. J. Density Functional Theory Study into the Adsorption of CO_2, H and CH_x (x = 0−3) as well as C_2H_4 on -Mo_2C(0001). *Surf. Sci.* **2006**, *600*, 2329−2337.

(49) Luo, Q. Q.; Wang, T.; Walther, G.; Beller, M.; Jiao, H. Molybdenum Carbide Catalysed Hydrogen Production from Formic Acid - A Density Functional Theory Study. *J. Power Sources* **2014**, *246*, 548−555.

(50) Shi, X. R.; Wang, S. G.; Wang, H.; Deng, C. M.; Qin, Z. F.; Wang, J. Structure and Stability of β-Mo_2C Bulk and Surfaces: A Density Functional Theory Study. *Surf. Sci.* **2009**, *603*, 852−859.

(51) Han, J. W.; Li, L.; Sholl, D. S. Density Functional Theory Study of H and CO Adsorption on Alkali-Promoted Mo_2C Surfaces. *J. Phys. Chem. C* **2011**, *115*, 6870−6876.

(52) Wang, T.; Liu, X. W.; Wang, S. G.; Huo, C. F.; Li, Y. W.; Wang, J.; Jiao, H. Stability of β-Mo_2C Facets from ab Initio Atomistic Thermodynamics. *J. Phys. Chem. C* **2011**, *115*, 22360−22368.

(53) Hanif, A.; Xiao, T. C.; York, A. P. E.; Sloan, J.; Green, M. L. H. Study on the Structure and Formation Mechanism of Molybdenum Carbides. *Chem. Mater.* **2002**, *14*, 1009−1015.

(54) Wang, X. H.; Hao, H. L.; Zhang, M. H.; Li, W.; Tao, K. Y. Synthesis and Characterization of Molybdenum Carbides Using Propane as Carbon Source. *J. Solid State Chem.* **2006**, *179*, 538−543.

(55) Nagai, M.; Zahidul, A. M.; Matsuda, K. Nano Structured Nickel-Molybdenum Carbide Catalyst for Low-Temperature Water-Gas Shift Reaction. *Appl. Catal., A* **2006**, *313*, 137−145.

(56) dos Santos Politi, J. R.; Vines, F.; Rodriguez, J. A.; IIlas, F. Atomic and Electronic Structure of Molybdenum Carbide Phases: Bulk and Low Miller-Index Surfaces. *Phys. Chem. Chem. Phys.* **2013**, *15*, 12617−12625.

(57) Fries, R. J.; Kempter, C. P. DiMolybdenum Carbide. *Anal. Chem.* **1960**, *32*, 1898−1898.

(58) Kresse, G.; Furthmüller, J. Efficiency of Ab-initio Total Energy Calculations for Metals and Semiconductors Using a Plane-Wave Basis Set. *Comput. Mater. Sci.* **1996**, *6*, 15−50.

(59) Kresse, G.; Furthmüller, J. Efficient Iterative Schemes for Ab initio Total-Energy Calculations Using a Plane-Wave Basis Set. *Phys. Rev. B* **1996**, *54*, 11169−11186.

(60) Blochl, P. E. Projector Augmented-Wave Method. *Phys. Rev. B* **1994**, *50*, 17953−17979.

(61) Kresse, G. From Ultrasoft Pseudopotentials to the Projector Augmented-Wave Method. *Phys. Rev. B* **1999**, *59*, 1758−1775.

(62) Perdew, J. P.; Burke, K.; Ernzerhof, M. Generalized Gradient Approximation Made Simple. *Phys. Rev. Lett.* **1996**, *77*, 3865−3868.

(63) Henkelman, G.; Jónsson, H. Improved Tangent Estimate in the Nudged Elastic Band Method for Finding Minimum Energy Paths and Saddle Points. *J. Chem. Phys.* **2000**, *113*, 9978−9985.

(64) Reuter, K.; Scheffler, M. Composition, Structure, and Stability of RuO_2(110) as a Function of Oxygen Pressure. *Phys. Rev. B* **2001**, *65*, 035406.

(65) Reuter, K.; Scheffler, M. Composition and Structure of the RuO_2(110) Surface in an O_2 and CO Environment: Implications for the Catalytic Formation of CO_2. *Phys. Rev. B* **2003**, *68*, 045407.

(66) Li, W. X.; Stampfl, C.; Scheffler, M. Insights into the Function of Silver as an Oxidation Catalyst by Ab Initio Atomistic Thermodynamics. *Phys. Rev. B* **2003**, *68*, 165412.

(67) Rogal, J.; Reuter, K.; Scheffler, M. Thermodynamic Stability of PdO Surfaces. *Phys. Rev. B* **2004**, *69*, 075421.

(68) Grillo, M. E.; Ranke, W.; Finnis, M. W. Surface Structure and Water adsorption on Fe_3O_4(111): Spin-Density Functional Theory and on-site Coulomb Interactions. *Phys. Rev. B* **2008**, *77*, 075407.

(69) Aray, Y.; Vidal, A. B.; Rodriguez, J.; Grillo, M. E.; Vega, D.; Coll, D. S. First Principles Study of Low Miller Index RuS_2 Surfaces in Hydrotreating Conditions. *J. Phys. Chem. C* **2009**, *113*, 19545−19557.

(70) Zasada, F.; Piskorz, W.; Cristol, S.; Paul, J. F.; Kotarba, A.; Sojka, Z. Periodic Density Functional Theory and Atomistic Thermodynamic Studies of Cobalt Spinel Nanocrystals in Wet Environment: Molecular Interpretation of Water Adsorption Equilibria. *J. Phys. Chem. C* **2010**, *114*, 22245−22253.

(71) Wang, T.; Li, Y. W.; Wang, J.; Beller, M.; Jiao, H. High Coverage CO Adsorption and Dissociation on the Orthorhombic Mo_2C(100) Surface. *J. Phys. Chem. C* **2014**, *118*, 3162−3171.

(72) Wang, T.; Wang, S. G.; Luo, Q. Q.; Li, Y. W.; Wang, J.; Beller, M.; Jiao, H. Hydrogen Adsorption Structures and Energetics on Iron Surfaces at High Coverage. *J. Phys. Chem. C* **2014**, *118*, 4181−4188.

(73) Ranhotra, G. S.; Bell, A. T.; Reimer, J. A. Catalysis over Molybdenum Carbides and Nitrides II. Studies of CO Hydrogenation and C_2H_6 Hydrogenolysis. *J. Catal.* **1987**, *108*, 40−49.

(74) Miyao, T.; Shishikura, I.; Matsuoka, M.; Nagai, M.; Oyama, S. T. Preparation and Characterization of Alumina-Supported Molybdenum Carbide. *Appl. Catal., A* **1997**, *165*, 419−428.

(75) Lewandowski, M.; Szymańska-Kolasa, A.; Sayag, C.; Beaunier, P.; Djéga-Mariadassou, G. Atomic Level Characterization and Sulfur Resistance of Unsupported W_2C During Dibenzothiophene Hydrodesulfurization. Classical Kinetic Simulation of the Reaction. *Appl. Catal., B* **2014**, *144*, 750−759.

(76) Digne, M.; Sautet, P.; Raybaud, P.; Euzen, P.; Toulhoat, H. Use of DFT to Achieve a Rational Understanding of Acid-Basic Properties of γ-Alumina Surfaces. *J. Catal.* **2004**, *226*, 54−68.

(77) Lee, J. S.; Oyama, S. T.; Boudart, M. Molybdenum Carbide Catalysts I. Synthesis of Unsupported Powders. *J. Catal.* **1987**, *106*, 125−133.

(78) Bugyi, L.; Oszko, A.; Solymosi, F. The Adsorption and Reactions of Propyl Iodide on Clean and Adsorbate-Modified Mo_2C/Mo(100) Surfaces. *Surf. Sci.* **2002**, *516*, 74−84.

(79) Barthos, R.; Bansagi, T.; Zakar, T. S.; Solymosi, F. Aromatization of Methanol and Methylation of Benzene over Mo_2C/ZSM-5 Catalysts. *J. Catal.* **2007**, *247*, 368−378.

(80) Farkas, A. P.; Solymosi, F. Adsorption and Reactions of Dimethyl and Diethyl Ethers on Mo_2C/Mo(100). *Surf. Sci.* **2008**, *602*, 1497−1506.

(81) Mims, C. A.; McCandlish, L. E. Evidence for Rapid Chain Growth in the Fischer−Tropsch Synthesis over Iron and Cobalt Catalysts. *J. Phys. Chem.* **1987**, *91*, 929−937.

(82) Ojeda, M.; Nabar, R.; Nilekar, A. U.; Ishikawa, A.; Mavrikakis, M.; Iglesia, E. CO Activation Pathways and the Mechanism of Fischer-Tropsch Synthesis. *J. Catal.* **2010**, *272*, 287−297.

(83) Loveless, B. T.; Buda, C.; Neurock, M.; Iglesia, E. CO Chemisorption and Dissociation at High Coverages during CO Hydrogenation on Ru Catalysts. *J. Am. Chem. Soc.* **2013**, *135*, 6107−6121.

(84) Wang, T.; Tian, X.; Li, Y. W.; Wang, J.; Beller, M.; Jiao, H. High Coverage CO Activation Mechanisms on Fe(100) from Computations. *J. Phys. Chem. C* **2014**, *118*, 1095−1101.

3.7 Coverage Dependent Adsorption and Co-adsorption of CO and H_2 on the CdI_2-antitype Metallic $Mo_2C(001)$ Surface

Tao Wang, Xinxin Tian, Yong Yang, Yong-Wang Li, Jianguo Wang, Matthias Beller, Haijun Jiao*

Physical Chemistry Chemical Physics **2015**, *17*, 1907-1917.

Summary: The adsorption and co-adsorption of CO and H_2 at different coverage on the CdI_2-antitype metallic $Mo_2C(001)$ surface termination have been systematically computed at the level of periodic density functional theory. Only molecular CO adsorption is possible and the monolayer coverage (1 ML) can have 16CO adsorbed at the top sites. Dissociative H_2 adsorption is favored thermos-dynamically and the monolayer coverage (1 ML) can have 16H adsorbed at the hollow sites. Since CO has much stronger adsorption energy than H_2, pre-adsorption of CO is possible. CO pre-adsorption strongly affects atomic hydrogen co-adsorption at high CO/H_2 ratio, while hardly affect that at low CO/H_2 ratio. Under ultra-high vacuum condition (200K, 10^{-12} atm and CO/H_2 = 1/1), the most stable adsorbed surface state has CO/H_2 = 15/1. Comparison among the metallic terminations of the CdI_2-antitype $Mo_2C(001)$, eclipsed $Mo_2C(001)$ and orthorhombic $Mo_2C(100)$ surfaces shows their different CO and hydrogen adsorption as well as activation properties, which reveals that the CdI_2-antitype $Mo_2C(001)$ surface is least active. These differences come from their surface bonding properties; the CdI_2-antitype $Mo_2C(001)$ surface is saturated and less metallic, while the eclipsed $Mo_2C(001)$ and orthorhombic $Mo_2C(100)$ surfaces are unsaturated and more metallic.

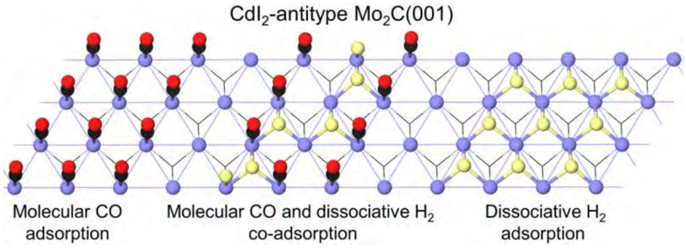
CdI₂-antitype Mo₂C(001)
Molecular CO adsorption
Molecular CO and dissociative H₂ co-adsorption
Dissociative H₂ adsorption

Contributions

In this paper, I planned, performed and analyzed most calculations for this manuscript. I have done the major part of writing of the manuscript. My contribution as co-author of this paper is approximately 80%.

PCCP

PAPER

Cite this: *Phys. Chem. Chem. Phys.*, 2015, **17**, 1907

Coverage dependent adsorption and co-adsorption of CO and H_2 on the CdI_2-antitype metallic $Mo_2C(001)$ surface†‡

Tao Wang,[a] Xinxin Tian,[bc] Yong Yang,[bc] Yong-Wang Li,[bc] Jianguo Wang,[b] Matthias Beller[a] and Haijun Jiao*[ab]

The adsorption and co-adsorption of CO and H_2 at different coverage on the CdI_2-antitype metallic $Mo_2C(001)$ surface termination have been systematically computed at the level of periodic density functional theory. Only molecular CO adsorption is possible and the monolayer coverage (1 ML) can have 16CO adsorbed at the top sites. Dissociative H_2 adsorption is favored thermodynamically and the monolayer coverage (1 ML) can have 16H adsorbed at the hollow sites. Since CO has much stronger adsorption energy than H_2, pre-adsorption of CO is possible. CO pre-adsorption strongly affects atomic hydrogen co-adsorption at a high CO/H_2 ratio, while hardly affects that at a low CO/H_2 ratio. Under ultra-high vacuum conditions (200 K, 10^{-12} atm and CO/H_2 = 1/1), the most stable adsorbed surface state has CO/H_2 = 15/1. Comparison among the metallic terminations of the CdI_2-antitype $Mo_2C(001)$, eclipsed $Mo_2C(001)$ and orthorhombic $Mo_2C(100)$ surfaces shows their different CO and hydrogen adsorption as well as activation properties, which reveals that the CdI_2-antitype $Mo_2C(001)$ surface is least active. These differences come from their surface bonding properties; the CdI_2-antitype $Mo_2C(001)$ surface is saturated and less metallic, while the eclipsed $Mo_2C(001)$ and orthorhombic $Mo_2C(100)$ surfaces are unsaturated and more metallic.

Received 25th September 2014,
Accepted 26th November 2014

DOI: 10.1039/c4cp04331f

www.rsc.org/pccp

1. Introduction

Transition metal carbides have attracted great interest in industrial and academic research because of their outstanding physical and chemical properties in materials sciences[1–3] and heterogeneous catalysis as noble metal substituents.[4–8] Especially the catalytic activities of molybdenum carbide (Mo_2C) in water–gas shift (WGS, $CO + H_2O = CO_2 + H_2$) reaction,[9,10] alcohol synthesis from CO hydrogenation,[11,12] hydrodesulfurization[13] and hydrodenitrogenation[14] in petroleum refining, hydro-treating,[15–17] and hydrogen production[18] as well as CH_4 aromatization[19,20] have been widely investigated.

The crystal structure of Mo_2C was first determined experimentally in 1926 by Westgren and Phragmen.[21] The lattice constants of Mo_2C were reported to be a = 3.002 Å and c = 4.724 Å by Kuo and Hägg in 1952,[22] and a = 3.00292 Å and c = 4.72895 Å by Fries and Kempter in 1960.[23] In this structure, the Mo atoms arrange in hexagonal close packing while the C atoms arrange statistically in the octahedral holes (the number of holes is twice the number of C atoms). This structure is the well-known hexagonal phase. However, this hexagonal phase can be further divided into two types on the basis of the arrangement of the carbon atoms.[24] One is the C6 type with the space group of $P\bar{3}m1$, where the carbon atoms only arrange in one layer, and the structure is similar to CdI_2 and also called the CdI_2-antitype. The second one is the L′3 type with the space group of $P6_3/mmc$, where the C atoms arrange randomly at all possible sites but in both layers systematically. Since the C atoms in the hexagonal L′3-type Mo_2C occupy half of the octahedral holes randomly, Haines *et al.*[25] considered different C atom arrangements on the basis of the experiment as well as *ab initio* calculations. They found that the eclipsed configuration is most stable and denotes

---

[a] *Leibniz-Institut für Katalyse e.V. an der Universität Rostock, Albert-Einstein Strasse 29a, 18059 Rostock, Germany*
[b] *State Key Laboratory of Coal Conversion, Institute of Coal Chemistry, Chinese Academy of Sciences, Taiyuan, 030001, PR China. E-mail: haijun.jiao@catalysis.de*
[c] *National Energy Center for Coal to Liquids, Synfuels China Co., Ltd, Huairou District, Beijing, 101400, China*

† In memory of Prof. Dr Paul von Ragué Schleyer (February 27, 1930–November 21, 2014): Paul was a great and aesthetic scientist; a pioneer and leader of computational chemistry as well as an excellent mentor and wonderful friend.

‡ Electronic supplementary information (ESI) available: PBE-D2 correction of CO and H_2 adsorption energies (Table S1); one CO adsorption on the CdI_2-antitype $Mo_2C(001)$ surface (Table S2 and Fig. S1); vibration frequencies of molecularly adsorbed CO on the CdI_2-antitype $Mo_2C(001)$ surface (Table S3); dissociative adsorption structures of H on the *n*CO precovered CdI_2-antitype $Mo_2C(001)$ surface (Fig. S2–S17); schematic structures of three Mo_2C surfaces (Fig. S18) and density of states of all three surfaces (Fig. S19). See DOI: 10.1039/c4cp04331f

the most likely candidate for the disordered hexagonal structure. Shi *et al.*[26] computed the energies of different structures of the hexagonal L′3-type Mo_2C and found that the eclipsed configuration is thermodynamically most stable. Apart from the hexagonal structure, an orthorhombic structure with the space group of *Pbcn* was also found, and the lattice constants were reported to be $a = 4.724$ Å, $b = 6.004$ Å and $c = 5.199$ Å by Parthe *et al.* in 1963[24] and $a = 4.732$ Å, $b = 6.037$ Å and $c = 5.204$ Å by Christensen in 1977.[27] In this structure, the Mo atoms are in hexagonal close packing, but deformed to an orthorhombic symmetry, and the C atoms orderly occupy half of the octahedral holes.

On the basis of these Mo_2C structures, Dubois *et al.*[28] and Epicier *et al.*[29] systematically studied their transformation at high temperatures. It revealed that the orthorhombic Mo_2C is most stable below 1350 °C and changes to the hexagonal CdI_2-antitype structure at 1350–1960 °C, while the hexagonal L′3-type structure is most stable at temperatures higher than 1960 °C. Generally, all three Mo_2C structures were widely accepted and analyzed. Here, we put these structures in three phases (Fig. 1); the CdI_2-antitype Mo_2C (hexagonal C6 type with the space group of *P*3*m*1), the hexagonal eclipsed Mo_2C (hexagonal L′3-type with the space group of *P*6$_3$*mmc*) and the orthorhombic Mo_2C (space group *Pbcn*).

Due to their high importance in heterogeneous catalysis, there are many theoretical studies about the terminations, adsorption properties and reactions on the surfaces of the orthorhombic,[30–44] hexagonal eclipsed[26,45–47] and hexagonal CdI_2-antitype[48–51] structures. For understanding the catalytic properties of these individual structures we studied the fundamental aspects of these catalysts. For example, we computed the properties of twenty-two terminations of low index orthorhombic Mo_2C surfaces[52] and found that structures and compositions as well as catalytic activities of surfaces have intrinsic relationships with carburization conditions. In addition, we investigated the coverage dependent CO adsorption, desorption and dissociation on the Mo- and C terminations of the orthorhombic $Mo_2C(100)$ surface and showed coverage dependent CO activation mechanisms.[53] On the basis of the computed Gibbs free energies, we studied the relationship among temperature, equilibrium coverage and partial pressure of CO and H_2 on the hexagonal eclipsed Mo_2C surfaces,[54,55] and found good agreement between the predicated and the experimentally detected spectra of temperature programmed CO and H_2 desorption at low temperature. Our atomistic thermodynamic study under the consideration of temperature and gas conditions showed that the (101) surface of the hexagonal eclipsed Mo_2C phase is most stable,[56] in agreement with the results from X-ray diffraction[57] and high resolution transmission electron microscopy.[58] The (101) surface of the hexagonal eclipsed Mo_2C is found to be promising for CO-free hydrogen production from formic acid decomposition.[59]

Our recent studies[53–55] mainly focused on the high coverage adsorption properties of CO and H_2 on the hexagonal eclipsed Mo_2C and orthorhombic Mo_2C surfaces. There were no reports about the interaction of CO and H_2 on the CdI_2-antitype Mo_2C surfaces by using DFT calculations. Apart from the individual adsorption of CO and H_2, their co-adsorption should also be important and promising. Therefore we systematically computed the adsorption of CO and H_2 as well as their co-adsorption on the CdI_2-antitype $Mo_2C(001)$ surface at different coverage. Our goal is to reveal the initial coverage and adsorption states of surface species (CO and H_2) as well as to demonstrate the effects of temperature, pressure and the CO/H_2 ratio on the adsorption properties of CO and H_2 by using atomistic thermodynamics.

2. Computational model and method

(a) Method

All calculations were performed by using the plane-wave based periodic DFT method implemented in the Vienna *ab initio* simulation package (VASP).[60,61] The electron ion interaction is described with the projector augmented wave method (PAW).[62,63] The electron exchange and correlation energy are treated within the generalized gradient approximation in the Perdew–Burke–Ernzerhof formalism (GGA-PBE).[64] To have accurate energies with errors less than 1 meV per atom, a cutoff energy of 400 eV and the Gaussian electron smearing method with $\sigma = 0.05$ eV were used. For the bulk optimization, the lattice parameters of the Mo_2C cells were determined by minimizing the total energy of the unit cell on the basis of a conjugated-gradient algorithm to relax the ions, and a 5 × 5 × 5 Monkhorst–Pack *k*-point grid was used for sampling the Brillouin zone. For the optimizations of the slab models, the 3 × 3 × 1 *k*-point grid was applied. The convergence criterion for the force is 0.02 eV Å^{-1} while that for the energy is 10^{-4} eV.

Adsorption energy (E_{ads}) is calculated by subtracting the total energies of gas phase species (X) and the clean surface from the

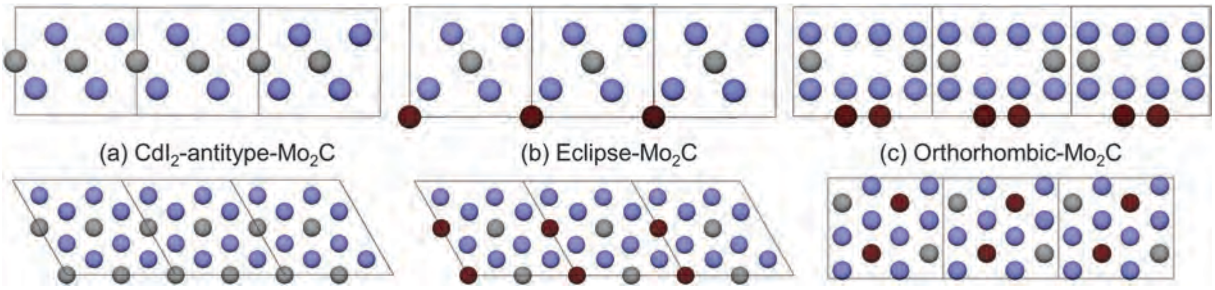

Fig. 1 Schematic side and top views of three Mo_2C cells (blue balls for Mo atoms, gray balls for the first layer C atoms and black balls for the second layer C atoms).

energy of the adsorbed system; $E_{ads} = E(X/slab) - [E(X) + E(slab)]$, and a more negative E_{ads} indicates a more stronger adsorption. For considering the coverage effect, stepwise adsorption energy ($\Delta E_x = E_{(X)n+1/slab} - [E_{(X)n/slab} + E_X]$) is applied to get the saturation coverage, where a positive ΔE_x for $n + 1$ adsorbed gas species indicates the saturation adsorption with n adsorbed gas species. It is worth noting that our stepwise adsorption energy defines the change of the adsorption energy by adding one more species to the surface; while the differential energy of adsorption defines the change of the average adsorption energy per coverage as the function of coverage.[65] In addition, we have also carried out a long-range dispersion correction for van der Waals interaction on the basis of the semi-empirical GGA-type functional (PBE-D2) proposed by Grimme.[66] As shown in the ESI‡ (Table S1), the PBE-D2 adsorption energies are larger than those from only PBE in the range of 0.25–0.54 eV for CO and 0.17–0.22 eV for H_2. It is reported that such empirical dispersion corrections overestimate the adsorption energies, not only for the weakly adsorbed systems[67–69] but also for the very strongly adsorbed systems.[70] Since the only PBE computed desorption energies and temperature of H_2,[71] CO,[72,73] and H_2O[70] on the iron surfaces as well as the orthorhombic $Mo_2C(100)$[53] and hexagonal eclipsed $Mo_2C(001)$[54] surfaces agree very well with the experimentally determined results, we are clearly confident that PBE can describe CO and H_2 co-adsorption on CdI_2-antitype Mo_2C reasonably.

To evaluate the energy barrier, the transition state (TS) was located using the nudged elastic band (NEB) method.[74] The TS structure was verified by vibration analysis; *i.e.*, only one imaginary frequency is found. The barrier (E_a) and reaction energy (ΔE_r) are calculated according to $E_a = E_{TS} - E_{IS}$ and $\Delta E_r = E_{FS} - E_{IS}$, where E_{IS}, E_{FS} and E_{TS} are the energies of the corresponding initial state (IS), final state (FS) and transition state (TS), respectively.

(b) Model

The calculated lattice parameters of the hexagonal CdI_2-antitype Mo_2C unit cell are $a = b = 6.118$ Å and $c = 4.682$ Å, which are very close to the experimental values.[23] For the adsorption and dissociation of CO and H_2, the Mo termination of the hexagonal CdI_2-antitype $Mo_2C(001)$ surface was chosen, and this surface was prepared and characterized experimentally and proved to be stable and representative.[75] Moreover, this surface is also widely applied in early DFT studies.[48–50] For the calculation of CO adsorption and dissociation, a $p(4 \times 4)$ periodic slab model (the area is 130 Å^2) with six atom layers (6L) was used, and this is thick enough for accurate calculation. A vacuum layer of 12 Å was set to exclude the slab interactions.

3. Results and discussion

The Mo termination of the CdI_2-antitype $Mo_2C(001)$ surface is flat and has pure Mo and C layers in different arrangements (Fig. 2a). The atom layers follow the Mo–C–Mo–Mo stacking pattern with a C free layer within a repeating period. Within the (4 × 4) surface size, there are sixteen surface Mo atoms, and each Mo atom interacts with three second layer C atoms. There are four possible adsorption sties, one top (t_1), one bridge (b_1) and two 3-folds hollow (h_1 and h_2) sites, where the h_1 site has a Mo atom in the third layer while the h_2 site has a carbon atom in the second layer.

3.1 CO adsorption and dissociation

At first we calculated the adsorption and dissociation of one CO molecule on the $Mo_2C(001)$ surface of the CdI_2-antitype phase. Four adsorption configurations were calculated. The top adsorption configuration (t_1) is the only energy minimum structure and most stable (Fig. 2b), while the other adsorption configurations are less stable and represent saddle points instead of energy minimums on the potential energy surfaces (Fig. S1 and Table S2, ESI‡).

On the basis of the top adsorption configuration (t_1), we also computed CO dissociation. In the transition state (Fig. 2c), the CO molecule goes from the top site to interact with the surface

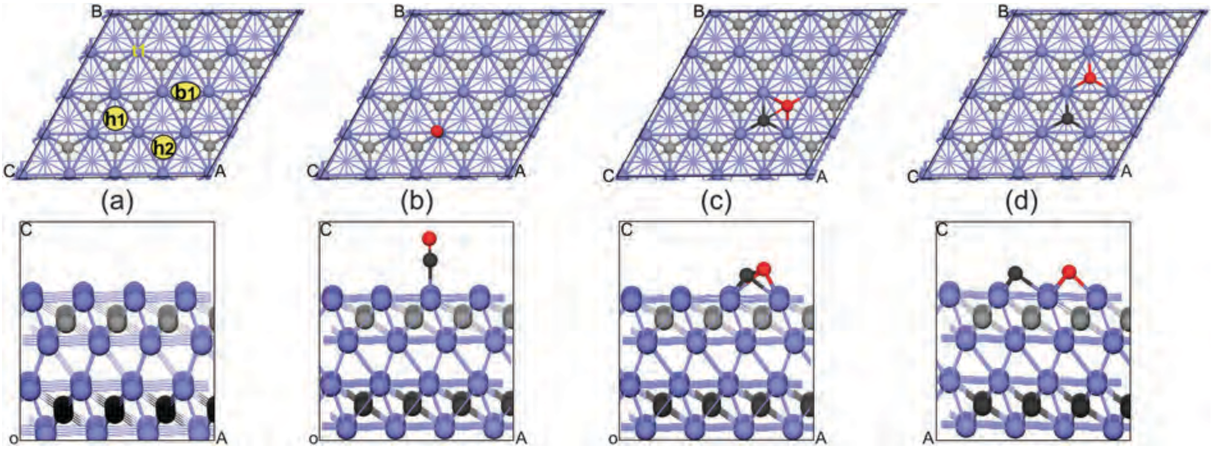

Fig. 2 Schematic structures of the Mo termination of the CdI_2-antitype $Mo_2C(001)$ surface and possible adsorption sites (a) as well as the structures of IS (b), TS (c) and FS (d) of CO dissociation on the top site (blue balls for Mo atoms, gray balls for first layer C atoms and black balls for C atoms in other layers, t for top, b for bridge and h for hollow).

Mo atoms and the breaking C–O distance is 1.74 Å. In the final state (Fig. 2d), both C and O are located at the 3-fold h_1 site. The computed CO dissociation barrier is 2.01 eV, which is very close to the CO adsorption energy (−2.08 eV); and the dissociation energy is only −0.08 eV. Such a high dissociation barrier indicates that it is very difficult to dissociate CO on the metallic termination of the CdI_2-antitype $Mo_2C(001)$ surface; and CO dissociation at high coverage is unlikely. Therefore, only molecular CO adsorption is possible at high coverage.

Apart from the lowest coverage of CO adsorption on the surface, we are also interested in high CO coverage adsorption because of the significant relevance to practical applications.[72,73,76–78] On the basis of the most stable adsorption configuration of one CO, we further increased the CO coverage on the CdI_2-antitype $Mo_2C(001)$ surface. The stepwise adsorption energy was used to estimate the saturation monolayer coverage. The energy and structure information of the most stable CO adsorption configurations at different coverage is shown in Fig. 3, while the C–O vibrational frequencies are given in the ESI‡ (Table S3). As expected, all stable adsorption configurations at different coverage are located on the top sites; and at the saturation monolayer coverage (n_{CO} = 16) each surface Mo atom can adsorb one CO molecule. The stepwise adsorption energy becomes positive for n_{CO} = 17, since no free top adsorption sites are available. As shown in Fig. 3, the adsorbed CO molecules can be divided into three groups on the basis of their close stepwise adsorption energies; the first six CO molecules (n_{CO} = 1–6); the second six CO molecules (n_{CO} = 7–12) and the last four CO molecules (n_{CO} = 13–16).

3.2 Hydrogen adsorption

Apart from CO, we also computed the adsorption properties of H_2 (Fig. 4). It is found that molecular H_2 adsorption is only located on the top site and the adsorption energy is −0.82 eV. The dissociation of H_2 has an energy barrier of only 0.08 eV and is highly exothermic by 0.79 eV. This shows that H_2 dissociative adsorption is exothermic by 1.61 eV and very favorable thermodynamically. Thus, we focus only on H_2 dissociative adsorption at different coverage.

As shown in Fig. 4, all adsorbed H atoms are located at the h_1 sites for n_H = 1–16 to form 1 ML adsorption. On the basis of their close stepwise adsorption energies, the adsorbed H atoms can be divided into three groups; the first four H atoms (n_H = 1–4); the second four H atoms (n_H = 5–8) and the last eight H atoms (n_H = 9–16). At n_H = 16, it forms monolayer H atoms on the surface. At n_H = 17 and 18, the adsorbed hydrogen atoms are located at the top sites and the stepwise adsorption energies are only −0.06 eV. At n_H = 17–32, the adsorbed H atoms go to the top sites, and the adsorption energy increases gradually (Fig. S2, ESI‡). At n_H = 32, all the surface sites were occupied by H atoms and further hydrogen adsorption on the

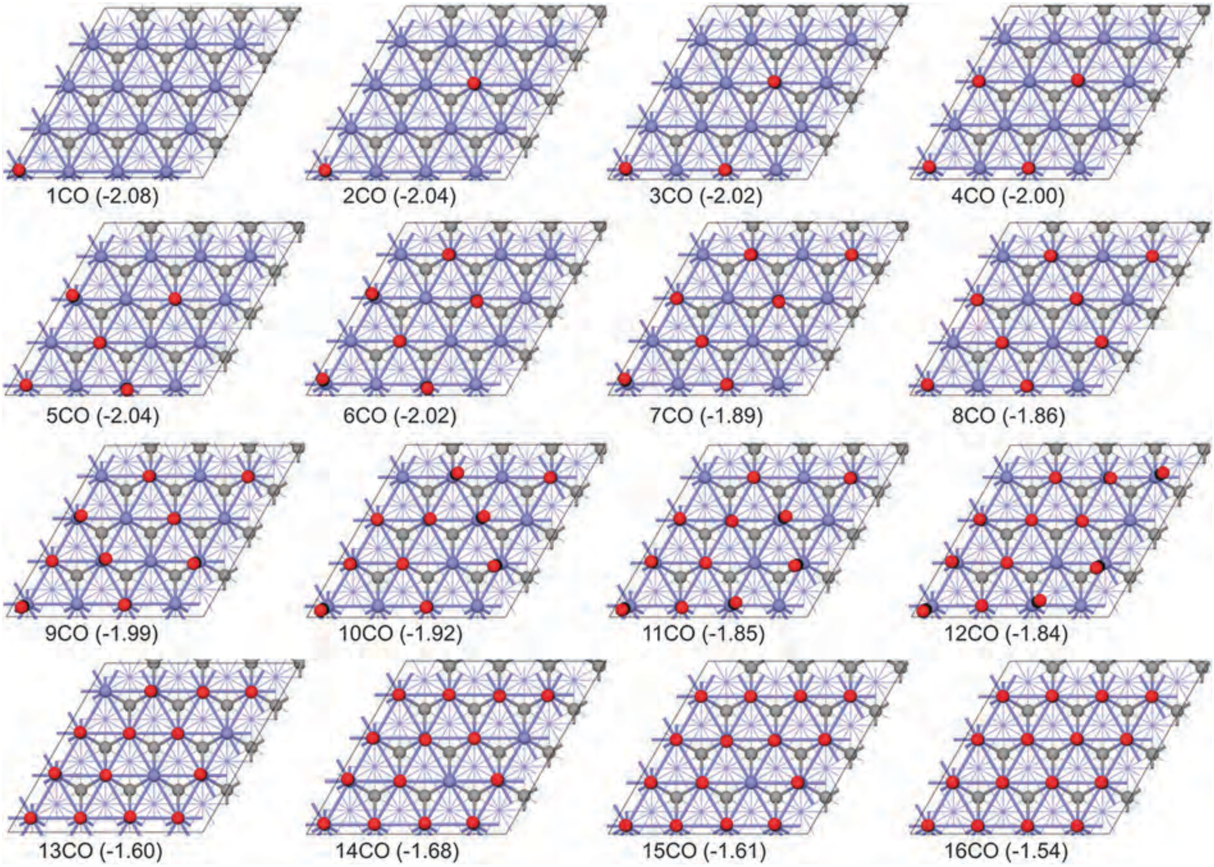

Fig. 3 Structures and energies (ΔE_{ads}/eV) of the most stable adsorption sites for stepwise CO adsorption on the Mo termination of the CdI_2-antitype $Mo_2C(001)$ surface (gray balls for the bulk C atoms, black ball for C atoms in CO, red ball for O and the blue balls for Mo atoms).

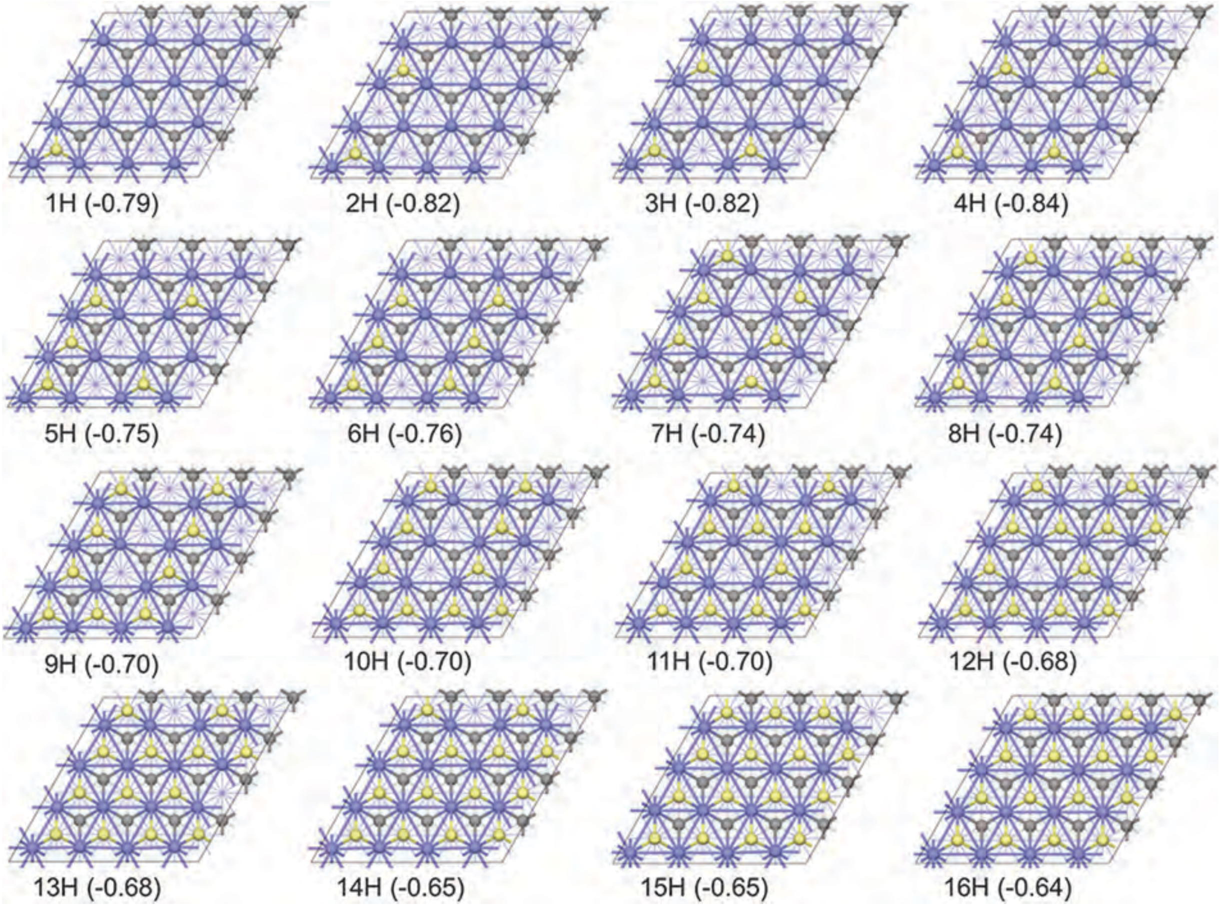

Fig. 4 Structures of stable dissociative *n*H adsorptions on the CdI_2-antitype $Mo_2C(001)$ surface (gray balls for the bulk C atoms, yellow balls for H atoms and blue balls for Mo atoms).

surface is impossible. Due to the large differences in stepwise adsorption energies, the adsorption of the first 16H at the hollow sites should be very easy at low pressure, while the second 16H at the top sites might only be possible at very high pressure.

It is interesting to compare the adsorption properties of CO and hydrogen and discuss their chemical consequences for reactions involving synthesis gas (CO/H_2) on catalysts, where CO and H_2 adsorption and activation are the initial and elementary steps. As shown in Fig. 3 and 4, the first molecular CO adsorption energy is −2.08 eV, which is much stronger than the first dissociative H_2 adsorption energy of −1.61 eV, which is, however, very close to those (from −1.68 to −1.54 eV) of the last four CO molecules (n_{CO} = 13–16). It is reasonable to expect that this Mo_2C surface will also be predominately covered by CO rather than H_2 under synthesis gas (CO/H_2) conditions, as observed experimentally in FTS catalysis,[76–78] and the ratio of surface adsorbed CO/H_2 must be different from that in the gas phase. On the other hand, it is also to be expected that at a low CO/H_2 ratio it is possible to have co-adsorption of CO and H_2 on the surface. All these raise very interesting questions about the stable adsorption state of CO and hydrogen on the surface and the reaction mechanisms of CO activation. Therefore we carried out CO and H_2 co-adsorption on this surface.

3.3 CO and hydrogen co-adsorption

Despite wide theoretical investigations[33–35,40,46,51–55] about the individual interactions of CO or H_2 with Mo_2C surfaces, there are no available studies about the co-adsorption of CO and H_2 as well as their mutual interaction. In this part, we calculated the dissociative H_2 adsorption on the CO pre-covered CdI_2-antitype $Mo_2C(001)$ surface to discuss their mutual interaction and finally determine the stable co-adsorption states of CO and H_2 on the surface. Table 1 and Fig. S2–S17 (ESI‡) collected the co-adsorption energy and structures of *n*CO pre-covered surface with dissociatively adsorbed mH_2 (*n*CO + 2*m*H), and the surface fully covered by CO and hydrogen can be found in Fig. 3 and 4, respectively. On the basis of the stronger CO adsorption than H_2 adsorption we used the most stable CO adsorption configurations (Fig. 3) as the pre-covered surfaces for searching the most stable CO and H_2 co-adsorption configurations at different coverage, *i.e.*; by fixing *n*CO and varying mH_2, and each co-adsorbed state has $n + m = 16$.

For n_{CO} = 16, all top adsorption sites are occupied, and it is not possible to adsorb any hydrogen atoms on the surface.

Table 1 Stepwise dissociative adsorption energies (eV) of mH_2 on the nCO pre-covered surface (nCO + 2mH)[a,b,c,d]

	16CO	15CO	14CO	13CO	12CO	11CO	10CO	9CO	8CO	7CO	6CO	5CO	4CO	3CO	2CO	1CO	No-CO
no-H_2	−1.54	−1.61	−1.68	−1.60	−1.84	−1.85	1.92	−1.99	−1.86	−1.89	−2.02	−2.04	−2.00	−2.02	−2.04	−2.08	
1H_2		−0.36	−0.36	−0.54	−0.61	−0.87	−1.01	−1.06	−1.17	−1.48	−1.55	−1.55	−1.55	−1.64	−1.64	−1.63	−1.61
2H_2			−0.50	−0.44	−0.47	−0.52	−0.74	−0.95	−1.01	−1.05	−1.32	−1.41	−1.49	−1.54	−1.56	−1.61	−1.66
3H_2				−0.44	−0.44	−0.39	−0.50	−0.67	−0.76	−0.93	−1.01	−1.30	−1.35	−1.33	−1.51	−1.53	−1.51
4H_2					−0.48	−0.31	−0.42	−0.42	−0.61	−0.65	−0.86	−0.98	−1.24	−1.27	−1.37	−1.49	−1.48
5H_2						−0.38	−0.37	−0.48	−0.34	−0.62	−0.58	−0.59	−0.82	−1.06	−1.27	−1.42	−1.40
6H_2							−0.48	−0.47	−0.45	−0.45	−0.46	−0.68	−0.73	−0.94	−1.02	−1.29	−1.38
7H_2								−0.41	−0.39	−0.35	−0.37	−0.34	−0.41	−0.83	−1.01	−1.05	−1.33
8H_2									−0.34	−0.23	−0.28	−0.38	−0.28	−0.28	−0.15	−0.61	−1.29
9H_2										−0.26	−0.36	−0.31	−0.45	−0.33	−0.19	−0.15	−0.12
10H_2											−0.19	−0.44	−0.30	−0.30	−0.30	−0.22	−0.22
11H_2												−0.07	−0.46	−0.30	−0.32	−0.26	−0.25
12H_2													−0.08	−0.22	−0.36	−0.32	−0.34
13H_2														−0.33	−0.31	−0.23	−0.19
14H_2															−0.39	−0.38	−0.25
15H_2																−0.46	−0.44
16H_2																	−0.46

[a] no-H_2 and no-CO mean that the surface is only covered by nCO molecules and n dissociative H_2 molecules, respectively. [b] The values in the no-H_2 line are the stepwise adsorption energies of CO molecules on the clean surface. [c] The values in the no-CO column are the stepwise adsorption energies of dissociative H_2 molecules. [d] nH_2 means n dissociative adsorbed H_2 molecules (also 2nH atoms).

On the 15CO pre-covered surface, there is one top site free for one H_2 adsorption and the adsorption energy is −0.36 eV, which is much lower than that of n_{CO} = 16 (−1.54 eV), indicating a rather weak H_2 dissociative adsorption. In 15CO + 2H, the two adsorbed H atoms are located at t_1 and h_1 sites. On the 14CO pre-covered surface, there are two top sites free for 2H_2 adsorption; and the adsorption energy is −0.36 and −0.50 eV, respectively. In 14CO + 2mH (m = 1–2), the adsorbed H atoms are located at t_1 and h_1 sites. On the 13CO pre-covered surface, there are three top sites free for 3H_2 adsorption; and the adsorption energy is −0.54, −0.44 and −0.44 eV. In 13CO + 2mH (m = 1–3), the adsorbed H atoms are located at t_1 and h_1 sites. On the 12CO pre-covered surface, there are four top sites free for 4H_2 adsorption; and the adsorption energy is −0.61, −0.47, −0.44 and −0.48 eV, respectively. In 12CO + 2mH (m = 1–4), the adsorbed H atoms are located at t_1 and h_1 sites. On the 11CO pre-covered surface, there are five top sites free for 5H_2 adsorption; and the adsorption energy is −0.87, −0.52, −0.39, −0.31, and −0.38 eV, respectively. In 11CO + 2mH (m = 1–5), the adsorbed H atoms are located at t_1 and h_1 sites. On the 10CO pre-covered surface, there are six top sites free for 6H_2 adsorption; and the adsorption energy is −1.01, −0.74, −0.50, −0.42, −0.37 and −0.48 eV, respectively. In 10CO + 2mH (m = 1–6), the adsorbed H atoms are located at t_1 and h_1 sites.

On the 9CO pre-covered surface, there are seven top sites free for 7H_2 adsorption; and the adsorption energy is −1.06, −0.95, −0.67, −0.42, −0.48, −0.47 and −0.41 eV, respectively. In 9CO + 2mH (m = 1–7), the adsorbed H atoms are located at t_1, b_1 and h_1 sites. On the 8CO pre-covered surface, there are eight top sites free for 8H_2 adsorption; and the adsorption energy of H_2 decreases with increasing coverage and that of the eighth H_2 is −0.34 eV. In 8CO + 2mH (m = 1–8), the adsorbed H atoms are located at t_1, h_1 and h_2 sites. On the 7CO pre-covered surface, there are nine top sites free for 9H_2 adsorption; and the adsorption energy of H_2 decreases with increasing coverage and that of the ninth H_2 is −0.26 eV. In 7CO + 2mH (m = 1–9), the adsorbed H atoms are located at t_1, h_1 and h_2 sites. On the 6CO pre-covered surface, there are ten top sites free for 10H_2 adsorption; and the adsorption energy of H_2 decreases with increasing coverage and that of the tenth H_2 is −0.19 eV. In 6CO + 2mH (m = 1–10), the adsorbed H atoms are located at t_1, h_1 and h_2 sites.

On the 5CO pre-covered surface, there are eleven top sites free for 11H_2 adsorption; and the H_2 adsorption energy decreases with increasing coverage and that of the eleventh H_2 is only −0.07 eV. In 5CO + 2mH (m = 1–11), the adsorbed H atoms are located at t_1 and h_1 sites. On the 4CO pre-covered surface, there are twelve top sites free for 12H_2 adsorption; and the H_2 adsorption energy decreases with increasing coverage and that of the twelfth H_2 is only −0.08 eV. In 4CO + 2mH (m = 1–12), the adsorbed H atoms are located at t_1 and h_1 sites. On the 3CO pre-covered surface, there are thirteen top sites free for 13H_2 adsorption; and the H_2 adsorption energy decreases with increasing coverage and that of the thirteenth H_2 is −0.33 eV. In 3CO + 2mH (m = 1–13), the adsorbed H atoms are located at t_1 and h_1 sites. On the 2CO pre-covered surface, there are fourteen top sites free for 14H_2 adsorption; and the H_2 adsorption energy decreases with increasing coverage and that of the fourteenth H_2 is −0.39 eV. In 2CO + 2mH (m = 1–14), the adsorbed H atoms are located at t_1 and h_1 sites. On the 1CO pre-covered surface, there are fifteen top sites free for 15H_2 adsorption; and the H_2 adsorption energy decreases with increasing coverage and that of the fifteenth H_2 is −0.46 eV. In 1CO + 2mH (m = 1–15), the adsorbed H atoms are located at t_1 and h_1 sites.

The above results reflect the energetic properties of CO and H_2 co-adsorption on the CdI_2-antitype $Mo_2C(001)$ surface. The predominant adsorption of CO on the CdI_2-antitype $Mo_2C(001)$ surface is very likely at a high CO/H_2 ratio; and the pre-adsorbed CO molecules affect obviously the adsorption energies and stable coverage of hydrogen atoms. For example, the dissociative adsorption energy of one H_2 molecule as well as the stepwise adsorption energies of H atoms at different coverage decrease with increasing coverage of pre-adsorbed CO molecules. Moreover, the numbers of H atoms at saturation coverage and the total coverage of surface species (nCO + 2mH) also decrease with the increase in pre-adsorbed CO molecules.

3.4 CO and hydrogen co-adsorption under given conditions

To determine the stable co-adsorption structures of CO and H_2 on the surface under experimental conditions, we applied atomistic thermodynamics under the consideration of temperature, pressure as well as the CO/H_2 ratio. In this method, the Gibbs free energy (ΔG) of nCO + $m$$H_2$ adsorption on the surface was chosen as the criterion, where a more negative ΔG indicates the more stable co-adsorption structure.

$$\begin{aligned}\Delta G^{\text{ads}}_{\text{Mo}_2\text{C}}(T,p,n\text{CO},m\text{H}_2) &= G[\text{Mo}_2\text{C}(001)/\{n\text{CO}+m\text{H}_2\}] \\ &\quad - G[\text{Mo}_2\text{C}(001)] \\ &\quad - nG_{\text{CO}}(T,p_{\text{CO}}) - mG_{\text{H}_2}(T,p_{\text{H}_2})\end{aligned} \tag{1}$$

where $G[\text{Mo}_2\text{C}(001)/n\text{CO} + m\text{H}_2]$, $G[\text{Mo}_2\text{C}(001)]$, $G_{\text{CO}}(T, p_{\text{CO}})$ and $G_{\text{H}_2}(T, p_{\text{H}_2})$ are the Gibbs free energies of corresponding systems, n and m are the numbers of adsorbed CO molecules and dissociative H_2 molecules, T is the temperature, p_{CO} and p_{H_2} are the partial pressures of CO and H_2 in the gas atmosphere. The values of $G_{\text{CO}}(T, p_{\text{CO}})$ and $G_{\text{H}_2}(T, p_{\text{H}_2})$ can be expressed as:

$$G_{\text{CO}}(T,p_{\text{CO}}) = E^{\text{total}}_{\text{CO}} + \tilde{\mu}_{\text{CO}}(T,p^{\theta}) + k_{\text{B}}T\ln\frac{p_{\text{CO}}}{p^{\theta}} \tag{2}$$

$$G_{\text{H}_2}(T,p_{\text{H}_2}) = E^{\text{total}}_{\text{H}_2} + \tilde{\mu}_{\text{H}_2}(T,p^{\theta}) + k_{\text{B}}T\ln\frac{p_{\text{H}_2}}{p^{\theta}} \tag{3}$$

where E^{total} is the total energies of CO and H_2 molecules including zero point vibration energies, $\tilde{\mu}_{\text{CO}}(T,p^{\theta})$ and $\tilde{\mu}_{\text{H}_2}(T,p^{\theta})$ are the standard chemical potentials of CO and H_2 at T and p^{θ} (1 atm), k_{B} is the Boltzmann constant. Compared to the large contribution of vibration to the gases, this contribution to the solid surfaces is negligible because of their large mass differences. Therefore, we apply the DFT calculated total energy to substitute the Gibbs free energies of solid surfaces. Indeed, the contribution of Gibbs free energy correction to the H_2 related process was found to be about 3 kcal mol^{-1} (2%) at 300 K in our previous work.[79] Such approximations were also widely applied in both early[80–82] and most recent[83] work related to atomistic thermodynamics methods. Then, eqn (1) can be rewritten to be:

$$\begin{aligned}\Delta G^{\text{ads}}_{\text{Mo}_2\text{C}}(T,p,n\text{CO},m\text{H}_2) &= E[\text{Mo}_2\text{C}(001)/\{n\text{CO}+m\text{H}_2\}] \\ &\quad - E[\text{Mo}_2\text{C}(001)] - nG_{\text{CO}}(T,p_{\text{CO}}) \\ &\quad - mG_{\text{H}_2}(T,p_{\text{H}_2})\end{aligned} \tag{4}$$

Inserting eqn (2) and 3 into eqn (4) came to

$$\begin{aligned}\Delta G^{\text{ads}}_{\text{Mo}_2\text{C}}(T,p,n\text{CO},m\text{H}_2) &= E[\text{Mo}_2\text{C}(001)/\{n\text{CO}+m\text{H}_2\}] \\ &\quad - E[\text{Mo}_2\text{C}(001)] - nE^{\text{total}}_{\text{CO}} \\ &\quad - mE^{\text{total}}_{\text{H}_2} - n\tilde{\mu}_{\text{CO}}(T,p^{\theta}) \\ &\quad - m\tilde{\mu}_{\text{H}_2}(T,p^{\theta}) - nk_{\text{B}}T\ln\frac{p_{\text{CO}}}{p^{\theta}} \\ &\quad - mk_{\text{B}}T\ln\frac{p_{\text{H}_2}}{p^{\theta}}\end{aligned} \tag{5}$$

On the basis of the individual CO and H_2 adsorption, we applied atomistic thermodynamics to study the effects of temperature and pressure on their stable coverage. The phase diagrams of CO and H_2 on the CdI_2-antitype $\text{Mo}_2\text{C}(001)$ surface at wide pressure and temperature ranges are shown in Fig. 5. Since desorption and reaction of CO and H_2 are inevitable at high temperatures and pressure, we compute their stable co-adsorption structures and composition on the CdI_2-antitype $\text{Mo}_2\text{C}(001)$ surface under only ultra-high vacuum conditions (200 K and 10^{-12} atm). Under UHV conditions full desorption of the adsorbed CO molecules takes places in the temperature range of 475–600 K (Fig. 5a); and full desorption of the adsorbed hydrogen atoms occurs at about 450–550 K (Fig. 5b).

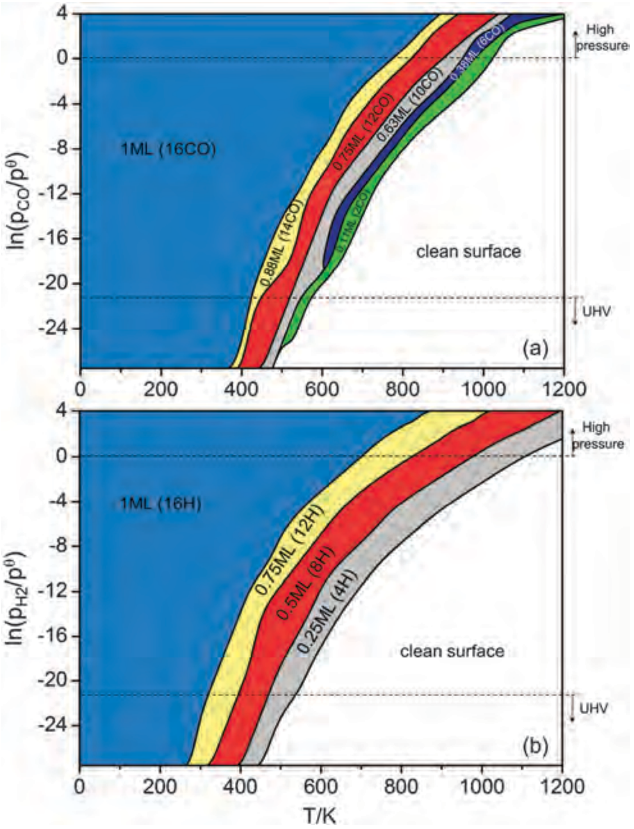

Fig. 5 Phase diagrams of stable CO (a) and H_2 (b) coverage under different conditions on the CdI_2-antitype $\text{Mo}_2\text{C}(001)$ surface.

Table 2 Adsorption Gibbs free energies (ΔG) of nCO + mH$_2$ adsorption on the surface at 200 K and $p = 10^{-12}$ atm as well as $p_{CO}/p_{H_2} = 1/1$ (mH$_2$ for dissociative H$_2$ adsorption)

ΔG	No CO	1CO	2CO	3CO	4CO	5CO	6CO	7CO	8CO	9CO	10CO	11CO	12CO	13CO	14CO	15CO	16CO
No H$_2$		−1.28	−2.52	−3.74	−4.94	−6.18	−7.40	−8.49	−9.55	−10.73	−11.85	−12.89	−13.94	−14.73	−15.61	−16.41	**−17.15**
1H$_2$	−0.95	−2.39	−3.82	−5.21	−6.50	−7.78	−9.07	−10.21	−11.10	−12.14	−13.15	**−14.09**	**−14.87**	**−15.73**	**−16.39**	**−17.18**	
2H$_2$	−1.94	−3.34	−4.71	−6.09	−7.32	−8.53	−9.73	−10.60	−11.45	−12.42	**−13.23**	−13.96	−14.67	−15.51	−16.23		
3H$_2$	−2.78	−4.21	−5.56	−6.75	−8.00	−9.17	−10.08	**−10.87**	**−11.55**	**−12.43**	−13.07	−13.69	−14.45	−15.29	−15.70		
4H$_2$	−3.60	−5.03	−6.27	−7.36	−8.58	**−9.48**	**−10.28**	−10.85	−11.50	−12.18	−12.84	−13.34	−14.27	−14.75			
5H$_2$	−4.34	−5.79	−6.88	−7.76	−8.74	−9.41	−10.20	−10.81	−11.17	−12.00	−12.55	−13.06	−13.74	−14.14			
6H$_2$	−5.06	−6.42	−7.24	−8.04	**−8.81**	−9.43	−9.99	−10.60	−10.96	−11.81	−12.37	−12.80	−13.21				
7H$_2$	−5.72	**−6.80**	**−7.59**	**−8.21**	−8.56	−9.11	−9.70	−10.29	−10.69	−11.56	−11.79	−12.29					
8H$_2$	**−6.35**	−6.74	−7.07	−7.83	−8.18	−8.83	−9.31	−9.86	−10.36	−11.13	−11.27						

As listed in Table 2 (200 K, $p = 10^{-12}$ atm and $p_{CO}/p_{H_2} = 1/1$), the value of ΔG changes with the numbers of surface species. For only H$_2$ adsorption, the most stable adsorption structure has sixteen hydrogen atoms at the hollow sites since it has the most negative ΔG (−6.35 eV). For only CO adsorption, the most stable adsorption structure has sixteen molecularly adsorbed CO at the top sites. In both cases, they form monolayer saturation coverage (1 ML) with 16H at the hollow sites and 16CO at the top sites (Fig. 3 and 4).

For nCO + mH$_2$ co-adsorption, the stable surface composition presents interesting changes. For $n_{CO} = 1$–3, the value of ΔG increases for $m = 1$–7 and then decreases for $m = 8$. The most stable co-adsorption states have seven dissociated H$_2$ and the surface composition is 1CO + 14H, 2CO + 14H and 3CO + 14H, respectively.

For $n_{CO} = 4$, the value of ΔG increases for $m = 1$–6, and then decreases for $m = 7$–8. The most stable co-adsorption states have six dissociated H$_2$ and the surface composition is 4CO + 12H.

For $n_{CO} = 5$–6, the value of ΔG increases for $m = 1$–4 and then decreases for $m = 5$–8. The most stable co-adsorption states have four dissociated H$_2$ and the surface composition is 5CO + 8H and 6CO + 8H, respectively.

For $n_{CO} = 7$–9, the value of ΔG increases for $m = 1$–3 and then decreases for $m = 4$–8. The most stable co-adsorption states have three dissociated H$_2$ and the surface composition is 7CO + 6H, 8CO + 6H and 9CO + 6H, respectively. For $n_{CO} = 10$, the most stable co-adsorption states have two dissociated H$_2$ and the surface composition is 10CO + 4H.

For $n_{CO} = 11$–15, the most stable co-adsorption state has only one dissociated H$_2$; and the surface composition is 11CO + 2H, 12CO + 2H, 13CO + 2H, 14CO + 2H and 15CO + 2H, respectively. Under these conditions, the thermodynamically most stable co-adsorption state is 15CO + 2H, which has the most negative Gibbs free energy (−17.18 eV).

3.5 Comparison of CO and H$_2$ adsorption on three Mo$_2$C phases

For CO adsorption and activation, there are many investigations on the basis of DFT calculations,[34,40,43,45,46,51] however, no coverage dependent CO activation was considered. Moreover, a systematic comparison is difficult since these results came from diverse methodologies. Our previous studies about CO activation on the orthorhombic Mo$_2$C(100) surface[53] and the eclipsed Mo$_2$C(001) surface[54] as well as CdI$_2$-antitype Mo$_2$C(001) surface in the present work at different coverage enable a systematic comparison about the similarities and differences in CO and H$_2$ adsorption and activation on these three Mo$_2$C phases.

These three Mo$_2$C surfaces have similarities and differences in structures and active sites of surface terminations (Fig. S18, ESI‡). At first, all three surface terminations are flat and metallic. The CdI$_2$-antitype Mo$_2$C(001) surface (Fig. S18a, ESI‡) has the Mo–C–Mo–Mo stacking pattern where there is an empty layer of C atoms in every fourth layer. The hexagonal eclipsed Mo$_2$C(001) surface (Fig. S18b, ESI‡) and orthorhombic Mo$_2$C(100) surface (Fig. S18c, ESI‡) have an alternative Mo–C–Mo–C stacking pattern. All three surface terminations have sixteen surface Mo atoms differing in coordination numbers (the saturated bulk Mo coordinates with three C atoms while that of the C atom coordinates with six Mo atoms). The Mo atoms on the CdI$_2$-antitype Mo$_2$C(001) surface are coordinated with three carbon atoms and therefore saturated. This is probably the reason why this metallic termination has weak CO adsorption energy and a high CO dissociation barrier. On the metallic terminations of the hexagonal eclipsed Mo$_2$C(001) and orthorhombic Mo$_2$C(100) surfaces, there are two types of surface Mo atoms, the first type Mo atoms have 2-fold bulk carbon coordination and one free coordination site; and the second type surface Mo atoms have 1-fold bulk carbon coordination and two free coordination sites. These different surface atom bonding properties result in different adsorption sites (Fig. S18, ESI‡). The computed density of states (DOS) show very high similarity between the coordinatively unsaturated eclipsed Mo$_2$C(001) and orthorhombic Mo$_2$C(100) surfaces, while differences to the coordinatively saturated CdI$_2$-antitype Mo$_2$C(001) surface (Fig. S19, ESI‡). The eclipsed Mo$_2$C(001) and orthorhombic Mo$_2$C(100) surfaces are more metallic, and the CdI$_2$-antitype Mo$_2$C(001) surface is less metallic.

The site preference of CO adsorption is different at low coverage; *i.e.*; the top site on the CdI$_2$-antitype Mo$_2$C(001) surface, while the 3-fold hollow sites on the orthorhombic Mo$_2$C(100) and on the eclipsed Mo$_2$C(001) surfaces. The CdI$_2$-antitype Mo$_2$C(001) surface has the lowest adsorption energy and highest dissociation barrier, while the other two Mo$_2$C surfaces have stronger CO adsorption energies and lower dissociation barriers. Up to monolayer CO coverage, only top site adsorption configuration is found on the CdI$_2$-antitype Mo$_2$C(001) surface, while the stable adsorption configuration changes from the 3-fold hollow site at low coverage to the bridge site and finally

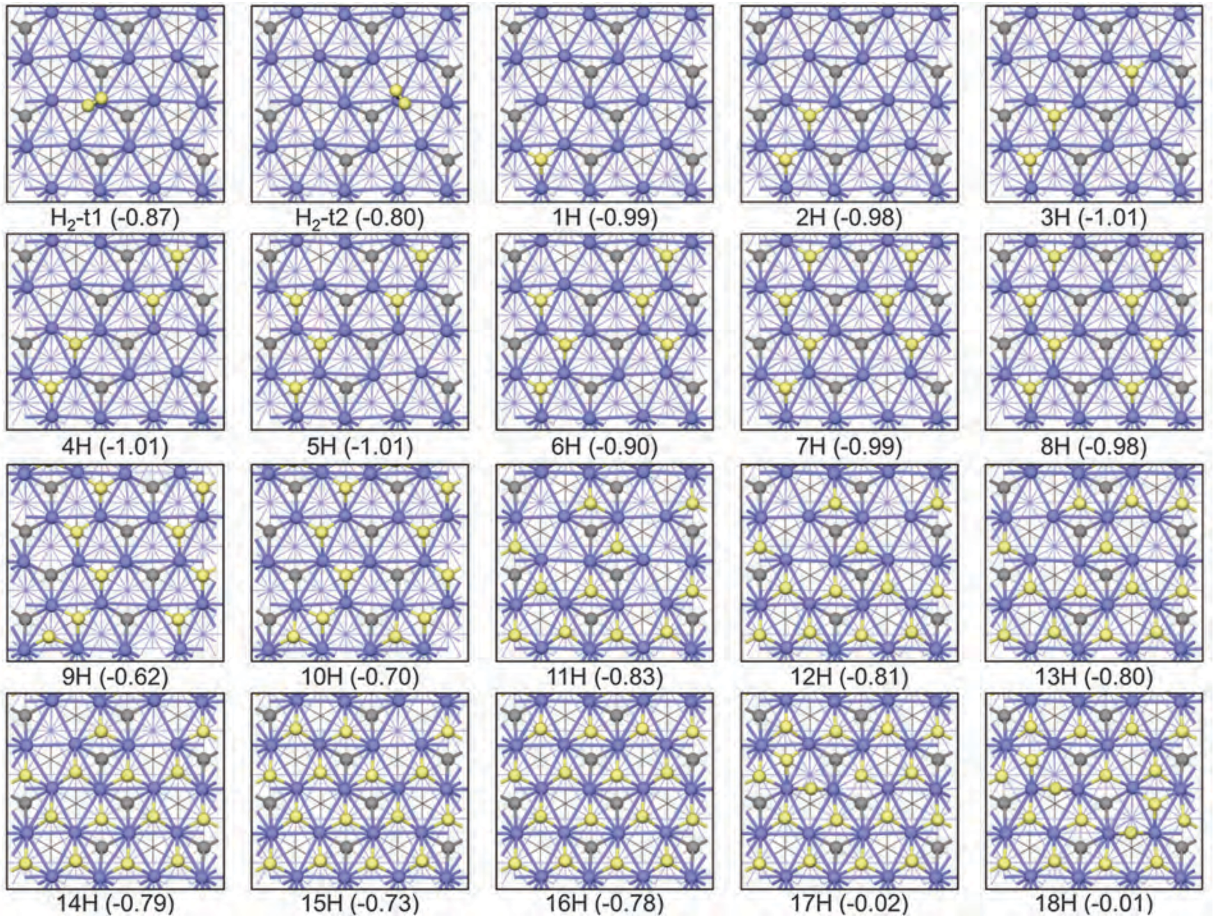

Fig. 6 Structures of stable molecular H_2 and dissociative *n*H adsorptions on the orthorhombic $Mo_2C(100)$ surface (gray balls for the bulk C atoms, yellow balls for H atoms and blue balls for Mo atoms).

to the top site at saturated coverage on the surfaces of other two Mo_2C phases.

These differences not only indicate their quite different CO activation mechanisms but also can be used to identity and differentiate these Mo_2C phases. Experimentally, the hexagonal and orthorhombic Mo_2C phases were prepared with different methods; *i.e.*, direct carburization of MoO_3 by $CH_4–H_2$ mixtures into the hexagonal Mo_2C,[84] while firstly reducing MoO_3 by NH_3 to form Mo_2N and then carburizing Mo_2N with $CH_4–H_2$ mixtures into the orthorhombic Mo_2C.[85] Both phases can be easily identified and differentiated.

However, it is difficult to differentiate the CdI_2-antitype Mo_2C phase from the eclipsed Mo_2C phase, since they are prepared from the same method. In this respect, the differences in CO adsorption properties can be applied to differentiate them. For example, the CdI_2-antitype Mo_2C phase should present only stretching frequencies for top molecularly adsorbed CO, while the eclipsed Mo_2C phase can have different CO stretching signals from the adsorbed CO molecules on the basis of the coverage dependent adsorption sites and configurations.

In addition to their differences in CO adsorption and activation, we also compare their hydrogen adsorption properties. On the eclipsed $Mo_2C(001)$ surface,[55] our recent study revealed that only dissociative hydrogen adsorption is possible and the saturation coverage has twenty H atoms (1.25 ML) as well as two adsorption configurations (hollow and bridge) coexist on the surface. For a full comparison, we also calculated the molecular adsorption of hydrogen at low coverage and dissociative adsorption at high coverage on the orthorhombic $Mo_2C(100)$ surface by using the same model and method as in our previous work.[53] As given in Fig. 6, two stable molecular adsorption configurations were located on the t_1 (−0.87 eV) and t_2 (−0.80 eV) sites. The dissociation of molecular H_2 from the most stable t_1 site is barrier-less (less than 0.01 eV) and exothermic by 1.10 eV. This indicates that hydrogen dissociative adsorption on this surface is also thermodynamically very favorable. For the stepwise adsorption of H atoms (Fig. 6), the saturation coverage is reached at $n_H = 16$ (1.00 ML) and there are also two adsorption configurations (hollow and bridge) coexisting on the surface. It clearly revealed that the CdI_2-antitype $Mo_2C(001)$ surface has a relatively weak adsorption at low hydrogen coverage.

4. Conclusion

Systematic density functional theory calculations and atomistic thermodynamic analysis were performed to investigate the adsorption and activation of CO and H_2 as well as their co-adsorption on the CdI_2-antitype metallic $Mo_2C(001)$ surface. The coverage effects were included throughout our studies. It is found that CO dissociation on this surface is very difficult and only molecular CO adsorption at the top sites is possible for n_{CO} = 1–16. For the dissociative hydrogen adsorption, the monolayer saturation coverage (1 ML) can have 16 hydrogen atoms.

Since the adsorption of CO is much stronger than that of hydrogen; and CO adsorption is predominant at a high CO/H_2 ratio, while the co-adsorption of CO and atomic hydrogen becomes possible at a low CO/H_2 ratio. CO pre-adsorption affects the co-adsorption of atomic hydrogen strongly. On the basis of atomistic thermodynamics, the stable co-adsorption state has 15CO + 2H under ultra-high vacuum conditions (200 K, 10^{-12} atm and $CO/H_2 = 1/1$), indicating CO pre-adsorption.

Since the orthorhombic $Mo_2C(100)$, eclipsed $Mo_2C(001)$ and CdI_2-antitype $Mo_2C(001)$ surfaces are widely applied for the investigation into the properties of Mo_2C, comparison of their similarities and differences in CO and H_2 activation is necessary and important. Our results revealed that the CdI_2-antitype $Mo_2C(001)$ surface has much weaker ability in CO adsorption and activation than the orthorhombic $Mo_2C(100)$ and eclipsed $Mo_2C(001)$ surfaces on the basis of CO adsorption energy and a dissociation barrier at low coverage. The CdI_2-antitype $Mo_2C(001)$ surface can only have CO adsorption configuration at the top site, while the orthorhombic $Mo_2C(100)$ and eclipsed $Mo_2C(001)$ surfaces can have coverage dependent CO adsorption configurations at the top, bridge and 3-fold hollow sites. Although all three surface terminations favor dissociative H_2 adsorption, the orthorhombic $Mo_2C(100)$ and eclipsed $Mo_2C(001)$ surfaces can adsorb hydrogen atoms more strongly than the CdI_2-antitype $Mo_2C(001)$ surface.

That the CdI_2-antitype $Mo_2C(001)$ surface is less active in CO and H_2 adsorption and activation than the orthorhombic $Mo_2C(100)$ and eclipsed $Mo_2C(001)$ surfaces comes from its surface bonding properties, *i.e.*; the Mo atoms on the CdI_2-antitype $Mo_2C(001)$ surface are coordinatively saturated, while those on the orthorhombic $Mo_2C(100)$ and eclipsed $Mo_2C(001)$ surfaces have unsaturated coordination sites. Although all three surface terminations are metallic, the orthorhombic $Mo_2C(100)$ and eclipsed $Mo_2C(001)$ surfaces are more metallic than the CdI_2-antitype $Mo_2C(001)$ surface on the basis of the computed density of states. Our results provide the basis for further systematic studies of the CO hydrogenation mechanisms on Mo_2C surfaces which is of great importance for practical industry applications in the field of energy.

Acknowledgements

This work was supported by National Basic Research Program of China (No. 2011CB201406), National Natural Science Foundation of China (No. 21073218), Chinese Academy of Sciences and Synfuels CHINA. Co., Ltd. We also acknowledge general finical support from the BMBF and the state of Mecklenburg-Western Pommerania.

References

1 L. E. Toth, *Transition Metal Carbides and Nitrides*, Academic Press, New York, 1971.
2 V. A. Gubanov, A. L. Ivanovsky and V. P. Zhukov, *Electronic Structure of Refractory Carbides and Nitrides*, Cambridge University Press, Cambridge, 1994.
3 Y. Liu, T. G. Kelly, J. G. Chen and W. E. Mustain, Metal Carbides as Alternative Electrocatalyst Supports, *ACS Catal.*, 2013, **3**, 1184–1194.
4 R. B. Levy and M. Boudart, *Science*, 1973, **181**, 547–549.
5 S. T. Oyama, *The Chemistry of Transition Metal Carbides and Nitrides*, Blackie Academic and Professional, Glasgow, 1996.
6 J. G. Chen, *Chem. Rev.*, 1996, **96**, 1447–1498.
7 J. G. Chen, J. Eng and S. P. Kelty, *Catal. Today*, 1998, **43**, 147–158.
8 H. H. H. Wu and J. G. Chen, *Chem. Rev.*, 2005, **105**, 185–212.
9 M. Nagai and K. Matsuda, *J. Catal.*, 2006, **238**, 489–496.
10 J. A. Schaidle, A. C. Lausche and L. T. Thompson, *J. Catal.*, 2010, **272**, 235–245.
11 M. L. Xiang, D. B. Li, W.-H. Li, B. Zhong and Y. H. Sun, *Fuel*, 2006, **85**, 2662–2665.
12 S. Zaman and K. J. Smith, *Catal. Rev.: Sci. Eng.*, 2012, **54**, 41–132.
13 V. Sundaramurthy, A. K. Dalai and J. Adjaye, *Appl. Catal., B*, 2006, **68**, 38–48.
14 H. A. Al-Megren, S. L. Gonzalez-Cortes, T. C. Xiao and M. L. H. Green, *Appl. Catal., A*, 2007, **329**, 36–45.
15 S. T. Oyama, *Catal. Today*, 1992, **15**, 179–200.
16 M. K. Neylon, S. Choi, H. Kwon, K. E. Curry and L. T. Thompson, *Appl. Catal., A*, 1999, **183**, 253–263.
17 S. J. Ardakani, X. B. Liu and K. J. Smith, *Appl. Catal., A*, 2007, **324**, 9–19.
18 R. Barthos and F. Solymosi, *J. Catal.*, 2007, **249**, 289–299.
19 F. Solymosi, J. Cserenyi, A. Szöke, T. Bansagi and A. Qszko, *J. Catal.*, 1997, **165**, 150–161.
20 K. Oshikawa, M. Nagai and S. Omi, *J. Phys. Chem. B*, 2001, **105**, 9124–9131.
21 A. Westgren and G. Z. Phragmen, *Z. Anorg. Allg. Chem.*, 1926, **156**, 27–36.
22 K. Kuo and G. Hägg, *Nature*, 1952, **170**, 245–246.
23 R. J. Fries and C. P. Kempter, *Anal. Chem.*, 1960, **32**, 1898.
24 E. Parthe and V. Sadagopan, *Acta Crystallogr.*, 1963, **16**, 202–205.
25 J. Haines, J. M. Leger, C. Chateau and J. E. Lowther, *J. Phys.: Condens. Matter*, 2001, **13**, 2447–2454.
26 X. R. Shi, S. G. Wang, H. Wang, C. M. Deng, Z. F. Qin and J. Wang, *Surf. Sci.*, 2009, **603**, 852–859.
27 A. N. Christensen, *Acta Chem. Scand., Ser. A*, 1977, **31**, 509–511.
28 J. Dubois, T. Epicier, C. Esnouf, G. Fantozzi and P. Convert, *Acta Metall.*, 1988, **8**, 1891–1901.
29 T. Epicier, J. Dubois, C. Esnouf, G. Fantozzi and P. Convert, *Acta Metall.*, 1988, **8**, 1903–1921.
30 P. Liu, J. A. Rodriguez and J. T. Muckerman, *J. Phys. Chem. B*, 2004, **108**, 15662–15670.

This journal is © the Owner Societies 2015

31 P. Liu, J. A. Rodriguez, T. Asakura, J. Gomes and K. Nakamura, *J. Phys. Chem. B*, 2005, **109**, 4575–4583.

32 P. Liu, J. A. Rodriguez and J. T. Muckerman, *J. Mol. Catal. A: Chem.*, 2005, **239**, 116–124.

33 P. Liu and J. A. Rodriguez, *J. Phys. Chem. B*, 2006, **110**, 19418–19425.

34 J. Ren, C. F. Huo, J. Wang, Y.-W. Li and H. Jiao, *Surf. Sci.*, 2005, **596**, 212–221.

35 J. Ren, C. F. Huo, J. Wang, Z. Cao, Y.-W. Li and H. Jiao, *Surf. Sci.*, 2006, **600**, 2329–2337.

36 J. Ren, J. Wang, C. F. Huo, X. D. Wen, Z. Cao, S. P. Yuan, Y.-W. Li and H. Jiao, *Surf. Sci.*, 2007, **601**, 1599–1607.

37 C. Pistonesi, A. Juan, A. P. Farkas and F. Solymosi, *Surf. Sci.*, 2008, **602**, 2206–2211.

38 M. E. Pronsato, C. Pistonesi, A. Juan, A. P. Farkas, L. Bugyi and F. Solymosi, *J. Phys. Chem. C*, 2011, **115**, 2798–2804.

39 C. Pistonesi, A. Juan, A. P. Farkas and F. Solymosi, *Surf. Sci.*, 2010, **604**, 914–919.

40 C. Pistonesi, M. E. Pronsato, L. Bugyi and A. Juan, *J. Phys. Chem. C*, 2012, **116**, 24573–24581.

41 A. J. Medford, A. Vojvodic, F. Studt, F. Abild-Pedersen and J. K. Nørskov, *J. Catal.*, 2012, **290**, 108–117.

42 J. R. dos Santos Politi, F. Vines, J. A. Rodriguez and F. IIIas, *Phys. Chem. Chem. Phys.*, 2013, **15**, 12617–12625.

43 K. Z. Qi, G. C. Wang and W. J. Zheng, *Surf. Sci.*, 2013, **614**, 53–63.

44 X. C. Liu, A. Tkalych, B. J. Zhou, A. M. Köster and D. R. Salahub, *J. Phys. Chem. C*, 2013, **117**, 7069–7080.

45 J. W. Han, L. Li and D. S. Sholl, *J. Phys. Chem. C*, 2011, **115**, 6870–6876.

46 X. R. Shi, J. Wang and K. Hermann, *J. Phys. Chem. C*, 2010, **114**, 13630–13641.

47 Y. H. Zhao, S. G. Li and Y. H. Sun, *J. Phys. Chem. C*, 2013, **117**, 18936–18946.

48 H. Tominaga and M. Nagai, *J. Phys. Chem. B*, 2005, **109**, 20415–20423.

49 H. Tominaga and M. Nagai, *Appl. Catal., A*, 2007, **328**, 35–42.

50 H. Tominaga and M. Nagai, *Appl. Catal., A*, 2008, **343**, 95–103.

51 H. Tominaga, Y. Aoki and M. Nagai, *Appl. Catal., A*, 2012, **423**, 192–204.

52 T. Wang, Q. Q. Luo, Y.-W. Li, J. Wang, M. Beller and H. Jiao, *Appl. Catal., A*, 2014, **478**, 146–156.

53 T. Wang, Y.-W. Li, J. Wang, M. Beller and H. Jiao, *J. Phys. Chem. C*, 2014, **118**, 3162–3171.

54 T. Wang, S. G. Wang, Y.-W. Li, J. Wang and H. Jiao, *J. Phys. Chem. C*, 2012, **116**, 6340–6348.

55 T. Wang, Y.-W. Li, J. Wang, M. Beller and H. Jiao, *J. Phys. Chem. C*, 2014, **118**, 8079–8089.

56 T. Wang, X. W. Liu, S. G. Wang, C. F. Huo, Y.-W. Li, J. Wang and H. Jiao, *J. Phys. Chem. C*, 2011, **115**, 22360–22368.

57 T. Miyao, I. Shishikura, M. Matsuoka, M. Nagai and S. T. Oyama, *Appl. Catal., A*, 1997, **165**, 419–428.

58 M. Nagai, A. M. Zahidul and K. Matsuda, *Appl. Catal., A*, 2006, **313**, 137–145.

59 Q. Q. Luo, T. Wang, G. Walther, M. Beller and H. Jiao, *J. Power Sources*, 2014, **246**, 548–555.

60 G. Kresse and J. Furthmüller, *Comput. Mater. Sci.*, 1996, **6**, 15–50.

61 G. Kresse and J. Furthmüller, *Phys. Rev. B: Condens. Matter Mater. Phys.*, 1996, **54**, 11169–11186.

62 P. E. Blochl, *Phys. Rev. B: Condens. Matter Mater. Phys.*, 1994, **50**, 17953–17979.

63 G. Kresse, *Phys. Rev. B: Condens. Matter Mater. Phys.*, 1999, **59**, 1758–1775.

64 J. P. Perdew, K. Burke and M. Ernzerhof, *Phys. Rev. Lett.*, 1996, **77**, 3865–3868.

65 M. Digne, P. Sautet, P. Raybaud, P. Euzen and H. Toulhoat, *J. Catal.*, 2004, **226**, 54–68.

66 S. Grimme, *J. Comput. Chem.*, 2006, **27**, 1787–1799.

67 E. R. McNellis, J. Meyer and K. Reuter, *Phys. Rev. B: Condens. Matter Mater. Phys.*, 2009, **80**, 205414.

68 D. L. Chen, W. A. A. Saidi and J. K. Johnson, *J. Phys.: Condens. Matter*, 2012, **24**, 424211.

69 T. Bučko, J. Hafner, S. Lebègue and J. G. Ángyán, *J. Phys. Chem. A*, 2012, **114**, 11814–11824.

70 S. L. Liu, X. X. Tian, T. Wang, X. D. Wen, Y.-W. Li, J. Wang and H. Jiao, *J. Phys. Chem. C*, 2014, **118**, 26139–26154.

71 T. Wang, S. Wang, Q. Luo, Y.-W. Li, J. Wang, M. Beller and H. Jiao, *J. Phys. Chem. C*, 2014, **118**, 4181–4188.

72 T. Wang, X.-X. Tian, Y.-W. Li, J. Wang, M. Beller and H. Jiao, *J. Phys. Chem. C*, 2013, **118**, 1095–1101.

73 T. Wang, X.-X. Tian, Y.-W. Li, J. Wang, M. Beller and H. Jiao, *ACS Catal.*, 2014, **4**, 1991–2005.

74 G. Henkelman and H. Jónsson, *J. Chem. Phys.*, 2000, **113**, 9978–9985.

75 M. Nagai and K. Matsuda, *J. Catal.*, 2006, **238**, 489–496.

76 C. A. Mims and L. E. McCandlish, *J. Phys. Chem.*, 1987, **91**, 929–937.

77 M. Ojeda, R. Nabar, A. U. Nilekar, A. Ishikawa, M. Mavrikakis and E. Iglesia, *J. Catal.*, 2010, **272**, 287–297.

78 B. T. Loveless, C. Buda, M. Neurock and E. Iglesia, *J. Am. Chem. Soc.*, 2013, **135**, 6107–6121.

79 T. Zeng, X.-D. Wen, Y.-W. Li and H. Jiao, *J. Phys. Chem. C*, 2005, **109**, 13704–13710.

80 K. Reuter and M. Scheffler, *Phys. Rev. B: Condens. Matter Mater. Phys.*, 2003, **68**, 045407.

81 F. Zasada, W. Piskorz, S. Cristol, J. F. Paul, A. Kotarba and Z. Sojka, *J. Phys. Chem. C*, 2010, **114**, 22245–22253.

82 S. Zhao, X. W. Liu, C. F. Huo, Y. W. Li, J. Wang and H. Jiao, *J. Catal.*, 2012, **294**, 47–53.

83 M. García-Mota, M. Rieger and K. Reuter, *J. Catal.*, 2015, **321**, 1–6.

84 J. S. Lee, S. T. Oyama and M. Boudart, *J. Catal.*, 1987, **106**, 125–133.

85 G. S. Ranhotra, G. W. Haddix, A. T. Bell and J. A. Reimer, *J. Catal.*, 1987, **108**, 24–39.

Universität Rostock
Dezernat 1
Referat 1.2

Doktorandinnen/Doktoranden-Erklärung gemäß § 4 Absatz 1 Buchstaben g und h der Promotionsordnung der Mathematisch-Naturwissenschaftlichen Fakultät der Universität Rostock

Name Wang, Tao ....
(Name, Vorname)

Anschrift Max-Planck-str.1.Zr.4.08.3, 18059, Rostock
…..
(Straße, PLZ, Wohnort)

Ich habe eine Dissertation zum Thema

About CO and H2 Activation Mechanisms on Fe and Mo2C Catalysts on the Basis of Density Functional
....
Theory Computation and Ab Initio Atomistic Thermodynamics

……………………………………………………………………………………………..

an der Mathematisch-Naturwissenschaftlichen Fakultät der Universität Rostock angefertigt. Dabei wurde ich von Frau/Herrn

Haijun Jiao
....
betreut.

Ich gebe folgende Erklärung ab:

1. Die Gelegenheit zum vorliegenden Promotionsvorhaben ist mir nicht kommerziell vermittelt worden. Insbesondere habe ich keine Organisation eingeschaltet, die gegen Entgelt Betreuerinnen/Betreuer für die Anfertigung von Dissertationen sucht oder die mir obliegenden Pflichten hinsichtlich der Prüfungsleistungen für mich ganz oder teilweise erledigt.

2. Ich versichere hiermit an Eides statt, dass ich die vorliegende Arbeit selbstständig angefertigt und ohne fremde Hilfe verfasst habe. Dazu habe ich keine außer den von mir angegebenen Hilfsmitteln und Quellen verwendet und die den benutzten Werken inhaltlich und wörtlich entnommenen Stellen habe ich als solche kenntlich gemacht.

Rostock, den ....
(Unterschrift)